Topology Optimization for Wave Propagation Problems with Experimental Validation

Christiansen, Rasmus Ellebæk

Publication date:
2016

Document Version
Publisher's PDF, also known as Version of record

Topology Optimization for Wave Propagation Problems with Experimental Validation

PhD Thesis

$$(EIv'')'' = q - \rho A\ddot{v}$$

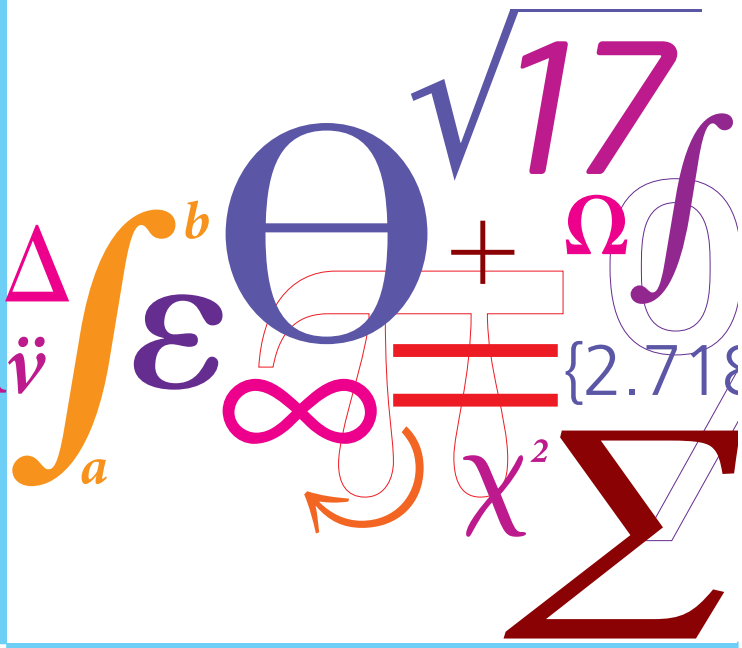

Rasmus E. Christiansen
DCAMM Special Report No. S208
June 2016

DTU Mechanical Engineering
Department of Mechanical Engineering

Topology Optimization for Wave Propagation Problems with Experimental Validation

Rasmus E. Christiansen

Kgs. Lyngby 2016
DCAMM Special Report No. S208

Topology Optimization for
Wave Propagation Problems
with Experimental Validation
June, 2016

PhD student:
Rasmus E. Christiansen

Main supervisor:
Professor Ole Sigmund
Technical University of Denmark

Co-supervisors:
Professor Jakob S. Jensen
Technical University of Denmark

Senior Researcher Boyan S. Lazarov
Technical University of Denmark

Technical University of Denmark
Department of Mechanical Engineering
Building 404, DK-2800 Kgs. Lyngby, Denmark
Phone: +45 45 25 25 25, Fax: +45 45 25 19 61
E-mail: info@mek.dtu.dk, URL: www.mek.dtu.dk

MEK-PHD: ISSN 0903-1685, ISBN 978-87-7475-460-2

Preface

This Thesis is written as the culmination of the PhD project titled *Topology Optimization for medium- to high frequency applications* funded through the research project *Topology Optimization - the Next Generation*, financially supported by Villum Fonden and the Technical University of Denmark (DTU). It is submitted as part of fulfilling the requirements for obtaining the degree of PhD from DTU. The work was carried out at the Department of Mechanical Engineering, Solid Mechanics at DTU in the period June 15$^{\text{th}}$ 2013 - June 14$^{\text{th}}$ 2016. The project supervisors were Professor dr.techn. Ole Sigmund and Senior Researcher Boyan Stefanov Lazarov (DTU Mechanical Engineering) and Professor dr.techn. Jakob Søndergaard Jensen (DTU Electrical Engineering).

I would like to thank my supervisors for the many instructive and inspiring conversations we have had concerning my research and for their open door policy allowing for immediate answers to pressing questions. In particular I thank my main supervisor Professor Ole Sigmund for being a great help in difficult periods which arose for different reasons over the course of the PhD project.

A 4 month research stay, visiting Professor Jan S Hesthavens group at École Polytechnique Fédérale de Lausanne (EPFL), was conducted as part of the PhD project. I would like to thank Professor Hesthaven for hosting me and for the instructive weekly meetings, and his secretary Delphine Vieira for helping me with the extensive practicalities surrounding the stay. I also thank all of Professor Hesthavens group for making me feel welcome and in particular Postdoctoral Assistant Paolo Gatto (EPFL) for good and continued research collaboration.

I thank Doctor Villads Egede Johansen (University of Cambridge Department of Chemistry) for valuable research inputs, Associate Professor Niels Aage (DTU Mechanical Engineering) for research collaboration and Assistant Professor Efren Fernandez-Grande (DTU Electrical Engineering) for close collaboration on multiple research projects. I thank Doctor Niels Morten Marslev Frandsen and Christopher Nellemann (DTU Mechanical Engineering) for many spirited and helpful conversations regarding my research and I extend my gratitude to Doctor Asger Schou Jacobsen (Max-Planck-Institut für Plasmaphysik) and Sebastian Arlund Nørgaard (DTU Mechanical Engineering) for proofreading this Thesis. I also thank all of my colleagues in the TopOpt Group and in the Section of Solid Mechanics at DTU, in particular my fellow PhD students, for contributing to a great work environment.

Warm thanks go to my friends and family who have all supported me throughout the PhD project. Finally a very special thanks goes to my wonderful girlfriend Lotte Lieutenant Pedersen who has supported me unconditionally and whose love and caring were of tremendous importance for the success of this project.

Kgs. Lyngby, June 14$^{\text{th}}$ 2016

Rasmus E. Christiansen

In memory of Jin Benny Junge
My dear friend
Strongest will and greatest loyalty

Abstract

This Thesis treats the development and experimental validation of density-based topology optimization methods for wave propagation problems. Problems in the frequency regime where design dimensions are between approximately one fourth and ten wavelengths are considered. All examples treat problems from acoustics, however problems for TE or TM polarized electromagnetic waves and shear waves in solids in two dimensions may be treated using the proposed methods with minor modifications.

A brief introduction to wave problems and to density-based topology optimization is included, as is a brief discussion of the finite element method and a hybrid of a wave based method and the finite element method, used to discretize the model problems under consideration.

A short discussion of the benefits and drawbacks of applying the hybrid method compared to the finite element method, used in conjunction with topology optimization, is included. Preliminary results for novel preconditioners used in conjunction with the generalized minimal residual method for the iterative solution of wave problems, potentially suited for use with topology optimization, are discussed.

The development of an extension to an existing method, for assuring geometric robustness of designs created using density-based topology optimization, is presented. The method is applied to acoustic cavity design, and a significant improvement in the geometric robustness of several cavities demonstrated. Experimental validation of an acoustic cavity designed using the proposed method is provided.

A novel approach for designing meta material slabs with selectively tuned negative refractive behavior is outlined. Numerical examples demonstrating the behavior of a slab under different conditions is provided. Results from an experimental study demonstrating agreement with numerical predictions are presented.

Finally an approach for designing acoustic wave shaping devices is treated. Three examples of applications are presented, a directional sound emission device, a wave-splitting device and a flat focusing lens. Experimental results for the first two devices, demonstrating good agreement between measurements and the numerical predictions, are provided.

Resumé

Afhandlingen omhandler udvikling og eksperimentel validering af densitetsbaseret topologioptimeringsmetoder til anvendelse for bølgeudbredelsesproblemer. Frekvensregimet hvor dimensionerne på de optimerede design er mellem en fjerdedel bølgelængde og ti bølgelængder betragtes. Alle eksempler behandler akustiske problemer, men elektromagnetiske problemer hvor TE eller TM polariserede bølger betragtes og problemer omhandlende tværgående bølger i faste stoffer i to dimensioner kan behandles ved hjælp af metoderne med mindre modifikationer.

En kort introduktion til bølgeproblemer og til densitetsbaseret topologioptimering er inkluderet. Ligeledes er en kort diskussion af finite element metoden og en hybrid af en bølge baseret metode og finite element metoden. Disse metoder anvendes til at diskretisere de behandlede modelproblemer.

En kort diskusion af fordele og ulemper ved at anvende hybridmetoden i stedet for finite element metoden i forbindelse med topologioptimering, er inkluderet. Indledende resultater for nye preconditionere anvendt med the generalized minimal residual method til iterativ løsning af bølgeproblemer, potentielt egnet til anvendelse sammen med topologioptimering, diskuteres.

En udvidelse til en eksisterende metode, der sikre geometrisk robusthed for designs skabt ved hjælp af densitetsbaserede topologioptimering, præsenteres. Metoden anvendes til akustisk kavitetsdesign, hvor en betydelig forbedring i den geometriske robusthed for flere kaviteter opnås. Eksperimentel validering af en akustisk kavitet, designet ved hjælp af den foreslåede metode, præsenteres.

En ny metode til design af metamaterialeblokke med negativt brydningsindeks skitseres. Numeriske eksempler demonstrerer opførslen af en blok under forskellige påvirkninger. Resultater fra en eksperimentel undersøgelse af en metamaterialeblok viser god overensstemmelse med de numeriske forudsigelser.

Endelig præsenteres en metode til design af enheder der udsender akustiske bølger. Tre eksempler på anvendelser præsenteres: En retningsbestemt lydudsendelsesenhed, en enhed der opdeler akustiske bølger efter frekvens og en flad fokuserende linse. Eksperimentelle resultater præsenteres for de første to enheder. Disse viser god overensstemmelse med de numeriske forudsigelser.

Publications

The following publications are submitted as part of this Thesis.

[P1] Paolo Gatto, Rasmus E. Christiansen and Jan Hesthaven. *A preconditioner based on a low-rank approximation with applications to topology optimization.* [manuscript].

[P2] Rasmus E. Christiansen, Boyan S. Lazarov, Jakob S. Jensen and Ole Sigmund. *Creating geometrically robust designs for highly sensitive problems using topology optimization - Acoustic cavity design.* Structural and Multidisciplinary Optimization, 52:737-754, 2015.

[P3] Rasmus E. Christiansen, Efren Fernandez-Grande and Ole Sigmund. *Experimental validation of a topology optimized acoustic cavity.* Journal of the Acoustical Society of America, 138(6):3470-3474, 2015.

[P4] Rasmus E. Christiansen and Ole Sigmund. *Designing meta material slabs exhibiting negative refraction using topology optimization.* Structural and Multidisciplinary Optimization, 54:469-482, 2016.

[P5] Rasmus E. Christiansen and Ole Sigmund. *Experimental Validation of Systematically Designed Acoustic Hyperbolic Meta Material Slab Exhibiting Negative Refraction.* Applied Physics Letters, 109, 101905 (2016).

[P6] Rasmus E. Christiansen and Efren Fernandez-Grande. *Designing Directional Acoustic Devices Using Topology Optimization - from method to experimental validation.* Journal of the Acoustical Society of America, [in review].

Contents

1 Introduction

1.1 Motivation and Goal

Wave propagation is a phenomenon existing within many areas of physics, such as acoustics, solid mechanics and electromagnetics. It is of fundamental importance to the transport of energy and information, e.g. acoustic sound waves, vibrations in solids and wireless communication through electromagnetic waves. An ever growing number of problems and applications involving wave propagation exists, in part ascribable to a mature theoretical understanding of wave phenomena, but also attributable to a growing toolbox of numerical methods and production techniques. New possibilities for application create a demand for improvements of design methods, enabling the design of better, smaller and novel devices.

This Thesis considers the application of the systematic design method of density-based topology optimization to wave propagation problems. Specifically the design of devices working robustly under geometric perturbations, of wave shaping devices and of meta materials with exotic properties, is considered. A main focus is the experimental validation of the proposed designs. This is a crucial step if the potentially highly complex designs obtained using topology optimization are to be given more consideration by researchers not familiar with the field. It is a step which is often neglected when new methods are proposed. Thanks to improvements in production methods, such as 3D-printing, it is now possible to produce and test designed devices as part of the research, as is demonstrated repeatedly in this Thesis.

The goals of this work may be summarized in three points as follows. 1. Expanding the catalog of methods for designing solutions to wave propagation problems by proposing novel methods and extensions for existing methods. 2. Developing and executing experiments to investigate numerical results in laboratory settings. 3. Considering different numerical methods for solving wave propagation problems to investigate their potential for treating computationally more demanding problems.

1.2 Structure

This Thesis is structured as follows. Chapter 2 provides a brief introduction to the physics of wave propagation and the equations used to model the wave problems considered in the following chapters. Chapter 3 introduces the main concepts from density-based topology optimization and states the general form of the optimization problems considered in this Thesis. Chapter 4 provides an overview of the numerical methods used to solve the wave equation. The chapter also presents preliminary results for two novel preconditioners usable in the solution of the wave equation for problems with high contrast in material parameters, [P1]. Chapter 5 treats work on the design of geometrically robust devices for wave propagation problems, [P2]. It also covers the experimental validation of a geometrically robust acoustic cavity, [P3]. Chapter 6 provides an overview of work done on the design of meta

material slabs exhibiting negative refraction using a novel design approach, [P4] together with an experimental validation, [P5]. Chapter 7 presents the numerical and experimental work done within the design of wave shaping devices, [P6]. Finally, Chapter 8 contains a brief summary, concluding remarks and areas of potential future work. Many figures included in this Thesis stem from the publications [P1]-[P6], which are included as part of this Thesis.

1.3 A Reader's Guide

This brief paragraph is meant to ease the reading by providing a few explanations and suggestions. Chapters 4-7 mainly provide an overview of the work submitted for publication during the PhD project. To get a deeper understanding of the work and results, the reader is encouraged to read the enclosed articles.

All abbreviations used in the Thesis are introduced at first use by writing the words to be abbreviated in italics followed by the abbreviation in parenthesis, e.g. *partial differential equation* (PDE). All subsequent uses of an abbreviated concept are made using the abbreviation without explanation. Citations are made using consecutive numbering in square brackets. Citations of the papers submitted as part of the Thesis are made in the format [PX] where X is a number from 1 to 6. Regarding the mathematical notation, all nontrivial symbols are defined at first use and are hereafter used consistently throughout the Thesis. This convention does not apply to the included publications, in which the notation is defined separately for each publication. It is recommended that the reader is familiar with:

- Algebra and calculus, [1–4].
- The concept of PDEs and the numerical tools used to solve PDEs, [5–11].
- The physics of acoustics, and to a lesser extend electromagnetism, and the concept of waves in physics. [6, 12–15].
- Mathematical optimization and constrained optimization, [16].
- Topology optimization, [17].

2 Wave Problems

The analysis of a wide range of dynamic problems across various areas of physics, e.g. acoustics [13], electromagnetics [12], optics [14] and solid mechanics [15] give rise to similar model PDEs, often collectively labeled as wave equations.

As a simple introductory example[1] of a problem governed by a wave equation consider the case of a long slender object consisting of an isotropic medium of density, ρ, modeled as *one-dimensional* (1D) subjected to a force, $F(x)$. For example a slender rod of constant cross sectional area, A, as sketched in Fig. 2.1. The question sought answered is; **what is the spatial displacement from equilibrium of any point of the object, denoted $\psi(x,t)$, as a function of space, $x \in \mathbb{R}$, and time, $t \in \mathbb{R}$?** $\mathbb{R}$ denoting the real numbers.

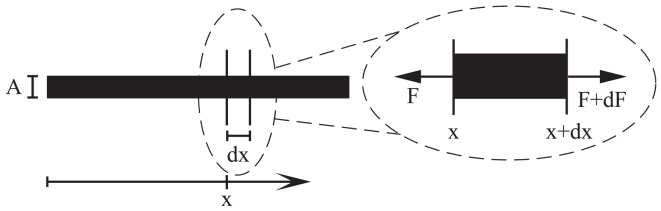

Figure 2.1: Illustration of 1D rod of cross sectional area, A, and an infinitesimal slice of width $\mathrm{d}x$. The rod is subjected to the force F at x and $F + \mathrm{d}F$ at $x + \mathrm{d}x$.

To answer this question, one derives the equilibrium equation (Newton's second law) for the forces acting on an infinitesimal slice of the rod of width dx, which here takes the form,

$$(F + dF) - F = \rho A dx \frac{\partial^2 \psi(x,t)}{\partial t^2}. \tag{2.1}$$

Here F is the force acting on the rod at x, $dF = \frac{\partial F}{\partial x} dx$ is the differential force across the infinitesimal slice, with $\frac{\partial}{\partial x}$ being the first partial derivative in x and $\frac{\partial^2}{\partial t^2} = \frac{\partial}{\partial t}\frac{\partial}{\partial t}$ denoting the second temporal partial derivative. For the isotropic medium the force F can be written as, $F = \sigma A$, where $\sigma = E\frac{\partial \psi}{\partial x}$ is the unit stress, E is the modulus of elasticity and $\frac{\partial \psi}{\partial x}$ the unit strain [18]. Inserting the expression for F into dF and the resulting expression into (2.1) and dividing by $\rho A dx$ one obtains the PDE,

$$\left(\frac{E}{\rho}\right) \frac{\partial^2 \psi(x,t)}{\partial x^2} = \frac{\partial^2 \psi(x,t)}{\partial t^2} \quad \Leftrightarrow \quad \frac{\partial^2 \psi(x,t)}{\partial x^2} = \frac{1}{c^2} \frac{\partial^2 \psi(x,t)}{\partial t^2}, \quad x \in \mathbb{R}, \quad t \in \mathbb{R}. \tag{2.2}$$

[1] Based on an example in [15, chap.6.3].

Here $c = \sqrt{\frac{E}{\rho}}$ is the speed of propagation of any displacement along the rod, often denoted as the wave speed. In this example the quantity, or field, of interest, $\psi(x,t)$, is the spatial displacement of the material along the rod as a function of space and time. This field is scalar for the 1D case but is a vector field for *two-dimensional* (2D) and *three-dimensional* (3D) cases, both of which require a more extensive derivation of the governing system of PDEs. In the problems treated in this Thesis all fields are scalar and therefore the following generalization of (2.2) is kept scalar in the field quantity. Extending (2.2) directly from one to n-dimensions in space, $n \in \{1,2,3\}$, yields the PDE,

$$\nabla^2\psi(\mathbf{x},t) = \frac{1}{c^2}\frac{\partial^2}{\partial t^2}\psi(\mathbf{x},t), \quad \mathbf{x} \in \boldsymbol{\Omega} \subseteq \mathbb{R}^n, \quad t \in T, \quad c > 0. \tag{2.3}$$

Here $\nabla^2 \equiv \nabla \cdot \nabla$, where $\cdot$ denotes the dot product and ∇ denotes the spatial gradient operator. The field of interest is again a function of space $\mathbf{x} \in \boldsymbol{\Omega} \subseteq \mathbb{R}^n$ in Cartesian coordinates and time $t \in T = [t_0, t_{\text{end}}], t_0 < t_{\text{end}}, t_0 \in \mathbb{R}, t_{\text{end}} \in \mathbb{R}$. That is, the field of interest is sought in $\boldsymbol{\Omega} \subseteq \mathbb{R}^n$, exemplified in 2D in Fig. 2.2.

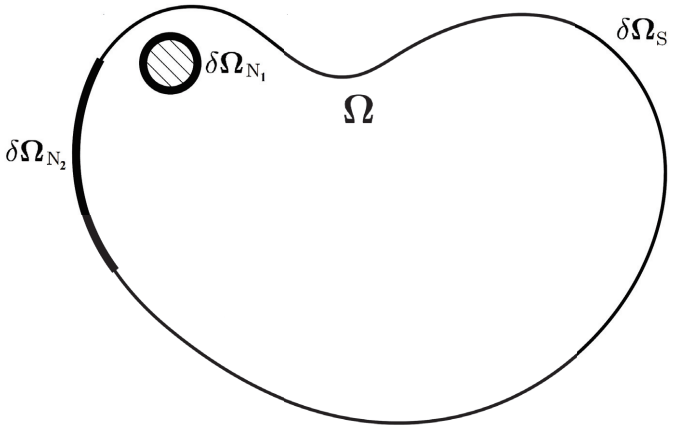

Figure 2.2: Sketch of model domain, $\boldsymbol{\Omega}$, with boundaries, $\delta\boldsymbol{\Omega}_*, * \in \{\mathrm{N}_1, \mathrm{N}_2, \mathrm{S}\}$.

By selecting an appropriate initial condition at $t = t_0$ and appropriate boundary conditions along $\delta\boldsymbol{\Omega}_*, * \in \{\mathrm{N}_1, \mathrm{N}_2, \mathrm{S}\}$, equation (2.3) constitutes a mathematically well-posed problem, i.e. a problem with an existing and unique solution which changes continuously with continuous changes in boundary and initial conditions. This definition is accredited to Hadamard [19]. Thus it is possible to identify a unique solution to (2.3). If the geometry of $\boldsymbol{\Omega}$ and the initial and boundary conditions are sufficiently simple it is possible to derive the solution analytically. However, in most cases this is not possible, and one must instead apply one of a range of numerical techniques to solve the problem. One approach for solving the problem is to discretize it in space using the *finite element method* (FEM) [5] and solve the resulting discrete system of equations in time using a time marching scheme, e.g. a Runge Kutta method [9], to obtain a discrete approximation of $\psi(\mathbf{x},t)$. Regardless of the approach, (2.3) must be solved in both space and time in order to obtain $\psi(\mathbf{x},t)$.

For a number of applications this is undesirably or even prohibitively expensive from a computational standpoint, a straightforward example being if the steady state behavior of ψ for a small set of n excitation frequencies, $\omega \in \{\omega_1, \omega_2, ..., \omega_n\}$ is of interest. Luckily it is possible to remove the temporal dependence in (2.3) and replace it with a frequency dependence, making solving the problem computationally cheaper for a range of problems.

2.1 Wave Problems in the Frequency Domain

If the time dependence of ψ can be assumed to be harmonic (see e.g. [14, pp 96-98]) it may be removed from (2.3) using separation of variables as follows (see e.g. [8, chap. 3.3]). Assume $\psi(\mathbf{x}, t) = \psi(\mathbf{x}) \exp(-\mathrm{i}\omega t)$ where exp denotes the natural exponential function, i is the imaginary unit, $\omega = 2\pi f$ is the angular frequency and f denotes the frequency. By inserting this expression for ψ in (2.3) and performing a simple reduction one obtains,

$$\nabla^2 \psi(\mathbf{x}) + \left(\frac{\omega}{c}\right)^2 \psi(\mathbf{x}) = 0, \quad \mathbf{x} \in \mathbf{\Omega} \subseteq \mathbb{R}^n, \quad \omega > 0, \quad c > 0. \tag{2.4}$$

Hence an equation is obtained which is independent of time while instead depending on the temporal angular frequency of the wave, ω. Equation (2.4) is known as the Helmholtz equation.

For the work presented in this Thesis a slightly more general form of the Helmholtz equation is considered,

$$\nabla \cdot \big(\alpha(\mathbf{x}) \nabla \psi(\mathbf{x})\big) + \omega^2 \beta(\mathbf{x}) \psi(\mathbf{x}) = 0, \quad \mathbf{x} \in \mathbf{\Omega} \subseteq \mathbb{R}^n, \quad \alpha > 0, \quad \beta > 0, \quad \omega > 0. \tag{2.5}$$

Here $\alpha(\mathbf{x})$ and $\beta(\mathbf{x})$ are material related parameters determined by the physics being modeled. The state field, ψ, is also determined by the physics in question.

In acoustics, the Helmholtz equation is used to model the sound pressure, p, in a fluid, (usually air). The state field is thus the sound pressure, $\psi = p$, while α and β are the inverse density $\alpha = \rho^{-1}$ and inverse bulk modulus $\beta = \kappa^{-1}$ of the material through which the waves propagate. A derivation of the Helmholtz equation for acoustics from fundamental principles, under certain assumptions, is provided in [13, chap. 2]. The main steps may be summarized as follows: Firstly, the principles of conservation of mass and momentum are applied on an infinitesimal cube of air. Secondly, the assumptions that the problem of sound propagation is adiabatic in nature and that the perturbations of the pressure field are small compared to the equilibrium value are made. Thirdly, it is assumed that the time variation of the field is harmonic in nature.

Considering (2.5) for out of plane shear waves in 2D, the state field is the out of plane displacement field, $\psi = u$ while α and β are related to the density, ρ, and the shear modulus, G, of the medium. For the electromagnetic/optical case ψ denotes either the out of plane electric field, E, or the out of plane magnetic field, B, and α

and β relate to the magnetic permeability, μ and electric permittivity ϵ. All examples presented in the following chapters consider parameters from acoustics, however in the interest of generality the state field is noted as ψ and the material parameters as α and β.

2.2 Boundary Conditions

The formulation of a well-posed PDE problem requires a set of boundary and/or initial conditions describing the behavior of the state field(s) along the boundary of the modeling domain and/or the field inside the domain at an initial time. In this work the following two types of boundary conditions are considered,

$$\lim_{|\mathbf{r}|\to\infty} |\mathbf{r}|^{\frac{n-1}{2}} \cdot \left(\frac{\partial \psi(\mathbf{r})}{\partial |\mathbf{r}|} - \mathrm{i}\frac{\omega}{c(\alpha,\beta)}\psi(\mathbf{r}) \right) = 0, \tag{2.6}$$

$$\mathbf{n}(\mathbf{x}) \cdot (\alpha(\mathbf{x})\nabla\psi(\mathbf{x})) = b(\mathbf{x}), \quad \mathbf{x} \in \delta\mathbf{\Omega}_{\mathrm{N}}. \tag{2.7}$$

Here n is the spatial dimension of the problem, $\mathbf{r}$ denotes the spatial position in polar coordinates, $\mathbf{n}(\mathbf{x})$ is the normal vector to the boundary and $b(\mathbf{x})$ is a function used to impose a desired value of the normal derivative of $\psi(\mathbf{x})$ along a boundary. (2.6) is known as the Sommerfeld radiation condition [6, chap. 1.6] and is a limit condition on the state field as $\mathbf{r}$ goes to infinity. This boundary condition is either approximately fulfilled by introducing an approximation of the condition along a truncation of the domain boundary, here denoted $\delta\mathbf{\Omega}_{\mathrm{S}}$, or by enforcing it directly in the numerical method. (2.7) is known as a Neumann boundary condition [8, chap. 3.10] and may be used to model a perfectly reflecting boundary (or symmetry condition) by selecting $b(\mathbf{x}) = 0$, or to prescribe a field entering the modeling domain at the boundary by selecting $b(\mathbf{x}) \neq 0$. This condition is imposed along $\delta\mathbf{\Omega}_{\mathrm{N}}$. Fig. 2.2 illustrates the truncated modeling domain with boundaries identified as either $\delta\mathbf{\Omega}_{\mathrm{S}}$ or $\delta\mathbf{\Omega}_{\mathrm{N}}$.

2.3 Discretized Model Equations

A way to obtain an approximate solution of the Helmholtz equation along with suitably chosen boundary conditions, (2.5)-(2.7), is by discretizing the problem into a linear system of equations. This system is in the following written as,

$$(\mathbf{K}(\alpha) + \omega^2\mathbf{M}(\beta))\boldsymbol{\psi} = \mathbf{f}(\omega) \Leftrightarrow \mathbf{S}(\alpha,\beta,\omega)\boldsymbol{\psi} = \mathbf{f}(\omega), \tag{2.8}$$

where $\mathbf{K}(\alpha)$ and $\omega^2\mathbf{M}(\beta)$ denote the discretization of the first and second terms in (2.5), respectively. The system of equation (2.8) is denoted as the state equations. $\boldsymbol{\psi}$ denotes the coefficients used in the discretization of ψ and $\mathbf{f}(\omega)$ contains the discretization of the boundary conditions. The state field ψ is recovered from $\boldsymbol{\psi}$ as a series expansion,

$$\psi(\mathbf{x}) = \sum_{i=1}^{\mathcal{N}_\psi} = \psi_i N_i, \tag{2.9}$$

where $N_i, i \in \{1, 2, ..., \mathcal{N}_\psi\}$ denote the basis functions used to discretize (2.5) and ψ_i is the i'th entry in the vector $\boldsymbol{\psi}$. For all problems considered in the following chapters, the model PDE is discretized using either the FEM or a *hybrid wave based and finite element method* (Hybrid WBM-FEM), both of which are discussed in more detail in chapter 4.

3 Topology Optimization

This Thesis considers a range of wave-based design problems, where the optimal topology of an object, designed to serve a given purpose under certain physical restrictions, is sought. Density-based topology optimization [17] is the tool used to solve the design problems.

Density-based topology optimization is a gradient based optimization technique used to solve PDE-constrained optimization problems. It has grown tremendously in popularity and use since its introduction to elasticity in the late 1980's by Bendsøe and Kikuchi [20]. The list of scientific papers describing work utilizing topology optimization is long and constantly growing. This paragraph lists a small subset of the work, selected as examples of interesting work within different areas of physics and/or due to its relevance to the topics considered in this Thesis.

Topology optimization was first applied to problems in linear elasticity (see e.g. [21]), still a major area of application, with recent work extending topology optimization to very large scale design considering hundreds of millions of degrees of freedom [22] and recent work in material design [23–25]. It has since been applied to a variety of problems across different areas of physics. Areas not directly considering wave propagation include thermal conduction and fluid mechanics. Examples from fluid mechanics are the seminal work on Stokes flow [26], work on fluid mixers [27] and work on applying topology optimization for unsteady flow problems [28,29]. Regarding fluids and thermal conduction recent work has been done on large scale 3D design of heat sinks, considering a coupling of the incompressible Navier-Stokes equation with the thermal convection-diffusion equation [30]. When considering wave problems, topology optimization has been applied in optics/electromagnetics, e.g. in the design of photonic crystals maximizing band gaps [31], in designing wave guide splitters and bends [32–35], wave guides with tailored dispersion properties [36], photonic switches [37], mode converters [38], electromagnetic and acoustic cloaking [39, 40], in meta material design such as optimizing for effective negative permeability [41] and for the design of structural colors [42]. A review of the applications within nano-photonics before 2011 is found in [43]. Topology optimization has also been applied in elastic wave propagation. Propagation in phononic crystals [44], with the recent work on self collimating phononic crystals [45]. Maximizing attenuation in viscoelastic composite materials [46] as well as elastic wave barriers [47]. In acoustics, early work utilizing topology optimization includes the design of an acoustic horn for optimal radiation efficiency [48], work on minimizing sound emitted from bi-material structures [49], on acoustic-structure interaction problems [50] and on noise reduction and noise barriers [51]. More recent work of interest includes, but is not limited to, design of noise barriers [52], acoustic design with fibrous material [53] and design of an acoustic mode converter [54].

The goal of the design problems considered in density-based topology optimization is to identify the optimal distribution of material, denoted as the physical design, inside a specified domain, $\mathbf{\Omega}_\mathrm{d} \subseteq \mathbf{\Omega}$, denoted as the design domain, in order to

minimize or maximize a given objective function, Φ, over a chosen target domain, $\mathbf{\Omega}_\mathrm{t} \subset \mathbf{\Omega}$. To reach this goal, density-based topology optimization relies on the introduction of a nonphysical, spatially dependent field, $\xi(\mathbf{x})$. ξ is allowed to take values in a finite interval, $\xi \in \Xi = [\xi^{\min}, \xi^{\max}]$, $0 \leq \xi^{\min} < \xi^{\max} < \infty$.[1] ξ is used to interpolate between the materials present in the design problem, e.g. between a solid (aluminum), and a fluid (air). This means that even though a design containing only material (aluminum) or no material (air) at any given point in space is sought, the introduction of ξ allows for a nonphysical mix of both material and no material at a given point. This point is considered in more detail in chapter 3.2.

The introduction of ξ turns the discrete problem of determining the distribution of the physical design into a continuous problem. This allows for the calculation of the gradients of Φ with respect to ξ; $\frac{\mathrm{d}\Phi}{\mathrm{d}\xi}$ which may be calculated efficiently using adjoint sensitivity analysis [17, 55], which in turn allows for the use of gradient based optimization algorithms to solve the design problem. A gradient based algorithm is in most cases significantly more efficient at solving PDE-constrained optimization problems than an algorithm which do not make use of gradient information, [56].

The manufacturability of the final designs is assured as follows: 1. As part of solving the design problem by applying a number of operations on ξ or by introducing a penalization term or constraint [57]. 2. In a post processing step, by applying a Heaviside projection on the final design field and manually cleaning the design. This results in a design consisting of a discrete distribution of the involved materials and not an unphysical mix thereof.

3.1 Design Problem

The design problems considered in the following chapters are formulated as minimization problems, subjected to a number of constraints, $c_i(\psi(\xi), \xi) \leq 0, i \in \{0, 1, 2, ...\}$. A functional, $\Phi(\psi(\xi), \xi)$ (the objective function) defined on a sub-domain of $\mathbf{\Omega}$ denoted $\mathbf{\Omega}_\mathrm{t}$ (the target domain), is minimized with respect to the scalar field $\xi(\mathbf{x}) \in \Xi \subset \mathbb{R}$ (the nonphysical design field), defined in a sub-domain of $\mathbf{\Omega}$ denoted $\mathbf{\Omega}_\mathrm{d}$ (the design domain). The condition $\mathbf{\Omega}_\mathrm{d} \cap \mathbf{\Omega}_\mathrm{t} = \emptyset$ is assumed in all cases. The different domains are illustrated in Fig. 3.1. The continuous optimization problem may be stated as,

$$\begin{aligned} \underset{\xi \in \Xi}{\text{minimize}} \quad & \Phi(\psi(\xi), \xi), \\ \text{subject to} \quad & c_i(\psi(\xi), \xi) \leq 0, \quad i \in \{0, 1, 2, ...\}, \\ & 0 \leq \xi(\mathbf{x}) \leq 1, \quad \forall\, \mathbf{x} \in \mathbf{\Omega_d}, \quad \xi(\mathbf{x}) = 0 \quad \forall\, \mathbf{x} \notin \mathbf{\Omega_d}. \end{aligned} \tag{3.1}$$

Prior to solving (3.1), ξ is discretized into a piecewise constant field consisting of $\mathcal{N}_\xi$ *design variables* (DVs) as,

$$\xi(\mathbf{x}) = \sum_{j=1}^{\mathcal{N}_\xi} \xi_j M_j(\mathbf{x}), \quad M_j = \begin{cases} 1 & \text{for } \mathbf{x} \in \mathbf{\Omega}_{\mathrm{d,j}} \\ 0 & \text{otherwise.} \end{cases} \quad \text{(see Fig. 3.1)} \tag{3.2}$$

[1] For the wave-propagation problems considered in this Thesis, $\xi^{\min} = 0$ and $\xi^{\max} = 1$.

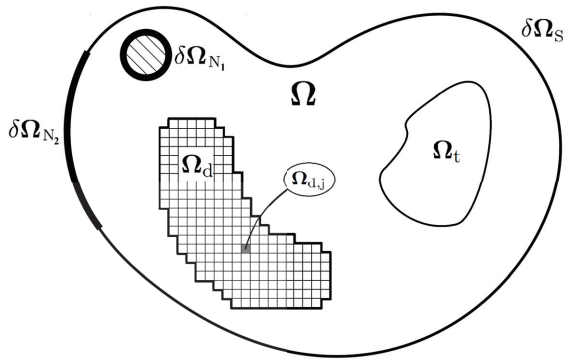

Figure 3.1: Sketch of model domain, $\mathbf{\Omega}$, with boundaries, $\delta\mathbf{\Omega}_*, * \in \{\mathrm{N}_1, \mathrm{N}_2, \mathrm{S}\}$, including the sub-domains, $\mathbf{\Omega}_\mathrm{d}$: the design domain, and $\mathbf{\Omega}_\mathrm{t}$: the target domain. The discretization of $\mathbf{\Omega}_\mathrm{d}$ into $\mathcal{N}_\xi$ disjoint patches is illustrated.

Furthermore all design problems consider the residual of the state equation (2.8) as an equality constraint. The problem of minimizing Φ over $\xi(\mathbf{x})$ is rewritten in discretized form in terms of the DVs, ξ_j, as,

$$\begin{aligned} \underset{\xi_j}{\text{minimize}} \quad & \Phi(\psi(\xi), \xi), \\ \text{subject to} \quad & c_0 : \mathbf{S}(\alpha(\xi), \beta(\xi), \omega)\boldsymbol{\psi} - \mathbf{f}(\omega) = 0, \\ & c_i(\psi(\xi), \xi) \leq 0, \quad i \in \{1, 2, ...\}, \\ & \xi_j^{\min} \leq \xi_j \leq \xi_j^{\max}, \quad j = 1, 2, ..., \mathcal{N}_\xi, \end{aligned} \tag{3.3}$$

where c_0 is fulfilled by solving the state equations for the current realization of ξ. This simultaneously yields ψ which is used to evaluate $\Phi(\psi(\xi), \xi)$. The problem (3.3) is solved iteratively using a gradient based optimization algorithm, with each iteration denoted as a design iteration. The optimization problem is terminated once a stopping criterion is met.

3.2 The (Non)Physical Design Field

For the design problems considered in the following chapters the nonphysical design field, ξ, is used to interpolate the material parameters α and β in (2.5) indirectly through a number of operators, the sequential application of which is denoted, P. α and β are thus interpolated between two materials, $\mathcal{M}_1, \mathcal{M}_2$, as $\alpha(P(\xi(\mathbf{x})))$ and $\beta(P(\xi(\mathbf{x})))$ using a simple linear interpolation,

$$*(P(\xi)) = *_{\mathcal{M}_2} + P(\xi)\left(*_{\mathcal{M}_1} - *_{\mathcal{M}_2}\right), \quad * \in \{\alpha, \beta\}. \tag{3.4}$$

Here $P(\xi(\mathbf{x})) = 1$ corresponds to material $\mathcal{M}_1$ at $\mathbf{x}$, while $P(\xi(\mathbf{x})) = 0$ corresponds to material $\mathcal{M}_2$ at $\mathbf{x}$. The quantity, $P(\xi)$, denoted the physical design field, is calculated from ξ using a smoothing and projection strategy coupled with a continuation scheme on the projection sharpness. This strategy has been developed

and contributed to in [58–62] and an extension is suggested in [P2] as described in detail in chapter 5. The smoothing and projection strategy consists in first applying a smoothing operator, P_s, to the design field, ξ,

$$P_s(\xi(\mathbf{x}_i)) = \frac{\int_{\mathbf{\Omega}_\mathrm{d}} w(\mathbf{x}_i - \mathbf{x}_j)\xi(\mathbf{x}_j)\mathrm{d}\mathbf{x}_j}{\int_{\mathbf{\Omega}_\mathrm{d}} w(\mathbf{x}_i - \mathbf{x}_j)\mathrm{d}\mathbf{x}_j}, \quad w(\mathbf{x}) = \begin{cases} R - |\mathbf{x}| & \forall\ |\mathbf{x}| \leq R \\ 0 & \text{otherwise} \end{cases}, \tag{3.5}$$

where $R \in [0, \infty[$ is the filter radius, followed by a projection operator, P_p,

$$P_p(P_s(\xi(\mathbf{x}_i))) = \frac{\tanh(\beta\eta) + \tanh(\beta(P_s(\xi(\mathbf{x}_i)) - \eta))}{\tanh(\beta\eta) + \tanh(\beta(1 - \eta))}, \tag{3.6}$$

where $\beta \in [1, \infty[$ is the projection sharpness and $\eta \in [\xi^{\min}, \xi^{\max}]$ is the threshold value. (3.6) may be thought of as a smoothed Heaviside function.

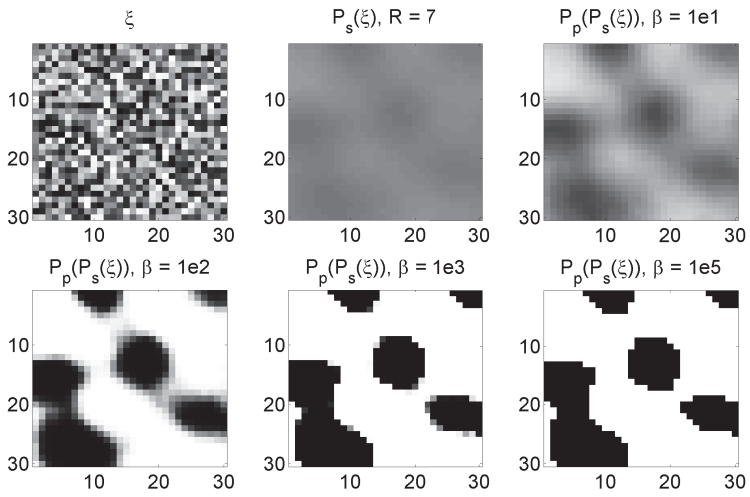

Figure 3.2: Application of the smoothing and projection operators (using $\eta = 0.5$) to a randomly generated field ξ. Black corresponds to a value of 1 and white to a value of 0. [Top left] Random design field, $\xi \in [0, 1]$. [Top middle] Smoothing operator applied to ξ with $R = 7$, $P_s(\xi)$. [Top right] Projection operator applied to $P_s(\xi)$ with $\beta = 1$. [Bottom row] Projection operator applied to $P_s(\xi)$ for increasing values of β.

$P(\xi)$ is in this case given as $P(\xi) = P_p(P_s(\xi))$. A continuation scheme is used for the projection sharpness as part of solving the optimization problem, (3.3). The scheme consists of increasing the value of β when a condition, on either the change in the objective function across design iterations, or on the number of design iterations since the last β-increase, is met. This process is continued until a predefined maximum value, $\beta_{\max}$, is reached. As $\beta \to \infty$ (a finite values is used in practice) the physical design field is forced to only take the values $P(\xi(\mathbf{x})) \in \{\xi^{\min}, \xi^{\max}\}$.[2] An illustration of the application of the smoothing and projection operators on ξ

[2] except in the unlikely case where $\xi(\mathbf{x}) = \eta \ \ \forall \ \ \mathbf{x} \in \mathbf{\Omega}_\mathrm{t} \equiv \mathbf{\Omega}$ ($\forall$ meaning for all)

and of the continuation approach is provided in Fig. 3.2 for a random nonphysical design field drawn from a uniform distribution. Black corresponds to the value 1 and white corresponds to the value 0. The first row in the figure illustrates the effect of applying the smoothing and projection operators. The effect of increasing the projection sharpness is illustrated by observing the change in the field from the last image in the first row and across the images in the second row from left to right.

The purpose of applying the smoothing and projection operators along with the continuation scheme is to push the optimization process to converge to a physical design field which consists purely of material $\mathcal{M}_1$ or material $\mathcal{M}_2$ at each point in space, and in part to avoid checkerboard like patterns in the design [17, chap. 1.3.2].

3.3 Sensitivities

A requirement when using a gradient based optimization algorithm is, as the name suggests, the availability of the gradient of the objective function, Φ, with respect to the DVs, ξ_j, i.e. $\frac{\mathrm{d}\Phi}{\mathrm{d}\xi_j},\ j \in \{1, 2, ..., \mathcal{N}_\xi\}$. This quantity is often in the literature denoted as the sensitivity of Φ with respect to ξ_j. $\frac{\mathrm{d}\Phi}{\mathrm{d}\xi_j}$ can be evaluated efficiently using the adjoint method [55]. An alternative to the adjoint method is to use finite differences to evaluate $\frac{\mathrm{d}\Phi}{\mathrm{d}\xi_j}$, however this requires solving (2.8) $\mathcal{N}_\xi$ times in each design iteration making it computationally infeasible to solve problems for large $\mathcal{N}_\xi$.

In short, the application of the adjoint method considering a complex system of equations may be outlined as follows (a full derivation is provided in [63, Appendix A]). First the residual state equation and its complex conjugate multiplied by the Lagrange multipliers, $\boldsymbol{\lambda}_1$ and $\boldsymbol{\lambda}_2$ respectively, are added to Φ,[3]

$$\tilde{\Phi} = \Phi + \boldsymbol{\lambda}_1^{\mathcal{T}}(\mathbf{S}\boldsymbol{\psi} - \mathbf{f}) + \boldsymbol{\lambda}_2^{\mathcal{T}}\overline{(\mathbf{S}\boldsymbol{\psi} - \mathbf{f})}, \tag{3.7}$$

where $(\cdot)^{\mathcal{T}}$ denotes the transpose and $\overline{(\cdot)}$ denotes the complex conjugate. Assuming that the residual equations are fulfilled, it is then shown that $\boldsymbol{\lambda} = \boldsymbol{\lambda}_1 = \overline{\boldsymbol{\lambda}_2}$ and that total derivative of $\tilde{\Phi}$ with respect to ξ_j takes the form,

$$\begin{aligned} \frac{\mathrm{d}\tilde{\Phi}}{\mathrm{d}\xi_j} = \frac{\mathrm{d}\Phi}{\mathrm{d}\xi_j} &= \frac{\partial\Phi}{\partial\xi_j} + \frac{\partial}{\partial\xi_j}\left(2\Re\left(\boldsymbol{\lambda}_1^{\mathcal{T}}(\mathbf{S}\boldsymbol{\psi} - \mathbf{f})\right)\right) \Leftrightarrow \\ \frac{\mathrm{d}\Phi}{\mathrm{d}\xi_j} &= \frac{\partial\Phi}{\partial\xi_j} + 2\Re\left(\boldsymbol{\lambda}^{\mathcal{T}}\left[\frac{\partial\mathbf{S}}{\partial\xi_j}\boldsymbol{\psi} - \frac{\partial\mathbf{f}}{\partial\xi_j}\right]\right), \end{aligned} \tag{3.8}$$

with $\boldsymbol{\lambda}$ being the solution to the adjoint problem,

$$\mathbf{S}^{\mathcal{T}}\boldsymbol{\lambda} = -\frac{1}{2}\left(\frac{\partial\Phi}{\partial\boldsymbol{\psi}_\Re} - \mathrm{i}\frac{\partial\Phi}{\partial\boldsymbol{\psi}_\Im}\right)^{\mathcal{T}}. \tag{3.9}$$

[3] Lagrange multipliers are treated in [64, chap. 17.6].

Here $\Re$ and $\Im$ denote the real and imaginary part respectively. Hence in order to calculate $\frac{\partial \Phi}{\partial \xi_j}$ in a given design iteration, it is only required to calculate $\frac{\partial \Phi}{\partial \boldsymbol{\psi}_\Re}$ and $\frac{\partial \Phi}{\partial \boldsymbol{\psi}_\Im}$ and solve the adjoint problem (3.9), hereby reducing the computational burden from solving $\mathcal{N}_\xi$ systems of linear equations to solving 2 systems of linear equations.

The application of P to ξ introduces additional factors in (3.8) calculated using the rules for the derivative of the composition of functions (the chain rule).

3.4 Solving the Optimization Problem

Two related algorithms have been used to solve the optimization problems considered in this Thesis. Both are developed by K. Svanberg and are described in [65] and [66] respectively. The first is *The Method of Moving Asymptotes* (MMA) and the second is a modified version of *The Globally Convergent Method of Moving Asymptotes* (GCMMA). Both methods rely on the calculation of convex approximations of the optimization problem being solved and using these approximations to update the DVs in an iterative process, such that the objective function is lowered without violating the constraints. A simplified description of the difference between MMA and GCMMA is that GCMMA introduces an iterative check of the quality of the convex approximations of the constraints and objective function values not present in MMA. If the values of the approximations are less than the true values (evaluated using the full model) better approximations are calculated and a new check performed. The modification applied to GCMMA for the problems considered in this Thesis consists of limiting the number of iterations of the procedure used to check the approximations to 3. The change from MMA to GCMMA was found to improve the convergence behavior significantly for most of the considered problems. The limitation to 3 iterations was found to significantly reduce the computational burden of applying GCMMA without impacting the convergence behavior significantly. MMA was used for the results published in [P1] and [P2] while the modified version of GCMMA was used for the results in [P4] and [P6].

Figure 3.3 presents a flowchart for the procedure used to solve a design problem.

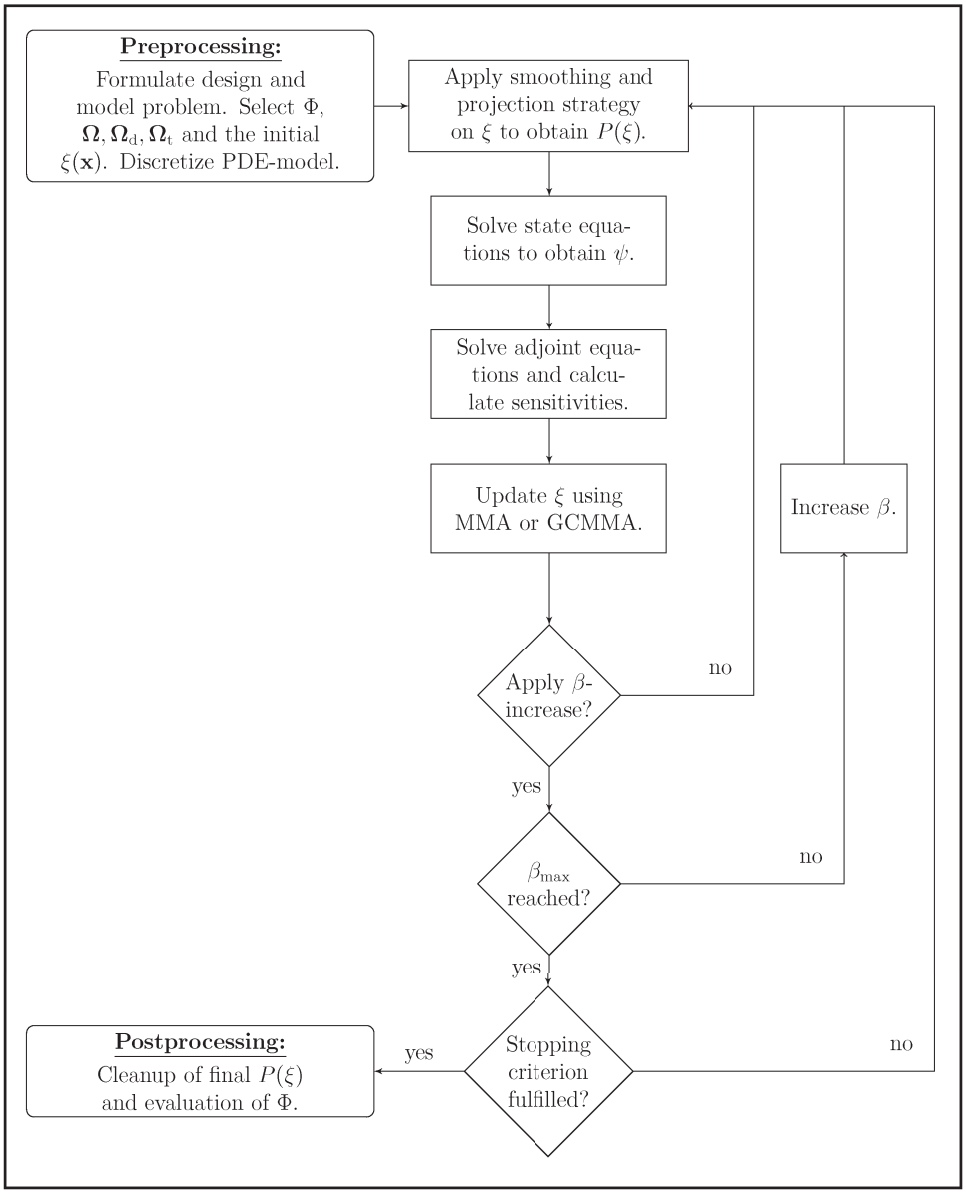

Figure 3.3: Flowchart illustrating the density-based topology optimization procedure.

4 Solving the Wave Problem, [P1]

For most PDE-problems of practical interest no analytical solution can be derived and one instead has to rely on a numerical approximation of the solution. Over the last century a large number of different numerical methods for solving PDEs has been developed. As examples of categories of methods may be mentioned: finite volume methods [7], finite element methods [5, 6, 10], finite difference methods [9] and spectral methods [11], each having different strengths and weaknesses.

Using an efficient numerical method to solve a PDE is naturally always of interest. The efficiency of the numerical method is often critical to density-based topology optimization problems however, since the solution of a typical design problem requires on the order of O(100)-O(1000) design iterations, in each of which the modeling PDE and the corresponding adjoint problem, must be solved. Furthermore, in most cases the majority of the computational cost expended in each design iteration stems from solving the discretized model PDE and adjoint problem.

4.1 Numerical Methods

The design problems considered in chapters 5-7 were all solved using either the FEM or the Hybrid WBM-FEM, both of which are treated briefly below.

4.1.1 The FEM

This section provides a non-rigorous outline of the FEM[1], meant to give the reader an overview of the method. For a comprehensive introduction to the FEM see e.g. [5].

Consider the model PDE in (2.5). As a first step the equation is recast into its weak form by multiplying it by a function, N, integrating it over the modeling domain and applying Greens theorem, [1, chap. 10.4]. After a rearrangement of terms one obtains,

$$\int_{\mathbf{\Omega}} \big(\alpha(\mathbf{x})\nabla\psi(\mathbf{x})\nabla N\big) - \omega^2\beta(\mathbf{x})\psi(\mathbf{x})N\mathrm{d}\mathbf{\Omega} = \int_{\delta\mathbf{\Omega}} \mathbf{n}(\mathbf{x})\cdot(\alpha(\mathbf{x})\nabla\psi(\mathbf{x}))N\mathrm{d}\delta\mathbf{\Omega}. \quad (4.1)$$

Next a suitable finite dimensional function space, $\mathbb{V}_f$, spanned by a set of functions, N_i; $\mathbb{V}_f = \mathrm{span}\{N_i\}_{i=1}^{\mathcal{N}_\psi}$, usually named test functions or trial functions, is introduced.[2]. Then ψ in (4.1) is replaced by an approximation given as an expansion in terms of the trail functions spanning $\mathbb{V}_f$, see (2.9). Finally the function N is replaced by the test functions, $N_j, \quad j \in 1, 2, ..., \mathcal{N}_\psi$ one by one, hereby obtaining $\mathcal{N}_\psi$ equations, equal to the number of unknown coefficients in (2.9).

The model domain is discretized into a set of $\mathcal{N}_e$, non-overlapping elements covering $\mathbf{\Omega}$. Each element has a number of nodes associated with it. In this work

[1] Assuming a Galerkin formulation. [6, chap. 2.1.3]

[2] A number of restrictions are imposed on $\mathbb{V}_f$ which are not covered here.

quadratic bilinear four node elements are considered, sketched in Fig. 4.1. This discretization of $\mathbf{\Omega}$ into nodes and elements is denoted as a mesh.

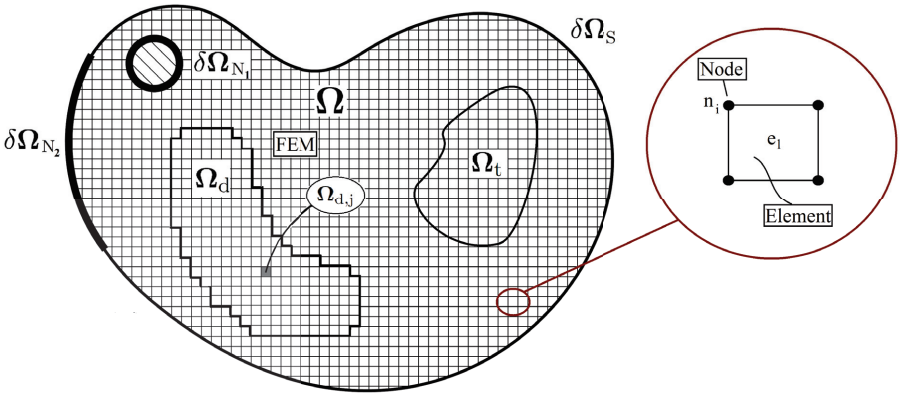

Figure 4.1: Sketch of mesh used for FEM discretization of model domain, $\mathbf{\Omega}$, with boundaries, $\delta\mathbf{\Omega}_*, * \in \{\mathrm{N}_1, \mathrm{N}_2, \mathrm{S}\}$, including the sub-domains, $\mathbf{\Omega}_{\mathrm{d}}$: the design domain, and $\mathbf{\Omega}_{\mathrm{t}}$: the target domain. The discretization of $\mathbf{\Omega}_{\mathrm{d}}$ into $\mathcal{N}_\xi$ disjoint elements (the FEM mesh) is illustrated. A zoom on the l'th element, e_l, is shown.

The total number of nodes in the mesh is equal to the number of functions, N_i, spanning $\mathbb{V}_f$, i.e. $\mathcal{N}_\psi$. Each N_i is chosen such that it fulfills; $N_i(\mathbf{x}_j) = 1$ for $i = j$ and $N_i(\mathbf{x}_j) = 0$ for $i \neq j$. Each N_i is also chosen to only have support on elements containing the node with which it is associated. After having selected N_i, the integration of (4.1) is performed to obtain a linear system of $\mathcal{N}_\psi$ discrete equations, see (2.8), for the $\mathcal{N}_\psi$ unknown coefficients in (2.9). Due to the choice of the mesh and N_i it is possible to consider each element individually and break the problem of integrating (4.1) over $\mathbf{\Omega}$ into $\mathcal{N}_e$ separate problems (one on each element), simplifying the process of forming the linear system significantly by considering a superposition of linear systems on each of the elements. The breakdown into local problems on elements allows for a high level of geometric flexibility in the shape of $\mathbf{\Omega}$.

4.1.2 The WBM and Hybrid WBM-FEM

The Hybrid WBM-FEM is used to discretize the model problem for the majority of the design problems considered in this Thesis, using the approach detailed in [67]. For a comprehensive derivation and explanation of the *wave based method* (WBM) and the Hybrid WBM-FEM see e.g. [67–70] and references therein. The following paragraphs aim at providing the reader with an introductory non-rigorous overview of the WBM and Hybrid WBM-FEM.

A general property of wave problems governed by the homogeneous Helmholtz equation is that, given a sufficiently simple geometry of the modeling domain, the solution ψ can be expanded using an analytically known and complete set of complex wave functions, $\phi_n \in \mathcal{S}_\phi, n \in \{1, 2, ...\}$, all of which are themselves solutions to the homogeneous Helmholtz equation for specific values of ω denoted ω_n, $n \in \{1, 2, ...\}$.

Thus the solution to the homogeneous Helmholtz equation in the simple geometry at a given frequency, ω, may be written as $\psi = \sum_{n=1}^{\infty} \psi_n \phi_n$. It is possible to approximate ψ by truncating the infinite series as $\psi \approx \sum_{n=1}^{\mathcal{N}_\phi} \psi_n \phi_n$, where the choice of $\mathcal{N}_\phi$ controls the accuracy of the approximation. This property means that a numerical scheme for solving wave problems in sufficiently simple geometries can be formulated, which significantly reduces the computational cost required to obtain ψ for a range of problems, when compared to the FEM outlined in the previous section.

A number of limitations of the WBM approach exist, however. Firstly the set of complex wave functions depends on the model problem geometry, limiting the approach to considering convex domains. Secondly, the set of complex wave functions used to expand the solution may potentially lead to an ill conditioned system matrix, which in turn results in inaccurate numerical approximations of ψ, unless appropriate precautions are taken. This effectively puts an upper limit on the frequency, ω, for which the method is applicable given a certain numerical accuracy of the machine on which it is implemented. Thirdly, the computational cost associated with constructing the WBM based system matrix is significantly larger than the cost for the FEM, due to the wave functions having global support on the modeling domain and to the high accuracy needed to assure good conditioning of the system matrix. The global support leads to a dense system matrix as opposed to the sparse banded matrix resulting from applying the FEM for domain discretization.

An additional limitation of the WBM, relevant in connection with density-based topology optimization, is that the complex wave functions are only solutions to the homogeneous Helmholtz equation in domains with constant material parameters. Hence the method is not directly applicable for problems where material parameters change spatially, i.e. it cannot be used directly for topology optimization problems.

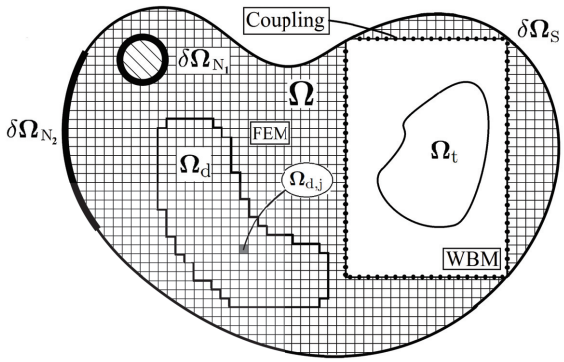

Figure 4.2: Sketch of the Hybrid WBM-FEM discretization of the model domain, $\mathbf{\Omega}$, with boundaries, $\delta\mathbf{\Omega}_*, * \in \{\mathrm{N}_1, \mathrm{N}_2, \mathrm{S}\}$, including the sub-domains, $\mathbf{\Omega}_\mathrm{d}$: the design domain, and $\mathbf{\Omega}_\mathrm{t}$: the target domain.

A hybrid method combining the FEM and the WBM was treated in [69]. The method combines the low computational cost of the WBM with the geometric flexibility of the FEM to create a hybrid method capable of handling wave problems in complex geometries at a reduced cost. In short the Hybrid WBM-FEM works by partitioning the modeling domain into large convex subdomains with simple geometry

and small subdomains of complex geometry. The convex subdomains are discretized using the WBM and the smaller geometrically complex subdomains are discretized using the FEM. The WBM and FEM subdomains are then connected using one of a number of coupling techniques [67, chap 7.3-7.4]. A discretization of $\mathbf{\Omega}$ using the Hybrid WBM-FEM approach is sketched in Fig. 4.2.

4.1.3 Topology Optimization using the Hybrid WBM-FEM

In contrast to the WBM it is possible to utilize the Hybrid WBM-FEM in connection with density-based topology optimization. This is done by discretizing the design domain, $\mathbf{\Omega}_\mathrm{d}$, using the FEM while the majority of the remaining model domain, $\mathbf{\Omega}$, is discretized using the WBM. The application of the Hybrid WBM-FEM in connection with topology optimization was suggested recently in [71].

As stated earlier, a significant part of the computational cost of applying the WBM is associated with the construction of the system matrix. This fact makes the Hybrid WBM-FEM interesting to use with density-based topology optimization, because neither the material parameters, nor the geometry in the part of $\mathbf{\Omega}$ where the WBM is applied, changes in the process of solving the design problem. It is therefore only necessary to perform the WBM discretization once in the pre processing step. Hereby one drawback of the WBM is all but eliminated, since the discretization cost is effectively averaged across the O(100)-O(1000) design iterations needed to solve the design problem.

The result of applying the Hybrid WBM-FEM instead of the FEM is a potentially significant reduction in the computational cost of solving density-based topology optimization problems, given that the design domain only constitute a small part of the full model domain. Numerical experiments revealed a significant computational cost reduction for problems where $\mathbf{\Omega}_\mathrm{d}$ constituted 10% or less of $\mathbf{\Omega}$.[3]

4.2 Issues with Solving Wave Problems in Very Large Scale

One of the many goals of the research effort dedicated to structural optimization methods, i.e. shape and topology, is to enable its use for very highly detailed PDE-models of (multi)-physics problems (in 3D). Such models may consist of billions of *degrees of freedom* (DOF). Hence, reaching the goal requires the development of highly efficient numerical solvers capable of handling problems with billions of DOF, a truly non-trivial task. While the development has been successful for a range of PDE-problems, there are still significant challenges to be overcome for time-harmonic wave propagation problems, as will be outlined in the following.

Two fundamentally different approaches to solving the systems of linear equations resulting from the discretization of PDE-problems exist: Direct methods and iterative methods [72]. In direct methods the system of equations is solved directly using e.g. LU-, LDL- or Cholesky-decomposition [1, chap. 20.2]. In the iterative approach a

[3] Using the author's implementation of the method in MATLAB 2013a, utilizing the built in linear system solver. The implementation was not highly optimized.

starting guess for the solution is provided, the residual of the equation system is calculated and gradually reduced using an iterative procedure, until it is sufficiently small in an appropriate error measure.

Using direct methods the solution to any system of linear equations with full rank can be obtained.[4] However, as the size of a system under consideration grows sufficiently large, it is no longer computationally feasible to solve the problem using a direct method. Using iterative methods, with appropriately chosen preconditioners [72, chap. 10], it is possible to parallelize the solution process for certain classes of problems in a highly scalable manner. The availability of such a solver setup makes it tractable to increase the problem size from millions to billions of DOFs. For some classes of PDE-problems, such as problems arising in elastostatic analysis in linear elasticity, it is currently possible to solve systems with more than a billion DOF using iterative methods. A solver based on an iterative method has recently been applied to density-based topology optimization problems within linear elasticity, considering more than 100 million design variables and 300 million DOF [22].

Wave problems governed by the Helmholtz equation are indefinite in nature and their associated Green's function has a non-local structure. This has proven to make solving such problems very difficult and in some cases impossible, using classical iterative methods and preconditioners. The problems associated with solving the Helmholtz equation using iterative methods are described in detail by Ernst and Gander in their book chapter *Why it is Difficult to Solve Helmholtz Problems with Classical Iterative Methods* [73].

A further complication related to density-based topology optimization, is the fundamental aspect that the material parameters in the PDE-problem vary throughout the modeling domain and change during the design process. This adds further difficulty for solving the discretized Helmholtz equation using an iterative method, due to the large (and a priori unpredictable) variations in the local wavelength of the solution to the model problem.

Highly specialized iterative methods for solving specific problems governed by the Helmholtz equations do exist, these are also touched upon in [73]. However, no generally applicable and simultaneously efficient iterative method, capable of handling high contrast in the modeling domain have, to the author's knowledge, been developed yet.

4.2.1 Investigated Preconditioners

A brief discussion of the applicability of two preconditioners used in conjunction with *the generalized minimal residual method* (GMRES) to solve the discretized Helmholtz equation in connection with topology optimization follows here. The preconditioners have been developed by researchers at the department of Computational Mathematics and Simulation Science MCSS at EPFL, [P1], [74].[5] They have been tested for topology optimization problems in collaboration between the author and the researchers at EPFL.

[4] Given infinite numerical accuracy which is not realizable in practice.

[5] Both papers are currently in review. [74] is found on arXiv.org.

Low-Rank Correction [P1]

The preconditioner proposed in [P1] consists of a banded Jacobi preconditioner with the addition of a low-rank correction term constructed using a probabilistic algorithm based on interpolative decomposition [75, chap. 3.2.3]. The preconditioner is used with GMRES to solve the discretized Helmholtz problem. It is remarked that no firm theoretical foundation currently exists which proves that the preconditioner is applicable to the Helmholtz problem, and thus this is a heuristic approach.

The preconditioner is cheap to apply, but the low-rank correction term is very expensive to compute. It requires a potentially large number of (perfectly parallelizable) solutions of linear systems, constructed from the indefinite system matrix in need of preconditioning. In spite of this limitation, the preconditioner could possibly still be of interest for topology optimization, where a large number of solutions of a slowly varying system is needed. This is because the banded Jacobi preconditioner is cheap to calculate in each design iteration and that it potentially is possible to recycle the low rank correction term between solutions. This idea was investigated in [P1] considering two different topology optimization problems.

It was demonstrated through numerical experiments that the expensive low-rank correction term could be recycled across ≈ 60 design iterations without incurring a significant increase in the number of GMRES iterations needed to solve the linear system. Numerical experiments also suggested that the efficiency of the preconditioner in terms of GMRES iterations improved with increasing systems size, and that the solution time scaled as $\mathrm{O}(n^{1.5})$.

While these results are interesting, there are several problematic issues. Firstly, only model problems with less than 10^5 DOF were considered in [P1], which is far from the number of interest in large scale application. Secondly, the construction of the low-rank correction term in the preconditioner required significantly more than 60 solutions of the considered system of equations. Hence, the preconditioner is extremely expensive to construct in terms of the total computational cost. Even though the calculation of the low-rank correction term can be done in parallel, it still requires the solution of several large scale indefinite linear problems, which themselves are difficult to solve in very large scale. Hence, it seems unlikely that the preconditioner will be usable as a general tool for topology optimization of wave problems. Large scale testing is required before any final conclusions about its applicability can be drawn.

Low-rank approximation of Schur Complements

The second preconditioner investigated for use with GMRES in the iterative solution of a density-based topology optimization problem governed by the Helmholtz equation, is proposed in [74]. It is constructed based on a nested dissection of the system matrix and low-rank approximations of Schur complements as *Hierarchical-Block-Separable* (HSS) matrices. As was the case for the preconditioner considered in the previous section it is remarked that the application of the preconditioner to indefinite Helmholtz problems is heuristic.

The construction of the preconditioner does not require the solution of large indefinite problems, however it is still potentially expensive. In [74] a theoretical estimate of the cost with a lower bound of linear complexity and an upper bound of quadratic complexity in terms of system size is reported. The application cost of the preconditioner is reported in [74] to be within linear complexity.

Parallelization of the HSS compression process is complicated, however the software package STRUMPACK provides a library for performing this compression and the application of HSS compressed matrices in parallel. A complete parallelization of the construction and the application of the preconditioner is thus feasible.

One reason for investigating the application of the preconditioner to topology optimization problems is that it may be possible to recycle it between design iterations, hereby avoiding a recomputation. As demonstrated by the preliminary results below, the state equation system may be solved iteratively using GMRES with the recycled preconditioner without experiencing a significant increase in iteration count for a number of consecutive design iterations.

An update scheme for the preconditioner based on Taylor expansion can be derived. This increases the number of possible design cycles before a recomputation is required. The cost of applying the update depends on the number of terms included in the expansion. The cost of including one additional term is equivalent to one application of the preconditioner. Hence the cost of considering a first order update is equivalent to two applications of the preconditioner.

Results of a preliminary study using a serial and non-optimized implementation of the preconditioner are reported in Fig. 4.3. The preconditioner is used in conjunction with GMRES to solve the system of state equations for a topology optimization problem governed by the Helmholtz equation. A discretization using $\approx 10^6$ DOF is considered. The design problem considers local pressure minimization inside a unit square acoustic cavity through the distribution of solid material (aluminum) in an air background in the cavity (see chapter 5 for a description of the model problem).

For the reported results the preconditioner is applied both with and without a first order update. In both cases the preconditioner is recycled until 40 or more GMRES iterations (considering the first order updated preconditioner) are used to solve the state equation system for a given design iteration. The first 100 design iterations are considered. Figure 4.3a shows the number of GMRES iterations as a function of design iteration with and without the first order update. It is observed that the number of GMRES iterations remain low, and near constant, for large portions of the design process. The vertical red lines denote the four design iterations for which the DV's and state field are shown in Fig. 4.3b and Fig. 4.3c, respectively. From Fig. 4.3b is it seen that the physical design field changes from gray to black and white in several regions across the 100 design iterations. From Fig. 4.3c it is observed that the pressure field changes significantly as well.

The preliminary results reported in Fig. 4.3a are promising and have motivated ongoing work on a parallel implementation of the preconditioner for large scale testing.

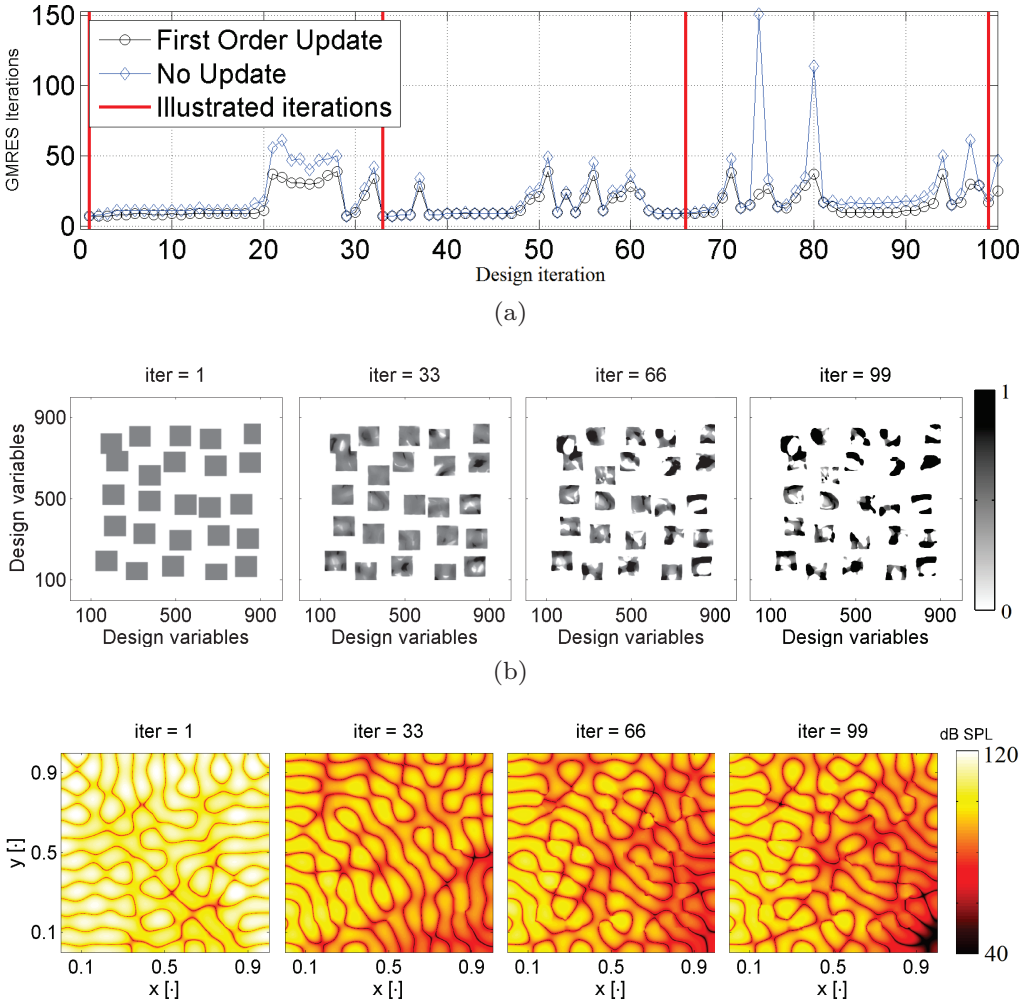

Figure 4.3: (a) GMRES iterations used to solve the state equation system throughout the design process. (b) Design variables in modeling domain, white is air and black is material. (c) Pressure field in modeling domain [dB SPL ref 20μPa].

5 Device Robustness [P2], [P3]

All practical problems in science and engineering suffer from uncertainty in most, if not all, involved parameters. Uncertainty which may stem from measurement limitations, measurement errors, production errors or an oversimplified mathematical model of the physical problem under consideration etc. In many cases such uncertainties are insignificant and can be ignored. However, for problems where highly sensitive parameters are involved, or where highly optimized solutions are sought, even small uncertainties in involved parameters may have a significant impact on the performance of an optimized design. This chapter focuses on the robustness of designs with respect to geometric uncertainties.

Several examples demonstrating that devices designed using density-based topology optimization, may be sensitive to small perturbations of their geometry are found in the literature. An example from linear elasticity is [76] where a highly optimized compliant mechanism is shown to break under geometric perturbations due to the presence of small connecting features in the design. Another is [77] where the optimization of a slender column for geometric robustness is considered. An example from optics is the robust design of a 1D photonic switch [37]. A recent review paper discussing the problem of assuring length scale, manufacturability and the robustness of designs created using density-based topology optimization is [78].

In the following, an overview of the work done in [P2] and [P3] is provided. In short, [P2] considers the minimization of sound pressure in a part an acoustic cavity through the modification of the material distribution along one of the cavity walls. The aim of the paper is twofold. Firstly, it demonstrates that an existing robust approach used to create designs which are robust towards geometric perturbations, proposed in [62] based on work in [79], cannot be applied directly to acoustic problems. A new double filtering strategy is proposed to enable the application of the robust approach. Secondly, it demonstrates that the problem under consideration is highly sensitive to geometric perturbations and that it is possible to improve the robustness significantly, by accounting for both uniform and non-uniform perturbations of the design geometry, as part of the design problem. [P3] documents the experimental investigation of a design proposed in [P2], demonstrating agreement between predicted and measured results.

5.1 The Robust Approach

In order to appreciate the contents of this chapter, a conceptual understanding of the robust approach [62], is needed. In short, the approach is a tool used with density-based topology optimization which enables the creation of designs that perform robustly under perturbations of their geometry.[1] The approach consists of solving the design problem for three realizations of the physical design field simultaneously.

[1] Under certain conditions the robust approach also assures a minimum length scale in the final design, however this aspect is left untouched here.

These are denoted as the eroded, $P_{\text{erode}}(\xi)$, intermediate, $P_{\text{intermediate}}(\xi)$, and dilated, $P_{\text{dilate}}(\xi)$, designs, respectively. The smoothing and projection procedure, outlined in chapter 3, (3.5)-(3.6), is utilized to obtain the three design fields by applying three different projection thresholds, $\eta \in \{\eta_{\text{dilate}}, \eta_{\text{intermediate}}, \eta_{\text{erode}}\}$, $\xi^{\min} < \eta_{\text{dilate}} < \eta_{\text{intermediate}} < \eta_{\text{erode}} < \xi^{\max}$, to the smoothed design field, the idea being that a small variation in η results in a small near-uniform change in the projected design field. The intermediate design constitutes the final optimized physical design field, while the eroded and dilated designs are included in the design process to assure that perturbations of the device geometry do not impact its performance significantly.

(a) (b) (c) (d) (e)

Figure 5.1: Illustration of robust approach for a topology optimized MBB beam. Black is material, white is void. (a) Problem sketch (b) Smoothed final design field, $P_s(\xi)$, (c) Eroded final design field, $P_{\text{erode}}(\xi)$ (d) Intermediate final design field, $P_{\text{intermediate}}(\xi)$ (e) Dilated final design field, $P_{\text{dilate}}(\xi)$.

An illustration of the robust approach applied to a topology optimized MBB beam is provided in Fig. 5.1. Figure 5.1a presents the model problem where the design domain, $\mathbf{\Omega}_{\text{d}} = \mathbf{\Omega}$, is colored gray, with a support in the lower right corner, a load in the upper left corner and a symmetry condition along the left boundary. The design problem is solved for minimum compliance of the design in $\mathbf{\Omega}_{\text{t}} = \mathbf{\Omega}_{\text{d}}$, [17, chap. 1.1.1]. Figure 5.1b shows the smoothed design field for the final design and Figs. 5.1c-5.1e show the eroded, intermediate and dilated physical design field respectively. The erosion and dilation of the intermediate design field is clearly observed to occur in a near uniform manner along the edges of each feature in the design.

It is possible to adapt the robust approach to consider non-uniform perturbations instead of, or in addition to, uniform perturbations of the design by replacing the constant projection threshold, η, with a spatially varying projection field, $\eta(\mathbf{x})$. This was first considered in [80] where a stochastic approach was combined with non-uniform perturbations of the design to assure additional geometric robustness. An example of applying this approach to mechanical systems is [81] where gripper mechanisms and force inverters are considered. Considering non-uniform perturbations is relevant as they in some cases provide a better approximation of the defects introduced in production or use of an optimized design, than uniform perturbations.

5.2 The Model and Design Problem

The model problem considered in [P2] and [P3] is an acoustic cavity with hard walls, also considered in [51]. The cavity is modeled as the domain $\mathbf{\Omega} \in \mathbb{R}^2$ sketched in Fig. 5.2. The boundary is denoted $\delta\mathbf{\Omega}$. The pressure field in the cavity is generated by an acoustic source at one of two positions, $\mathbf{P}_a$ or $\mathbf{P}_b$ modeled using (2.7) with

$b(\mathbf{x}) = -\mathrm{i}\omega U$, where U is the vibrational velocity. The physics in $\mathbf{\Omega}$ is modeled using (2.5) and the hard walls are modeled using (2.7) with $b(\mathbf{x}) = 0$. The design problem considers the minimization of the sound pressure in $\mathbf{\Omega}_\mathrm{t}$ by introducing solid material in $\mathbf{\Omega}_\mathrm{d}$ using two different formulations.

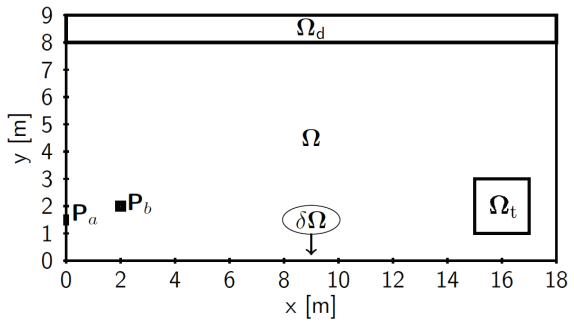

Figure 5.2: Sketch of model problem domain: $\mathbf{\Omega}$. Design domain: $\mathbf{\Omega}_\mathrm{d}$. Target domain: $\mathbf{\Omega}_\mathrm{t}$. Domain boundary: $\delta\mathbf{\Omega}$. Pressure excitation: $\mathbf{P}_a$, $\mathbf{P}_b$.

A “standard" minimization problem using a single projection threshold,

$$\begin{aligned} \underset{\boldsymbol{\xi}\in\Xi}{\text{minimize}} \quad & \Phi = \frac{1}{\int \mathrm{d}\mathbf{\Omega}_\mathrm{t}} \int |\psi(P(\boldsymbol{\xi}))|^2 \mathrm{d}\mathbf{\Omega}_\mathrm{t}, \\ \text{subject to} \quad & \mathbf{S}(P(\boldsymbol{\xi}))\boldsymbol{\psi} - \mathbf{f} = 0, \quad \psi = \sum_{n=1}^{\mathcal{N}_\psi} \psi_n N_n, \\ & 0 \leq \xi_j \leq 1 \ \ \forall\ j \in 1, 2, .., \mathcal{N}_\xi, \end{aligned} \tag{5.1}$$

and a “robust" problem considering $\mathcal{N}_\mathrm{k} = 3$ projection thresholds,

$$\begin{aligned} \underset{\boldsymbol{\xi}\in\Xi}{\text{minimize}} \quad & \max_k \left(\Phi = \frac{1}{\int \mathrm{d}\mathbf{\Omega}_\mathrm{t}} \int |\psi(P_k(\boldsymbol{\xi}))|^2 \mathrm{d}\mathbf{\Omega}_\mathrm{t} \right), \quad k \in 1, 2, ..., \mathcal{N}_k \\ \text{subject to} \quad & \mathbf{S}(P_k(\boldsymbol{\xi}))\boldsymbol{\psi}_k - \mathbf{f} = 0, \quad \psi = \sum_{n=1}^{\mathcal{N}_\psi} \psi_{n,k} N_n, \quad k \in 1, 2, ..., \mathcal{N}_k \\ & 0 \leq \xi_j \leq 1 \ \ \forall\ j \in 1, 2, .., \mathcal{N}_\xi \end{aligned} \tag{5.2}$$

The operator P is defined as the application of either the single filter, $P(\xi) = P_p(\eta, P_s(\xi))$ or the double filter, $P(\xi) = P_{p,2}(\eta_2, P_{s,2}(P_{p,1}(\eta, P_{s,1}(\xi))))$, explained in detail in chapter 5.3. The performance measure considered in the following is, $\langle L \rangle_{\mathbf{\Omega}_\mathrm{t}}$, ($\Phi$ reported in dB SPL ref 20μPa).

An example from [P2] demonstrating the effect of introducing an optimized design in $\mathbf{\Omega}_\mathrm{d}$, is shown in Fig. 5.3. The design was created by solving the standard problem, (5.1), for a source placed at position $\mathbf{P}_b$ oscillating at $f = 51.32$ Hz. Figure 5.3a shows the pressure field in the empty cavity while Fig. 5.3b shows the pressure field when the optimized design is placed in $\mathbf{\Omega}_\mathrm{d}$. A clear reduction in the overall pressure

level is observed, with the maximum dropping from 112 dB to 95 dB. This reduction is due to a shift in the natural frequency of the cavity caused by the introduction of the design. An even larger reduction is seen in the average pressure in $\mathbf{\Omega}_\mathrm{t}$; $\langle L \rangle_{\mathbf{\Omega}_\mathrm{t}}$, which changes from 103 dB to 38.8 dB. This reduction in sound pressure is caused by a displacement of the nodal lines into $\mathbf{\Omega}_\mathrm{t}$.

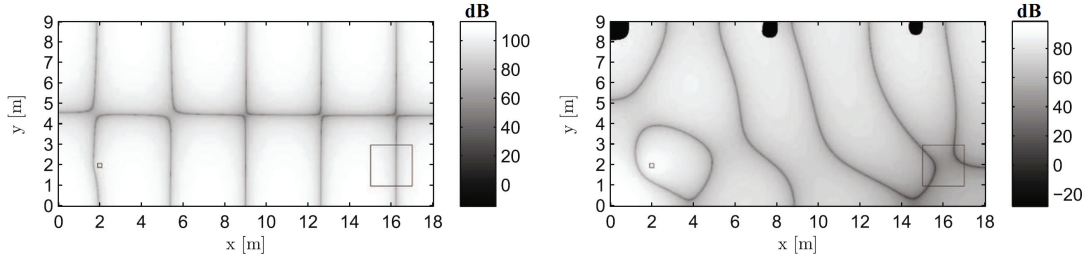

(a) (b)

Figure 5.3: Pressure field (dB SPL ref 20μPa) at $f = 51.32$ Hz in (a) empty acoustic cavity, (b) acoustic cavity with optimized design introduced in $\mathbf{\Omega}_\mathrm{d}$.

5.3 Double Filtering

While the robust approach has been applied successfully for a range of design problems, its application to the design problem considered in [P2] failed.[2] An assumption of the original approach is that a limited variation in the projection threshold, η, result in a limited near-uniform variation in the projected design field with the design staying connected with unchanged topology. For the present model problem this was found not to be the case. Instead, varying η resulted in unpredictable variations in the projected design field.

Consider a design created using the robust approach, (5.2), with three realizations of the design field obtained for $\eta_\mathrm{dilate} = 0.3$, $\eta_\mathrm{intermediate} = 0.5$, $\eta_\mathrm{erode} = 0.7$. The source is placed at $\mathbf{P}_b$ and is vibrating at $f = 69.42$ Hz, (see [P2] for further details). The smoothed design field, $P_s(\xi)$, and the physical design field at $\eta_\mathrm{intermediate}$, $P_p(\eta = 0.5, P_s(\xi))$, resulting from solving the design problem are presented in Fig. 5.4a. While the physical design field consists almost purely of solid and void regions it is seen that $P_s(\xi)$ contains large gray regions. The result of projecting $P_s(\xi)$ at four different values of η, is illustrated in Fig. 5.4c. It is clearly observed from Fig. 5.4a and Fig. 5.4c, that the three realizations have large differences in geometry. Hence by solving the design problem using the robust approach with the single filtering step it was not possible to represent near-uniformly perturbed realizations of the same design.

The presence of the large gray regions in the smoothed field, see Fig. 5.4a, inspired the development of a novel filtering procedure, the double filter, enabling the use of

[2]The robust approach was also found to fail for all other acoustic and electromagnetic model problems tested during the PhD study.

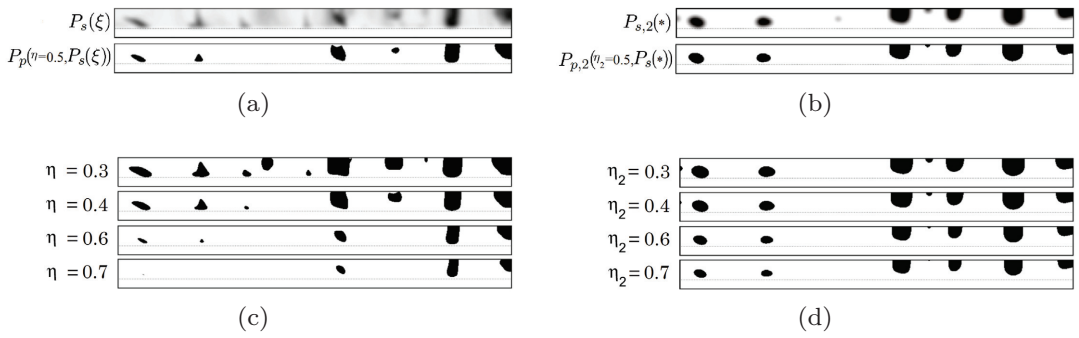

Figure 5.4: Design variable field, subjected to smoothing, P_s and projection P_p at different thresholds η. (a) [top] $P_s(\xi)$, [bottom] $P_p(\eta = 0.5, P_s(\xi))$. (b) [top] $P_{s,2}(*)$, [bottom] $P_{p,2}(\eta = 0.5, P_{s,2}(*))$, with $* = P_{p,1}(\eta = 0.5, P_{s,1}(\xi)$ (c) $P_p(\eta, P_s(\xi))$ for different η. (d) $P_{p,2}(\eta_2, P_{s,2}(*))$ for different η_2.

the robust approach. The idea of the procedure is simple. It consists of applying the smoothing and projection operation to the design field twice.

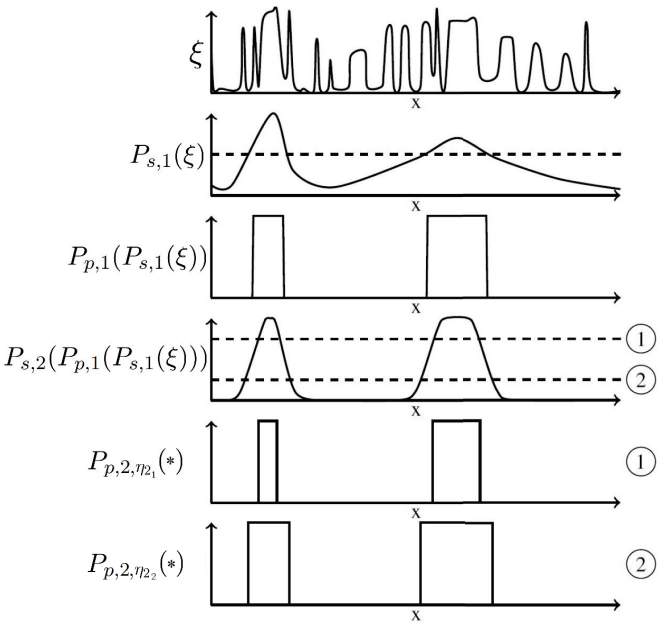

Figure 5.5: 1D illustration of the four steps involved in applying the double filter to the nonphysical auxiliary field ξ. $* = P_{s,2}(P_{p_1}(P_{s,1}(\xi)))$.

Figure 5.5 provides an illustration of the approach in 1D. In short, for high values of the projection sharpness, β, the first application of the smoothing and projection operators result in a solid/void design, as illustrated in the first three rows in Fig. 5.5. The second application of the smoothing operator results in a smoothing of the edges of this solid/void design, while the second application of the projection operator is used to generate the desired realizations of the physical design field, as

illustrated in the last three rows in Fig. 5.5.

The effect of using the double filter is illustrated by solving the same design problem as in the previous example, except replacing the single filtering step with the double filtering step, (see [P2] for further details). The resulting smoothed design field, $P_{s,2}(P_{p,1}(\eta = 0.5, P_{s,1}(\xi)))$, and physical design field, $P(\xi) = P_{p,2}(\eta_2 = 0.5, P_{s,2}(P_{p,1}(\eta = 0.5, P_{s,1}(\xi))))$, are presented in Fig. 5.4b. The effect of projecting $P_{s,2}(P_{p,1}(\eta = 0.5, P_{s,1}(\xi)))$ at four different values of η_2, is illustrated in Fig. 5.4d. A small variation in η_2 now corresponds to a small near-uniform variation in the physical design field. Hence the intermediate physical design field has been optimized to function robustly under near-uniform erosion and dilation. The difference between using the single filter and the double filter is clearly observed by comparing Figs. 5.4c and 5.4d. An alternative approach for controlling the spatial variations in the physical design field when varying η is proposed in [82].

5.4 Optimizing for Geometric Robustness

A range of design problems for different frequencies, f, were solved in [P2] using both the standard approach (5.1) and the robust approach (5.2), both applying the double filter to obtain $P(\xi)$. The sensitivity of the designs towards geometric perturbations was investigated. It was found that the sensitivity could be reduced significantly by including geometric perturbations in the design problems. As one might intuitively expect the sensitivity was also found to increase significantly with operating frequency, f, for a fixed size of the geometric variations.

5.4.1 Optimizing for Near-Uniform Geometric Perturbations

Consider an example from [P2] investigating the effect of near-uniform geometric perturbations on a design optimized for a source placed at $\mathbf{P}_b$ vibrating at $f = 206.3$ Hz. Figure 5.6a shows the physical design field obtained using the standard approach. Fig. 5.6ci shows the decrease in sound pressure in $\mathbf{\Omega}_\mathrm{t}$ when a design is introduced in $\mathbf{\Omega}_\mathrm{d}$ relative to the sound pressure in $\mathbf{\Omega}_\mathrm{t}$ in the empty cavity, as a function of projection threshold, η_2; $\langle L_p \rangle_{\mathbf{\Omega}_\mathrm{op}} / \langle L_p \rangle_{\mathbf{\Omega}_{\mathrm{op_{ED}}}}(\eta_2)$. The circle denotes the decrease if the design in Fig. 5.6a is introduced in $\mathbf{\Omega}_\mathrm{d}$. The thin line shows the performance change when the design is eroded/dilated in a near-uniform manner by varying η_2. It is clearly seen that even small variations cause significant decreases in performance. The same design problem is solved using the robust approach with the double filter. Figure 5.6b shows the physical design variables for the optimized design. Fig. 5.6cii shows $\langle L_p \rangle_{\mathbf{\Omega}_\mathrm{op}} / \langle L_p \rangle_{\mathbf{\Omega}_{\mathrm{op_{ED}}}}(\eta_2)$. As before, the circle denote the decrease if the design in Fig. 5.6b is introduced in $\mathbf{\Omega}_\mathrm{d}$. The asterisks at $\eta_2 \in \{0.3, 0.5, 0.7\}$, correspond to $\langle L_p \rangle_{\mathbf{\Omega}_\mathrm{op}} / \langle L_p \rangle_{\mathbf{\Omega}_{\mathrm{op_{ED}}}}(\eta_2)$ for the three realizations considered in the optimization.

When comparing the performance of the two designs at $\eta_2 = 0.5$, seen in Fig. 5.6ci and Fig. 5.6cii, an increase of ≈ 0.17 in $\langle L_p \rangle_{\mathbf{\Omega}_\mathrm{op}} / \langle L_p \rangle_{\mathbf{\Omega}_{\mathrm{op_{ED}}}}$ is observed. However, the design optimized for robustness maintains a value of $\langle L_p \rangle_{\mathbf{\Omega}_\mathrm{op}} / \langle L_p \rangle_{\mathbf{\Omega}_{\mathrm{op_{ED}}}}$ close to the value at $\eta_2 = 0.5$ across the full interval $\eta_2 \in [0.3, 0.7]$ while the value of $\langle L_p \rangle_{\mathbf{\Omega}_\mathrm{op}} / \langle L_p \rangle_{\mathbf{\Omega}_{\mathrm{op_{ED}}}}$ goes up by ≈ 0.35 for the design optimized using the standard

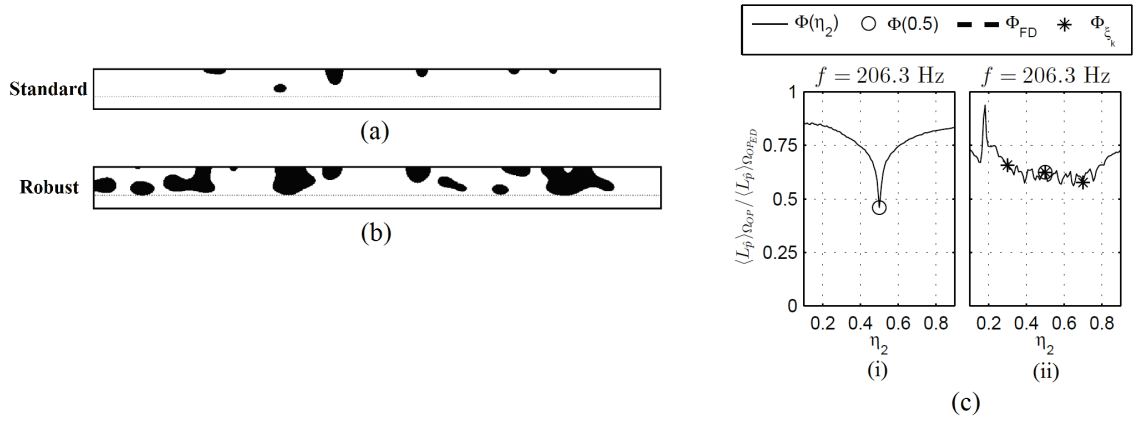

Figure 5.6: (a)-(b) Physical design field obtained using (a) the standard approach with the double filter and (b) the robust approach with the double filter. (c) The sensitivity of the performance of the optimized designs in (i): (a) and (ii): (b) towards near-uniform geometric perturbation.

approach. In conclusion, a significant improvement in geometric robustness has been obtained at the cost of a performance decrease for the design at $\eta_2 = 0.5$.

5.4.2 Optimizing for Non-Uniform Perturbations

It is also possible to take non-uniform geometric pertubations in the design problem into account. This is illustrated using an example from [P2] showing that improved robustness may be obtained by considering both near-uniform and non-uniform geometric pertubations. To include the non-uniform perturbations, the second projection threshold is now a spatially varying field, [80], defined as,

$$\begin{aligned} &\eta_2(\mathbf{x}) = \eta_{\min} + (\eta^{\max} - \eta^{\min}) \cdot \mathrm{CDF}(A \cdot \cos(Bx + C)), \\ &A \in \mathbb{R}, \quad B \in \mathbb{R}^+, \; C \in \mathbb{R}, \quad \eta^{\min} \in [\xi^{\min}, \eta^{\max}[, \; \eta^{\max} \in]\eta^{\min}, \xi^{\max}], \quad \mathbf{x} \in \mathbf{\Omega}. \end{aligned} \tag{5.3}$$

Where CDF is the normal cumulative distribution function with unit standard deviation and mean. A, B and C control the amplitude, frequency and phase of the variations in η_2. $\eta^{\min}$ and $\eta^{\max}$ determine the minimum and maximum of $\eta(\mathbf{x})$, respectively. Figure 5.7a shows examples of $\eta(\mathbf{x})$ for different values of B and C using $(A, \eta^{\min}, \eta^{\max}) = (6, 0.4, 0.6)$.

A design problem with the source placed at $\mathbf{P}_a$ vibrating at $f = 206.3$ Hz is considered. It is first solved using the robust approach with the double filter considering $\mathcal{N}_k = 3$ realizations with $\eta_{2,\mathrm{dilate}} = 0.3, \eta_{2,\mathrm{intermediate}} = 0.5$ and $\eta_{2,\mathrm{erode}} = 0.7$, respectively. The physical design field for $\eta_2 = 0.5$ is presented in Fig. 5.7b. The same design problem is then solved for a total of $\mathcal{N}_k = 18$ realizations of the physical design field. Three of which are obtained using the same near-uniform perturbations while the remaining fifteen consist of non-uniform perturbations of the design field, obtained using all combinations of $A = 6$, $B \in \{2, 4, 8\}$ and $C \in \{\frac{2}{5}\pi, \frac{4}{5}\pi, \frac{6}{5}\pi, \frac{8}{5}\pi, 2\pi\}$. The physical design field for $\eta_2 = 0.5$ is presented in Fig. 5.7c.

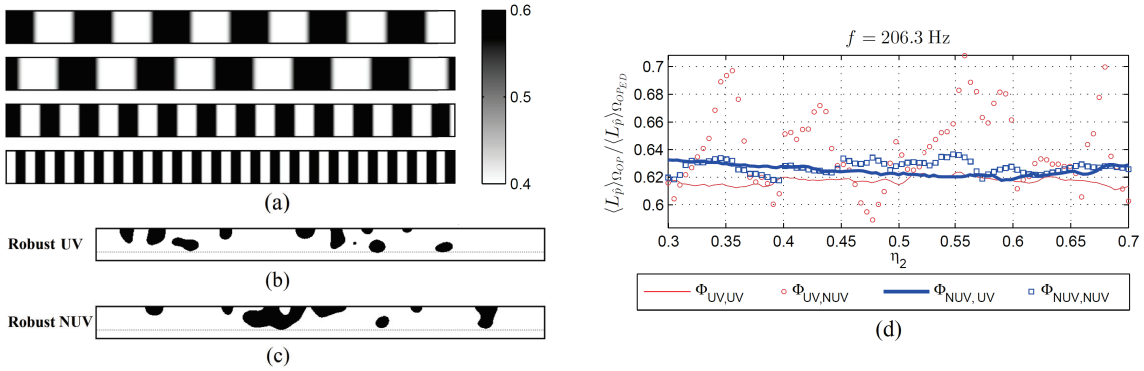

Figure 5.7: (a) Examples of the non-uniformly varying projection field for, [top]: $B = 2, C = \frac{4}{5}\pi$, [second]: $B = 2, C = \frac{6}{5}\pi$, [third]: $B = 4, C = \frac{6}{5}\pi$, [bottom]: $B = 8, C = \frac{8}{5}\pi$. (b)-(c). Physical design field. (d). Performance sensitivity for the optimized designs in (b) using red and (c) using blue, towards near-uniform [lines] and non-uniform [symbols] geometric perturbation.

The performance of the designs in Figs. 5.7b and 5.7c, when subjected to both near-uniform and non-uniform geometric perturbations, is presented in Fig. 5.7d. The performance variation under 80 different realizations of the non-uniform variations, generated using all combinations of $A = 6$, $B \in \{2, 4, 8, 16\}$ and C uniformly distributed at 20 points in $[0, 2\pi[$, is reported. Consider first the design in Fig. 5.7b. The red line in Fig. 5.7d shows the performance under near-uniform variations for $\eta_2 \in [0.3, 0.7]$, which is seen to only vary slightly around, $\langle L_p \rangle_{\mathbf{\Omega}_{\mathrm{op}}} / \langle L_p \rangle_{\mathbf{\Omega}_{\mathrm{opED}}} \approx 0.62$. The red circles show the performance under the 80 non-uniform variations, which is seen to vary from ≈ 0.58 to ≈ 0.71, demonstrating that optimizing for near-uniform perturbations alone was not enough to assure robustness to smaller non-uniform perturbations. Consider now the performance of the design in Fig. 5.7c. The full blue line shows the performance under near-uniform variations of $\eta_2 \in [0.3, 0.7]$. A slightly worse performance is observed compared to the previous design. The blue squares show the performance under the non-uniform perturbations. Here variations from ≈ 0.62 to ≈ 0.64 are observed, a significant improvement compared to the previous design.[3] This result clearly demonstrates the benefit of including both near-uniform and non-uniform perturbations as part of the design problem for the considered model problem.

5.5 Experimental Validation [P3]

It is this author's firm conviction that no method of design should be trusted until it has been experimentally investigated. With this philosophy in mind an experiment was designed for investigating the performance of a design from [P2], presented in Fig. 5.8a. A brief description of the experiment may be found in [83], while the full

[3] The conclusions were validated by investigating the performance under more than 2500 realizations of the non-uniform perturbations using uniformly distributed value of $B \in [2, .., 16]$ and $C \in [0, 2\pi]$.

details of the experiment and complete results are provided in [P3]. As stated in [P3] only little previous work has been reported on the experimental validation of topology optimization for acoustic problems, see e.g. the work in [84] and [85].

Recall that the goal of the design problem is to minimize the average sound pressure in $\mathbf{\Omega}_\mathrm{t}$, highlighted using a red square in Fig. 5.8b. The design in Fig. 5.8a was optimized to operate at the frequency, $f = 6.942$ kHz, for the model problem sketched in Fig. 5.2, with the source placed at $\mathbf{P}_a$, and the cavity dimensions $\mathbf{\Omega} = [0\text{ cm}, 18\text{ cm}] \times [0\text{ cm}, 9\text{ cm}]$.[4]

The average sound pressure in $\mathbf{\Omega}_\mathrm{t}$ at $f = 6.942$ kHz, obtained numerically for the cavity without a design in $\mathbf{\Omega}_\mathrm{d}$, is $\langle L \rangle_{\mathbf{\Omega}_{\mathrm{op,empty}}} \approx 125$ dB. Introducing the optimized design in $\mathbf{\Omega}_\mathrm{d}$ reduces the average to a mere $\langle L \rangle_{\mathbf{\Omega}_{\mathrm{op,design}}} \approx 44.9$ dB. A decrease of more than four orders of magnitude measured in Pascal.

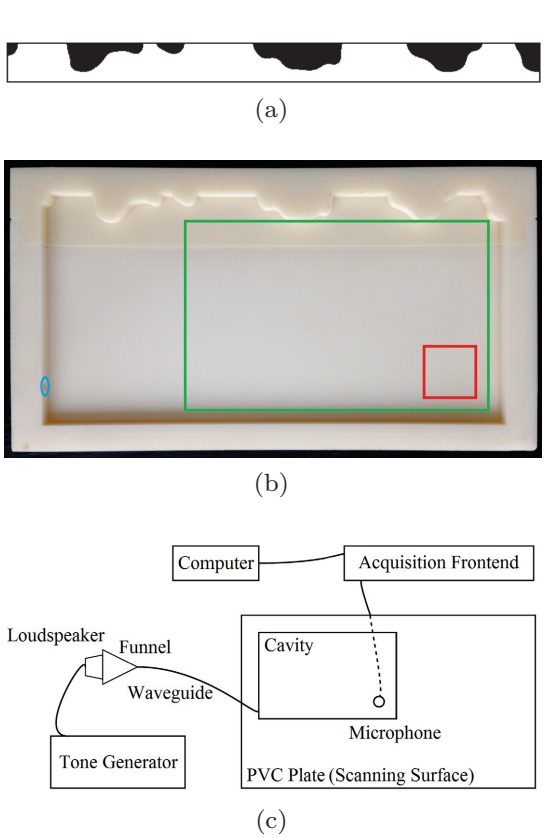

Figure 5.8: (a) Physical design field, black is solid and white is air. (b) 3D-printed cavity with overlay. (blue) circular hole for source placement, (red) $\mathbf{\Omega}_\mathrm{t}$, (green) $\mathbf{\Omega}_\mathrm{M}$. (c) Sketch of experimental setup.

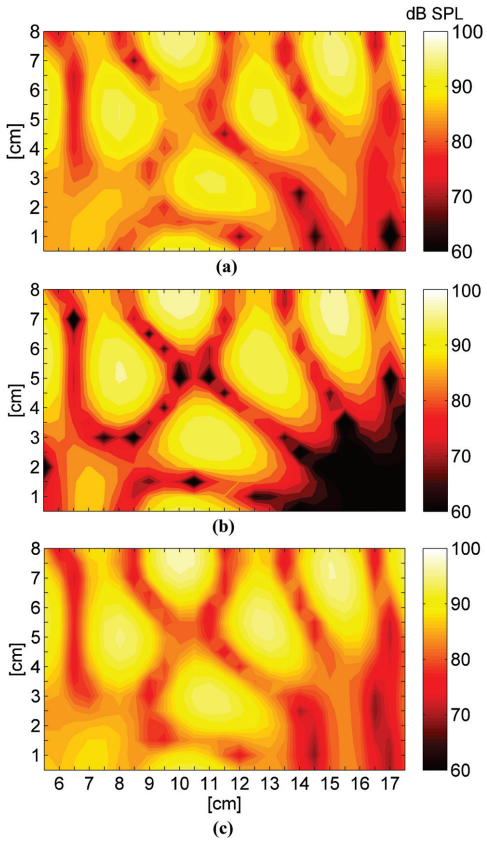

Figure 5.9: Contour plot of pressure field in $\mathbf{\Omega}_\mathrm{M}$ in dB SPL ref 20μPa. (a) Experimental measurements. (b) Simulation. (c) Simulation with attenuation.

An open faced and thick walled extruded version of the cavity including the design was 3D-printed in ABS plastic, see Fig. 5.8b. In the experiment the cavity

[4]Note the rescaling in space and frequency from the numerical model to the experiment.

was sealed by placing it face down on a massive PVC plate, with an 1/8 inch microphone flush mounted at its center. The microphone was connected to a computer, through an acquisition front end, for data collection. The pressure field inside the cavity was generated by a tone generator, using a loudspeaker connected to the cavity through a wave guide, attached at the hole highlighted in Fig. 5.8b by the blue ellipsis. The pressure was measured by moving the cavity relative to the PVC plate, hereby scanning the microphone inside the cavity. See Fig. 5.8c for a schematic of the experimental setup. Measurements were performed in regular grid with 5 mm spacing in both spatial directions over the area $\mathbf{\Omega}_{\mathrm{M}} = [5.5 \text{ cm}, 17.5 \text{ cm}] \times [0.5 \text{ cm}, 8.0 \text{ cm}]$, highlighted using the green rectangle in Fig. 5.8b. The operating frequency was adjusted to $f_{\mathrm{adj}} = 7.011$ kHz to account for the operating conditions at the experimental location. The pressure measured in $\mathbf{\Omega}_{\mathrm{M}}$ is shown in Fig. 5.9a.

To facilitate a fair comparison with the experimental data, the simulated pressure field in the cavity was sampled in a manner comparable to measurements. The simulated field inside $\mathbf{\Omega}_{\mathrm{M}}$ is presented in Fig. 5.9b using a contour plot. Comparing the results in Fig. 5.9a and 5.9b good qualitative agreement is observed. The location of all pressure maxima and nodal lines are seen to agree. The largest discrepancies are observed in the lower left and right corners of $\mathbf{\Omega}_{\mathrm{M}}$. As is discussed in [P3] the observed discrepancy may be explained by viscous and thermal boundary effects which occur near walls, see e.g. [13, chap. 7.7 and chap. 8]. These effects are not accounted for in the simulations, and hence neither in the design process. Mass proportional attenuation was added to the numerical model with a fitted damping parameter and a new simulation performed. The result of this simulation is shown in Fig. 5.9c. By comparing this result to Fig. 5.9a a remarkable agreement is found.

The average sound pressure in $\mathbf{\Omega}_{\mathrm{op}}$, obtained using the sampled simulated data is $\langle L \rangle_{\mathbf{\Omega}_{\mathrm{op,sim}}} \approx 59.1$ dB. The increase in $\langle L \rangle_{\mathbf{\Omega}_{\mathrm{op}}}$ compared to $\langle L \rangle_{\mathbf{\Omega}_{\mathrm{op,design}}}$ is introduced by the sampling procedure extending the sampled pressure field outside $\mathbf{\Omega}_{\mathrm{op}}$ due to the emulation of the finite size of the microphone used for the measurements. The average measured sound pressure over $\mathbf{\Omega}_{\mathrm{op}}$ is $\langle L \rangle_{\mathbf{\Omega}_{\mathrm{op,meas}}} \approx 78.6$ dB, a substantial increase from $\langle L \rangle_{\mathbf{\Omega}_{\mathrm{op,sim}}}$ although still significantly lower than $\langle L \rangle_{\mathbf{\Omega}_{\mathrm{op,empty}}}$. Finally the average sound pressure in $\mathbf{\Omega}_{\mathrm{op}}$ obtained from the simulation using attenuation is $\langle L \rangle_{\mathbf{\Omega}_{\mathrm{op,atten}}} \approx 78.1$ dB. Hence, by including attenuation in the numerical model, the discrepancy between the measured and simulated result has been reduced significantly.

In summary, [P3] presented an approach for experimentally investigating the pressure field in a quasi 2D cavity and demonstrated that a design optimized using the approach treated in [P2] functioned as expected, when accounting for attenuation. Even without introducing attenuation very good qualitative agreement was demonstrated.

6 Meta Material Slabs [P4], [P5]

This chapter provides an introduction and overview of work done on designing *meta materials* (MMs) exhibiting negative refraction with high transmittance. The design was performed using a novel approach developed by the author during his PhD study, in collaboration with his main supervisor [P4]. The chapter also presents results from experimental work performed to investigate one of the designed MM slabs [P5].

A meta material may be thought of as a periodically arranged collection of matter, engineered to exhibit a behavior not normally found in any material in nature.

The topic of MMs exhibiting negative refraction (and MMs in general) has experienced massive interest over the latest decades. This interest was sparked by the work of Pendry [86, 87] discussing the application of engineered MMs exhibiting negative refraction to the design of a perfect optical lens capable of surpassing the diffraction limit. Pendry's work was based on the earlier work by Veselago [88], who discussed the idea and application of materials simultaneously exhibiting negative magnetic permeability and electric permittivity. An extensive treatment of the topic of MMs within optics and electromagnetics may be found in [89]. While Pendry considered a problem in electromagnetics, the idea of developing MMs exhibiting negative refraction have spread to other areas of physics such as acoustics and solid mechanics, see e.g. [90–92] for examples from the different areas. Several applications of MMs have been discussed in the literature, including beating the diffraction limit and designing cloaking devices [89, 93], collimation of waves [94] and flat lenses [95].

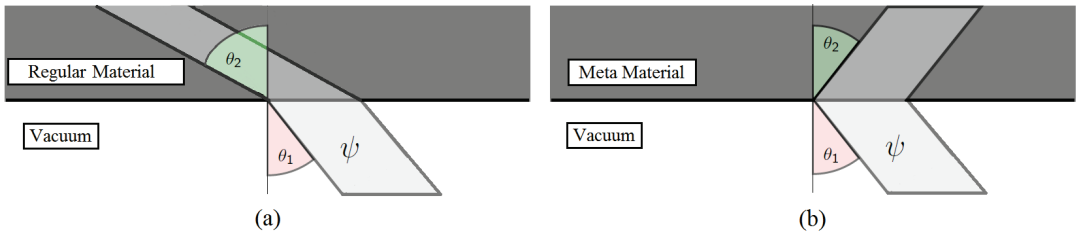

Figure 6.1: Illustration of the refraction (at the angle θ_2) of a localized wave ψ, incident at the angle θ_1, at an interface between vacuum and (a) a regular material, (b) a meta material exhibiting negative refraction.

An illustration of the difference between a material exhibiting regular refraction and one exhibiting negative refraction at a material vacuum interface is provided in Fig. 6.1. The angles θ_1 and θ_2 are measured positively as seen in Fig. 6.1a. The definition of the refractive index for a material placed in vacuum used in the following, is given by Snell's law [14, pp. 17],

$$n = \frac{\sin(\theta_1)}{\sin(\theta_2)}. \tag{6.1}$$

Here n is the refractive index. From (6.1) it is seen why the material in Fig. 6.1b is said to exhibit negative refraction.

6.1 Tuning the Refractive Behavior of MM Slabs [P4]

The approach proposed in [P4] considers a finite MM slab consisting of an array of identical unit cells, along with a model of the full wave field in and around the slab. Hereby the approach implicitly account for the field excited in the MM slab, edge effects as well as the coupling of the field into and out of the MM slab. This is in contrast to most previous work on MM design which has relied on a number of simplifying assumptions, including assuming applicability of homogenization techniques, assuming infinite periodicity of the MM or considering band diagrams and identifying regions with negative slope for $\frac{\delta\omega}{\delta k}$ under the assumption that only a single mode is excited, (as stated in [P4]).

The method proposed in [P4] has been successfully tested for problems using parameters from acoustics, from solid mechanics and from electromagnetics. The acoustic case was found to be the hardest to treat numerically due to the high contrast in material parameters. An example from acoustics is presented in the following.

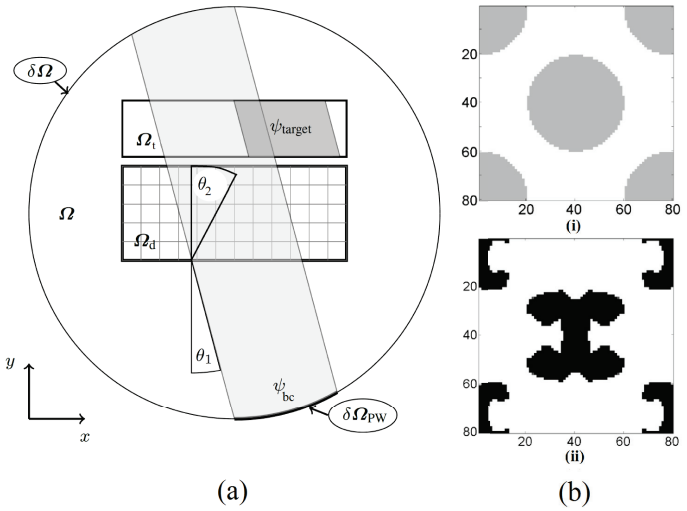

Figure 6.2: (a) Exterior model problem domain: $\mathbf{\Omega}$. Design domain: $\mathbf{\Omega}_\mathrm{d}$. Target domain: $\mathbf{\Omega}_\mathrm{t}$. Domain boundaries: $\delta\mathbf{\Omega}$, $\delta\mathbf{\Omega}_\mathrm{PW}$. Incident localized pressure wave: ψ_bc. Target wave: ψ_target. Angle of incidence: θ_1. Angle of refraction: θ_2. (b)i Start guess for the material distribution in the unit cell. (b)ii Final physical design field in the unit cell. Black is material.

The design problem formulation is briefly outlined here. The goal of the problem is to determine the layout of material inside the unit cell constituting the MM slab, such that the full slab exhibits a prescribed (negative) refractive index, n, with high transmittance, T, of the field through the slab, for a number of angles of incidence $\theta_{1,i}, i \in \{1, 2, ..., \mathcal{N}_\mathrm{theta}\}$, $\mathcal{N}_\mathrm{theta} \in \mathbb{N}^+$ and frequencies $f_j, j \in \{1, 2, ..., \mathcal{N}_\mathrm{f}\}$, $\mathcal{N}_\mathrm{f} \in \mathbb{N}^+$.

The full slab is considered when evaluating the physics and objective function, while the design problem considers a single unit cell replicated throughout the slab.

The distribution of material is controlled by ξ discretized into $\mathcal{N}_\xi$ DVs and the smoothing and projection operators and β-continuation scheme discussed in chapter 3.2 are applied. In order to solve the design problem an exterior model problem, defined on $\mathbf{\Omega} \subset \mathbb{R}^2$, is considered, see Fig. 6.2a. Here a MM slab to be designed, consisting of $n_x \times n_y$ unit cells, is placed in $\mathbf{\Omega}_\mathrm{d}$. The Helmholtz equation is used to model the physics. Far field matching conditions are imposed along $\delta\mathbf{\Omega} \cup \delta\mathbf{\Omega}_\mathrm{PW}$ by assuring that the solution to the Helmholtz equation fulfills (2.6). A spatially localized near-plane wave, ψ_bc, entering $\mathbf{\Omega}$ at the angle $\theta = \theta_1$ is introduced through the boundary condition (2.7) on $\delta\mathbf{\Omega}_\mathrm{PW}$ with $b(\mathbf{x})$ calculated by inserting (6.2) into (2.7).

$$\psi_\mathrm{bc} = \mathrm{e}^{-\left(\frac{(\mathbf{x}-\mathbf{x}_w)\cdot\mathbf{d}^\mathcal{T}}{\delta_x}\right)^2} \mathrm{e}^{-\mathrm{i}\hat{\omega}(\mathbf{x}\cdot\mathbf{d})}, \quad \mathbf{d} = \begin{pmatrix}\cos(\pi/2+\theta)\\ \sin(\pi/2+\theta)\end{pmatrix}, \quad \mathbf{x}_w = \begin{pmatrix}x_w\\ y_w\end{pmatrix}. \tag{6.2}$$

Here δ_x controls the width of the Gaussian envelope, $\mathbf{d}$ is the propagation direction and $\mathbf{x}_w$ denotes the position of the center of the wave. Due to the relatively small size of $\mathbf{\Omega}_\mathrm{d}$ compared to $\mathbf{\Omega}$ ($\approx 10\%$) the hybrid WBM-FEM is used to discretize the model problem. $\mathbf{\Omega}_\mathrm{d}$ is discretized using the FEM and $\mathbf{\Omega}\backslash\mathbf{\Omega}_\mathrm{d} = \{\mathbf{x} \in \mathbf{\Omega} | \mathbf{x} \notin \mathbf{\Omega}_\mathrm{d}\}$ is discretized using the WBM.

A spatially localized target field, ψ_target, modeled using (6.2) with $\theta = \theta_1$ and δ_x identical to that chosen for ψ_bc, is prescribed in the target domain, $\mathbf{\Omega}_\mathrm{t}$, behind the MM slab. The desired refractive index of the slab is selected implicitly by choosing the position of the center of ψ_target, $\mathbf{x}_{w,\mathrm{target}}$, hereby determining the refraction angle, θ_2, which aligns the field transmitted through the MM slab with ψ_target. The objective function, Φ, in the design problem is the standard deviation, **STD**, over $\mathbf{\Omega}_\mathrm{t}$ of the difference between the magnitude squared of the solution to the model problem, ψ, and the target field, ψ_target,

$$\Phi = \underset{\mathbf{\Omega}_\mathrm{t}}{\mathbf{STD}}\left(|\psi|^2 - |\psi_\mathrm{target}|^2\right), \quad \underset{\mathbf{\Omega}_\mathrm{t}}{\mathbf{STD}}(x) = \frac{\int \left(x - \frac{\int x \; d\mathbf{\Omega}_\mathrm{t}}{\int d\mathbf{\Omega}_\mathrm{t}}\right)^2 d\mathbf{\Omega}_\mathrm{t}}{\int d\mathbf{\Omega}_\mathrm{t}}. \tag{6.3}$$

The design problem is formulated as a min/max optimization problem with a volume constraint, where the maximum value of Φ over a number of angles of incidence, θ_1, and frequencies, f, is minimized over ξ. The design problem is solved in two phases. In the first phase the designable area of the unit cell is restricted to an FCC like pattern as illustrated in Fig. 6.2bi. In the second phase the design is allowed to change freely in unit cell.

The MM slab, treated as an example in the following, was designed for an acoustic problem, with the unit cell consisting of aluminum distributed in an air background. A MM slab consisting of 6×22 identical unit cells of non-dimensionalized size $(a_x, a_y) = (1/6, 1/6)$ consisting of $80 \times 80 = 6400$ finite elements was considered in

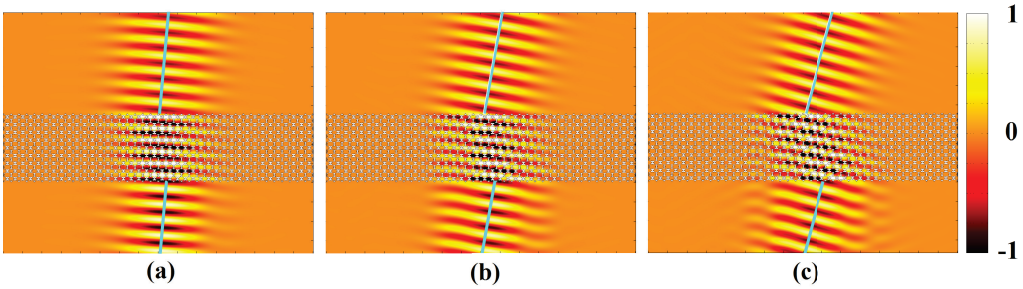

Figure 6.3: Normalized pressure field for $\tilde{f} = 3$ in and around MM slab consisting of 40 × 9 unit cells for a localized pressure wave entering the domain from below incident at (a) $\theta_1 = 5^o$, (b) $\theta_1 = 10^o$, (c) $\theta_1 = 15^o$.

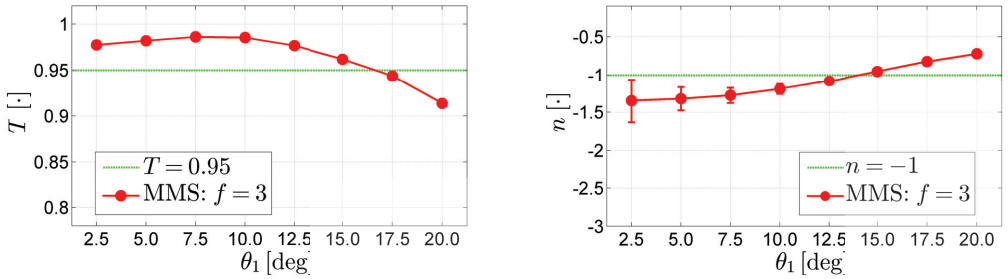

Figure 6.4: (a) Transmittance, T, and (b) refractive index, n, including error bars (see [P4]), for MM slab consisting of 22 × 12 unit cells operating at $\tilde{f} = 3$.

the design problem. A single non-dimensionalized frequency, $\tilde{f} = 3$ corresponding to $\lambda = 1/3$, and three angles of incidence $\theta_1 \in \{5^o, 10^o, 15^o\}$ were considered (see [P4] for more details on the design procedure and parameter choices).

The final physical design field constituting the unit cell is shown in Fig. 6.2bii. The results presented in the following were obtained using a pure acoustic model in COMSOL 5.2a. The MM slab was modeled as a collection of hard wall boundaries imposed along the material interface in the unit cell. Figure 6.3 shows a normalized localized near-plane pressure wave incident on a slab of the MM consisting of 40 × 9 unit cells at the three angles $\theta_1 \in \{5^o, 10^o, 15^o\}$. The center of the wave on both sides of the MM slab is highlighted using a cyan line. The high transmittance through the slab as well as its negative refractive index is clearly observed.

The transmittance of the field through the full slab (both surfaces) and the refractive index, both as a function of angle, is estimated for a slab consisting of 22 × 12 unit cells (as described in [P4]). $T(\theta_1)$ and $n(\theta_1)$ for $\theta_1 \in [2.5^o, 20^o]$ are presented in Figs. 6.4a and 6.4b, respectively. It is seen that T remains above 0.95 for $\theta_1 \in [2.5^o, 15^o]$ and that the refractive index remains negative across the full angular range. The data also reveals that n varies significantly with θ_1. These results for T and n agree qualitatively with results obtained for other MM slabs designed

using the proposed method.[1]

The collimating capability of the MM slab, due to its negative n, is illustrated in Fig. 6.5, showing the pressure field magnitude in dB SPL ref 20μPa. The slab is illuminated by a spatially diverging acoustic wave, excited at $\tilde{f} = 3$ and entering the model domain from below at $\theta_1 = 0^o$. By comparing the field in Fig. 6.5a without the MM slab with the field in Fig. 6.5b with the MM slab, the collimation of the field inside the slab is clearly observed.

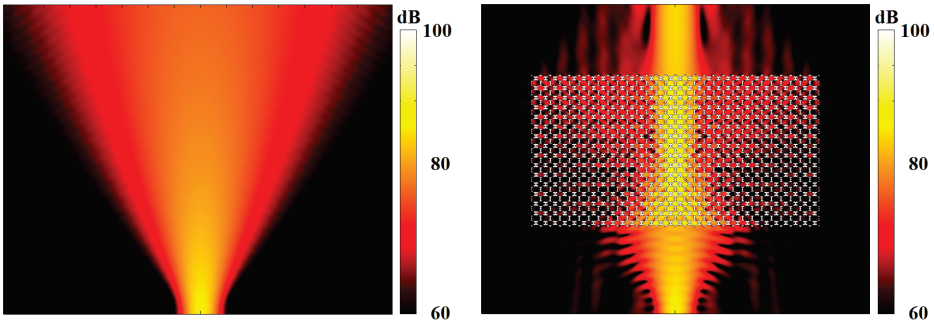

(a) (b)

Figure 6.5: Effect of MM slab (30 × 16 unit cells) on a spreading acoustic pressure wave incident on the slab at $\theta_1 = 0^o$ oscillating at $\tilde{f} = 3$. (a) Reference (b) MM slab.

The effect of placing the MM slab around a point radiating into free space is shown in Fig. 6.6. A non-dimenionalized and normalized pressure field is used for the demonstration. A single unit cell at the center of the slab has been removed and replaced with an acoustic monopole vibrating at $\tilde{f} = 3$. By comparing the field in Fig. 6.6a with the field in Fig. 6.6b, collimation of the field along the two principal axes is clearly observed.

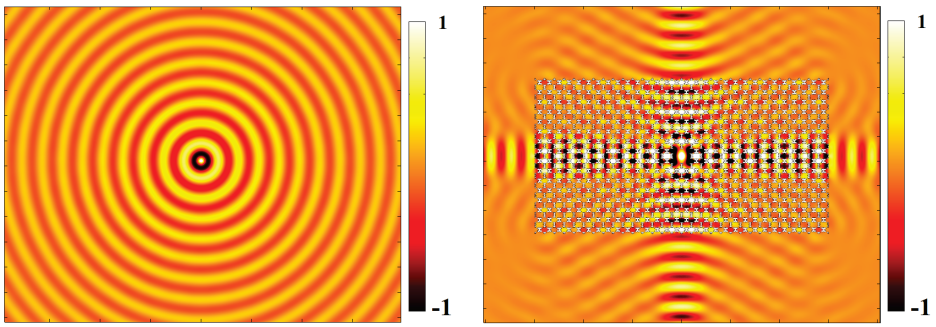

(a) (b)

Figure 6.6: Effect of placing a point source, radiating at $\tilde{f} = 3$, at the center of a MM slab (16 × 30 unit cells). (a) Reference (b) MM slab.

[1]For problems considering electromagnetic parameters the author found it possible to obtain $T > 0.99$ at the angle of incidence and frequency for which the MM slab was optimized.

The designed MM slab is found to exhibit negative refraction across more than a 10% frequency band, with varying transmittance. The broad band effect is demonstrated in Fig. 6.7 where the excitation frequency has been shifted down to $\tilde{f} = 2.8$ and the pressure field recording for a localized near-plane wave incident on the MM slab (40×9 unit cells) in a 5 degree interval across $\theta_1 \in [0^o, 35^o]$. The pressure field magnitude is reported in dB SPL ref 20 μPa.

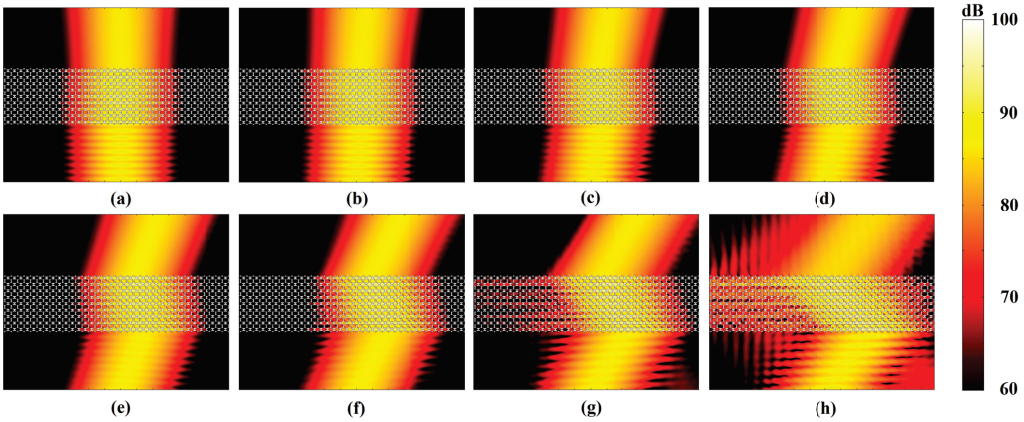

Figure 6.7: $|\psi(\tilde{f} = 2.8)|$ in dB SPL ref 20μPa around and in a MM slab consisting of 40×9 unit cells for a localized pressure wave entering the domain from below incident at the angle (a) $\theta_1 = 0^o$, (b) $\theta_1 = 5^o$, (c) $\theta_1 = 10^o$ (d) $\theta_1 = 15^o$, (e) $\theta_1 = 20^o$, (f) $\theta_1 = 25^o$ (g) $\theta_1 = 30^o$, (h) $\theta_1 = 35^o$.

The figure clearly illustrates that at this frequency the MM slab exhibits no or negative refraction across the full angular range $\theta_1 \in [0^o, 35^o]$. The transmittance through the slab is calculated and the result presented in Fig. 6.8. It is observed that $T > 0.95$ for $\theta_1 \in [0^o, 30^o]$ after which it quickly drops off,

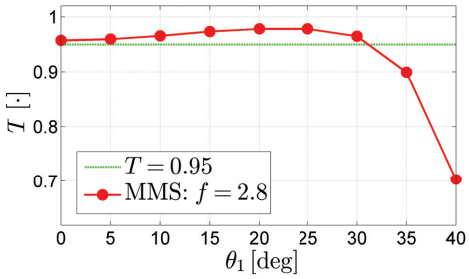

Figure 6.8: Transmittance, T, for the MM slab consisting of 40×9 unit cells operating at the frequency, $\tilde{f} = 2.8$.

6.2 Experimental Validation of MM Slab [P5]

Staying true to the conviction that design methods must be experimentally validated, an experiment for testing the 2D MM slab investigated numerically in the previous

section was designed. A picture of the setup is presented in Fig. 6.9a. In short, it consists of a quasi two dimensional anechoic chamber of height of 0.6 cm ensuring a near-two dimensional sound field below the cutoff frequency of $f_c \approx 28.5$ kHz.[2] At the center of the chamber is a freely rotatable disc into which a test specimen is placed. A microphone used to measure the pressure is flush mounted in the movable chamber ceiling. A line array of 8 mini-loudspeakers is inserted in the chamber floor. By modulating the amplitude of the loud speakers it is possible to generate an approximation of a spatially localized near-plane pressure wave. An aerial view of the test specimen placed inside the chamber is provided in Fig. 6.9b, with illustrations of a measurement area and measurement lines. A strength of the setup worth highlighting is that it allows for the measurement of the field inside the MM slab by aligning the microphone with regions void of material in the slab. A complete description of the experimental setup and measurement procedure is found in [P5].

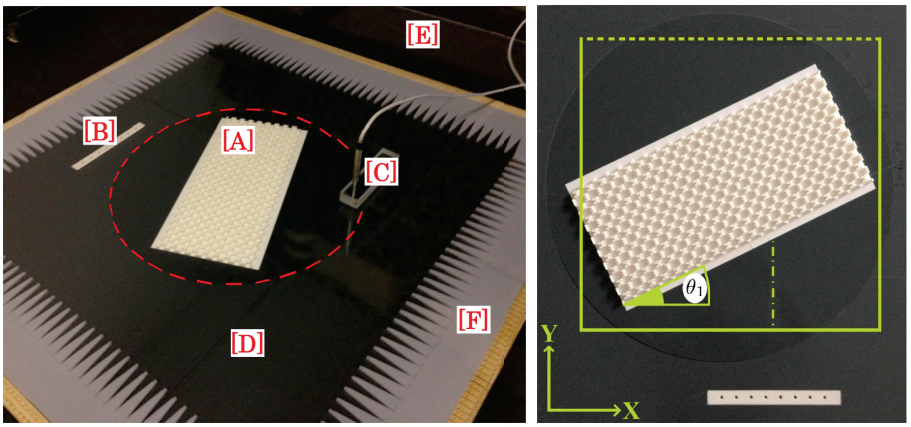

Figure 6.9: **(a)** Overview of experimental setup. [A]: MM slab, [B]: mini-loudspakers array, [C]: Flush mounted microphone, [D]: PVC baseplate, [E] Acrylic top plate, [F] Absorbing foam. The dashed red line outlines the rotatable disk. **(b)** Aerial view of experimental setup. The square outlines the measurement area for the data presented in Fig. 6.10ai. The data in Fig. 6.11i was obtained by measuring along the dashed line above the MM slab. The data in Fig. 6.11ii was obtained along the dash-dotted vertical line.

3D-printing was used to produce an extruded version of the MM slab consisting of 20×9 unit cells. The physical design field in the unit cell is shown in Fig. 6.10bi and a representative unit cell from the 3D-printed slab is shown in Fig. 6.10bii. The size of the printed unit cell was scaled to comply with the spatial resolution of the 3D-printer (0.2 mm) and the operation frequency selected accordingly at $f = 8575$ Hz. The 3D-printed MM slab was placed inside the cavity and the pressure field measured inside the green square in Fig. 6.9b for an angle of incidence of $\theta_1 = 14^{\circ}$. A contour plot of the pressure field magnitude is shown in Fig. 6.10ai. A numerical

[2] Assuming the speed of sound, $c = 343$ m/s.

model mimicking the experimental setup was created in COMSOL 5.2a and used to evaluate the pressure field in and around the MM slab at $\theta_1 = 14^o$. The result of the simulation is presented using a contour plot in Fig. 6.10aii. Good qualitative agreement is seen between Fig. 6.10ai and Fig. 6.10aii, although attenuation is observed in the measured data. By including an experimentally estimated value for the attenuation inside the cavity (≈ 0.4 dB per wavelength) in the numerical model the result in Fig. 6.10aiv was obtained. An estimate of the attenuation inside the MM slab (≈ 0.56 dB per wavelength) was performed using a fit to the experimental data. Including this additional attenuation in the numerical model the result in Fig. 6.10aiii is obtained. The agreement between the measured data in Fig. 6.10ai and the simulated data in Fig. 6.10aiii is remarkable.

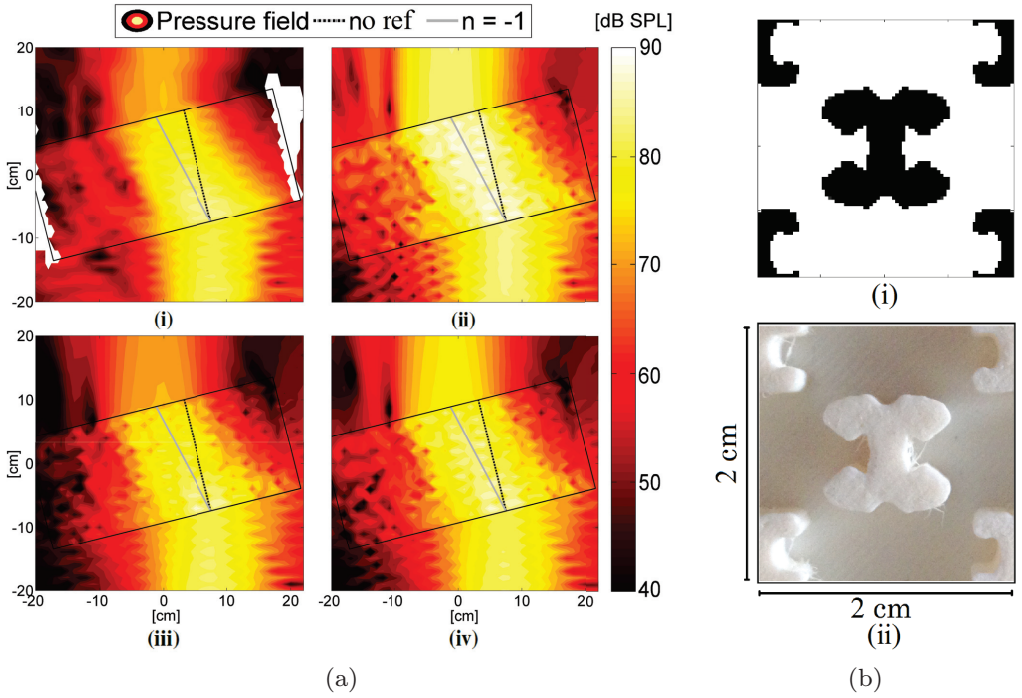

Figure 6.10: (a) Pressure field (dB SPL ref 20μPa) in the area marked by the square in Fig. 6.9ii, with $\theta_1 = 14^o$ and $f = 8575$ Hz. **(i)** Measured field. **(ii)** Simulated field (no attenuation). **(iii)** Simulated field (attenuation in cavity and MM slab). (**iv**) Simulated field (attenuation in cavity). Black square: Outline of MM slab. The black and gray lines show the direction of no refraction and the direction with $n = -1$ respectively. (b) MM slab unit cell. (i) Physical design field (ii) 3D-printed unit cell.

The angle of refraction, θ_2, through the slab as a function of θ_1 for three frequencies in a 10% band, was estimated numerically without attenuation. It was also estimated from experimental data using a series of measurements along the dashed line in Fig. 6.9b. A plot of $\theta_2(\theta_1, f_i)$, $f_i \in \{8150 \text{ Hz}, 8575 \text{ Hz}, 9000 \text{ Hz}\}$ is provided in Fig. 6.11a. The values of $\theta_2(\theta_1, f_i)$ obtained numerically are shown in full lines and experimentally in dashed lines with markings denoting the measured angles. The data clearly demonstrate that the MM slab exhibits negative refraction across the

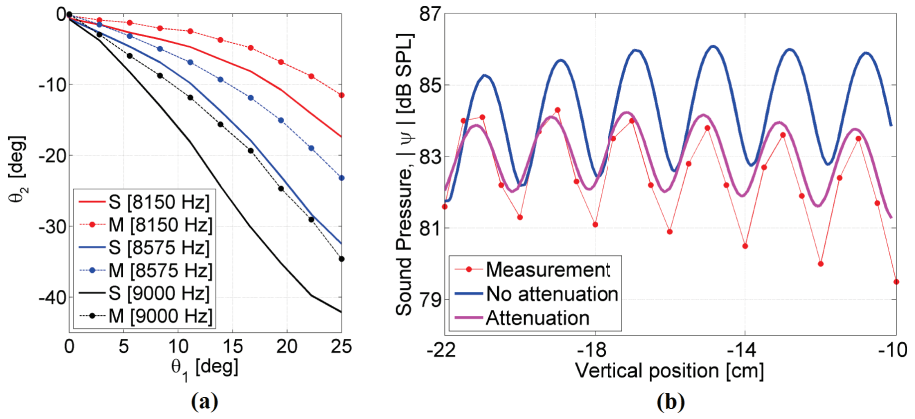

Figure 6.11: (a) Angle of refraction through the MM slab, θ_{ref}, as a function of θ_1. Full lines correspond to simulated data. Dashed lines correspond to the measured data with the markings denoting measured points. (b) Pressure field along the vertical dash dotted line in Fig. 6.9ii with $\theta_1 = 0^{\text{o}}$ and $f = 8575$ Hz.

full 10% frequency band. An upwards shift is observed from the numerical to the experimental results believed to stem from a combination of the effect of going from a 2D numerical model to the quasi 2D experimental setup; the effect of a shift in the speed of sound stemming from operating conditions (e.g. temperature); thermal and viscous boundary effects which affect the phase speed [13, chap. 7.7].

Due to the attenuation it was not possible to calculate the transmittance through the full slab in the way it was done in the previous section. Therefore another approach was used [13, chap. 3.1].

The pressure field was measured along the vertical dash dotted line in Fig. 6.9b. The result is presented in Fig. 6.11b along with numerical results with and without attenuation. The peak ratio, $s = \max|\psi| \backslash \min|\psi|$, was then used to calculate the magnitude of the reflection factor, $|R| = (1-s)\backslash(1+s)$, which was used to determine the transmittance at the MM slab to air interface as $T = 1 - |R|^2$. A transmittance of $T \approx 0.973$ was obtained from the experimental data while $T \approx 0.965$ was obtained for the simulation without attenuation and $T \approx 0.986$ was obtained for the simulation with attenuation. The single interface transmittance for a pressure wave at normal incidence obtained using the numerical model used to solve the design problem is $T \approx 0.985$ for $f = 8575$ Hz (corresponding to $\tilde{f} = 3$ used in the design problem).

The attenuation observed inside the MM slab is likely attributable to boundary layer effects. This suggests that the inclusion of attenuation at the material to air interface, in the numerical model, could result in improved MM slab designs in terms of minimizing the effect of the attenuation, a topic for future work.

7 Wave Shaping Devices [P6]

This chapter considers the design of devices capable of manipulating the pressure field emitted by one or more acoustic sources into a desired shape under free-field conditions (in 2D), denoted as *acoustic wave shaping devices* (AWSD). The design of a directional sound emission device (AWSD1), of an acoustic beam-splitting device (AWSD2) and of a flat acoustic lens (AWSD3) are considered. To this end, three closely related design problem formulations are used. They are all based on density-based topology optimization, inspired by the literature and developed and implemented by the author. Numerical results are presented for all three cases and experimental data validating the optimized devices are presented for AWSD1 and AWSD2. Although parameters for acoustic problems are considered, the described approaches may be applied to problems in electromagnetics as well.[1]

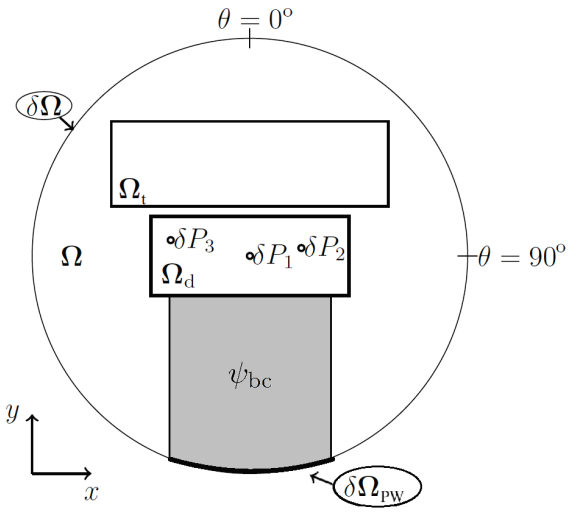

Figure 7.1: Sketch of exterior model problem domain: $\boldsymbol{\Omega}$. Design domain: $\boldsymbol{\Omega}_{\text{d}}$. Target domain: $\boldsymbol{\Omega}_{\text{t}}$. Domain boundaries: $\delta\boldsymbol{\Omega}$, $\delta\boldsymbol{\Omega}_{\text{PW}}$. Acoustic sources: δP_i. Incident localized near-plane pressure wave: ψ_{bc}. $\theta = 0^{\text{o}}$ and $\theta = 90^{\text{o}}$: Angular convention.

Three closely related exterior model problems are considered for the three design problems. A sketch of the model domain is provided in Fig. 7.1. The model PDE is (2.5). A far field matching condition is imposed along $\delta\boldsymbol{\Omega} \cup \delta\boldsymbol{\Omega}_{\text{PW}}$ to fulfill the boundary condition (2.6). The pressure field is excited by either a set of point-like sources distributed in $\boldsymbol{\Omega}_{\text{d}}$ or a spatially localized near-plane wave, ψ_{bc}, incident from outside the model domain, both of which are imposed using the boundary condition (2.7). In the design problem the designs are modeled as aluminum embedded in an air background and the material parameters, α and β in (2.5), are chosen accordingly.

[1] With appropriate modifications of boundary conditions and assumptions regarding the field polarization.

Due to the relatively small size of $\mathbf{\Omega}_\mathrm{d}$ compared to $\mathbf{\Omega}$ (in the range of $5\% - 10\%$) the model problem is discretized using the Hybrid WBM-FEM. The FEM is used to discretize $\mathbf{\Omega}_\mathrm{d}$ while the WBM is used to discretize $\mathbf{\Omega} \backslash \mathbf{\Omega}_\mathrm{d} = \{\mathbf{x} \in \mathbf{\Omega} | \mathbf{x} \notin \mathbf{\Omega}_\mathrm{d}\}$. For the design problems AWSD1 and AWSD2 the resolution of the finite element discretization of $\mathbf{\Omega}_\mathrm{d}$ was chosen to coincide with the resolution of the 3D-printer.

The objective function used in all three design problems considers the difference in magnitude of the solution, ψ, and a desired target field, ψ_target,

$$\Phi = \int \left(|\psi|^2 - |\psi_\mathrm{target}|^2 \right)^2 \mathrm{d}\mathbf{\Omega}_\mathrm{t} \geq 0. \tag{7.1}$$

The design problems AWSD1, considered in chapter 7.1, and AWSD2, considered in chapter 7.2, respectively, are formulated using the robust approach with the double filter, see (5.2), with Φ replaced by (7.1). The design problem AWSD3 considered in chapter 7.3 is formulated using the standard approach with the single filter, see (5.1), i.e. it is solved without geometric robustness. The objective function is again replaced by (7.1). Instead of considering a single frequency as is done in (5.1) and (5.2), the design problems are formulated to consider several frequencies simultaneously. An in-depth description of the modeling, optimization, and experimental procedure for AWSD1 is presented in [P6]. Both AWSD2 and AWDS3 follow the same procedures except that different values for the design domain $\mathbf{\Omega}_\mathrm{d}$, target domain $\mathbf{\Omega}_\mathrm{t}$, acoustic sources δP_i or ψ_bc and target field ψ_target, are considered.

All numerical post processing results reported in the following sections have been obtained using the acoustic module in COMSOL 5.2a. The optimized designs created by solving the design problems are post processed using a Heaviside projection to obtain designs consisting purely of solid and air regions before being imported into COMSOL 5.2a for analysis.

7.1 Directional Wave Emission Device - AWSD1 [P6]

For several applications in acoustics, it is of interest to create solutions which can produce directionally focused sound fields confining the acoustic energy in space. As mentioned in [P6] this is of fundamental interest for sound field reproduction [96–98], long range emission [99, 100], noise control and by considering the reciprocal problem also for measurement purposes [101, 102]. Several approaches to solving problems of this type exist, including active solution consisting of using loudspeaker/microphone arrays or passive solutions using a parabolic reflector or a horn. Extensive work on the optimization of an acoustic horn for transmission and directionality has been performed in [103, 104] among others, focusing on optimizing the shape of the horn, and in [48] where topology optimization is applied. Being inspired by this work an investigation of the possibility of applying topology optimization in designing/optimizing acoustically small devices capable of focusing acoustic energy in a specified direction, was made. That is, devices with spatial dimensions comparable to the wavelength, for the frequency interval where the devices are designed to operate. Based on a lack of reported experimental work on the validation of directional sound emission devices designed using topology optimization[2], an experimental setup for testing optimized devices was designed. It is noted that the experimental study on an acoustic horn designed using shape optimization is reported in [105]. The results of the experiments clearly demonstrated the feasibility of utilizing the proposed approach (and topology optimization in general) to design such devices. The results presented in the following considers one of the devices presented in [P6].

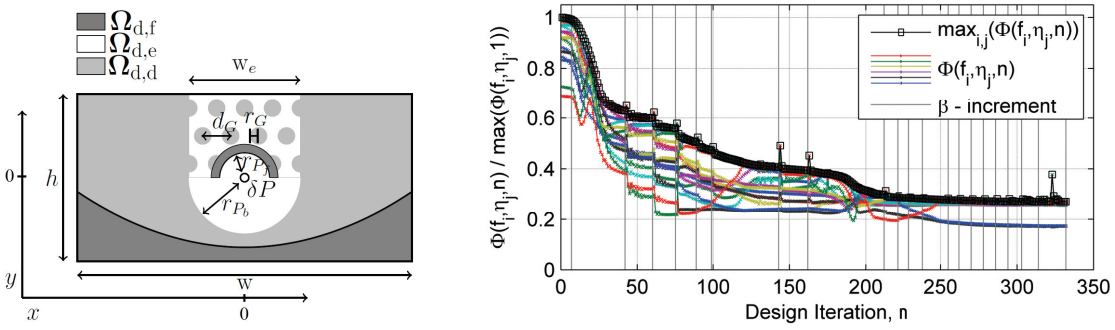

Figure 7.2: (a) Rectangular design domain configuration for AWSD1. The values for the parameters, h, w, etc. are found in [P6]. (b) Convergence history for AWSD1 showing the 18 realization of Φ considered in the design problem scaled by the initial maximum value as a function of iteration number. The gray lines denote iterations with β-increments in the projection continuation scheme.

In short, the ultimate goal is to create a device which focuses all of the acoustic energy emitted by one or more sources in one direction. To this end the target field,

[2]To the author's knowledge no experimental work has been reported.

ψ_{target}, considered in the objective function Φ in (7.1) is defined as,

$$\psi_{\text{target}} = A\mathrm{e}^{-\left(\frac{(\mathbf{x}-\mathbf{x}_w)\cdot\mathbf{d}^{\mathcal{T}}}{\delta_w}\right)^2}\mathrm{e}^{-\mathrm{i}\omega(\mathbf{x}\cdot\mathbf{d})}\mathrm{H}((\mathbf{x}-\mathbf{x}_w)\cdot\mathbf{d}), \mathbf{d} = \begin{pmatrix} d_x \\ d_y \end{pmatrix}, \mathbf{x}_w = \begin{pmatrix} x_w \\ y_w \end{pmatrix}. \quad (7.2)$$

Here A is the wave amplitude, $\mathbf{d}$ is the propagation direction, $\mathbf{x}_w$ is the position of the center of the wave, δ_w controls the width of the envelope and $\mathrm{H}(\cdot)$ denotes the Heaviside function. The layout of the design domain, $\mathbf{\Omega}_{\mathrm{d}}$, is illustrated in Fig. 7.2a. It consists of a rectangle of width, w, and height, h, partitioned into three sub-domains: $\mathbf{\Omega}_{\mathrm{d,f}}$ being fixed to be full of material, $\mathbf{\Omega}_{\mathrm{d,e}}$ being fixed to be empty of material and $\mathbf{\Omega}_{\mathrm{d,d}}$ where the material distribution is allowed to change as part of the design process. The choice of $\mathbf{\Omega}_{\mathrm{d,e}}$ observed in the figure which restricts the design in front of the point source is made based on findings from numerical experiments which showed that it improved the reliability of the design procedure. The choice of $\mathbf{\Omega}_{\mathrm{d,f}}$ is made to mimic the parabolic reflector chosen as the reference for the design problem. The parabolic reflector can, under ideal conditions in the high frequency limit where the wavelength, λ, is much smaller than the width of the parabola, w, be shown to be an optimal solution to the problem. However as f decreases a space for improving the design opens. (see [P6] for more details).

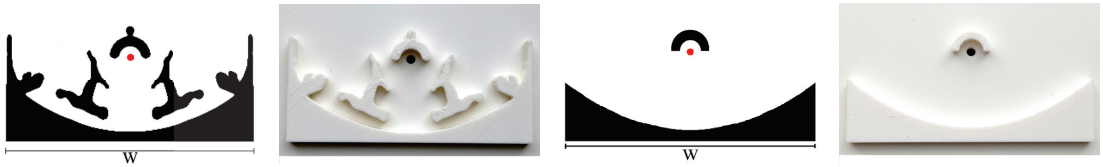

(a) (b) (c) (d)

Figure 7.3: (a) Postprocessed physical design field, D_1. (b) Printed test specimen for D_1. (c) Physical design field for the reference parabolic reflector, R_p. (d) Printed test specimen for R_p. The red circles denote the position of δP.

The example in the following considers the design of a device operating in a 50% frequency band, ΔF, around the central frequency, f_c, corresponding to the wavelength $\lambda_c = 0.89\mathrm{w}$. The height to width ratio is, $h/w = 1/2$ and $\mathbf{\Omega}_{\mathrm{d}}$ is discretized using 300×150 DVs. The emission direction, $\mathbf{d}$, is perpendicular to the reflector, $\mathbf{d} = \langle 0, 1\rangle$. The design process is executed using two realizations of the physical design field ($\eta_2 \in \{0.3, 0.7\}$), each considering nine frequencies evenly distributed across ΔF. Figure 7.2b show a plot of the convergence history presenting Φ for the 18 realizations as a function of iteration number. The stopping criterion is fulfilled after 333 design iterations. Stable convergence is observed with small jumps in Φ occurring each time the projection sharpness is increased in the continuation process (described in chapter 3.2). By studying the figure one observes that the realization of Φ attaining the largest value shifts several times during the optimization, illustrating the need for considering several frequencies in the design process.

Figure 7.3a shows $P(\xi)$ obtained from solving AWSD1 after minor post processing is applied, denoted D_1. Figure 7.3c shows the physical design field for the reference parabolic reflector, denoted R_p. Test specimens used in the experimental investigation, consisting of extruded versions of D_1 and R_p, 3D-printed in ABS plastic are shown in Figs. 7.3b and 7.3d, respectively.

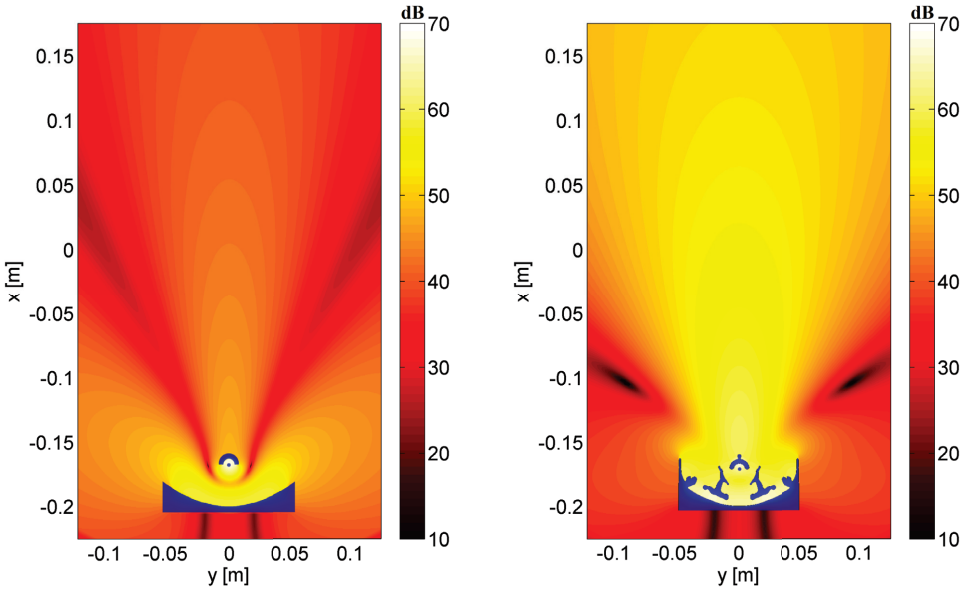

Figure 7.4: Magnitude of the pressure field in dB SPL ref 20μPa at the frequency corresponding to $\frac{w}{\lambda} = 1.2$ for (a) the reference parabolic refractor, R_p in Fig. 7.3c and (b) the post processed optimized design, D_1 in Fig. 7.3a. The designs and acoustic sources are overlaid using dark blue.

The effect of replacing the parabolic reflector, R_p, with the optimized design, D_1, at a representative frequency in the frequency band of operation for D_1 is demonstrated in Fig. 7.4. The figure shows the pressure field magnitude close to the device. Figure 7.4a considers R_p and Fig. 7.4b considers D_1. It is clear to see that D_1 outperforms R_p both in terms of directing the acoustic energy forward and in terms of its total transmission of acoustic energy.

A schematic of the experimental setup used to investigate the performance of the devices is shown in Fig. 7.5a. The setup consists of a 2D "anechoic" chamber, in which a test specimen with an acoustic source at its center is tightly fitted in a hole in the chamber floor, and a microphone flush mounted in its movable ceiling. A photo of the experimental setup with a test specimen in the chamber is shown in Fig. 7.5b. Measurements are performed by scanning the microphone along a circular path of radius $r_{\mathrm{M}} = 0.22\ \mathrm{m} \pm 10^{-3}\ \mathrm{m}$, centered at the acoustic source, in the angular interval $\theta \in [0^{\mathrm{o}}, 180^{\mathrm{o}}]$ with a resolution of 2.5°, (see [P6] for a detailed description).

Two performance measures are used to evaluate the performance of the designed device in terms of directivity and on-axis power. The far field sound pressure,

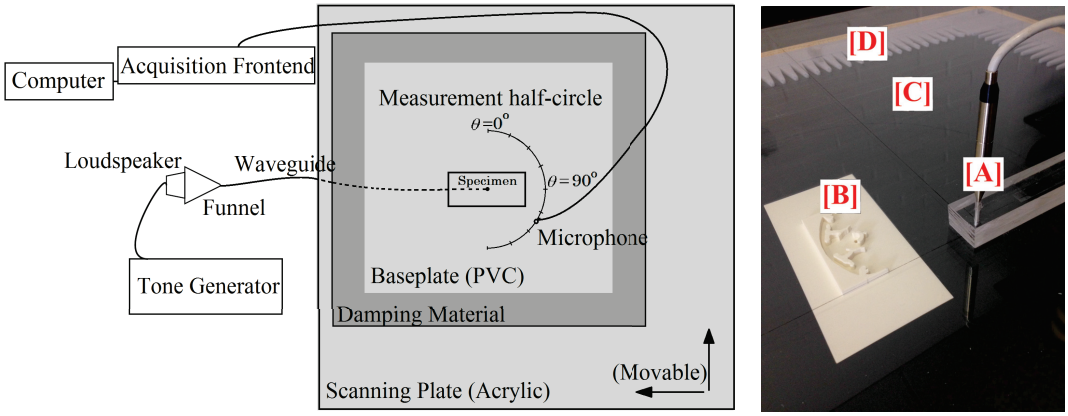

(a) (b)

Figure 7.5: (a) Schematics for the experimental setup used to investigate the performance of the 3D-printed test specimens. (b) Photo of the experimental setup including [A] flush mounted microphone, [B] 3D-printed test specimen, [C] PVC baseplate under acrylic top plate, [D] Absorbing foam.

$\psi_{\text{far}}(\theta, f)$, relative to the on axis sound pressure, $\psi_{\text{far}}(\theta = 0, f)$: (7.3), and far field sound pressure on axis, $\psi_{\text{far}}(\theta = 0, f)$, relative to the far field sound pressure of a monopole, $\psi_{\text{monopole,far}}$, radiating identical power into free space: (7.4).

$$P_m(\theta, f) = 20 \log_{10} \left(\frac{|\psi_{\text{far}}(\theta, f)|}{|\psi_{\text{far}}(\theta = 0^{\text{o}}, f)|} \right), \tag{7.3}$$

$$\Delta L_{\text{dB}}(f) = 20 \log_{10} \left(\frac{|\psi_{\text{far}}(\theta = 0^{\text{o}}, f)|}{|\psi_{\text{monopole,far}}(f)|} \right). \tag{7.4}$$

Figures 7.6a-7.6d show $P_m(\theta, f)$ for $f \sim \frac{\text{w}}{\lambda} \in [0.6, 1.7]$ and $\theta \in [-180^{\text{o}}, 180^{\text{o}}]$. The frequency interval in which D_1 was designed to operate is outlined using cyan vertical lines and a horizontal bar. Figure 7.6a and Fig. 7.6c show the numerically obtained value of $P_m(\theta, f)$ for R_p in Fig. 7.3c and for D_1 in Fig. 7.3a, respectively. It is clearly observed that D_1 outperforms R_p in terms of directing the sound forward. The sound pressure emitted in the main lobe for D_1 is at least 15 dB higher than outside the main lobe across the full frequency interval of operation. For R_p it is observed that the sound pressure emitted in the main lobe and in the side lobes for $\frac{\text{w}}{\lambda} \in [1.1, 1.4]$ is almost identical and that $P_m(\theta, f)$ is consistently higher outside the main lobe for R_p compared to D_1.

The experimentally measured $P_m(\theta, f)$ for R_p and D_1 is shown in Figs. 7.6b and 7.6d. Here $P_m(\theta, f)$ is calculated using the measured pressure directly in (7.3) and not a far field approximation, i.e. $\psi_{\text{far}} \rightarrow \psi_{\text{measured}}$. Unmeasured regions and regions where the pressure is within 3 dB of (or below) the background noise are colored dark gray. Good agreement is observed between the measured data with the numerically obtained data, not only in terms of the overall pressure distribution but also in terms of the value of $P_m(\theta, f)$. The largest discrepancy between the numerical

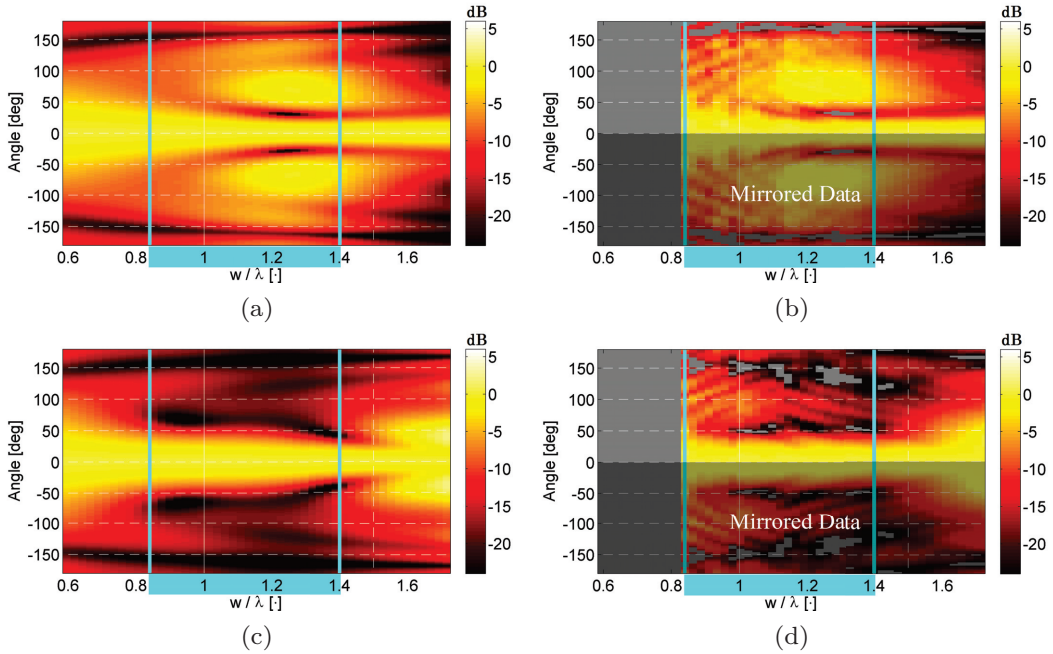

Figure 7.6: (a) Numerically obtained $P_{\mathrm{m}}(\theta, f)$ for R_p in Fig. 7.3c. (c) Numerically obtained $P_{\mathrm{m}}(\theta, f)$ for D_1 in Fig. 7.3a. (b) Experimentally measured $P_{\mathrm{m}}(\theta, f)$ for the 3D-printed test specimen in Fig 7.3d. (d) Experimentally measured $P_{\mathrm{m}}(\theta, f)$ for the 3D-printed test specimen in Fig 7.3b. (ψ_{far} is replaced by ψ_{measured} in (7.3) in both (b) and (d)). The unmeasured data below $\frac{\mathrm{w}}{\lambda} < 0.85$ and any data near the background noise have been colored dark gray. (a)-(d) The vertical cyan lines and horizontal bars mark the frequency interval considered in the optimization.

and experimental data is the oscillations in $P_m(\theta, f)$ observed for $\frac{\mathrm{w}}{\lambda} < 1.4$. These oscillations are believed to stem from the decrease in the absorption coefficient at lower frequencies, of the melamine foam placed around the edges of the chamber to obtain "anechoic" conditions. The fact that near-identical oscillations are observed for both R_p and D_1 (as well as for a reference measurement performed without a test specimen in the chamber) supports this claim. The agreement between measurements and numerical results demonstrate that the design method is capable of designing devices which function as expected under actual experimental operating conditions.

The improvement in ΔL_{dB} obtained by replacing R_p with D_1 is shown in Fig. 7.7. The blue line with circles shows ΔL_{dB} for D_1 and the black line with squares shows ΔL_{dB} for R_p. An increase in ΔL_{dB} of between 5 dB and 10 dB is observed across ΔF. Hence D_1 emits significantly more energy on axis compared to R_p. The variation in ΔL_{dB} also decreases from ≈ 6 dB for R_p to ≈ 3 dB for D_1, i.e. D_1 provides a more consistent energy emission.

A potential application for devices created using the proposed approach, deemed interesting enough to ponder here, is the custom design of sound field emission devices for experimental setups. I.e. if a given sound field is desired for an experiment a custom device for emitting a good approximation of the desired sound field can be

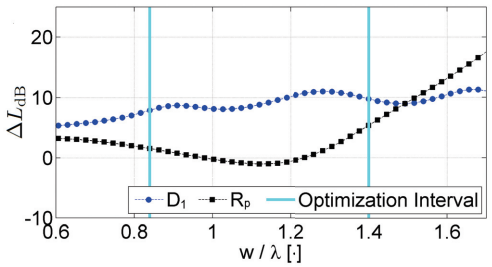

Figure 7.7: ΔL_{dB} for D_1 in Fig. 7.3a and R_p in Fig. 7.3c. The frequency interval of operation is marked using vertical cyan lines.

designed and produced directly using 3D-printing. With the current implementation of the design method this is limited to 2D-experiments, but with further work the method is extensible to 3D (barring computational limitations).

7.2 Beam-Splitting Device - AWSD2

This section considers a different application of the method detailed in [P6]. A device is presented, which is designed to direct the sound pressure emitted by a source in different directions depending on the frequency. The device operates in the frequency range where the wavelength, λ, is near the width, w, of the device: $1.2\lambda < w < 2.3\lambda$. The performance of the device is investigated both numerically and experimentally. A device capable of splitting an incoming wave in several (usually 2) directions is known from optics as a beam-, signal- or λ-splitter. Such devices are used in interferometry, [14, chap. 8], among others. Recent works on acoustic beam-splitters, consisting of a metal cylinder array with line defects placed in a water background, are reported in [106] and [107] and their use in creating acoustic logic gates in [108]. Topology optimization has not previously been applied in the design of an acoustic beam-splitting device.

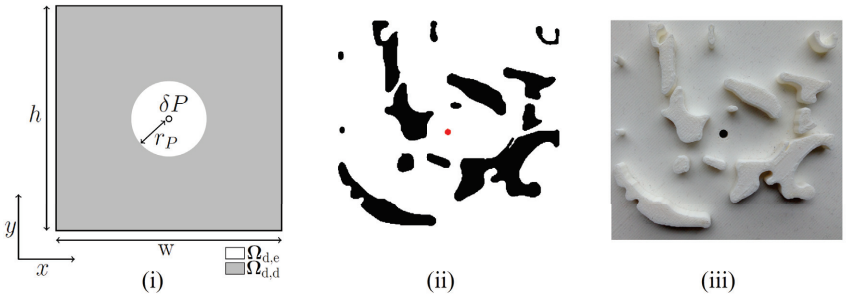

(a)

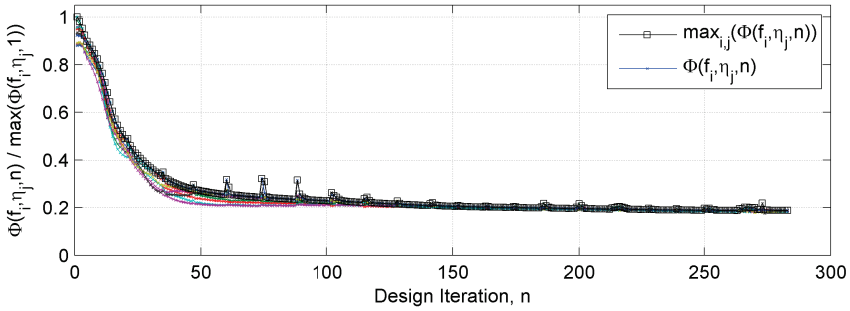

(b)

Figure 7.8: (a)i Design domain for AWSD2. $\mathbf{\Omega}_{\mathrm{d,e}}$: circular sub-domain empty of material. $\mathbf{\Omega}_{\mathrm{d,d}}$: designable sub-domain. δP: source position. r_p: radius of $\mathbf{\Omega}_{\mathrm{d,e}}$. h: height of $\mathbf{\Omega}_{\mathrm{d}}$. w: width of $\mathbf{\Omega}_{\mathrm{d}}$. (a)ii Post processed design, D_S, the red circle denote the position of δP. (a)iii 3D-printed test specimen. (b) Convergence history for AWSD2.

The goal of AWSD2 is to create a device, consisting of solid material placed in an air background, with an acoustic source at its center, which directs the energy emitted by the source in one frequency band in a prescribed direction and the energy emitted in a second frequency band in another direction. The target field, ψ_{target},

defined in (7.2) is used in Φ with different values for $\mathbf{d}$ in the two frequency bands. The target domain is defined as $\mathbf{\Omega}_\mathrm{t} = \mathbf{\Omega} \backslash \mathbf{\Omega}_\mathrm{d}$. The layout of the design domain, $\mathbf{\Omega}_\mathrm{d}$ is illustrated in Fig. 7.8ai. It consists of a square, $\mathrm{w} = h$, partitioned into two sub-domains. $\mathbf{\Omega}_{\mathrm{d,e}}$, consisting of a circular area of radius r_P, centered at the acoustic source δP, and $\mathbf{\Omega}_{\mathrm{d,d}} = \mathbf{\Omega}_\mathrm{d} \backslash \mathbf{\Omega}_{\mathrm{d,e}}$, the meaning of both defined as in chapter 7.1.

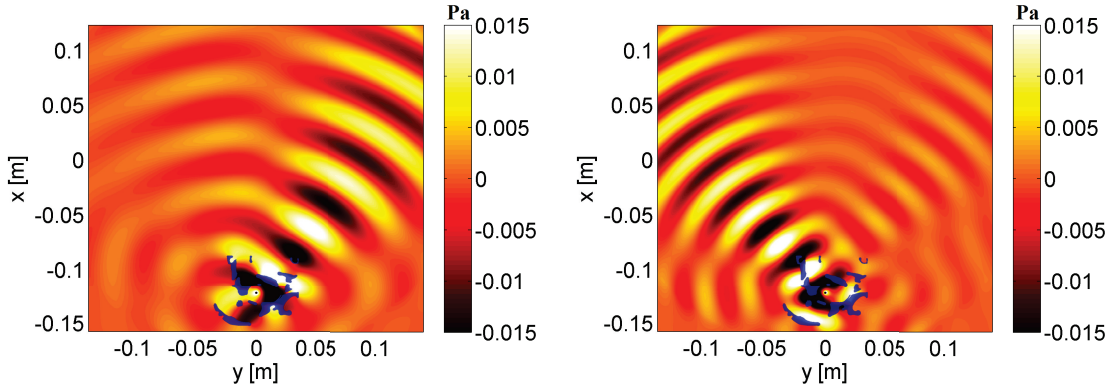

Figure 7.9: Sound pressure field in Pa emitted by D_S at the frequencies corresponding to (a) $\frac{\mathrm{w}}{\lambda} \approx 1.4$ and (b) $\frac{\mathrm{w}}{\lambda} \approx 2.0$. The design and acoustic source is overlaid using dark blue.

The device considered in the following is designed to operate in a 60% frequency band, ΔF, corresponding to the interval $\frac{\mathrm{w}}{\lambda} \in [1.26, 2.34]$, split into three sub-bands, denoted ΔF_1, ΔF_2 and ΔF_3, respectively. The lowest band, ΔF_1, was selected to correspond to $\frac{\mathrm{w}}{\lambda} \in [1.26, 1.62]$, the middle band, ΔF_2, to $\frac{\mathrm{w}}{\lambda} \in [1.62, 1.82]$ and the highest band ΔF_3, to $\frac{\mathrm{w}}{\lambda} \in [1.82, 2.34]$, respectively. For frequencies in ΔF_1 the device is designed to maximize the sound pressure emitted in the direction $\mathbf{d}_1 = \langle \frac{1}{2}, \frac{1}{2} \cdot \sqrt{3} \rangle$ corresponding to $\theta = 30^\mathrm{o}$ in Fig. 7.1. For frequencies in ΔF_3 the device is designed to maximize the sound pressure emitted in the direction $\mathbf{d}_3 = \langle -\frac{1}{2}, \frac{1}{2} \cdot \sqrt{3} \rangle$ corresponding to $\theta = -30^\mathrm{o}$ in Fig. 7.1. The optimization process is executed using two realizations of the physical design variables ($\eta_2 \in \{0.3, 0.7\}$). Four frequencies equally distributed across ΔF_1 and four frequencies equally distributed across ΔF_3 are considered for each of the two realizations of the physical design variables. A plot of the convergence history is provided in Fig. 7.8b showing Φ for each of the 16 realizations as a function of iteration number. The design process fulfills the stopping criterion after 283 design iterations. As for the example in chapter 7.1 stable convergence is observed with small jumps in Φ occurring each time the projection sharpness is increased in the continuation process. The physical design field for the device subjected to post processing is presented in Fig. 7.8aii including a red circle denoting the position of the acoustic source. An extruded version of the design, 3D-printed in ABS plastic for experimental investigation, is shown in Fig. 7.8aiii.

To illustrate the functionality of the device, Figs. 7.9a and 7.9b show the simulated pressure field emitted by the device at a representative frequency in ΔF_1 and a

representative frequency in ΔF_2, respectively. The frequencies correspond to $\frac{w}{\lambda} \approx 1.4$ and $\frac{w}{\lambda} \approx 2.0$.

An experimental investigation of D_S was performed on the test specimen in Fig. 7.8aiii, using the setup and procedure described in chapter 7.1, the only significant change being that the pressure field was measured in the angular interval $\theta \in [-90^o, 90^o]$, see Fig. 7.1.

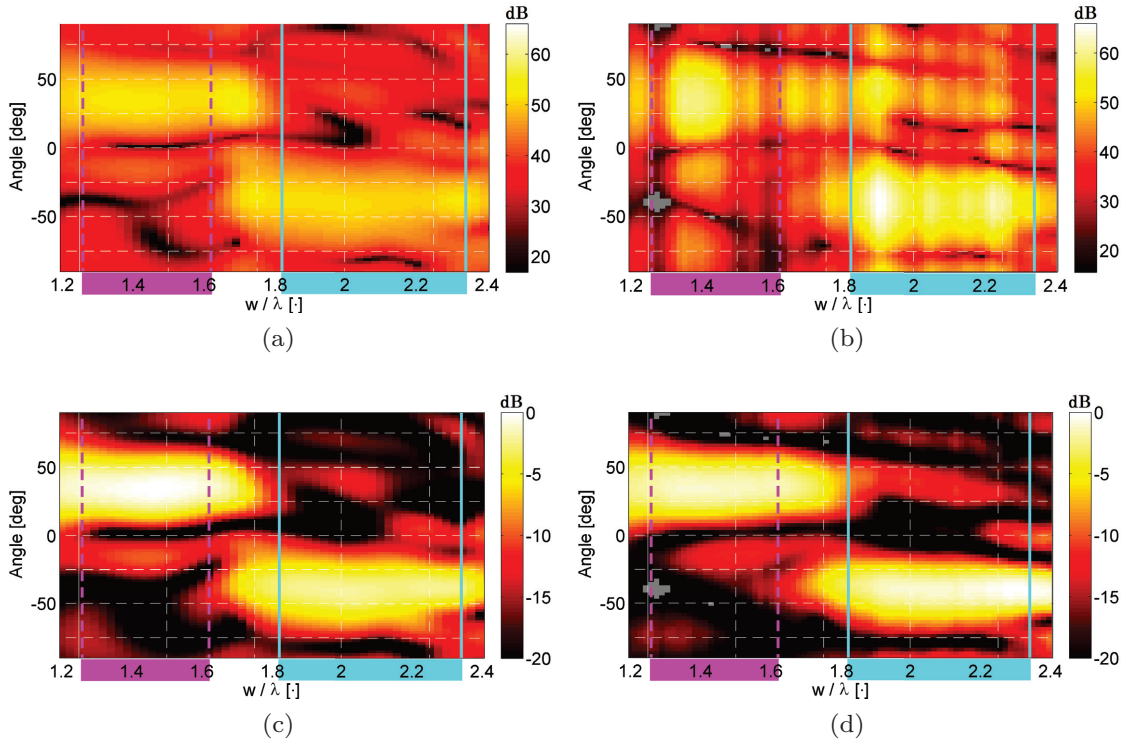

Figure 7.10: (a) Magnitude of numerically obtained far field pressure in dB SPL ref 20μPa as a function of angle and frequency for D_S in Fig. 7.8aii. (b) Magnitude of the experimentally measured pressure field at r_M for the test specimen in Fig. 7.8aiii. (c) Numerically obtained $P_S(\theta, f)$ for D_S in Fig. 7.8aii. (d) Experimentally measured $P_S(\theta, f)$ for the test specimen in Fig. 7.8aiii. The vertical dashed magenta and full cyan lines and horizontal bars mark the frequency intervals ΔF_1 and ΔF_2, respectively.

The numerically calculated far field pressure for D_S is shown in Fig. 7.10a and the pressure measured in the experiment at $r_M = 0.22$ m $\pm\, 10^{-3}$ m is shown in Fig. 7.10b. While the overall trend for the pressure field in the two figures is seen to be similar, significant variations in the magnitude as a function of frequency are observed in the measure data. These variations are not a result of the design failing, however. Instead they stem from variations in the termination impedance of the waveguide used to transmit the sound from the loudspeaker to the hole in the test specimen (see [P6] for further details about the experimental setup). This fact is realized by considering the measure presented in (7.5) instead,

$$P_S(\theta, f) = 20\log_{10}\left(\frac{|\psi(\theta,f)|}{\int_{\theta=-90^\circ}^{\theta=90^\circ}|\psi(\theta,f)|\mathrm{d}\theta}\Bigg/\max_{\theta,f}\left(\frac{|\psi(\theta,f)|}{\int_{\theta=-90^\circ}^{\theta=90^\circ}|\psi(\theta,f)|\mathrm{d}\theta}\right)\right). \quad (7.5)$$

In short, P_S is the pressure (in dB) at a given frequency and angle, scaled by the total pressure emitted in the measured angular interval at that frequency.[3] By considering P_S the varying termination impedance of the waveguide is scaled away, providing a more fair comparison between the numerical and measured data. Figures 7.10c and 7.10d show P_S for the data presented in Figs. 7.10a and 7.10b, respectively. By comparing the numerical and experimental data a very high level of agreement is observed. A clear separation of two regions of high pressure is observed. The pressure emitted across the full intervals of ΔF_1 at $\theta \approx 30^\circ$ and ΔF_2 at $\theta \approx -30^\circ$, respectively, only varies by 2.5 dB, while the change in pressure when measuring at $\theta \approx -30^\circ$ compared to $\theta \approx 30^\circ$ for any frequency in ΔF_1 and ΔF_2 is at least 9.5 dB. It is thus possible to clearly identify if signal emitted by the source inside the device lies in ΔF_1 or ΔF_2.

This example of an acoustic beam-splitting device operating in an air background, is to the author's knowledge, the first of its kind. A device capable of performing spatial filtering is interesting on its own, and could serve as a basis for several applications where spatial filtering is of interest.

[3] P_S is further scaled by the maximal value in the full frequency and angular interval, hereby setting the maximum of P_S to 0 dB.

7.3 Flat Focusing Lens - AWSD3

This section presents the design of a flat acoustic lens made using a modified version of the method in [P6]. This design problem is denoted AWSD3. The layout of $\mathbf{\Omega}_\mathrm{d}$ seen in Fig. 7.11ai is used. The meaning of the sub-domains $\mathbf{\Omega}_\mathrm{d,e}$ and $\mathbf{\Omega}_\mathrm{d,d}$ is defined in chapter 7.1. Instead of an acoustic source inside $\mathbf{\Omega}_\mathrm{d}$ a spatially localized near-plane wave, ψ_bc, incident on $\mathbf{\Omega}_\mathrm{d}$ from below is considered (see Fig. 7.1). This wave is generated by the boundary condition (2.7) imposed on $\delta\mathbf{\Omega}_\mathrm{PW}$, as described in chapter 6.1 with $\mathbf{d} = \langle 0, 1\rangle$, $\mathbf{x}_w = \langle 0\text{ m}, 0\text{ m}\rangle$, $\delta_x = 0.8$ m. A small target domain, $\mathbf{\Omega}_\mathrm{t} = [-0.02\text{ m}, 0.02\text{ m}, 0.48\text{ m}, 0.52\text{ m}]$, in which the the incident wave is to be focused, is considered. To this end, $|\psi_\mathrm{target}|$ in (7.1), is defined as,

$$|\psi_\mathrm{target}(\mathbf{x})| = A_\mathrm{max},\ \forall\ \mathbf{x} \in \mathbf{\Omega}_\mathrm{t}. \tag{7.6}$$

A_max is chosen such that the energy in $|\psi_\mathrm{target}|$ over $\mathbf{\Omega}_\mathrm{t}$ is greater than the energy in ψ_bc.

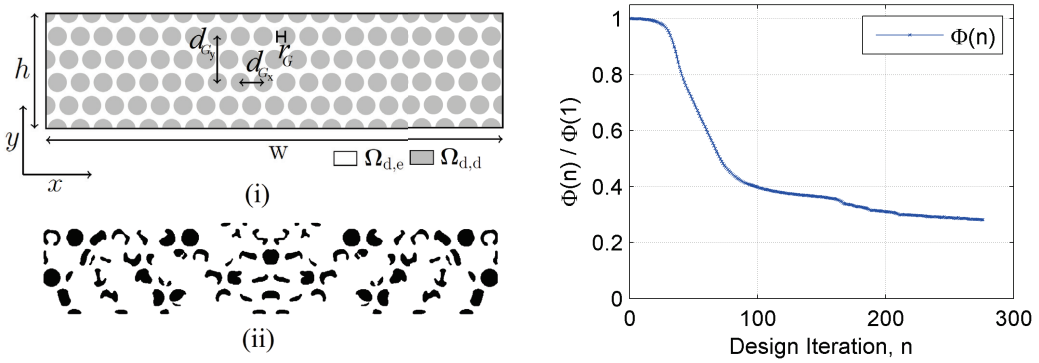

Figure 7.11: (a)i $\mathbf{\Omega}_\mathrm{d}$ for AWSD3 restricting the design to a hexagonal grid. $\mathbf{\Omega}_\mathrm{d,d}$ denotes the designable part and $\mathbf{\Omega}_\mathrm{d,e}$ denotes the areas fixed to be empty of material. (a)ii Post processed physical design field for AWSD3, denoted D_F, black is material and white is void. (b) Convergence history for AWSD3 showing $\Phi(n)$ scaled by $\Phi(1)$ as a function of iteration number, n. A total of 276 design iterations is used to reach the stopping criterion.

The formulation of the design problem is inspired by [109], which proposes a method, based on a genetic algorithm, for designing flat acoustic lenses which focus the energy from a plane sound pressure wave impinging on the lens in the focal point, $\mathbf{x}_f$, behind the lens. The lens consists of an array of metallic rods of varying radius placed in a hexagonal grid. Four radii are allowed (including zero) and a genetic algorithm is used to select the radius of the rods. In [109] it is reported that the algorithm typically requires ≈ 50000 iterations to "converge". The goal of the method in [109] is to maximize the *sound amplification* (SA) at the focal point, $\mathbf{x}_f$, denoted SA_f. SA being defined as,

$$\mathrm{SA}(\mathbf{x}) = 20 \log_{10} \left(\frac{|\psi_L(\mathbf{x})|}{|\psi_{NL}(\mathbf{x})|} \right). \tag{7.7}$$

$\psi_L(\mathbf{x})$ and $\psi_{NL}(\mathbf{x})$ denoting the pressure at $\mathbf{x}$ with and without the lens in $\mathbf{\Omega}$.

The lens presented in [109, Fig. 5c] (also investigated experimentally in [110]) is used as a benchmark in the following. The values for the operating frequency, position of the focal point, dimensions of the lens and the distribution of the designable rods for the design problem AWSD3 are chosen such that they are as close as possible to those of the benchmark.

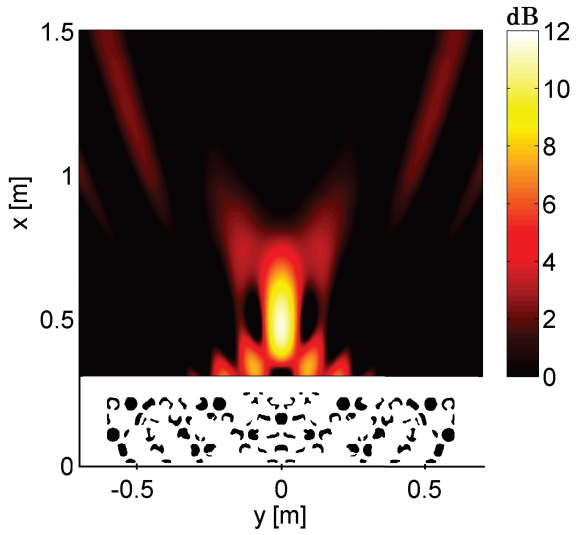

Figure 7.12: SA($\mathbf{x}$) behind the designed lens shown in Fig. 7.11aii. A maximum value of $\mathrm{SA}_f \approx 11.5$ dB is obtained at $\mathbf{x}_f = \langle 0.0 \text{ m}, 0.5 \text{ m} \rangle$. The position of the lens is included using black for material and white for air.

The lens design is designed by solving AWSD3 for a single realization of the physical design field, $\eta = 0.5$, and a single frequency, $f = 1700$ Hz, along with the following additional choices. The width and height of the lens is $w = 1.2$ m and $h = 0.24$ m, respectively. A total of 800×160 finite elements are used to discretize $\mathbf{\Omega}_\mathrm{d}$ (see Fig. 7.11ai). The design consists of a hexagonal grid of freely designable circular regions of radius, $r_\mathrm{G} = 0.0220$ m with a grid spacing of $d_{G_x} = 0.06105$ m and $d_{G_y} \approx 0.106$ m. Note that the rods in the outer rows and columns are cut in half, this is a result of the implementation and may easily be changed. The focal point is selected to lie a distance of 0.38 m behind the lens, exactly as for the benchmark. A post processed version of the physical design field, denoted D_F, obtained from solving AWSD3 is presented in Fig. 7.11aii. The convergence history for AWSD3 is presented in Fig. 7.11b. A total of 276 design iterations are used to reach fulfillment of the stopping criterion.

The sound amplification behind D_F is shown in Fig. 7.12 for a plane wave incident on the lens from below. A value of $\mathrm{SA}_f \approx 11.5$ dB is obtained at the focal point.

Comparing this to the value $\mathrm{SA}_f \approx 8.35$ dB reported in [110] for the benchmark, an increase of ≈ 3.2 dB is obtained. This significant increase can most likely be attributed to the added design freedom in allowing the shape and topology of the circular regions to vary, instead of only allowing four distinct radii. In addition to the performance increase, a significant decrease in the number of design iterations is observed. From the typical value of 50000 reported in [109] to merely 276 iterations. It is stressed that the computational resources needed in each design iteration in [109] is not known and that it therefore is difficult to draw an absolute conclusion regarding the large decrease, without a more rigorous investigation. However it is certainly a thought provoking result, illustrating the effectiveness of density-based topology optimization.

8 Concluding Remarks

This Thesis has presented the development and extensions of a number of density-based topology optimization approaches for wave propagation problems, with a clear focus on acoustics. It has provided a description of experiments developed for testing designs created using these approaches, along with experimental results showing good agreement with numerical data.

The Thesis provided a brief introduction to the modeling of wave problems using PDEs, to density-based topology optimization and to the FEM and Hybrid WBM-FEM used to discretize the model problems. It included a short discussion of the benefits and drawbacks of the Hybrid WBM-FEM compared to the FEM and discussions of two preconditioners applied in the iterative solution of wave propagation problems using GMRES.

An extension to an existing robust design approach, enabling its application to wave propagation problems, was described. Using the extended approach it was demonstrated to be possible to attain a significant improvement in the geometric robustness of several acoustic cavities. Presented experimental results demonstrated good agreement with numerical predictions.

A novel approach for meta material design was presented, a defining feature of the approach being that it considers a full slab of material instead of only a single unit cell. The behavior of a meta material slab exhibiting negative refraction with high transmittance was demonstrated numerically and realized experimentally. The experimental study revealed a shift in the refraction angle between numerical and measured results consistent with a frequency shift, possibly caused by a change in the effective speed of sound in the experimental setup.

A method for designing acoustic wave shaping devices was discussed in the context of three different applications, the first being the design of a directional sound emission device, shown to outperform a reference parabolic reflector both numerically and experimentally. The second example considered a spatial beam-splitting device, exhibiting an emission pattern systematically controlled by the operating frequency. The behavior of the device was investigated both numerically and experimentally, and good agreement was demonstrated in terms of the fraction of the pressure emitted at a given frequency and angle. To the author's knowledge, such an acoustic beam-splitting device operating in an air background is the first of its kind reported in the literature. The final example treated the design of a flat sound focusing lens considering a design problem from the literature as a benchmark. The optimized lens was shown to outperform the benchmark in terms of sound amplification by more than 3 dB and a decrease of two orders of magnitude in the number of design iterations needed to solve the design problem was reported.

During the research work forming the foundation of this Thesis, it was consistently found that using GCMMA, with the modifications outlined in chapter 3.4, instead of MMA significantly improved the convergence behavior observed when solving the

considered design problems. This is believed to be due to a high general sensitivity of the considered wave problems.

It was consistently found that small variations in the initial choice of ξ, the operating frequency f, and the model/design/target domain configurations potentially lead to large changes in the final design geometry. In the vast majority of cases the changes were found not to have any significant impact on the objective function value, however.

The quasi 2D experimental setups developed as part of this PhD enables the direct investigation of the pressure field surrounding 2D acoustic designs under both interior and exterior conditions. The use of such setups as tools for validating 2D acoustic design proposed in the future is strongly recommended.

8.1 Future Work

Many interesting challenges and much future work on the application of density-based topology optimization to wave propagation problems exist. A short list of work related to the topics touched upon in this Thesis follows here.

- Further research of the benefits and limitations of applying the Hybrid WBM-FEM to topology optimization based design problems.
- Implementation and large scale testing of the preconditioners, for which preliminary results were presented in section 4.2.1, in a parallel computing framework.
- Introduction of a model for attenuation near material surfaces in the design problems to account for the experimentally observed attenuation.
- Extended research on the application of topology optimization to the design of beam-splitting devices and flat focusing lenses.
- Further development and application of the experimental procedures developed as part of the PhD.
- An extension of the proposed design methods to 3D.

Bibliography

[1] Erwin Kreyszig. *Advanced Engineering Mathematics - Tenth Edition*. John Wiley & Sons (Asia) Pte Ltd, 2011.

[2] Jens Eising. *Lineær Algebra*. Institut for Matematik - Danmarks Tekniske Universitet, 1999.

[3] Per W. Karlsson and Vagn Lundsgaard Hansen. *Matmatisk Analyse 2*. Institut for Matematik - Danmarks Tekniske Universitet, 1998.

[4] Helge Elbrønd Jensen, Steen Markvorsen, Poul Hjorth, and Wolfhard Kleim. *Matematisk Analyse 1*. Institut for Matematik - Danmarks Tekniske Universitet, 2000.

[5] Robert D. Cook, Davis S. Malkus, Michael E. Plesha, and Robert J. Witt. *Concepts and Applications of Finite Element Analysis - Fourth Edition*. John Wiley & Sons Inc., 2002.

[6] Jianming Jin. *The Finite Element Method in Electromagnetics - Second Edition*. John Wiley & Sons Inc. New York, 2002.

[7] Randall J. LeVeque. *Finite Volume Methods for Hyperbolic Problems*. Cambridge University Press, 2002.

[8] Nakhlé H. Asmar. *Partial Differential Equations - with Fourier Series and Boundary Value Problems - Second Edition*. Pearson Education, Inc., 2005.

[9] Randall J. LeVeque. *Finite Difference Methods for Ordinary and Partial Differential Equations - Steady-State and Time-Dependent Problems*. SIAM - Society for industrial and Applied Mathematics, 2007.

[10] Jan S. Hesthaven and Tim Warburton. *Nodal Discontinuous Galerkin Methods - Algorithms, Analysis, and Applications*. Springer Science+Business Media, LCC, 2008.

[11] David A. Kopriva. *Implementing Spectral Methods for Partial Differential Equations - Algorithms for Scientists and Engineers*. Springer Science+Business Media B. V., 2009.

[12] David J. Griffiths. *Introduction to Electrodynamics - Third Edition*. Pearson Education, Inc., 2008.

[13] Finn Jacobsen and Peter Møller Juhl. *Fundamentals of General Linear Acoustics*. WILEY, 2013.

[14] S.J. Frank L. Pedrotti, Leno M. Pedrotti, and Leno S. Pedrotti. *Introduction to Optics - Third Edition*. Pearson Education, Inc, 2007.

[15] Daniel J. Inman. *Engineering Vibrations - Third Edition*. Pearson Education, 2009.

[16] Jorge Nocedal and Stephen J. Wright. *Numerical Optimization - Second Edition*. Springer Science+Business Media LCC, 2006.

[17] M. P. Bendsøe and O. Sigmund. *Topology Optimization*. Springer, 2003.

[18] Viggo Tvergaard, Niels Olhoff, Ann Bettina Richelsen, and Arne Gudmann Nielsen. *Dimensionering og styrke*. DTU Mekanik - Faststofmekanik - Danmarks Tekniske Universitet, 2005.

[19] Jacques Hadamard. Sur les problèmes aux dérivées partielles et leur signification physique [it has not proven possible to aquire a copy of the paper]. *Princeton university bulletin 13.*, 28:49–52, 1902.

[20] Martin Philip Bendsøe and Noboru Kikuchi. Generating optimal topologies in structural design using a homogenization method. *Computer Methods in Applied Mechanics and Engineering*, 71:197–224, 1988.

[21] Katsuyuki Suzuki and Noboru Kikuchi. A homogenization method for shape and topology optimization. *Computer Methods in Applied Mechanics and Engineering*, 93:291–318, 1991.

[22] Niels Aage, Erik Andreassen, and Boyan Stefanov Lazarov. Topology optimization using PETSc: An easy-to-use, fully parallel, open source topology optimization framework. *Structural and Multidiciplinary Optimization*, 51:565:572, 2015.

[23] Joe Alexandersen and Boyan S. Lazarov. Topology optimization of manufacturable microstructural details with length scale separation using a spectral coarse basis preconditioner. *Computer Methods in Applied Mechanics and Engineering*, 290:156–182, 2015.

[24] Erik Andreassen, Boyan S. Lazarov, and Ole Sigmund. Design of manufacturable 3D extremal elastic microstructure. *Mechanics of Materials*, 69:1–10, 2014.

[25] Anders Clausen, Fengwen Wang, Jakob S. Jensen, Ole Sigmund, and Jennifer A. Lewis. Topology optimized architectures with programmable poisson's ratio over large deformations. *Advanced Materials*, 27:5523–5527, 2015.

[26] Thomas Borrvall and Joakim Petersson. Topology optimization of fluids in stokes flow. *International Journal for Numerical Methods in Fluids*, 41:77–107, 2003.

[27] Casper Schousboe Andreasen, Allan Roulund Gersborg, and Ole Sigmund. Topology optimization of microfluidic mixers. *International Journal for Numerical Methods in Fluids*, 61:498–513, 2009.

[28] Sebastian Kreissl, Georg Pingen, and Kurt Maute. Topology optimization of unsteady flow. *International Journal for Numerical Methods in Engineering*, 87:1229–1253, 2011.

[29] Sebastian Nørgaard, Ole Sigmund, and Boyan Lazarov. Topology optimization of unsteady flow problems using the lattice boltzmann method. *Journal of Computational Physics*, 307:291–307, 2016.

[30] Joe Alexandersen, Ole Sigmund, and Niels Aage. Large scale three-dimensional topology optimisation of heat sinks cooled by natural convection. *International Journal of Heat and Mass Transfer*, 100:876–891, 2016.

[31] Steven J. Cox and David C. Dobson. Maximizing band gaps in two-dimensional photonic crystals. *SIAM Journal of Applied Mathematics*, 59(6):2108–2120, 1999.

[32] Jakob S. Jensen and Ole Sigmund. Topology optimization of photonic crystal structures: a high-bandwidth low-loss t-junction waveguide. *Optical Society of America*, 22(6), 2005.

[33] J. S. Jensen, O. Sigmund, L. H. Frandsen, P. I. Borel, A. Harpøth, and M. Kristensen. Topology design and fabrication of an efficient double 90^o photonic crystal waveguide bend. *IEEE Photonics Technology Letters*, 17(6):1202–1204, 2005.

[34] Peter I. Borel, Brian Bilenberg, Lars H. Frandsen, Theodor Nielsen, Jacob Fage-Pedersen, Andrei V. Lavrinenko, Jakob S. Jensen, Ole Sigmund, and Anders Kristensen. Imprinted silicon-based nanophotonics. *Optical Express*, 15:(3), 2007.

[35] Y. Elesin, B. S. Lazarov, J. S. Jensen, and O. Sigmund. Time domain topology optimization of 3d nanophotonic devices. *Photonics and Nanostructures - Fundamentals and Applications*, 12:23–33, 2014.

[36] Fengwen Wang, Jakob S. Jensen, and Ole Sigmund. Robust topology optimization of photonic crystal waveguides with tailored dispersion properties. *Journal of the Optical Society of America B*, 28(3):387–397, 2011.

[37] Y. Elesin, B. S. Lazarov, J. S. Jensen, and O. Sigmund. Design of robust and efficient photonic switches using topology optimization. *Photonics and Nanostructures - Fundamentals and Applications*, 10:153–165, 2012.

[38] Lars H. Frandsen, Yuriy Elesin, Louise F. Frellsen, Miranda Mitrovic, Yunhong Ding, Ole Sigmund, and Kresten Yvind. Topology optimized mode conversion in a photonic crystal waveguide fabricated in silicon-on-insulator material. *Optical Express*, 22:No. 7, 2014.

[39] Jacob Andkjær and Ole Sigmund. Topology optimized low-contrast all-dielectric optical cloak. *Applied Physics Letters*, 98:021112, 2011.

[40] Jacob Andkjær and Ole Sigmund. Topology optimized cloak for airborn sound. *Journal of Vibration and Acoustics*, 135:041011–1 – 041001–5, 2013.

[41] Alejandro R. Diaz and Ole Sigmund. A toplogy optimization method for design of negative permeability metamaterials. *Structural and Multidiciplinary Optimization*, 41:163–177, 2010.

[42] Jacob Andkjær, Villads Egede Johansen, Kasper Storgaard Friis, and Ole Sigmund. Inverse design of nanostructured surfaces for color effects. *Journal of the Optical Society of America B*, 31:164–174, 2014.

[43] Jakob S. Jensen and Ole Sigmund. Topology optimization for nano-photonics. *Laser Photonics Reviews*, 5(2):308–321, 2011.

[44] Ole Sigmund and Jakob Søndergaard Jensen. Systematic design of phononic band-gap materials and structures by topology optimization. *Philosophical Transactions of the Royal Society A*, 361(1806):1001–1019, 2003.

[45] Jun Hyeong Park, Pyung Sik Ma, and Yoon Young Kim. Design of phononic crystals for self-collimation of elastic waves using topology optimization method. *Structural and Multidiciplinary Optimization*, 51:1199–1209, 2015.

[46] Erik Andreassen and Jakob Søndergaard Jensen. Topology optimization of periodic microstructures for enhanced dynamic properties of viscoelastic composite materials. *Structural and Multidiciplinary Optimization*, 49:695–705, 2014.

[47] C. Van hoorickx, O.Sigmund, M.Schevenels, B.S.Lazarov, and G.Lombaert. Topology optimization of two-dimensional elastic wave barriers. *Journal of Sound and Vibration*, 376:95–111, 2016.

[48] Eddie Wadbro and Martin Berggren. Topology optimization of an acoustic horn. *Computer Methods in Applied Mechanics and Engineering*, 196:420–436, 2006.

[49] Jianbin Du and Niels Olhoff. Minimization of sound radiation from vibrating bimaterial structures using topology optimization. *Structural and Multidiciplinary Optimization*, 33:305–321, 2007.

[50] Gil Ho Yoon, Jakob Søndergaard Jensen, and Ole Sigmund. Topology optimization of acoustic-structure interaction problems using a mixed finite element formulation. *International Journal for Numerical Methods in Engineering*, 70:1049–1075, 2007.

[51] Maria B. Dühring, Jakob S. Jensen, and Ole Sigmund. Acoustic design by topology optimization. *Journal of Sound and Vibration*, 317:557–575, 2008.

[52] Jungwan Kook, Kunmo Koo, Jaeyub Hyun, Jakob S. Jensen, and Semyung Wang. Acoustical topology optimization for zwicker's loudness model - application to noise barriers. *Computer Methods in Applied Mechanics and Engineering*, 237-240:130–151, 2012.

[53] Gil Ho Yoon. Acoustic topology optimization of fibrous material with delany-bazley empirical material formulation. *Journal of Sound and Vibration*, 332:1172–1187, 2013.

[54] Eddie Wadbro. Analysis and design of acoustic transition sections for impedance matching and mode conversion. *Structural and Multidiciplinary Optimization*, 50:395–408, 2014.

[55] Daniel A. Tortorelli and Panagiotis Michaleris. Design sensitivity analysis: Overview and review. *Inverse Problems in Engineering*, 1:71–105, 1994.

[56] Ole Sigmund. On the usefulness of non-gradient approaches in topology optimization. *Structural and Multidiciplinary Optimization*, 43:589–596, 2011.

[57] Thomas Borrvall and Joakim Petersson. Topology optimization using regularized intermediate density control. *Computer Methods in Applied Mechanics and Engineering*, 190:4911–4928, 2001.

[58] Blaise Bourdin. Filters in topology optimization. *International Journal for Numerical Methods in Engineering*, 50:2143–2158, 2001.

[59] Tyler E. Bruns and Daniel A. Tortorelli. Topology optimization of non-linear elastic structures and compliant mechanisms. *Computer Methods in Applied Mechanics and Engineering*, 190:3443–3459, 2001.

[60] J. K. Guest, J. H. Prévost, and T. Belytschko. Achieving minimum length scale in topology optimization using nodal design variables and projection functions. *International Journal for Numerical Methods in Engineering*, 61:238–254, 2004.

[61] Shengli Xu, Yuanwu Cai, and Gengdong Cheng. Volume preserving nonlinear density filter based on heaviside projections. *Structural and Multidiciplinary Optimization*, 41:495–505, 2010.

[62] Fengwen Wang, Boyan S. Lazarov, and Ole Sigmund. On projection methods, convergence and robust formulations in topology optimization. *Structural Multidiciplinary Optimization*, 43:767–784, 2011.

[63] Niels Aage. *Topology optimization of radio frequency and microwave structures*. PhD thesis, The Technical University of Denmark, Department of Mechanical Engineering, DCAMM Special Report No. S129, 2011.

[64] George B. Arfken and Hans J. Weber. *Mathematical Methods for Physicists - Sixth Edition*. Elsevier Academic Press, 2005.

[65] Krister Svanberg. The method of moving asymptotes - a new method for structural optimization. *International Journal for Numerical Methods in Engineering*, 24:359–373, 1987.

[66] Krister Svanberg. A class of globally convergent optimization methods based on conservative convex seperable approximations. *SIAM Journal of Optimization*, 12:555–573, 2002.

[67] B Pluymers. *Wave Based Modelling Methods for Steady-State Vibro-Acoustics*. PhD thesis, Katholieke Universiteit Leuven, 2006.

[68] Wim Desmet. *A Wave Based Prediction Technique for Coupled Vibro-Acoustic Analysis*. PhD thesis, Katholieke Universiteit Leuven, 1998.

[69] Bastiaan van Hal. *Automation and Performance Optimization of the Wave Based Method for Interior Structural-Acoustic Problems*. PhD thesis, Katholieke Universiteit Leuven, 2004.

[70] Elke Deckers, Onur Atak, Laurens Coox, Roberto D'Amico, Hendrik Devriendt, Stijn Jonckheere, Kunmo Koo, Bert Pluymers, Dirk Vandepitte, and Wim Desmet. The wave based method: An overview of 15 years of research. *Wave Motion*, 51:550–565, 2014.

[71] Seongyeol Goo, Junghwan Kook, Kunmo Koo, Jaeyub Hyun, and Semyung Wang. Acoustic topology optimization for interior acoustic problem using the hybrid finite element - wave based method. In *The Eighth China-Japan-Korea Joint Symposium on Optimization of Structural and Mechanical Systems*, 2014.

[72] Yousef Saad. *Iterative Methods for Sparse Linear Systems*. Society for Industrial and Applied Mathematics, 2003.

[73] Ivan G. Graham, Thomas Y. Hou, Omar Lakkis, and Robert Scheichl. *Lecture Notes in Computational Science and Engineering 83*. Springer, 2014.

[74] P. Gatto and J.S. Hesthaven. A preconditioner based on low-rank approximation of schur complements. *Journal of Computational Physics*, [In review], arXiv:1508.07798.

[75] N. Halko, P. G. Martinsson, and J. A. Tropp. Finding structure with randomness: Probabilistic algorithms for constructing approximate matrix decompositions. *SIAM Journal of Applied Mathematics*, 53(2):217–288, 2011.

[76] Boyan S. Lazarov, Mattias Schevenels, and Ole Sigmund. Robust design of large-displacement compliant mechanisms. *Mechanical Sciences*, 2:175–182, 2011.

[77] Miche Jansen, Geert Lombaert, Moritz Diehl, Boyan S. Lazarov, Ole Sigmund, and Mattias Schevenels. Robust topology optimization accounting for misplacement of material. *Structural Multidiciplinary Optimization*, 47:317–333, 2013.

[78] Boyan S. Lazarov, Fengwen Wang, and Ole Sigmund. Length scale and manufacturability in density-based topology optimization. *Archive of Applied Mechanics*, 86:189–218, 2016.

[79] O. Sigmund. Manufacturing tolerant topology optimization. *Acta Mechanica Sinica*, 25:227–239, 2009.

[80] M. Schevenels, B.S. Lazarov, and O. Sigmund. Robust topology optimization accounting for spatially varying manufacturing errors. *Computer Methods in Applied Mechanics and Engineering*, 200:3613–3627, 2011.

[81] Boyan S. Lazarov, Mattias Schevenels, and Ole Sigmund. Topology optimization considering material and geometric uncertainties using stochastic collocation methods. *Structural Multidiciplinary Optimization*, 46:597–612, 2012.

[82] Mingdong Zhou, Boyan S. Lazarov, Fengwen Wang, and Ole Sigmund. Minimum length scale in topology optimization by geometric constraints. *Computer Methods in Applied Mechanics and Engineering*, 293:266–282, 2015.

[83] Richard J. Fitzgerald. Validating topology optimization for acoustics. *Physics Today*, 69(2):18, 2016.

[84] W. Akl, A. El-Sabbagh, K. Al-Mitani, and A. Baz. Topology optimization of a plate coupled with acoustic cavity. *International Journal of Solids and Structures*, 46:2060–2074, 2009.

[85] Jin Woo Lee. Optimal topology of reactive muffler achieving target transmission loss values: Design and experiment. *Applied Acoustics*, 88:104–113, 2015.

[86] J. B. Pendry. Negative refraction makes a perfect lens. *Physical Review Letters*, 85(18):3966–3969, 2000.

[87] JB Pendry. Negative refraction. *Comtemporary Physics*, 45:3:191–202, 2004.

[88] V. G. Veselago. The electrodynamics of substances with negative values of ϵ and μ. *Soviet Physics Uspekhi*, 10:509–514, 1968.

[89] Clifford M. Krowne and Yong Zhang. *Physics of Negative Refraction and Negative Index Material - Optical and Electronic Aspects and Diversified Approaches*. Springer-Verlag Berlin Heidelberg, 2007.

[90] Xiangdong Zhang and Zhengyou Liu. Negative refraction of acoustic waves in two-dimensional phononic crystals. *Applied Physics Letters*, 85:341–343, 2004.

[91] Shuang Zhang, Wenjun Fan, N. C. Panoiu, K. J. Malloy, R. M. Osgood, and S. R. J. Brueck. Experimental demonstration of near-infrared negative-index metamaterials. *Physical Review Letters*, 95:137404, 2005.

[92] Franck D. Philippe, Todd W. Murray, and Claire Prada. Focusing on plates: Controlling guided waves using negative refraction. *Scientific Reports*, 5:11112 – 1 – 11112 – 4, 2015.

[93] Richard V. Craster and Sébastien Guenneau. *Acoustic Metamaterials - Negative Refraction, Imaging, Lensing and Cloaking*. Springer Science+Business Media Dordrecht, 2013.

[94] Victor M. Garciá-Chocano, Johan Christensen, and José Sánchez-Dehesa. Negative refraction and energy funneling by hyperbolic materials: An experimental demonstration in acoustics. *Physical Review Letters*, 112:144301, 2014.

[95] Patanjali V. Parimi, Wentao T. Lu, Plarenta Vodo, and Srinivas Sridhar. Imaging by flat lens using negative refraction. *Nature*, 426:404, 2003.

[96] Mark S. Ureda. Analysis of loudspeaker line arrays. *Journal of the Audio Engineering Society*, 52(5):467–495, 2004.

[97] Ji-Ho Chang and Finn Jacobsen. Sound field control with a circular double-layer array of loudspeakers. *Journal of the Acoustical Society of America*, 131(6)(6):4518–4525, 2012.

[98] Ji-Ho Chang and Finn Jacobsen. Experimental validation of sound field control with a circular double-layer array of loudspeakers. *Journal of the Acoustical Society of America*, 133(4)(4):2046–2054, 2013.

[99] T. F. Hueter. Twenty years in underwater acoustics: generation and reception. *Journal of the Acoustical Society of America*, 51(3)(3):1025–1040, 1972.

[100] Sten Wahlström. The parabolic reflector as an acoustic amplifier. *Journal of the Audio Engineering Society*, 33(6)(6):418–429, 1985.

[101] M. Jean McKemie and Chester M. McKinney. An experimental investigation of the parabolic reflector as a nearfield calibration device for underwater sound transducers. *Journal of the Acoustical Society of America*, 67:523–529, 1980.

[102] Raymond van der Rots and Arthur Berkhoff. Directional loudspeaker arrays for acoustic warning systems with minimised noise pollution. *Applied Acoustics*, 89:345–354, 2015.

[103] Erik Bängtsson, Daniel Noreland, and Martin Berggren. Shape optimization of an acoustic horn. *Computer Methods in Applied Mechanics and Engineering*, 192:1533–1571, 2003.

[104] Rajitha Udawalpola and Martin Berggren. Optimization of an acoustic horn with respect to efficiency and directivity. *International Journal for Numerical Methods in Engineering*, 73:1571–1606, 2007.

[105] D Noreland, R Udawalpola, P Seoane, E Wadbro, and M Berggren. An efficient loudspeaker horn designed by numerical optimization: an experimental study. Report UMINF 10.1. Sweden: Department of Computing Science, Umeå University; 2010.

[106] Bo Li, Jun-Jun Guan, Ke Deng, and Heping Zhao. Splitting of self-colimated beams in two-dimensional sonic crystals. *Journal of Applied Physics*, 112:124514, 2012.

[107] Jing Li, Fugen Wu, Huilin Zhong, Tuanwei Yao, and Xin Zhang. Acoustic beam splitting in two-dimensional phononic crystals using self-collimation effect. *Journal of Applied Physics*, 118:144903, 2015.

[108] Ting Zhang, Ying Cheng, Jian zhong Guo, Jian yi Xu, and Xiao jun Liu. Acoustic logic gates and boolean operations based on self-colimating acoustic beams. *Applied Physics Letters*, 106:113503, 2015.

[109] A. Håkansson, J. Sánchez-Dehesa, and L. Sanchis. Acoustic lens design by genetic algorithms. *Physical Review B*, 70:214302, 2004.

[110] Andreas Håkansson, Francisco Cervera, and José Sánchez-Dehesa. Sound focusing by flat acoustic lenses without negative refraction. *Applied Physics Letters*, 86:054102, 2005.

Publications

Publication [P1]

A preconditioner based on a low-rank approximation with applications to topology optimization

Noname manuscript No.
(will be inserted by the editor)

A preconditioner based on a low-rank approximation with applications to topology optimization

Paolo Gatto · Rasmus E. Christiansen · Jan S. Hesthaven

the date of receipt and acceptance should be inserted later

Abstract Probabilistic algorithms for constructing matrix decompositions have recently gained vast popularity due to their ability to handle very large problems. This paper pursues the idea of improving a standard Jacobi preconditioner with a low rank correction, to enhance its performance for the iterative solution of finite element discretizations. This is based on the well-known fact that, in the case of elliptic problems, the Green function is numerically low-rank. We follow the same approach in the context of wave propagation problems. Although the Green function is no longer low-rank, we show that, in the case of moderate wave numbers, a low-rank update can be successfully employed to construct an effective preconditioner. We investigate the behavior of such preconditioner when applied to subsequent discretizations of the Helmholtz equation that arise in the context of topology optimization.

1 Introduction

Classical linear algebra techniques are ill-suited for applications that yield extremely large matrices whose entries are inherently affected by errors. Consequently, the employment of a highly accurate matrix decomposition makes little sense when the efficient handling of large amounts of data becomes paramount. This new scenario calls for randomized techniques and provides the opportunity to design algorithms that fit recent developments in computer hardware, where

P. Gatto
École Polytechnique Fédérale de Lausanne (EPFL) CH-1015 Lausanne, Switzerland
E-mail: paolo.gatto@epfl.ch

R.E. Christiansen
Department of Mechanical Engineering, Technical University of Denmark, Nils Koppels Allé, Building 404, DK- 2800 Kgs. Lyngby, Denmark
E-mail: raelch@mek.dtu.dk

J.S. Hesthaven
École Polytechnique Fédérale de Lausanne (EPFL) CH-1015 Lausanne, Switzerland
E-mail: jan.hesthaven@epfl.ch

the role of data transfer is central to achieve efficiency. For an extensive survey of randomized matrix approximations see [11].

Among randomized matrix decompositions, the Interpolative Decomposition (ID) is a powerful tool that allows to compress a numerically low-rank matrix A. In fact, for every ε, it is possible to determine a "skeletonization" $A^{(\text{skel})}$, *i.e.*, a collection of k columns of A, such $\|A - A^{(\text{skel})}P\| \leq \varepsilon$, where P contains the k-order identity as a submatrix. In the case of well-behaved elliptic problems posed on a domain Ω, the approximation $G(x_i, y_j)$ to the Green function, where $\{x_i\}, \{y_j\}$ are sets of points in Ω, is numerically low-rank. This property is commonly exploited in the context of boundary integral methods, in which a boundary value problem (BVP) is recast as a boundary integral equation (BIE) involving a Fredholm operator of the second kind. If A is the matrix approximation of the integral in the BIE, then the matrix-vector product Av can be evaluated cheaply. As a result, Fast Multipole Methods of linear complexity have been developed for a variety of kernels (heat equation, wave equation, Stokes equations, etc.), see [13, 14, 9].

In this paper we apply similar ideas to the context of Finite Elements (FE) discretizations. When A is the stiffness matrix arising from a FE discretization of an elliptic problem, the off-diagonal part of A^{-1} is a low-rank matrix as a result of the decay of the Green function. We exploit this property to build a preconditioner by adding a low-rank update to a banded Jacobi preconditioner. As we transition from elliptic to hyperbolic problems, more specifically to the Helmholtz equation, the behavior of the Green function changes such that a low rank update, *a priori*, no longer exists or, rather, k is no longer guaranteed to be small when compared to the size of the matrix. Nevertheless, if we apply this same machinery in the case of low frequencies ω or, equivalently, low wave numbers κ, numerical evidence demonstrates that, even for modest values of k, the preconditioner remains effective.

Linear systems that arise from the discretization of wave propagation phenomena are typically highly indefinite, which makes the construction of an effective preconditioner both vital and challenging. Standard multigrid methods generally do not work well, mainly because of the fact that the oscillations on the scale of the wavelength cannot be carried on to the coarse grids. Incomplete LU decompositions are fairly expensive to compute and still lead to a number of iterations that scales linearly with respect to ω. Recently, a class of methods that rely on the idea of preconditioning *via* a shifted Laplacian has gained popularity, see [8, 7, 12]. Although those methods lead to significant improvements, the iteration count still grows linearly with ω. The latest development is the so-called "sweeping preconditioner" of Engquist and Ying, see [6, 5], developed in the context of finite difference approximations. It employes the compressibility of the half-space Green function to produce an approximate factorization, sweeping the domain layer by layer. Both the construction and the application of the preconditioner are of linear complexity.

The construction of the sweeping preconditioner rests upon a specific ordering of the degrees of freedom, namely layer by layer, hence the name, and exploits the physical meaning of the tridiagonal block structure of the resulting matrix. The goal of this work is to develop a preconditioner that is still robust when such a tight connection between physics and numerical approximation cannot be established. In fact, the only core assumption of our construction is that a "reasonable" ordering of the degrees of freedom has been selected, *e.g.*, by means of a space-filling curve,

so that, to a set tolerance ε, the ID can be determined with an effectively small numerical rank k.

The paper is organized as follows. In Section 2 we review the Interpolative Decomposition and some facts from linear algebra. In Section 3 we discuss the construction of the preconditioner in details and give a few illustrative numerical examples. Section 4 is dedicated to an application of the preconditioner to a topology optimization problem. Finally, in Section 5 we draw conclusions from the presented work and point to possible future directions of research.

2 Facts from linear algebra

In numerical linear algebra, producing a low-rank approximation to a matrix is a central question. To make the discussion precise, for a positive error tolerance ε, we wish to construct an approximation X to a given matrix A, such that $\|A-X\| \leq \varepsilon$ and $\operatorname{rank}(X)$ is as small as possible. Henceforth, $\|\cdot\|$ indicates the spectral norm. A natural answer is provided by the Singular Value Decomposition (SVD): if k is the number of singular values of A that exceed ε, the choice $X = QQ^*A$, where the columns of Q are the k dominant left singular vectors of A, yields the minimizer of $\|A-X\|$ over all matrices of rank k.

A different way to realize a rank-k approximation of A is through an Interpolative Decomposition (ID). In simple words, for every $\varepsilon > 0$, it is possible to determine a collection of k columns of A, *i.e.*, a "skeletonization" $A^{(\mathrm{skel})}$, such that $\|A - A^{(\mathrm{skel})}P\| \leq \varepsilon$, where some subset of k columns of P makes up the identity matrix and no entry of P has absolute value greater than 1. The decomposition is interpolative in the sense that each column of A can be expressed as a linear combination of k fixed columns with bounded coefficients.

The precise statement is provided by the following theorem, see [19], Lemma 3.1.

Lemma 1 *For every $m \times n$ complex matrix A and every integer k such that $k \leq \min\{m,n\}$, there exist a complex $k \times n$ matrix P and a complex $m \times k$ matrix B, whose columns constitute a subset of the columns of A, such that:*

1. *some subset of the columns of P makes up the identity of order k;*
2. *no entry of P has an absolute value greater than 1;*
3. *$\|P\| \leq \sqrt{k(n-k)+1}$;*
4. *the least (that is the k-th greatest) singular value of P is at least 1;*
5. *$BP = A$ when $k = m$ or $k = n$;*
6. *$\|BP - A\| \leq \sqrt{k(n-k)+1}\,\sigma_{k+1}$ when $k < m$ and $k < n$, where σ_{k+1} is the $(k+1)$-st greatest singular value of A.* ∎

Existing algorithms for computing B and P that satisfy the properties listed above are computationally expensive. In [19], an algorithm whose cost is proportional to $mn\log(k) + l^2(m+n)$ floating point operations (here l is an integer near to, but greater than, k), is obtained by slightly weakening the conditions on the factors B and P:

$2'$. no entry of P has an absolute value greater than 2;
$3'$. $\|P\| \leq \sqrt{4k(n-k)+1}$;
$6'$. $\|BP - A\| \leq \sqrt{4k(n-k)+1}\,\sigma_{k+1}$.

Furthermore, the algorithm parallelizes trivially.

3 Preconditioner

The Krylov methods are projection methods that minimize the residual norm over the affine subspace $x_0 + \mathcal{K}_m$, where x_0 is an initial guess for the solution, and $\mathcal{K}_m$ is the m-th Krylov subspace, see [15]. Some variants such as the GMRES method are guaranteed to converge in a number of iterations equal to the size of the system. However, its restarted version, which is used in practice, tends to stagnate in the case of an indefinite matrix. This shortcoming is usually overcome through the use of an appropriate preconditioner. In this work we shall employ the left-preconditioned GMRES.

A Jacobi preconditioner is perhaps the simplest of all preconditioners. In the standard splitting $A = M - N$, see, *e.g.*, [15], it corresponds to the choice $M = \text{diag}(A)$. A simple variant is a banded Jacobi preconditioner, which is built from the band of A, namely the diagonal and b[1] sub- and super-diagonals. While extremely cheap to apply, a Jacobi preconditioner is effective only in a limited number of cases, *e.g.*, diagonally dominant, symmetric positive definite matrices.

Following the approach outlined in [2], we build our preconditioner as a low-rank correction to a banded Jacobi preconditioner G. The low-rank correction δG is obtained from a skeletonization of A, *i.e.*, a collection of its columns.

The construction is as follows. For some bandwidth b, let G be the inverse of the band of A. We proceed to construct a matrix Y whose range is a sample of the range of $A^{-1} - G$. Let l be a sampling parameter and N be an $l \times m$ random matrix whose entries are drawn from independent trials of a normal distribution with zero mean and unit variance. We build Y by applying the random matrix $R := NA$, as:

$$Y := R(A^{-1} - G) = N - NAG$$

As a next step, we perform an ID of Y to a desired tolerance ε:

$$\|Y - Y^{(\text{skel})}P\| \leq \varepsilon$$

where $Y^{(\text{skel})}$ is an $m \times k$ matrix comprising k columns of Y. As a final and most critical step, we construct an $m \times k$ matrix B by selecting k columns of $A^{-1} - G$ in the same fashion as the columns of $Y^{(\text{skel})}$ were chosen from those of Y. The construction of $B = [u_1|\cdots|u_k]$ is tantamount to the solution of linear systems:

$$A\,u_i = (I - AG)(:, j_i) \quad , \quad i = 1, \ldots, k$$

where $\{j_1, \ldots, j_k\}$ are the indices of the columns of Y that form $Y^{(\text{skel})}$. Although the construction of δG is k times more expensive than a single linear solve, this is a trivially parallellizable process. Finally, we formally set $\delta G = BP$, although such matrix is never formed explicitly. The whole procedure is detailed in Algorithm 1.

As a first test case, we investigate the performance of the preconditioner on a finite element (FE) approximation of the Poisson problem $-\Delta u = f$ posed on the unit square $\Omega = (0, 1)^2$. Rather than solving a specific problem, we are interested in the behavior of the preconditioner with respect to the discretization of the differential operator. Thus, we set the load vector equal to a vector with unit entries. We employ uniform $n \times n$ quadrilateral grids with constant order of approximation

[1] Here b is an integer called *bandwidth*. In the case $b = 0$, a standard Jacobi preconditioner is recovered.

Algorithm 1: construction of δG.

Input: l, ε

build an $l \times m$ standard Gaussian matrix N;
compute $R = NA$;
compute $Y = R(A^{-1} - G)$;
perform an ID of Y to precision ε:

$$\|Y - Y^{(\mathrm{skel})} P\| \leq \varepsilon$$

let $\{j_1, \ldots, j_k\}$ be indices of the k columns of Y that form $Y^{(\mathrm{skel})}$;
solve linear systems:

$$A\, u_i = (I - AG)(:, j_i) \quad , \quad i = 1, \ldots, k$$

and form $B = [u_1 | \cdots | u_k]$;
set $\delta G = BP$;

p and elements ordered lexicographically.[2] As is customary, within each element we enumerate the modes from high to low order. Figure 1 shows typical sparsity patterns of the resulting stiffness matrices. The choice of the banded Jacobi preconditioner suggests itself, namely $b = (p+1)^2 - 1$. As a consequence of the element ordering, this is an n-block diagonal matrix. We construct the low-rank correction by selecting values for l and ε and following the procedure described in Algorithm 1. At this preliminary stage, we measure the effectiveness of the preconditioner in terms of GMRES iterations needed to reach a set error tolerance, and regard the banded Jacobi preconditioner as a reference for the impact of the low-rank correction.

We investigate the behavior of the preconditioner for (uniform) orders of approximation $p = 2, \ldots, 8$, set l to be half of the matrix dimension, and decrease ε in order to obtain approximations of growing rank. The results are recast in terms of (average) number of GMRES iterations per relative rank, namely the rank divided by the matrix dimension, see Figure 2 for results relative to approximations of even order. Although the banded Jacobi preconditioner is quite effective in the case of symmetric positive definite (SPD) matrices that arise from discretizations of elliptic problems, the low-rank update does indeed improve its performance in the case of high orders of approximation. In the case of lower order approximations, as the rank grows, we observe the desirable decrease in the number of GMRES iterations only after an initial, and possibly substantial, increase. Nevertheless, numerical evidence as presented in Figure 2 suggests that the behavior of the preconditioner improves as the order of approximation increases. Since we are ultimately interested in developing a preconditioner for the Helmholtz problem, where high orders of approximation are crucial, the preconditioner appears to have the desirable properties.

In the case of an SPD problem, it is natural to construct a preconditioner that is SPD as well. It is possible to recover an SPD preconditioner, by complimenting Algorithm 1 with the following steps. Let us replace δG by its symmetric part

[2] This is to say that, if each element is identified to its centroid $(\frac{i}{n} - \frac{1}{2n}, \frac{j}{n} - \frac{1}{2n})$, the ordering is $(j-1)n + i$.

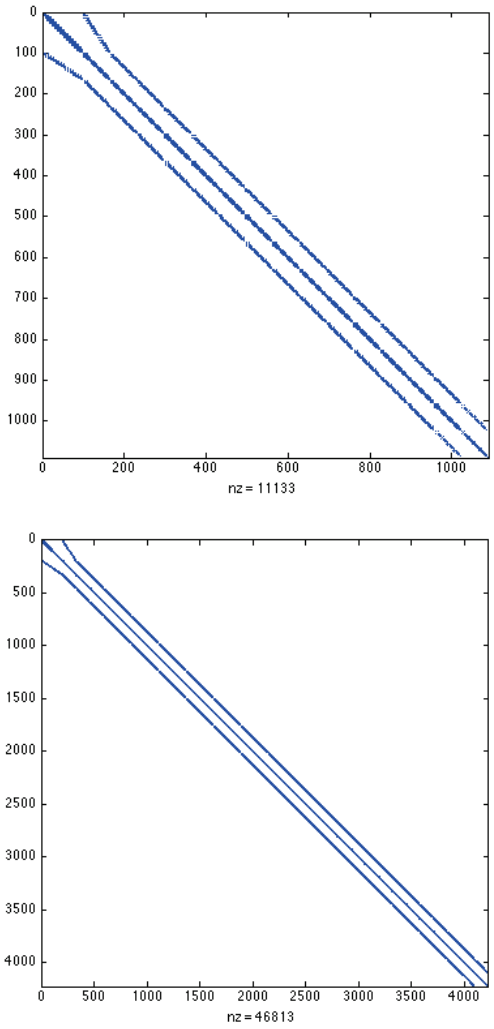

Fig. 1 Stiffness matrices arising from second order finite element discretizations of the Laplace operator. The matrices are obtained from subsequent levels of uniform h-refinements.

$\delta G^{(\mathrm{sym})}$ and assume the spectral decomposition

$$\delta G^{(\mathrm{sym})} = V \mathrm{diag}\{\lambda_1, \ldots, \lambda_n\} V'$$

where $V = [v_1|\cdots|v_n]$ is an orthonormal basis of eigenvectors and $\{\lambda_1, \ldots, \lambda_n\}$ are the eigenvalues ordered from smallest to largest. Let the first k eigenvalues be non-positive and seek an approximation of the form:

$$\left(I - V_k \mathrm{diag}\{c_1, \ldots, c_k\} V_k'\right) \delta G^{(\mathrm{sym})}$$

where $V_k = [v_1|\cdots|v_k]$, and $c_1, \ldots, c_k$ are suitable constants to be determined. We immediately see that:

$$\begin{aligned}\left(I - V_k \mathrm{diag}\{c_1, \ldots, c_k\} V_k'\right) V \mathrm{diag}\{\lambda_1, \ldots, \lambda_n\} V' = \\ = V \mathrm{diag}\{\lambda_1, \ldots, \lambda_n\} V' - V_k \,\mathrm{diag}\{c_1, \ldots, c_k\} \,\mathrm{diag}\{\lambda_1, \ldots, \lambda_k\}\, V_k' = \\ = V \mathrm{diag}\{\lambda_1(1-c_1), \ldots, \lambda_k(1-c_k), \lambda_{k+1}, \ldots, \lambda_n\} V'\end{aligned}$$

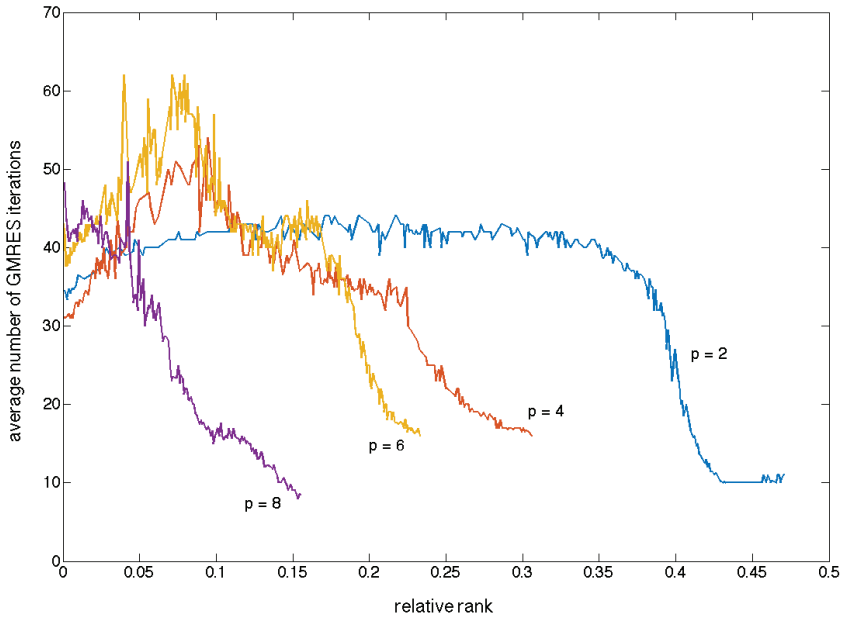

Fig. 2 Discrete Laplace operator. Average number of GMRES iterations as a function of the ID rank for different orders of approximation. The rank is reported as relative to the matrix size.

Thus, the approximation is positive-definite for any choice of constants c_i's such that $\lambda_i(1 - c_i) > 0$ for $i = 1, \ldots, k$. Since the sum of SPD matrices is itself SPD, the preconditioner is SPD provided that G is SPD (which is usually the case.)

Let us turn our attention to an FE discretization of the Helmholtz equation $-\Delta u - \kappa^2 u = f$ on Ω, complemented with a homogenous Neumann boundary condition on $\partial\Omega$. We employ the same FE discretization as in the case of the Poisson problem, and set the load vector equal to a vector with unit entries. We select non-dimensional wave numbers $\kappa = 10, 50$ and perform simulations for $p = 2, \ldots, 8$, see Figure 3 for selected results. As expected, and contrary to the case of the Laplace operator, the low-rank correction is crucial for the convergence of the iterative solver. Every curve features an initial plateau, which indicates that GMRES fails to converge for small values of the rank of the ID. It follows a sharp drop, especially evident in the case $\kappa = 50$, which conveys that the preconditioner becomes effective once a target rank has been reached. Similarly to the case of the Laplace operator, as the order of approximation increases, the target rank for the low-rank correction to become effective decreases.

4 Application to Topology Optimization

The construction of the preconditioner is tantamount to the solution of k linear systems. Consequently, it is of practical interest for problems whose nature allows the solution cost to outweigh the construction cost. A favorable scenario arises when the solution of a large number of instances of the same problem, under slowly varying conditions, is needed. In such cases, we can recompute G at each

instance of the varying conditions, while attempting to recycle δG between different instances. Topology optimization fits this framework very well.

Topology optimization is an iterative method, used mainly for PDE constrained optimization problems, to create highly optimized designs by determining a distribution of material that fulfills a specific task in a locally optimal manner without the need to enforce any *a priori* restrictions on the designs topology, see [1]. Applying the efficient technique of adjoint sensitivity analysis to obtain gradient information for the objective function allows the use of continuous optimization techniques in topology optimization. In this work the *Method of Moving Asymptotes*, introduced by Svanberg in [16], has been used as the optimization algorithm. The use of gradient-based techniques results in a significant reduction in the number of iterations needed to obtain a good design, compared to other methods. However, for many problems the method still requires O(100)-O(1000) iterations to recover a locally optimal and physically admissible design. This unavoidably implies that the governing equations for the problem under consideration must be solved a large number of times for a slowly changing material distribution. When PDE problems of several millions of degrees of freedom are considered, as is often the case for real world problems, their solution through traditional direct techniques becomes infeasible. Considering such problems therefore naturally raises the interest in using highly scalable parallel iterative techniques. For physical problems governed by the Helmholtz equation, like acoustic, electromagnetic and structural vibration problems, no general scalable parallel iterative techniques currently exists. Therefore it is of interest to investigate the preconditioner presented in this paper in the context of topology optimization.

We investigate two model problems governed by the Helmholtz equation in order to investigate the preconditioners performance for both reflecting and absorbing boundary conditions. We consider topology optimization of an acoustic cavity and of an acoustic lens constructed from a periodic array of unit cells. We base our formulation of the topology optimization problem on the work done by [4] and the approach presented in [3]. It is emphasized that the considered optimization problems are highly non-convex and therefore small changes in any parameter value may result in different final designs.

4.1 Pressure Minimization in Acoustic Cavity

We consider the case of an acoustic cavity optimization problem in the domain $\Omega \subset \mathbb{R}^2$. The objective is to minimize the average sound pressure in a small target sub-domain of $\Omega_{\mathrm{OP}} \subset \Omega$, by introducing material acting as a hard wall, in another sub-domain $\Omega_{\mathrm{d}} \subset \Omega$. The boundary of the cavity $\delta\Omega$ is taken to be perfectly reflecting, except for a small section P where a pure tone is excited, see Figure 4. The pressure field p is governed by the Helmholtz equation with appropriate

boundary conditions:

$$\operatorname{div}\left(\frac{1}{\rho}\nabla p\right)+\frac{\omega^2}{\kappa}p=0 \qquad \text{in } \Omega \tag{1a}$$

$$\frac{1}{\rho}\nabla p\cdot\boldsymbol{n}=0 \qquad \text{on } \operatorname{int}(\partial\Omega\setminus P) \tag{1b}$$

$$\frac{1}{\rho}\nabla p\cdot\boldsymbol{n}=-\mathrm{i}\omega U \qquad \text{on } P \tag{1c}$$

Here 'i' denotes the imaginary unit, $\omega = 2\pi f$ is the angular frequency, f is the frequency, and U is the vibrational velocity of the source. Like the pressure, the density ρ and bulk modulus κ depend on the spatial position. The physics of the problem dictates that a given spatial position either contains solid or void. The parameters for the void regions are taken to be those of air at 0 % humidity, a temperature of 20 °C and a background pressure of 1 atm: $\rho_{\text{air}} = 1.204$ kg m^{-3}, $\kappa_{\text{air}} = 141.921 \cdot 10^3$ Pa. The parameters for the solid are taken to be those of aluminum: $\rho_{\text{solid}} = 2643$ kg m^{-3}, $\kappa_{\text{solid}} = 6.87 \cdot 10^{10}$ Pa. This choice for the solid assures that any point containing solid will act as a hard wall, *i.e.*, a zero Neumann boundary condition. An excitation frequency $f = 90$ Hz and a vibrational velocity $U = 0.01$ m/s is used. This choice of frequency corresponds to a normalized non-dimensional wavenumber of $k \approx 30$. For the optimization a rescaling of the modeling equation is performed where $\tilde{\omega} = \frac{\omega}{c}$, $c = \sqrt{\frac{\rho_{\text{air}}}{\kappa_{\text{air}}}}$, $\tilde{\rho}_{\text{air}} = 1, \tilde{\rho}_{\text{solid}} = \frac{\rho_{\text{solid}}}{\rho_{\text{air}}}$, $\tilde{\kappa}_{\text{air}} = 1, \tilde{\kappa}_{\text{solid}} = \frac{\kappa_{\text{solid}}}{\kappa_{\text{air}}}$ is introduced.

In order to employ a continuous optimization approach, an auxiliary field, ξ, such that $0 \le \xi(\mathbf{x}) \le 1$ when $\mathbf{x} \in \Omega_{\text{d}}$, and $\xi(\mathbf{x}) = 0$ when $\mathbf{x} \in \Omega \backslash \Omega_{\mathbf{d}}$, is introduced to interpolate between the inverse material parameters of solid and air. Thus, a location where $\xi = 1$ consists of solid material, while a location where $\xi = 0$ is occupied by air. A straightforward application of this strategy often results in fragmented and not physically admissible designs, consisting of large areas of intermediate values of ξ. To assure a physically admissible design consisting of solid and air regions only and to control the spatial variations of the auxiliary field, we employ smoothing and projection. Such operators are defined, respectively, as:

$$\tilde{\xi}(\xi,\mathbf{x}) = \frac{\int_\Omega w(\mathbf{y}-\mathbf{x})\xi(\mathbf{y})d\mathbf{y}}{\int_\Omega w(\mathbf{y}-\mathbf{x})d\mathbf{y}}, \quad w(\mathbf{x}) = \begin{cases} R-|\mathbf{x}|, & |\mathbf{x}|<R \\ 0 & \text{otherwise} \end{cases} \tag{2}$$

$$\hat{\tilde{\xi}}(\xi,\mathbf{x}) = \frac{\tanh(\beta\eta)+\tanh(\beta(\tilde{\xi}(\xi,\mathbf{x})-\eta))}{\tanh(\beta\eta)+\tanh(\beta(1-\eta))}. \tag{3}$$

Here R is the smoothing radius, η is the projection level, and β is the projection strength. A continuation scheme, where the projection strength is gradually increased, is applied to enforce pure solid and void for the final optimized design while allowing the design to form freely at the beginning of the optimization, see [10,18]. The interpolation between solid and air is performed as $\hat{\rho}^{-1}\hat{\tilde{\xi}} = \tilde{\rho}_{\text{air}}^{-1} + \hat{\tilde{\xi}}\left(\tilde{\rho}_{\text{solid}}^{-1} - \tilde{\rho}_{\text{air}}^{-1}\right)$ and $\hat{\kappa}^{-1}\hat{\tilde{\xi}} = \tilde{\kappa}_{\text{air}}^{-1} + \hat{\tilde{\xi}}\left(\tilde{\kappa}_{\text{solid}}^{-1} - \tilde{\kappa}_{\text{air}}^{-1}\right)$.

For the cavity optimization $R = 0.72$ m and $\eta = 0.5$ are used. The projection strength β is initiated at 1 and incremented for the continuation scheme as $\beta_{\text{new}} = 1.2\beta_{\text{old}}$. Its maximal value $\beta_{\max}$ is set to 100. The increase in β is applied every fifth iteration until $\beta > 3$, after which β is increased every fifteenth iteration until $\beta_{\max}$ is reached.

The minimization of the average of p in Ω_{OP} may be stated as the continuous optimization problem

$$\min_{\xi} \left\{ \Phi(\xi) := \int_{\Omega_{\mathrm{OP}}} \left| p\big(\mathbf{x}, \hat{\tilde{\xi}}(\xi, \mathbf{x})\big) \right|^2 \right\} \tag{4}$$

where p is obtained by solving (1) for a given realization of ξ. Adjoint sensitivity analysis is applied to obtain the gradient of the objective function with respect to ξ. The optimization problem is solved with the change in the design variables restricted to $\Delta\xi = 0.1$ for each iteration.

The model problem is discretized using a structured quadrilateral mesh and linear finite elements. The auxiliary field ξ is discretized in a piecewise constant fashion so that each finite element is associated to a single variable determining the value ξ in that element. These variables are termed "design variables." The discretization approach, filtering strategy, adjoint sensitivity analysis results, and the continuation approach, see [3], are used in the optimization process.

For the discretization we employ 5 different grids, resulting in approximations of size $n = 8646$, 10011, 20301, 31626, 42486, see Figure 5 for a sample matrix. For our test of the preconditioner we limit ourselves to the first 115 iterations of the optimization process. Figure 6 and Figure 7 illustrate the evolution of the design and the pressure field for the case $n = 31626$ by showing selected iterations.

We employ the inverse of the diagonal of A as the Jacobi preconditioner G. The low-rank correction δG is constructed by selecting $l = n/2$ as the oversampling parameter. Numerical experiments, see Figure 9, strongly suggests that, for set ε, the rank of the ID grows linearly with respect to the problem size. In other words, to every ε, there is a corresponding relative rank, independent of the problem size. The performance of the preconditioner is investigated for $\varepsilon = 0.48$ and $\varepsilon = 0.53$, which yield relative ranks of roughly 11 % and 7 %, respectively.

In all numerical experiments, the low-rank correction δG computed at the first step is effective throughout the whole optimization process, namely we do not observe a dramatic increase in the number of GMRES iterations. For example, for $n = 8646$ and $\varepsilon = 0.53$, the initial number of GMRES iterations is 37, while the final number is 57; the maximum number iterations is 74, and it occurs at step 77.

Numerical evidence supports the fact that, as the relative rank of δG increases, the total number of GMRES iterations needed to solve the optimization process decreases, see Figure 8. Nevertheless, since the rank of the ID grows linearly with respect to the problem size, the cost of applying the preconditioner is still proportional to n^2. The key observation is that the number of GMRES iterations decreases as the problem size increases. In other words, the preconditioner becomes increasingly effective as the size of the problem grows. In fact, the smallest number of iterations is attained for the largest problem size, see Figure 8. Thus, we expect the solution cost to grow slower than $\mathrm{O}(n^2)$. This is indeed supported by the numerical experiments, see Figure 9. We clearly see that the solution cost grows slower that $\mathrm{O}(n^2)$, and appears to approach $\mathrm{O}(n^{1.5})$ asymptotically.

4.2 Sound Focusing by Periodic Lens

As a second topology optimization problem, we consider the design of a periodic lens. We consider the problem in $\mathbb{R}^2$, illustrated in Figure 10. As for the previ-

ous case, the physics is governed by the Helmholtz equation, complemented with appropriate boundary conditions, see (5). The lens is tasked with focusing the acoustic pressure into a small target area Ω_{OP}, and is constructed as a periodic array of 5×1 cells, Ω_{p}, placed in the design domain Ω_{d}. Axial symmetry is enforced in each cell. The sound pressure is generated by a piston-like source at $\mathbf{P}$, placed in a rigid baffle modeled by zero Neumann conditions on $\delta\Omega_{\mathrm{ref}}$. For this problem we consider first order absorbing boundary conditions on $\delta\Omega_{\mathrm{abs}}$ to model the far field truncation. The resulting boundary value problem is:

$$\operatorname{div}\left(\frac{1}{\rho}\,\nabla p\right)+\frac{\omega^2}{\kappa}p=0 \qquad \text{in } \Omega \tag{5a}$$

$$\frac{1}{\rho}\,\nabla p\cdot\mathbf{n}=0 \qquad \text{on } \partial\Omega_{\mathrm{ref}} \tag{5b}$$

$$\nabla p\cdot\mathbf{n}=-\mathrm{i}\frac{\omega}{c}p \qquad \text{on } \partial\Omega_{\mathrm{abs}} \tag{5c}$$

$$\frac{1}{\rho}\,\nabla p\cdot\mathbf{n}=-\mathrm{i}\omega U \qquad \text{on } P \tag{5d}$$

We choose the same material parameter values for the void and solid regions as in the previous case and perform the same rescaling of parameters for the optimization. The excitation frequency and the vibrational velocity of the source are set to $f = 12$ kHz and $U = 0.01\,\mathrm{m/s}$ respectively. This choice of frequency corresponds to a normalized non-dimensional wavenumber of $k \approx 43$.

We again introduce an auxiliary field, ξ, defined as in the previous case with the additional periodicity condition $\xi(\mathbf{x}) = \xi(\mathbf{x}+(2,0))$ for all $\mathbf{x} \in \Omega_{\mathrm{d}}$. This is dictated by the fact that we consider a periodic array of cells within Ω with a period of 2 in the x-direction. The periodicity of the array and the axial symmetry about the center of each unit cell substantially reduce the number of design variables. To obtain a physically admissible design, we again employ the smoothing and projection operators, and the continuation scheme that were all described in the previous section. Due to the filtering operators reaching outside the design domain, the periodicity of the design variables does not translate directly to a perfect periodicity of the final design. The filter range is chosen as $R = 1.25\,\mathrm{cm}$ and the values for η, β, $\beta_{\max}$ are set as for the cavity optimization problem. The increment for the continuation scheme is set as: $\beta_{\mathrm{new}} = 2\beta_{\mathrm{old}}$ and β is increased every 50 iterations until $\beta_{\max}$ is reached.

The optimization problem is defined formally as in (4), with the additional periodicity requirement on the field ξ. This time the changes in the design variables are restricted to $\Delta\xi = 0.01$ for each iteration, and the suggested move limits are used. The same filtering and continuation approach as for the previous example are used. As a consequence of the absorbing boundary conditions, the finite element approximation produces a symmetric, complex-valued stiffness matrix A. Following a standard procedure, we recast the problem into an antisymmetric real problem for the stiffness matrix $\left[\begin{smallmatrix}\Re(A) & -\Im(A)\\ \Im(A) & \Re(A)\end{smallmatrix}\right]$, see Figure 11.

We consider a discretization such that the periodic design cells are discretized using $[80 \times 8]$ finite elements. This choice leads to a total number of degrees of freedom for the discretized Helmholtz problem of $n = 13122$ in the complex system matrix. Again we consider the first 115 iterations of the optimization when investigating the performance of the preconditioner.

Figure 12 and Figure 13 illustrate the evolution of the design and the pressure field by showing selected iterations in the optimization.

As before, we employed the inverse of the diagonal as the Jacobi preconditioner G, and selected $l = n/2$ as an oversampling parameter for the construction of δG. We conducted numerical experiments for ID tolerances $\varepsilon = 0.32$, $\varepsilon = 0.35$ and $\varepsilon = 0.40$, which yields relative ranks of approximately 20 %, 17 % and 15 % respectively. The behavior is qualitatively the same for all cases, see Figure 14. The low-rank correction δG computed at the first step is remarkably effective throughout the first half of the optimization process, in the sense that the number of GMRES iterations is nearly constant. Afterwards, although we do observe an increase in the number of iterations, the preconditioner is still effective. In principle, a strategy should be devised to determine whether, at each step of the optimization process, δG should be recycled from the previous step or recomputed.

5 Conclusions

We present a general purpose preconditioner built as a low-rank correction to a Jacobi or block-Jacobi preconditioner. The motivation for the construction arises from the exponential decay of the Green function in the context of 2D elliptic problems. This property is routinely exploited in boundary element methods, since it is naturally embedded in the problem discretization. Lately, the properties of the Green function have been the foundation of the so-called sweeping preconditioner. It was originally developed in the context of finite difference approximations of the acoustic wave equation, see [6, 5]. More recently, it was extended to spectral finite elements discretizations of the elastic wave equation, see [17].

In this work we apply related ideas to *hp*-finite elements approximations. Since the inverse stiffness matrix can be understood as a discretization of the Green function, its off-diagonal part, in the case of 2D elliptic problem, is rank-deficient. This allows for building a preconditioner of the form $M = G + \delta G$, where G is a Jacobi or block-Jacobi preconditioner, and δG is constructed from the off-diagonal part of the inverse stiffness matrix, and acts as a low-rank correction to G. Since δG is a low-rank update, M can be applied cheaply.

While elliptic problems provide the motivation to our approach, we are ultimately interested in the performance of the preconditioner in the context of wave propagation problems. As discussed in Section 1, the construction of a good precondtioner for wave propagation problems is still an open problem. Our preconditioner proves successful in the case of moderate wave numbers, see Section 3, although a low-rank approximation no longer exists *a priori*. The construction of δG is rather expensive. In fact, if k is the (small) rank of δG, it is k times more expensive than a single linear solve. In order to outweigh the cost of construction, thus making our approach competitive, we tested the preconditioner in the context of topology optimization for acoustics. Topology optimization is an iterative technique where the governing equations, *e.g.*, the Helmholtz equation, need to be solved a number of times, *e.g.*, 1000 times, for a slow changing design. We computed δG at the first iteration and were able to employ it throughout the entire optimization process, see Section 4.

Since we are ultimately interested in solving large systems of equations, *i.e.*, several millions of unknowns, scaling properties are crucial. Although we have no

theoretical explanation, numerical evidence suggests that solution cost is $O(n^{1.5})$. Furthermore, this result should be dimension-independent and thus carry over to 3D problems.

As future directions of research, we shall address the parallelization of the preconditioner implementation.

Acknoledments

P. Gatto and J.S. Hesthaven were partially supported by NSF DMS-1115416, by OSD/AFOSR FA9550-09-1-0613 and by AFOSR FA9550-12-1-0463. R.E. Christiansen was supported by the Villum Foundation through the research project *Topology Optimization – the Next Generation* NextTop.

References

1. M.P. Bendsøe and O. Sigmund. *Topology Optimization*. Springer, 2003.
2. M. Beroiz, T. Hagstrom, S.R. Lau, and R.H. Price. Multidomain, sparse, spectral-tau method for helically symmetric flow. *Computers & Fluids*, 102(0):250 – 265, 2014.
3. R.E. Christiansen, B.S. Lazarov, J.S. Jensen, and O. Sigmund. Creating geometrically robust design for highly sensitive problems using topology optimization - acoustic cavity design. *Structural and Multidiciplinary Optimization*, XXX:XXX, Submitted.
4. M.B. Dühring, J.S. Jensen, and O. Sigmund. Acoustic design by topology optimization. *Journal of Sound and Vibration*, 317:557–575, 2008.
5. B. Engquist and L. Ying. Sweeping preconditioner for the helmholtz equation: hierarchical matrix representation. *Communications on pure and applied mathematics*, 64(5):697–735, 2011.
6. B. Engquist and L. Ying. Sweeping preconditioner for the helmholtz equation: moving perfectly matched layers. *Multiscale Modeling & Simulation*, 9(2):686–710, 2011.
7. Y.A. Erlangga. Advances in iterative methods and preconditioners for the helmholtz equation. *Archives of Computational Methods in Engineering*, 15(1):37–66, 2008.
8. Y.A. Erlangga, C. Vuik, and C.W. Oosterlee. On a class of preconditioners for solving the helmholtz equation. *Applied Numerical Mathematics*, 50(3):409–425, 2004.
9. L. Greengard and P. Lin. Spectral approximation of the free-space heat kernel. *Applied and Computational Harmonic Analysis*, 9(1):83 – 97, 2000.
10. J.K. Guest, J.H. Prévost, and T. Belytschko. Achieving minimum length scale in topology optimization using nodal design variables and projection functions. *International Journal for Numerical Methods in Engineering*, 61:238–254, 2004.
11. N. Halko, P. Martinsson, and J. Tropp. Finding structure with randomness: Probabilistic algorithms for constructing approximate matrix decompositions. *SIAM Review*, 53(2):217–288, 2011.
12. D. Osei-Kuffuor and Y. Saad. Preconditioning helmholtz linear systems. *Applied numerical mathematics*, 60(4):420–431, 2010.
13. V. Rokhlin. Rapid solution of integral equations of classical potential theory. *Journal of Computational Physics*, 60(2):187–207, 1985.
14. V. Rokhlin. Rapid solution of integral equations of scattering theory in two dimensions. *Journal of Computational Physics*, 86(2):414 – 439, 1990.
15. Y. Saad. *Iterative methods for sparse linear systems*. Siam, 2003.
16. K. Svanberg. The method of moving asymptotes - a new method for structural optimization. *International Journal for Numerical Methods in Engineering*, 24:359–373, 1987.
17. P. Tsuji, J. Poulson, B. Engquist, and L. Ying. Sweeping preconditioners for elastic wave propagation with spectral element methods. *ESAIM: M2AN*, 48(2):433–447, 2014.
18. F. Wang, B.S. Lazarov, and O. Sigmund. On projection methods, convergence and robust formulations in topology optimization. *Structural Multidiciplinary Optimization*, 43:767–784, 2011.
19. F. Woolfe, E. Liberty, V. Rokhlin, and M. Tygert. A fast randomized algorithm for the approximation of matrices. *Appl. Comput. Harmon. Anal.*, 25(3):335–366, November 2008.

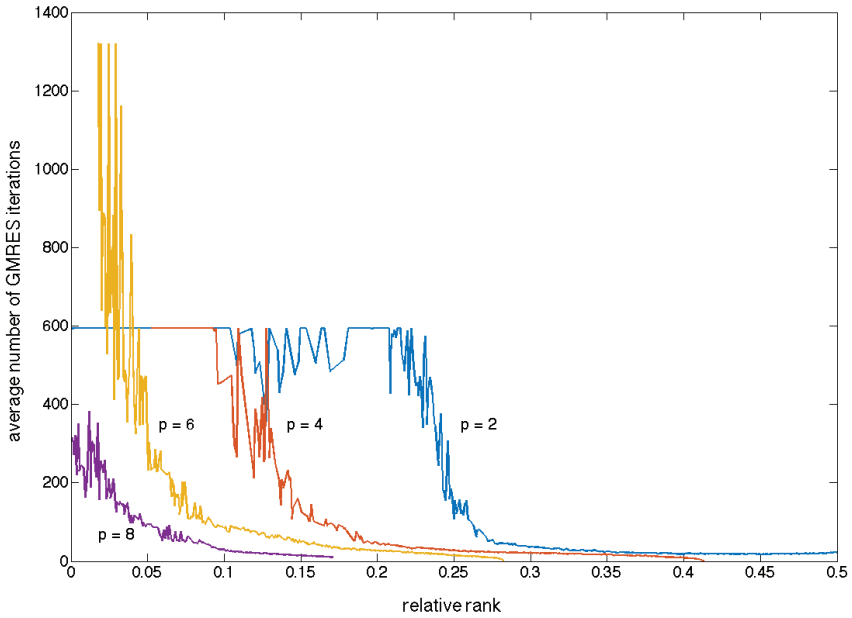

(a) $\kappa = 10$

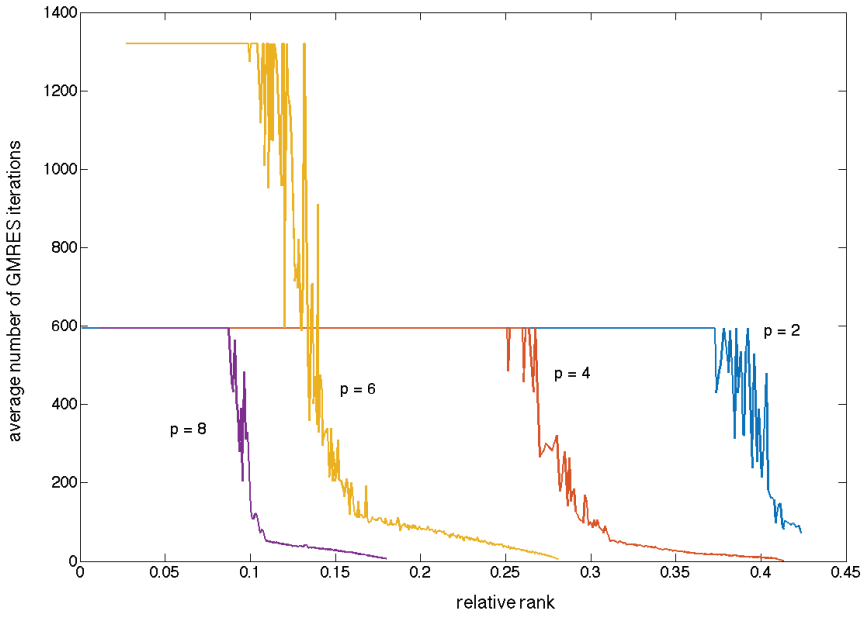

(b) $\kappa = 50$

Fig. 3 Discrete Helmholtz problem. Average number of GMRES iterations as a function of the ID rank for different orders of approximation. The rank is reported as relative to the matrix size. Two different wave numbers, $\kappa = 10$ and $\kappa = 50$, were considered.

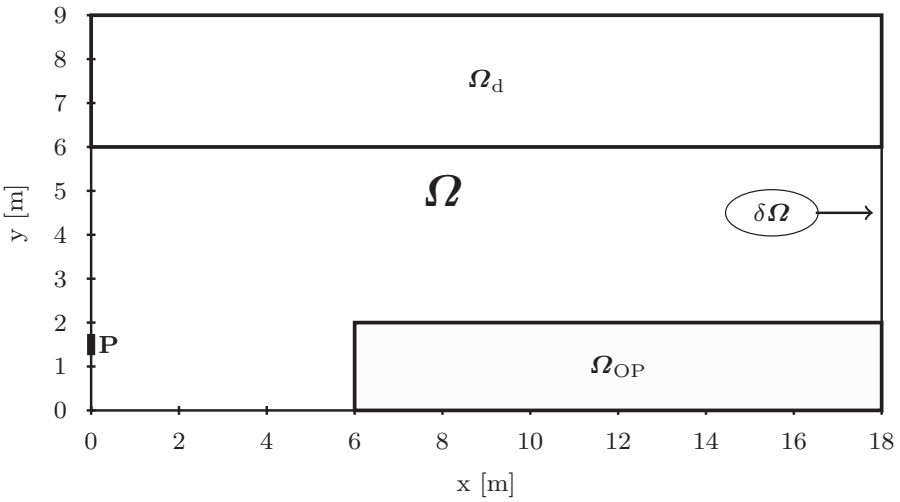

Fig. 4 Acoustic cavity problem diagram. All measurements are given in meters. Domain: $\Omega = [0, 18] \times [0, 9]$. Target sub-domain: $\Omega_{\mathrm{OP}} = [6, 18] \times [0, 2]$. Design sub-domain: $\Omega_{\mathrm{d}} = [0, 18] \times [6, 9]$. Reflecting boundary: $\delta\Omega$. Excitation boundary: $P = 0 \times [1.3, 1.7]$.

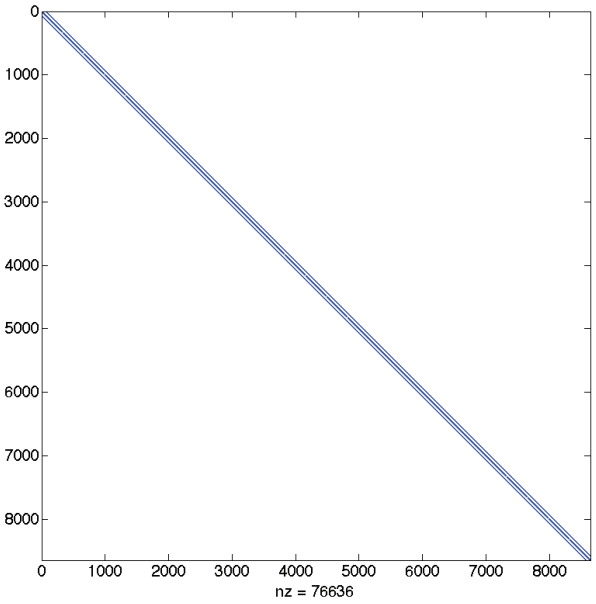

Fig. 5 Acoustic cavity problem stiffness matrix. The problem discretization gives rise to a nine-diagonal real-valued matrix.

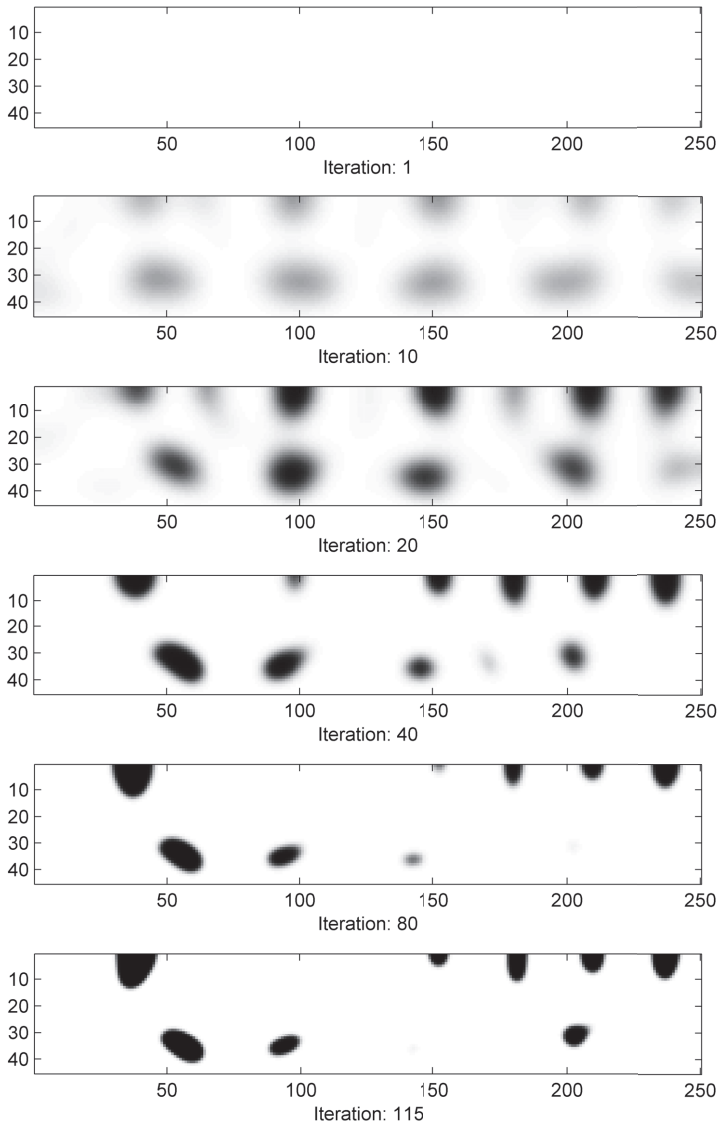

Fig. 6 Snapshots of design evolution across the 115 optimization iterations. The coordinate axes shows the elements in the finite element discretization. White corresponds to air and black corresponds to solid.

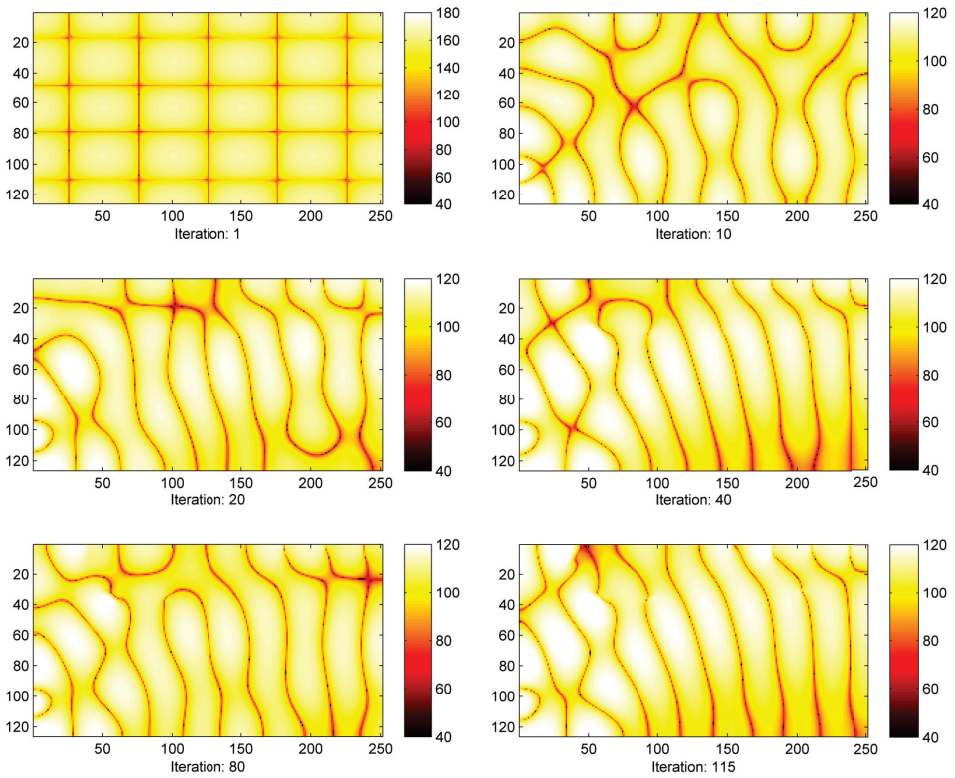

Fig. 7 Snapshots of pressure field evolution, across the 115 optimization iterations. The pressure is reported in dB, $\mathrm{SPL}_{\mathrm{ref}=20\mu\,\mathrm{Pa}}$. The coordinate axes shows the nodes in the finite element discretization.

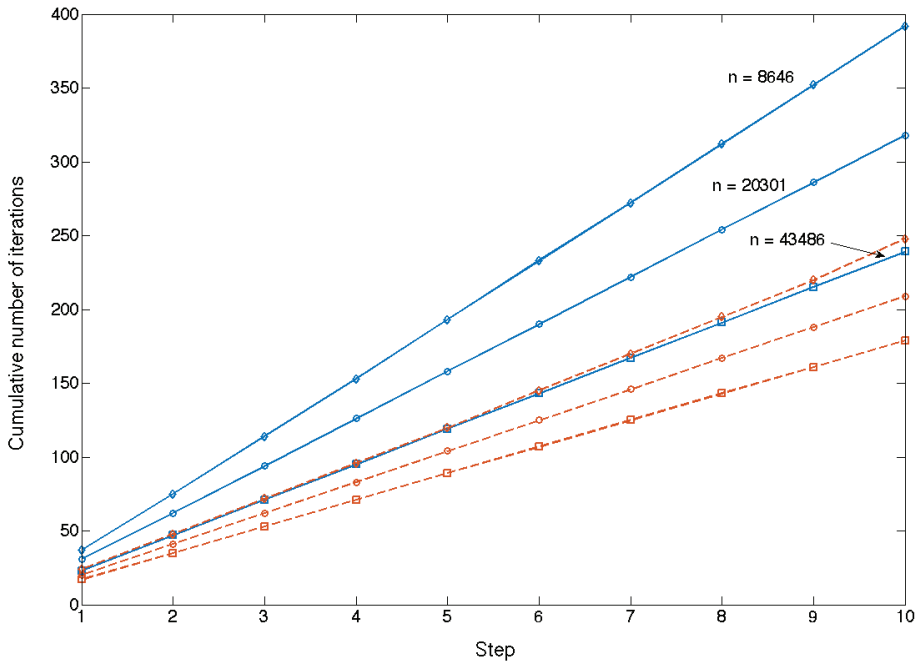

Fig. 8 Cumulative number of GMRES iterations needed to solve the first 10 iterations of the acoustic cavity topology optimization problem for different problem sizes n. Solid lines refer to results obtained with $\varepsilon = 0.53$, dashed lines to results obtained with $\varepsilon = 0.48$. Matching markers refer to the same problem size n.

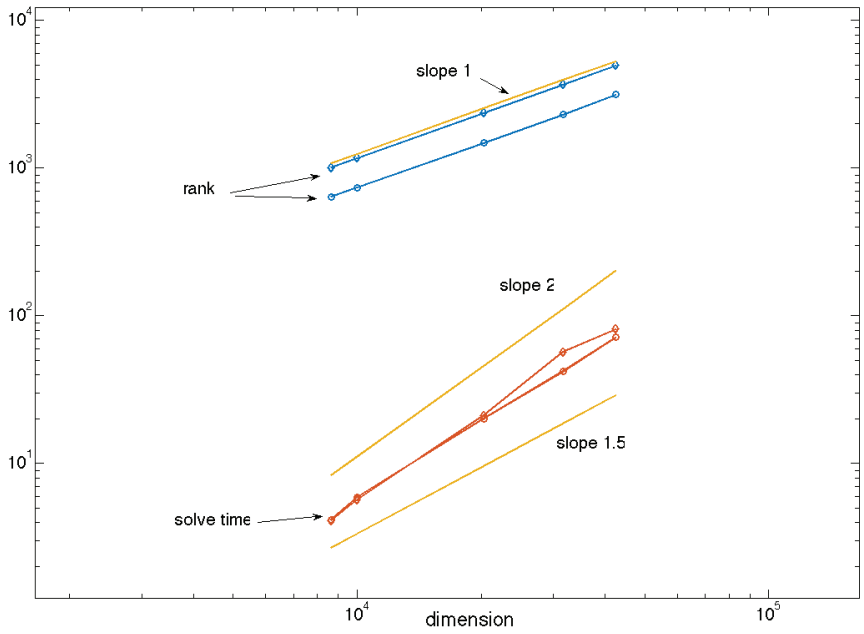

Fig. 9 Dependence of the ID rank and solution time upon the problem size. Circles refer to results obtained for $\varepsilon = 0.53$, diamonds refer to results obtained for $\varepsilon = 0.48$.

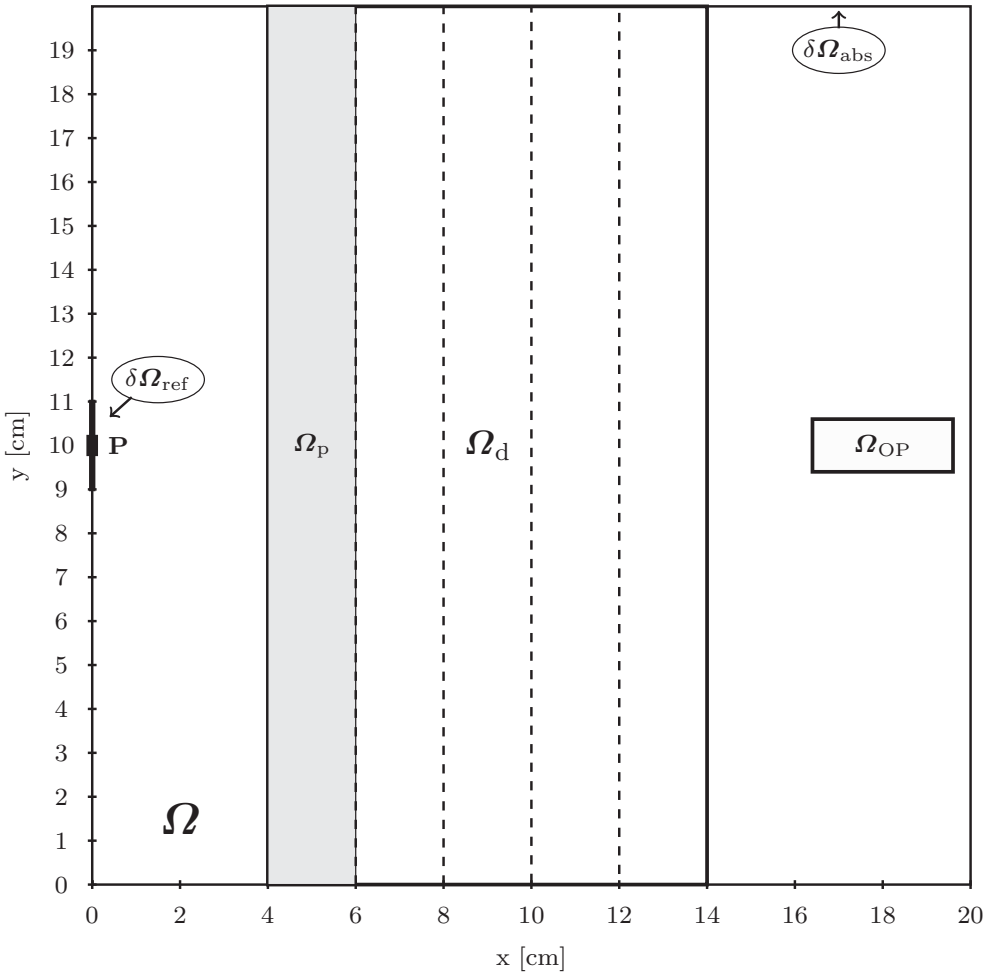

Fig. 10 Acoustic lens problem diagram. All measurements are given in centimeters. Domain: $\Omega = [0, 20] \times [0, 20]$. Target sub-domain: $\Omega_{\mathrm{OP}} = [16.4, 19.6] \times [9.4, 10.6]$. Design sub-domain: $\Omega_{\mathrm{d}} = [4, 14] \times [0, 20]$. Periodic design cell: $\Omega_{\mathrm{p}} = [4 + 2n, 6 + 2n] \times [0, 20], n \in \{0, 1, 2, 3, 4\}$. Absorbing boundary: $\delta\Omega_{\mathrm{abs}}$. Reflecting boundary: $\delta\Omega_{\mathrm{ref}}$. Excitation boundary condition: $P = 0 \times [9.8, 10.2]$.

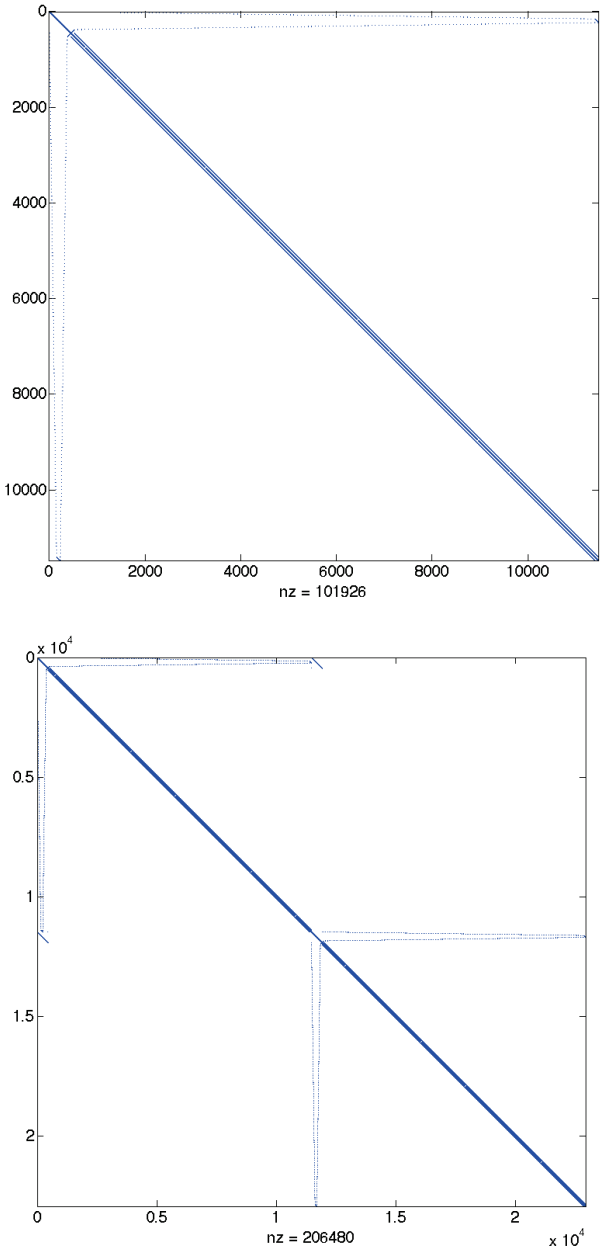

Fig. 11 Acoustic lens problem stiffness matrix. As a consequence of the absorbing boundary conditions, the finite elements stiffness matrix A (left) is symmetric and complex-valued. By separating the real and imaginary part, we obtain the antisymmetric real-valued matrix $\begin{bmatrix} \Re(A) & -\Im(A) \\ \Im(A) & \Re(A) \end{bmatrix}$ (right).

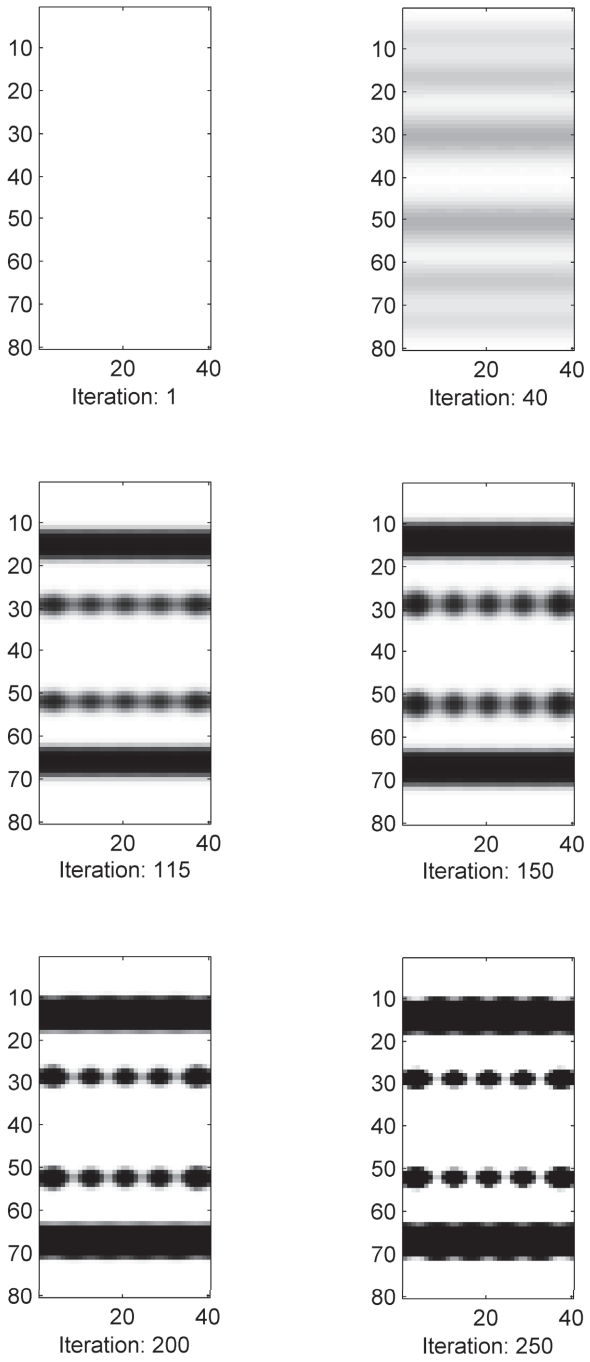

Fig. 12 Snapshots of design evolution across the optimization. The coordinate axes shows the elements in the finite element discretization. Black corresponds to solid and white corresponds to air.

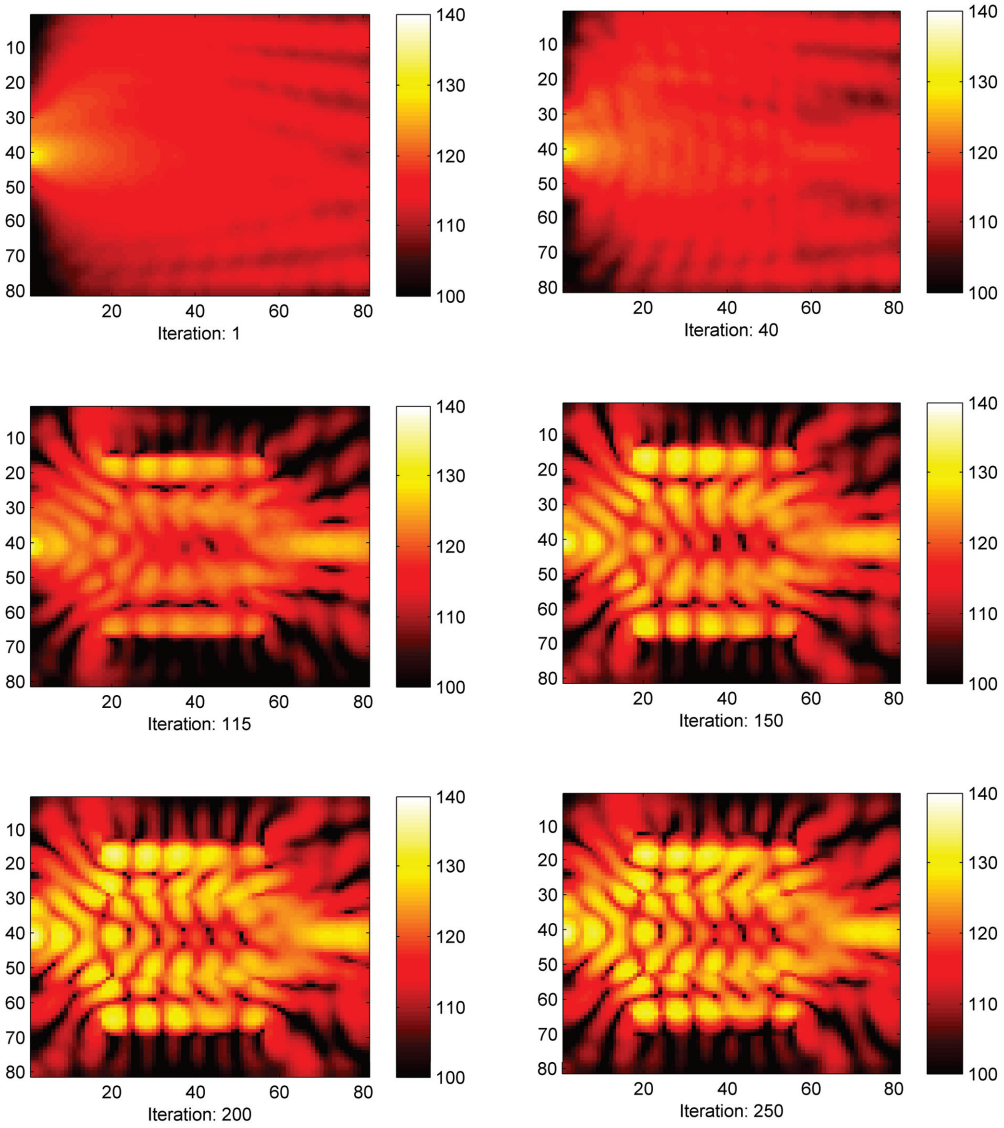

Fig. 13 Snapshots of pressure field evolution, across the optimization. The pressure is reported in dB, $\mathrm{SPL}_{\mathrm{ref}=20\mu\,\mathrm{Pa}}$. The coordinate axes shows the nodes in the finite element discretization.

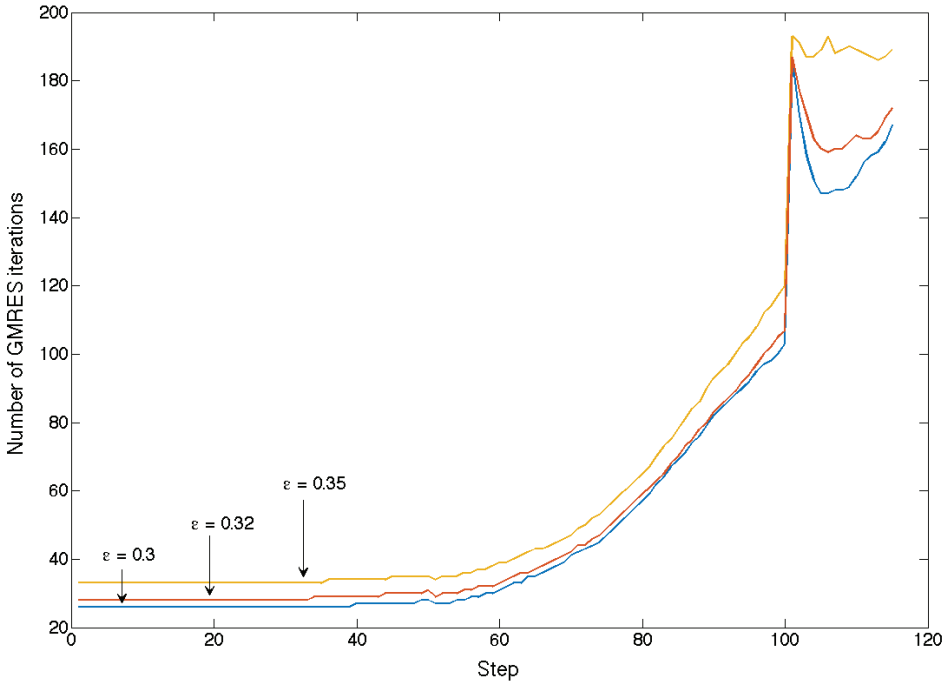

Fig. 14 Number of GMRES iterations needed to solve the acoustic lens topology optimization problem. The ID tolerances $\varepsilon = 0.30, 0.32, 0.35$ correspond to a relative ranks of about 20 %, 17 % and 15 % respectively. Although a marked increase in the number of GMRES iterations is observed in the second half of the considered part of the optimization process, the preconditioner appears to be remarkably effective.

Publication [P2]

Creating geometrically robust designs for highly sensitive problems using topology optimization - Acoustic cavity design

Struct Multidisc Optim (2015) 52:737–754
DOI 10.1007/s00158-015-1265-5

RESEARCH PAPER

Creating geometrically robust designs for highly sensitive problems using topology optimization

Acoustic cavity design

Rasmus E. Christiansen[1] · Boyan S. Lazarov[1] · Jakob S. Jensen[2] · Ole Sigmund[1]

Received: 26 August 2014 / Revised: 7 April 2015 / Accepted: 7 May 2015 / Published online: 21 June 2015

Abstract Resonance and wave-propagation problems are known to be highly sensitive towards parameter variations. This paper discusses topology optimization formulations for creating designs that perform robustly under spatial variations for acoustic cavity problems. For several structural problems, robust topology optimization methods have already proven their worth. However, it is shown that direct application of such methods is not suitable for the acoustic problem under consideration. A new double filter approach is suggested which makes robust optimization for spatial variations possible. Its effect and limitations are discussed. In addition, a known explicit penalization approach is considered for comparison. For near-uniform spatial variations it is shown that highly robust designs can be obtained using the double filter approach. It is finally demonstrated that taking non-uniform variations into account further improves the robustness of the designs.

Keywords Topology optimization · Robust design · Wave propagation · Acoustics · Noise reduction · Projection filtering · Uniform design variations · Non-uniform design variations

✉ Rasmus E. Christiansen
raelch@mek.dtu.dk

[1] Department of Mechanical Engineering, Solid Mechanics, Technical University of Denmark, Nils Koppels Alle, B. 404, 2800 Lyngby, Denmark

[2] Department of Electrical Engineering, Centre for Acoustic-Mechanical Micro Systems, Technical University of Denmark, Ørsteds Plads, B. 352, 2800 Lyngby, Denmark

1 Introduction

It is widely known that solutions to interior acoustic problems in the medium to high frequency range are highly sensitive to parameter variations (Jacobsen and Juhl 2013). For high frequencies the problems are so sensitive that only statistical methods are viable, e.g. statistical energy analysis (Lyon and DeJONG 1998). In this paper we are interested in deterministic solutions for the pressure field and thus restrict ourselves to the low/medium frequency range. We consider a 2D interior acoustics problem with reflecting boundaries for single frequencies. We seek to minimize the sound pressure in part of the domain utilizing interference phenomena by placing material in the domain using topology optimization (Bendsøe and Sigmund 2003). We base our approach on the work by Dühring et al. (2008) where the topology optimization formulation for interior acoustic problems was presented. It was shown to be possible to significantly reduce the sound pressure in a designated part of the domain by placing material elsewhere. We demonstrate that the pressure field is very sensitive to variations in the geometry of the optimized design even at medium frequencies. This is problematic from an application point of view since it is likely impossible to manufacture or install the designs exactly to specifications, leaving the designs useless in real world applications.

We present a topology optimization based approach for creating designs that maintain high performance under substantial near-uniform and small non-uniform geometric variations. For problems in structural mechanics, heat conduction (Wang et al. 2011b), and optics (Wang et al. 2011a; Elesin et al. 2012), it has been shown that using a robust optimization approach leads to a significant improvement in the robustness of the design's performance under spatial variations. We base our approach on the work by

Wang et al. (2011b). Here the design is optimized for a nominal, an eroded and a dilated realization simultaneously using a min/max formulation. The realizations are obtained using continuous projection of smoothed design variables. We demonstrate that applying the robust scheme directly is insufficient for the present acoustic problem due to unpredictable variations in the eroded and dilated designs, making it impossible to perform meaningful robust optimization. To alleviate the problem we present a double filter which restricts design features to vary along their edges as the projection level changes. This allows for optimization of designs towards geometric variations. Promising results for designs optimized under both near-uniform and non-uniform geometric variations are presented. A related double filter approach developed independently of the approach presented in this paper is used in a structural mechanics topology optimization formulation for creating coated structures (Clausen et al. 2015). Other papers have treated and demonstrated the usefulness of topology optimization for problems in acoustics e.g. Wadbro and Berggren (2006), Lee and Kim (2009), Kook et al. (2012), and Wadbro (2014) and for acoustic structure interaction, e.g. Yoon et al. (2007) and Du and Olhoff (2007). The question of geometric robustness of the designs have, to our knowledge, not been investigated elsewhere. As a final note it is stressed that the optimization problems considered here are highly non-convex. Hence small changes in problem or optimization parameters may lead the optimization procedure to converge to different robust designs.

2 Model problem

We seek to minimize the square of the average sound pressure amplitude, $|\hat{p}|^2$, in the sub-domain $\mathbf{\Omega}_{\mathrm{OP}}$ of the model domain $\mathbf{\Omega} \subset \mathbb{R}^2$. A small source domain $\mathbf{P}$ is used to excite acoustic waves. The reduction in $|\hat{p}|^2$ is achieved by introducing solid material in a region $\mathbf{\Omega}_{\mathrm{d}}$ replacing the acoustic medium. $\mathbf{\Omega}_{\mathrm{OP}}$, $\mathbf{\Omega}_{\mathrm{d}}$ and $\mathbf{P}$ are sub-domains of $\mathbf{\Omega}$ and are assumed to be non-intersecting. The boundary of $\mathbf{\Omega}$, denoted $\delta\mathbf{\Omega}$, is taken to be perfectly reflecting. Figure 1 shows the domain configuration used, unless otherwise noted.

3 Physics model

Time-harmonic acoustic wave-propagation in an adiabatic medium is governed by the Helmholtz equation,

$$\nabla \cdot (\rho(\mathbf{x})^{-1} \nabla \hat{p}(\mathbf{x})) + \omega^2 \kappa(\mathbf{x})^{-1} \hat{p}(\mathbf{x}) = 0, \quad \mathbf{x} \in \mathbf{\Omega}. \tag{1}$$

Here ∇ denotes the spatial derivative, $\hat{p}$ is the complex sound pressure and ρ and κ are the density and bulk modulus of the medium, respectively. $\omega = 2\pi f$ is the angular frequency where f is denoted the excitation frequency. The spatial dependence in (1) is suppressed in the following for brevity. The perfectly reflecting boundaries and the source are imposed using,

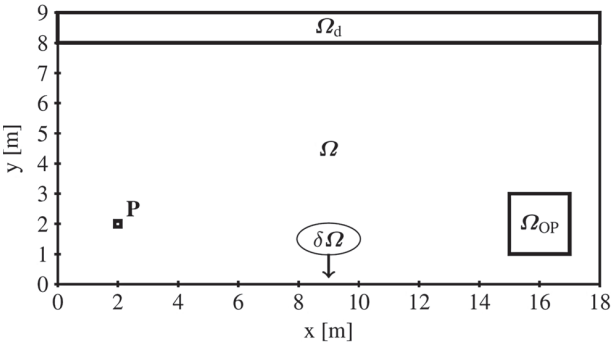

Fig. 1 Illustration of the domain configuration, $\mathbf{\Omega} = [0, 18] \times [0, 9]$, $\mathbf{\Omega}_{\mathrm{OP}} = [15, 17] \times [1, 3]$ is the optimization domain, $\mathbf{\Omega}_{\mathrm{d}} = [0, 18] \times [8, 9]$ is the design domain and $\mathbf{P} = [1.9, 2.1] \times [1.9, 2.1]$ denotes the region where an acoustic wave is exited

$$\mathbf{n} \cdot (\rho^{-1} \nabla \hat{p}) = 0, \quad \forall\, \mathbf{x} \in \delta\mathbf{\Omega}, \tag{2}$$

$$\mathbf{n} \cdot (\rho^{-1} \nabla \hat{p}) = -\mathrm{i}\omega U, \quad \forall\, \mathbf{x} \in \delta\mathbf{P}. \tag{3}$$

Here $\mathbf{n}$ is the outward pointing normal vector to the boundary in question and U is the vibrational velocity.

The material parameters of solid and air are chosen to have a very large contrast between them. This justifies disregarding the structural problem of the solid material as it will simply act as hard wall boundary conditions for the acoustic waves. The material parameters have been chosen to match those for atmospheric air and aluminum given by,

$$\text{air: } \rho_1 = 1.204\ \mathrm{kg\,m^{-3}}, \quad \kappa_1 = 141.921 \cdot 10^3\ \mathrm{N\,m^{-2}}. \tag{4}$$

$$\text{Al: } \rho_2 = 2643.0\ \mathrm{kg\,m^{-3}}, \ \kappa_2 = 6.87 \cdot 10^{10}\ \mathrm{N\,m^{-2}}. \tag{5}$$

We perform a rescaling of the parameters in the model,

$$(\hat{\rho}, \hat{\kappa}) = \begin{cases} (1, 1) & \text{air} \\ \left(\frac{\rho_2}{\rho_1}, \frac{\kappa_2}{\kappa_1}\right) & \text{solid} \end{cases}, \ \hat{\omega} = \frac{\omega}{c}, \ c = \sqrt{\frac{\kappa_1}{\rho_1}}, \tag{6}$$

where c is the speed of sound in the gas (acoustic medium). By applying the rescaling (1), (2) and (3) becomes,

$$\nabla \cdot (\hat{\rho}^{-1} \nabla \hat{p}) + \hat{\omega}^2 \hat{\kappa}^{-1} \hat{p} = 0, \quad \mathbf{x} \in \mathbf{\Omega}, \tag{7}$$

$$\mathbf{n} \cdot (\hat{\rho}^{-1} \nabla \hat{p}) = 0, \quad \forall\, \mathbf{x} \in \delta\mathbf{\Omega}, \tag{8}$$

$$\mathbf{n} \cdot (\hat{\rho}^{-1} \nabla \hat{p}) = -\mathrm{i}\hat{\omega} U \sqrt{\kappa_1 \rho_1}, \quad \forall\, \mathbf{x} \in \delta\mathbf{P}. \tag{9}$$

All results are reported using the sound pressure level, abbreviated SPL, for a given, $\hat{p}$, which is calculated as,

$$L_{\hat{p}} = 10 \log_{10} \left(\frac{|\hat{p}|^2}{{p_{\mathrm{ref}}}^2} \right), \quad p_{\mathrm{ref,air}} = 20\ \mu\mathrm{Pa}. \tag{10}$$

p_{ref} is the material dependent reference pressure for air, (Jacobsen and Juhl 2013).

4 The optimization problem

Minimizing the average of $|\hat{p}|^2$ over $\mathbf{\Omega}_{\mathrm{OP}}$, is equivalent to minimizing the average of $L_{\hat{p}}$ over $\mathbf{\Omega}_{\mathrm{OP}}$, henceforth denoted $\langle L_{\hat{p}} \rangle_{\mathbf{\Omega}_{\mathrm{OP}}}$. The discrete problem of placing material in $\mathbf{\Omega}_{\mathrm{d}}$ is replaced by a continuous problem, see Dühring et al. (2008). A design variable field, $0 \leq \xi(\mathbf{x}) \leq 1, \ \forall \, \mathbf{x} \in \Omega_{\mathrm{d}}, \ \xi(\mathbf{x}) = 0 \, \forall \, \mathbf{x} \in \mathbf{\Omega} \backslash \mathbf{\Omega}_{\mathrm{d}}$, is introduced and a linear interpolation of the inverse density and bulk modulus is used. This interpolation is given by,

$$\hat{\rho}(\xi)^{-1} = 1 + \xi \left(\left(\frac{\rho_2}{\rho_1} \right)^{-1} - 1 \right), \tag{11}$$

$$\hat{\kappa}(\xi)^{-1} = 1 + \xi \left(\left(\frac{\kappa_2}{\kappa_1} \right)^{-1} - 1 \right). \tag{12}$$

The optimization problem may be stated as,

$$\begin{aligned} &\min_{\xi} . : \ \Phi = \frac{1}{A_{\mathrm{OP}}} \int |\hat{p}(\xi)|^2 d\mathbf{\Omega}_{\mathrm{OP}}, \ A_{\mathrm{OP}} = \int d\mathbf{\Omega}_{\mathrm{OP}}, \\ &\text{s.t.} : \ 0 \leq \xi(\mathbf{x}) \leq 1 \ \ \forall \, \mathbf{x} \in \mathbf{\Omega}_{\mathrm{d}}, \end{aligned} \tag{13}$$

Here Φ denotes the objective. $\hat{p}(\xi)$ is obtained by solving (7)-(9) for a given design variable field, $\xi(\mathbf{x})$. Solving (13) using the approach outlined in Sections 4–6 is in the rest of the paper denoted as *the standard approach*.

5 The discrete problem

The domain $\mathbf{\Omega}$, governing PDE (7) and corresponding boundary conditions (8)–(9) are discretized using the finite element method (FEM). For the discretization Q4 elements of equal size are used throughout $\mathbf{\Omega}$ with a total of $\mathcal{N}$ nodes in the mesh. The linear basis function connected to node k is denoted N_k. The discretization yields the linear system,

$$\mathbf{S}\hat{\mathbf{p}} = (\mathbf{K}(\hat{\rho}) - \hat{\omega}^2 \mathbf{M}(\hat{\kappa}))\hat{\mathbf{p}} = \mathbf{F}. \tag{14}$$

$\mathbf{F}$ stems from the boundary condition (9), and is given as,

$$F_k = \sum_{i \in \mathcal{N}_{b,k}} \int_{\delta \mathbf{\Omega}_i} \mathbf{n} \cdot (\hat{\rho}^{-1} \nabla \hat{p}) N_k d\mathbf{\Omega} \tag{15}$$

Here $\mathcal{N}_{b,k}$ denotes the boundary edges connected to node k. $\mathbf{K}$ and $\mathbf{M}$ in (14) are given by,

$$K_{ij} = \int \hat{\rho}^{-1} \nabla N_i \nabla N_j d\mathbf{\Omega}, \ M_{ij} = \int \hat{\kappa}^{-1} N_i N_j d\mathbf{\Omega}, \tag{16}$$

where $i \in \{1, 2, ..., \mathcal{N}\}, \quad j \in \{1, 2, ..., \mathcal{N}\}$. Neither $\mathbf{M}$ nor $\mathbf{K}$ needs modifications to take the boundary conditions into account. The solution to (7), $\hat{p}$, is approximated by,

$$\hat{p} \approx \sum_{k \in \mathcal{N}} \hat{p}_k N_k, \tag{17}$$

where $\hat{p}_k$ is the k'th entry in $\hat{\mathbf{p}}$, the solution of (14).

The design variable field, $\xi(\mathbf{x})$, is discretized in a discontinuous manner using piecewise constant values in each finite element.

5.1 Sensitivities

The sensitivities required for the topology optimization procedure are obtained using adjoint sensitivity analysis, see Dühring et al. (2008) and references therein. They are,

$$\frac{\mathrm{d}\Phi}{\mathrm{d}\xi_i} = \frac{\partial \Phi}{\partial \xi_i} + \Re \left(\boldsymbol{\lambda}^{\mathrm{T}} \frac{\partial \mathbf{S}}{\partial \xi_i} \hat{\mathbf{p}} \right). \tag{18}$$

Here $\Re$ denotes the real part, T denotes the transpose and $\boldsymbol{\lambda}$ is obtained by solving,

$$\mathbf{S}^{\mathrm{T}} \boldsymbol{\lambda} = - \left(\frac{\partial \Phi}{\partial \hat{\mathbf{p}}_R} - i \frac{\partial \Phi}{\partial \hat{\mathbf{p}}_I} \right)^{\mathrm{T}}, \ \ \hat{\mathbf{p}} = \hat{\mathbf{p}}_R + i \hat{\mathbf{p}}_I, \tag{19}$$

with the k'th entry in the right hand side given as,

$$\left(\frac{\partial \Phi}{\partial \hat{\mathbf{p}}_R} - i \frac{\partial \Phi}{\partial \hat{\mathbf{p}}_I} \right)_k = \frac{1}{A_{\mathrm{OP}}} \int 2(\hat{p}_R - i \, \hat{p}_I) N_k d\mathbf{\Omega}_{\mathrm{OP}}. \tag{20}$$

6 Filtering and projection strategy

A density filter is used for smoothing followed by a projection to ensure a 0/1-design, (Guest et al. 2004; Xu et al. 2010; Wang et al. 2011b). In the following $\tilde{\cdot}$ is used to denote smoothed variables and $\bar{\cdot}$ denotes projected variables. When multiple operations are applied to a variable the symbols are ordered with the latest operation on top. Equation (21) presents the discretized version of the applied density filter (Bourdin 2001; Bruns and Tortorelli 2001),

$$\tilde{\xi}_i = \frac{\sum_{j \in \mathcal{B}_{e,i}} w(\mathbf{x}_i - \mathbf{x}_j) A_j \xi_j}{\sum_{j \in \mathcal{B}_{e,i}} w(\mathbf{x}_i - \mathbf{x}_j) A_j}. \tag{21}$$

A_j is the area of the j'th element, $\mathcal{B}_{e,i}$ denotes the design variables which are within a given filter radius R of design variable i. Here $\mathbf{x}_j$ is taken to be the average of the nodal positions in element j. The filter function w is given by,

$$w(\mathbf{x}) = \begin{cases} R - |\mathbf{x}| \ \forall \, |\mathbf{x}| \leq R \ \wedge \ \mathbf{x} \in \mathbf{\Omega}_{\mathrm{d}} \\ 0 \qquad \text{otherwise} \end{cases}, \tag{22}$$

where R is the aforementioned filter radius. To allow the design to vary with projection level along the edge of $\mathbf{\Omega}_{\mathrm{d}}$ facing into the domain an extended filter area reaching outside of $\mathbf{\Omega}_{\mathrm{d}}$ was used. In the extended filter area the design variables are all identically zero. A dashed line is included on all designs presented in figures to denote the edge of $\mathbf{\Omega}_{\mathrm{d}}$.

The projection operator used is the one suggested by Wang et al. (2011b) and is given as,

$$\bar{\xi}_i = \frac{\tanh(\beta\eta) + \tanh(\beta(\xi_i - \eta))}{\tanh(\beta\eta) + \tanh(\beta(1 - \eta))}, \tag{23}$$

where β is a parameter used to control the sharpness of the projection and $\eta \in [\xi_{\min}, \xi_{\max}]$ defines the projection level. $\eta = 0.5$ has been used as the target for the final (nominal) designs in all cases. When applying the density filter and projection the pressure field will depend explicitly on the filtered and projected variables, $\bar{\tilde{\xi}}$. Hence the optimization problem (13) and the sensitivities should be modified accordingly.

6.1 Modification of sensitivities

Applying the smoothing (21) and projection (23) operations on ξ requires the following sensitivity modifications,

$$\frac{\mathrm{d}\Phi}{\mathrm{d}\xi_i} = \sum_{h \in \mathcal{B}_{e,i}} \frac{\partial \tilde{\xi}_h}{\partial \xi_i} \frac{\partial \bar{\tilde{\xi}}_h}{\partial \tilde{\xi}_h} \frac{\mathrm{d}\Phi}{\mathrm{d}\bar{\tilde{\xi}}_h}, \tag{24}$$

with,

$$\frac{\partial \tilde{\xi}_h}{\partial \xi_i} = \frac{w(\mathbf{x}_h - \mathbf{x}_i) A_i}{\sum_{j \in N_{e,h}} w(\mathbf{x}_h - \mathbf{x}_j) A_j}, \tag{25}$$

$$\frac{\partial \bar{\tilde{\xi}}_h}{\partial \tilde{\xi}_h} = \frac{\beta \operatorname{sech}^2(\beta(\tilde{\xi}_h(\mathbf{x}) - \eta))}{\tanh(\beta\eta) + \tanh(\beta(1 - \eta))}, \tag{26}$$

and $\frac{\mathrm{d}\Phi}{\mathrm{d}\bar{\tilde{\xi}}_h}$ given by (18).

6.2 β-continuation scheme

The projection step is used together with a continuation scheme for β, see Guest et al. (2004), which gradually increases the projection strength during the optimization process. This scheme prevents that the optimization gets stuck prematurely in a local minimum during the first iterations due to the design being projected to 0/1 immediately. A more conservative scheme than the one suggested by Wang et al. (2011b) is used here, see algorithm 1. In the present scheme β is only increased if Φ has not changed significantly for n_{sc} iterations.

Algorithm 1 β continuation scheme

```
Current objective: Φ_c, Previous n_sc objectives: Φ_{n_sc}.
if (n_sc or more iterations have occurred since last β increase.) then
    if |Φ_c − max(Φ_{n_sc})| < α|Φ_c| then
        β = 1.2 · β.
    end if
end if
return β
```

7 Implementation, validation and parameter choices

MATLAB was used for the implementation and the minimization problems were solved using the Method of Moving Asymptotes, MMA (Svanberg 1987). The MATLAB solver was validated using the method of manufactured solutions and through comparison with COMSOL MULTIPHYSICS Version 4.3b's acoustics module. COMSOL was also used to validate the performance of selected final designs.

Table 1 lists the parameter values which have been used in all numerical experiments unless stated otherwise.

8 Sample solution

An example of the effect on the pressure field of placing an optimized design in $\boldsymbol{\Omega}_{\mathrm{d}}$ is presented here. Figure 2i shows the $L_{\hat{p}}$-field for the excitation frequency $f = 51.32$ Hz in an empty domain. Figure 2ii shows the $L_{\hat{p}}$-field in the same domain after a design optimized for this frequency using the standard approach is introduced. It is clearly seen that the minimization of $L_{\hat{p}}$ in $\boldsymbol{\Omega}_{\mathrm{OP}}$ is achieved by a combination of two mechanisms. First a reduction of the overall sound pressure in $\boldsymbol{\Omega}$ from a maximum of 112 dB to 95 dB has occurred and secondly nodal lines have been moved into $\boldsymbol{\Omega}_{\mathrm{OP}}$ leading to a significant reduction of the average sound pressure level in $\boldsymbol{\Omega}_{\mathrm{OP}}$, $\langle L_{\hat{p}} \rangle_{\boldsymbol{\Omega}_{\mathrm{OP}}}$.

$\langle L_{\hat{p}} \rangle_{\boldsymbol{\Omega}_{\mathrm{OP}}}$, has been reduced from approximately 103 dB for the empty domain to approximately 38.8 dB when the

Table 1 Parameters used in simulations

Parameter [Unit]	Value
$\mathcal{N}_x$ [elements]	720
$\mathcal{N}_y$ [elements]	360
$\xi_{\mathrm{ini}}\ \forall\ \mathbf{x} \in \boldsymbol{\Omega}_{\mathrm{d}}$	0.15
R [elements]	20
$U\ [\frac{\mathrm{m}}{\mathrm{s}}]$	0.01
β_{init}	1
$\beta_{\max}$	500
n_{sc}	10
α	0.01
$x_{\boldsymbol{\Omega}}$ [m] $\times$ $y_{\boldsymbol{\Omega}}$ [m]	$[0, 18] \times [0, 9]$
$x_{\boldsymbol{\Omega}_{\mathrm{d}}}$ [m] $\times$ $y_{\boldsymbol{\Omega}_{\mathrm{d}}}$ [m]	$[0, 18] \times [8, 9]$
$x_{\boldsymbol{\Omega}_{\mathrm{OP}}}$ [m] $\times$ $y_{\boldsymbol{\Omega}_{\mathrm{OP}}}$ [m]	$[15, 17] \times [1, 3]$
$x_{\mathbf{P}}$ [m] $\times$ $y_{\mathbf{P}}$ [m]	$[1.9, 2.1] \times [1.9, 2.1]$

$\mathcal{N}_x, \mathcal{N}_y$: number of elements in the $x-$ and $y-$ direction. ξ_{ini}: initial design variable value. R: filter radius. U: vibrational velocity. $\beta_{\mathrm{ini}}, \beta_{\max}$: initial and final β-value. n_{sc}: minimum iterations between β increases. α: objective variation parameter. $x_\bullet, y_\bullet$: spatial extend of the domain $\bullet$

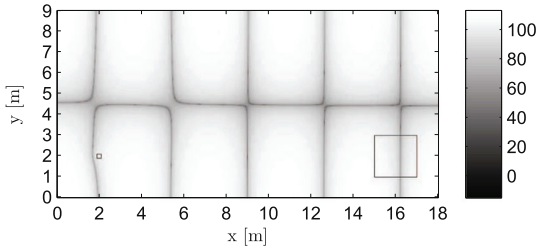

(i) $L_{\hat{p}}$ in empty model domain.

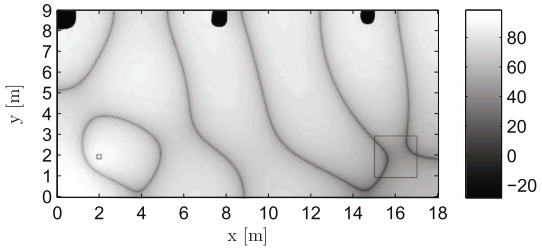

(ii) $L_{\hat{p}}$ in model domain where optimized design has been introduced.

Fig. 2 Pressure fields measured using $L_{\hat{p}}$ at the excitation frequency $f = 51.32$ Hz. The acoustic source and $\mathbf{\Omega}_{\mathrm{OP}}$ are outlined using thin black lines

optimized design is introduced. An important note here is that the magnitude of the reduction in $\langle L_{\hat{p}} \rangle_{\mathbf{\Omega}_{\mathrm{OP}}}$ clearly depends on how the nodal lines of the field in the empty room line up with $\mathbf{\Omega}_{\mathrm{OP}}$. In the present example a larger magnitude of the reduction could possibly have been obtained by moving $\mathbf{\Omega}_{\mathrm{OP}}$ to $[13.5, 15.5] \times [1.3]$. The magnitude of the reduction is not the main interest of this study however. The fact that a significant reduction in sound pressure may be obtained by introducing the design is of course important. It is however the robustness of this reduction towards variations in the design which is the concern in the following.

9 Intermediate design variables

In order for the final designs to be meaningful for real world application they must consist of design variables taking the values 0 or 1, corresponding to no material or material at each position in space. The projection operator presented in (23) enforces a 0/1 design by projecting at the threshold value $\eta \in [\eta_{\min}, \eta_{\max}]$, $\eta_{\min} \in [0, \eta_{\max}[$, $\eta_{\max} \in]\eta_{\max}, 1]$. As described in the introduction it is possible to use a varying projection level, η, to optimize the design towards worst case spatial variations. However, as will be shown in the following there is no guarantee that this approach results in an appropriately varying design. In this context appropriately should be understood as follows: Firstly, when η is varied all changes in the design features should only occur along their edges. Secondly, all design features should change near-uniformly in size if η is varied.

In this section it is shown that for the interior acoustic problem the design does not vary appropriately with η and that this behavior increases significantly with frequency. The issue has been found to exist independent of discretization level and filter radius. Section 9.1 presents the results of solving (13) for four excitation frequencies using the standard approach. In Section 9.2 a min/max formulation for the optimization problem is introduced which will serve as the basis for creating designs that perform robustly under geometric variations. The problem of the inappropriately varying designs is shown to exist for both approaches.

9.1 Optimizing using the standard approach

An initial attempt at obtaining highly performing designs is made by solving (13) using filtering, (21) and projection (23). Results for four excitation frequencies, $f \in \{34.36\ \mathrm{Hz}, 51.32\ \mathrm{Hz}, 69.42\ \mathrm{Hz}, 206.3\ \mathrm{Hz}\}$ are presented below. These frequencies have been chosen to coincide with resonances in the empty domain.

The smoothed design variables for the final designs are shown in Fig. 3i while the final designs after projection at $\eta = 0.5$ are shown in Fig. 3ii. The value for the objective measured in SPL, $\langle L_{\hat{p}} \rangle_{\mathbf{\Omega}_{\mathrm{OP_{XX}}}}$ with an empty design domain **ED**, a full design domain **FD** ($\xi_i = 1\ \forall\ i$), and with the optimized designs introduced **OD**, are shown in Table 2. $\langle L_{\hat{p}} \rangle_{\mathbf{\Omega}_{\mathrm{OP_{FD}}}}$ is included to illustrate the benefit of creating an optimized solution compared to simply attempting to move away from the resonance by filling the design domain with material.

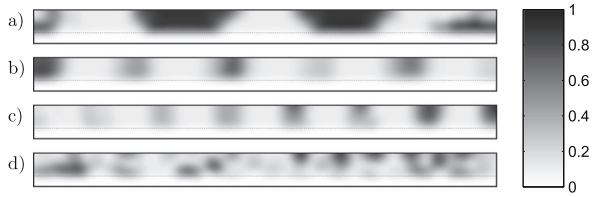

(i) Smoothed design variables, $\tilde{\xi}(\mathbf{x})$.

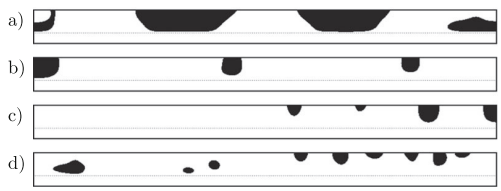

(ii) Final designs. (Physical design variables, $\bar{\tilde{\xi}}(\mathbf{x})$ projected at $\eta = 0.5$).

Fig. 3 **(i)** Smoothed, $\tilde{\xi}$, and **(ii)** physical, $\bar{\tilde{\xi}}$, design variables for four excitation frequencies, **a)** $f = 34.36$ Hz, **b)** $f = 51.32$ Hz, **c)** $f = 69.42$ Hz, **d)** $f = 206.3$ Hz. The standard approach has been used for the optimization. The dashed line denote the edge of $\mathbf{\Omega}_{\mathrm{d}}$

Table 2 Average sound pressure level in Ω_{OP} at four different excitation frequencies, for the cases: Empty design domain, $\langle L_{\hat{p}} \rangle_{\Omega_{\mathrm{OP_{ED}}}}$. Design domain filled with material; $\langle L_{\hat{p}} \rangle_{\Omega_{\mathrm{OP_{FD}}}}$. Optimized design introduced, $\langle L_{\hat{p}} \rangle_{\Omega_{\mathrm{OP_{OD}}}}$

f [Hz]	$\langle L_{\hat{p}} \rangle_{\Omega_{\mathrm{OP_{ED}}}}$ [dB]	$\langle L_{\hat{p}} \rangle_{\Omega_{\mathrm{OP_{FD}}}}$ [dB]	$\langle L_{\hat{p}} \rangle_{\Omega_{\mathrm{OP_{OD}}}}$ [dB]
34.36	≈ 114	≈ 80.5	≈ 64.4
51.32	≈ 99.0	≈ 59.0	≈ 38.8
69.42	≈ 127	≈ 91.8	≈ 46.1
206.3	≈ 120	≈ 116	≈ 64.4

A significant reduction in sound pressure level from both $\langle L_{\hat{p}} \rangle_{\Omega_{\mathrm{OP_{ED}}}}$ and $\langle L_{\hat{p}} \rangle_{\Omega_{\mathrm{OP_{FD}}}}$ to $\langle L_{\hat{p}} \rangle_{\Omega_{\mathrm{OP_{OD}}}}$ is observed for all cases. By comparing $\langle L_{\hat{p}} \rangle_{\Omega_{\mathrm{OP_{OD}}}}$ to $\langle L_{\hat{p}} \rangle_{\Omega_{\mathrm{OP_{FD}}}}$ it is seen to be clearly beneficial to create an optimized design. However if the performance of the designs is highly sensitive to small spatial variations they lose much of their attractiveness. Hence it is important to be able to investigate the design's sensitivity to spatial variations. Considering the smoothed design variables in Fig. 3i large areas of $\tilde{\xi}(\mathbf{x})$ taking intermediate values can be seen. These intermediate values make it impossible to establish a meaningful relation between the projection level and the resulting variations in the design. Figure 4 shows the smoothed design variables projected at four η-values to clarify this point. It is seen that the changes in the designs lack any uniformity in space and that the topology changes in several cases as η is varied. Thus the formulation needs a modification to remove the problem if varying η is to be a useful measure of robustness of $\langle L_{\hat{p}} \rangle_{\Omega_{\mathrm{OP}}}$ towards geometric variations.

9.2 Robust design

Next we introduce a min/max formulation where the objective is minimized for $\mathcal{N}_r \in \mathbb{N}$ different realizations of the projected design variables simultaneously[1].

$$\min_{\xi} . : \max_{k} \left(\frac{1}{A_{\mathrm{OP}}} \int |\hat{p}(\bar{\bar{\xi}}_k)|^2 d\Omega_{\mathrm{OP}} \right),$$
$$\text{s.t.} : 0 \leq \xi(\mathbf{x}) \leq 1 \ \ \forall \, \mathbf{x} \in \Omega_{\mathrm{d}} \ \wedge \ k \in \{1, 2, ..., \mathcal{N}_r\}. \quad (27)$$

Here $\mathcal{N}_r$ is the number of projection realizations used. In the rest of the paper solving (27) instead of (13) is denoted as *the robust approach*. The min/max formulation forms the basis for creating designs which perform robustly under spatial variations presented in a later section. Direct application of the scheme, suggested for performing robust topology optimization in Sigmund (2009), has been shown to perform well for structural and heat problems Wang et al. (2011b) and problems in optics Wang et al. (2011a) when creating robust designs. As will be shown in the following this is not the case for the acoustic cavity problem under consideration.

[1]The projection level for each realization may be taken to be constant throughout Ω_{d} or one may introduce a projection-field $\eta(\mathbf{x})$ which is allowed to vary throughout Ω_{d}, as will be considered in Section 11.

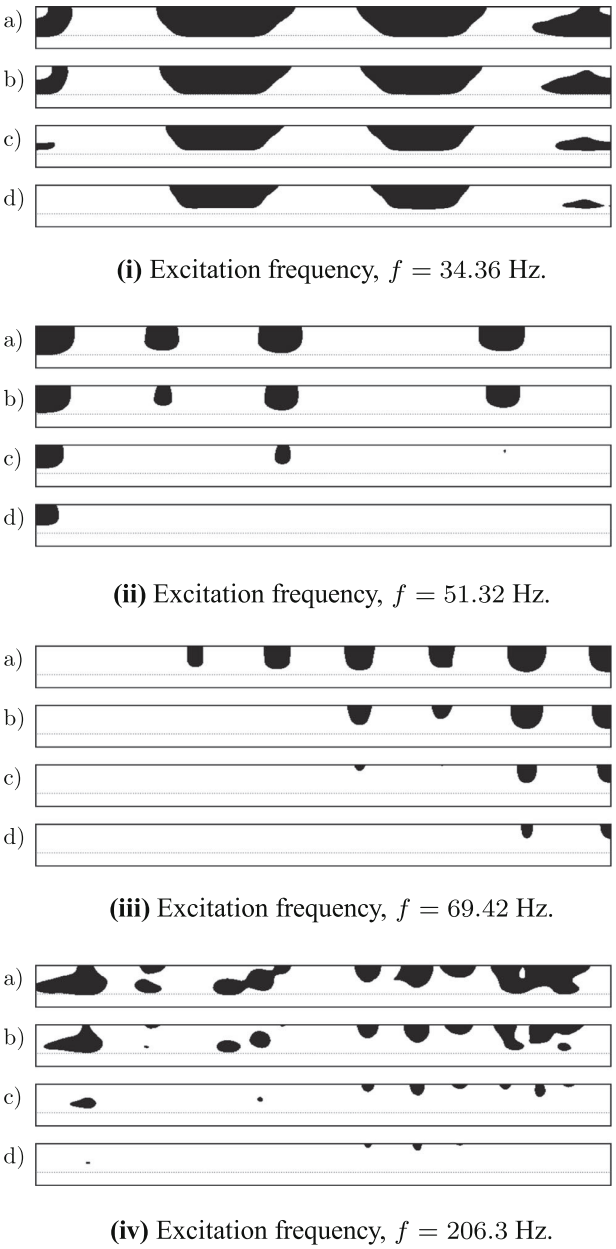

Fig. 4 Projection of smoothed design variables for the four cases shown in Fig. 3 at four η-values, **a**) $\eta = 0.3$, **b**) $\eta = 0.4$: **c**) $\eta = 0.6$, **d**) $\eta = 0.7$

9.3 Optimization using the robust approach

By solving (27), with $\mathcal{N}_r = 3$ using $\eta_k \in \{0.3, 0.5, 0.7\}$ new optimized designs have been found for the same four

excitation frequencies. $\eta_k = 0.5$ corresponds to the desired nominal design while $\eta_k = 0.3$ and $\eta_k = 0.7$ corresponds to dilated and eroded versions of the nominal design respectively. The smoothed design variables and the final designs projected at $\eta = 0.5$ are presented in Fig. 5i and ii respectively. Figure 5i shows that the problem of large areas of non-systematically varying $\tilde{\xi}(\mathbf{x})$-values remains for the robust formulation. Again the problem is seen to increase significantly with frequency. The reason why the problem remains when using the robust approach is believed to be the increasing non-convexity of the optimization problem with increasing frequency, caused by the increasing modal density. This leads to a high number of local minima which allows the optimizer to shape the design field such that a variation in η may result in unpredictable variations in the design while still providing good performance for the projected designs at the η-values used in the optimization.

Results of projecting the smoothed design variables presented in Fig. 5i at different η-values are shown in Fig. 6. The results for the design optimized for $f = 34.36$ Hz seen in Fig. 6 show that using $\mathcal{N}_r = 3$ instead of a single realization appears to have mitigated the problem of the unpredictable variations in the final design as η is varied. However, the figure clearly illustrates that for $f \geq 51.32$ Hz the problem of unpredictably varying designs with projection level remains. By comparing Figs. 5ii and 3ii it is seen that the designs for the lowest frequency $f = 34.36$ Hz are very similar indicating that this design is robust towards variations in its geometry.

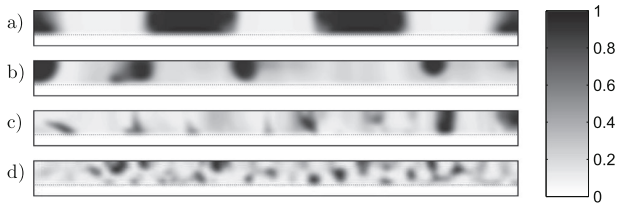

(i) Smoothed design variables

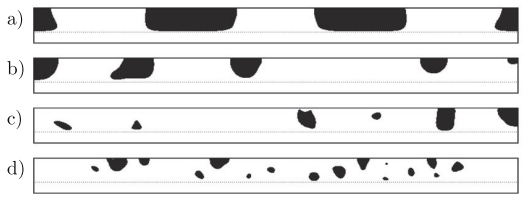

(ii) Final designs, projected at $\eta = 0.5$.

Fig. 5 **(i)** Smoothed and **(ii)** projected design variables for the four excitation frequencies, **a)** $f = 34.36$ Hz, **b)** $f = 51.32$ Hz, **c)** $f = 69.42$ Hz, **d)** $f = 206.3$ Hz, obtained using the robust approach given in (27) with a smoothing and projection step

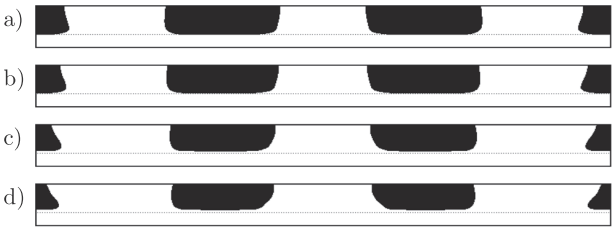

(i) Excitation frequency, $f = 34.36$ Hz.

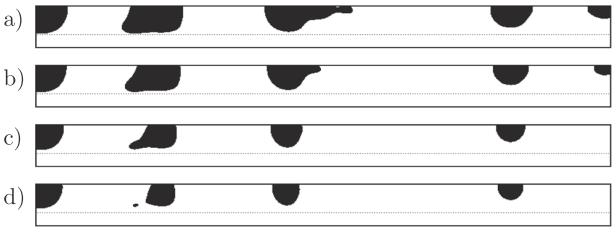

(ii) Excitation frequency, $f = 51.32$ Hz.

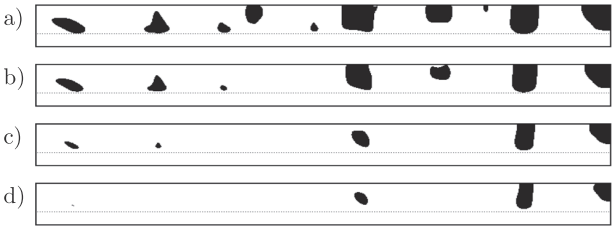

(iii) Excitation frequency, $f = 69.42$ Hz.

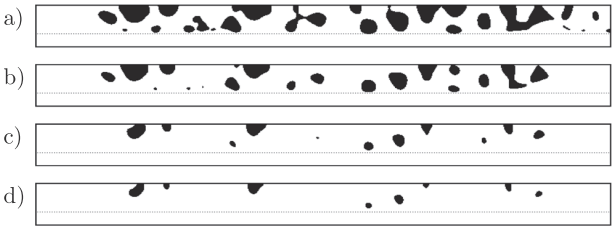

(iv) Excitation frequency, $f = 206.3$ Hz.

Fig. 6 Projection of smoothed design variables for the four cases presented in Fig. 5i at different η-values: **a)** $\eta = 0.3$, **b)** $\eta = 0.4$, **c)** $\eta = 0.6$, **d)** $\eta = 0.7$

10 Limiting the variations in $\tilde{\xi}$

This section presents two different methods for controlling the variation of the smoothed design variable field, $\tilde{\xi}$ along with results of numerical experiments showing the benefits and limitations of the approaches. The first method is a new double filter approach. The second method, included for comparison, is a well known explicit penalization method (Bendsøe and Sigmund 2003) which here is applied to the filtered field, $\tilde{\xi}$, instead of the physical

design variables. Both methods allow the enforcement of a near 0/1 $\tilde{\xi}$-field with intermediate values only near feature edges.

10.1 The double filter approach

The double filter approach consists of applying the density filter and projection introduced in Section 6 a second time on the already filtered and projected variables $\bar{\tilde{\xi}}(\mathbf{x})$. In order to distinguish the two filter steps a subscript 1 and 2 are introduced to denote the first and second filter step respectively. The application of the double filter effectively solves the problem of the uncontrolled changes in the final smoothed design variables as will be demonstrated in the following.

The double filter approach introduces three additional parameters. These are a second filter radius R_2, a second projection strength β_2 and a second projection level η_2. For all simulations done in the context of this paper, the parameters have been chosen to depend in a trivial manner on the parameters of the first filtering step effectively eliminating them. The second filter radius and projection strength have been chosen as $R_2 = \frac{1}{2}R_1$ and $\beta_2 = \frac{1}{2}\beta_1$ respectively. Regarding the projection level, $\eta_2 = \eta_1$ has been chosen for the standard approach while for the robust approach it is no longer η_1 that varies across realizations but instead η_2. For the robust approach the first projection level has been chosen as $\eta_1 = \min_k \eta_{2,k}$. These choices have worked well for all investigated cases.

Due to the β-continuation scheme the double filter works very similarly to the single filter in the beginning of the optimization process. This is because the projection for low values of β is close to inactive. Thus the second filter only further smooths the design variables without introducing other restrictions on the optimization. As β_1 increases the first smoothing and projection step will produce a near 0/1 design. The second smoothing step then smooths the design along its edges while the second projection step controls the amount of material added/removed from each edge. For high β_2-values this gives control on how much the size of each feature in the design is changed as the projection level is varied. The amount of material removed in the projection step is controlled by η_2 together with R_2. The relationship between η_2 and the change in the size of the design features is analyzed for a 1D case in Schevenels et al. (2011). Here a lower bound is found which shows a nearly linear relationship for $\eta_2 \in [0.3, 0.7]$. Based on this analysis it is suggested to limit η_2 to this, or a shorter, interval centered at 0.5 to ensure that for $\beta_1 \gg 1$ all changes in the design will occur along its edges in a predictable near-uniform manner as the second projection level is varied. If features appear/disappear or agglomerate/separate as η_2 is varied they do so in a predictable fashion in contrast to what was observed with the single filter approach.

The choice of R_2 relative to R_1 is important. If R_2 is chosen too large compared to R_1 the functionality of the double filter is lost for the following reason. The first smoothing operation creates a functional dependence between design variables which are less than R_1 apart. Thus the field $\bar{\tilde{\xi}}$ may in some sense be seen as a coarser version of the original design field. Filtering a second time with a large radius R_2 can therefore be seen as functionally equivalent to smoothing only a single time on the unfiltered design variables. Thus unpredictable variations in the design with projection level may be observed if R_2 is chosen to large. From our experimentation for the acoustic cavity problem it has been found that choosing R_2 such that $R_2 \leq \frac{R_1}{2}$ works well for all investigated cases. Choosing $R_2 \geq R_1$ has been found to destroy the effect of the double filter in several cases.

The choice of β_2 controls the sharpness of the second projection. Just as for the single filter, if β_2 is chosen with to high initial value, it will force the optimizer to converge to a suboptimal local minimum since the design variable field is forced immediately towards 0/1.

The application of the double filter in 1D using high β-values in both projection steps is sketched in Fig. 7.

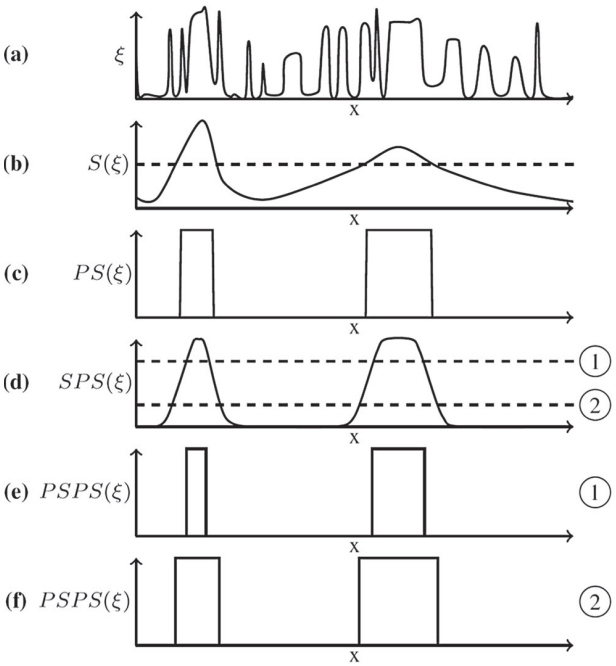

Fig. 7 Sketch of the double filter applied to a function, $\xi(x)$ in 1D (with $\beta_1 \gg 1, \beta_2 \gg 1$). Two different projection levels are used for the second projection. $S(\cdot)$ denotes smoothing and $P(\cdot)$ denotes projection. **a** $\xi(x)$, **b** $S_1(\xi(x))$, **c** $P_1(S_1(\xi(x)))$, **d** $S_2(P_1(S_1(\xi(x))))$, **e** $P_{2,1}(S_2(P_1(S_1(\xi(x)))))$, **f** $P_{2,2}(S_2(P_1(S_1(\xi(x)))))$

For $\beta_1 \gg 1, \beta_2 \gg 1$ the sensitivity $\frac{\mathrm{d}\Phi}{\mathrm{d}\tilde{\bar{\xi}}_i}$ is zero unless ξ_i lie within the filter radius of the edge of a design feature. This effectively turns the optimization problem into a shape optimization problem at high β-values. Thus initially when the projection strength is low the design is free to form without any restrictions on its topology while in the final part of the optimization design features are only allowed to change shape or disappear. To ease the referencing of the design variables at different stages in the filtering process each stage will henceforth be denoted as S, PS, SPS and PSPS respectively. The S and P are short for, S: Smoothing, and P: Projecting. The ordering of the letters corresponds to the order of the application of the operators read from right to left.

A final note of importance is that the double filter approach does not guarantee a length scale in the design and therefore not a fixed topology across all projection levels. However in most practically considered cases a length scale was found to be present.

10.1.1 Sensitivities

Applying the density filter and projection on $\tilde{\bar{\xi}}$ is operationally identical to applying the same operations on ξ. Therefore the sensitivity modifications are straightforward[2]. The sensitivities for the double filter are given by,

$$\frac{\mathrm{d}\Phi}{\mathrm{d}\xi_i} = \sum_{h \in \mathcal{B}_{e,i}} \frac{\partial \tilde{\xi}_h}{\partial \xi_i} \frac{\partial \tilde{\bar{\xi}}_h}{\partial \tilde{\xi}_h} \Delta\Phi_h, \quad i \in \{1, 2, ..., N\}, \tag{28}$$

$$\Delta\Phi_h = \sum_{j \in \mathcal{B}_{e,h}} \frac{\partial \tilde{\bar{\xi}}_j}{\partial \tilde{\bar{\xi}}_h} \frac{\partial \tilde{\bar{\xi}}_j}{\partial \tilde{\bar{\xi}}_j} \frac{\mathrm{d}\Phi}{\mathrm{d}\tilde{\bar{\xi}}_j}, \quad h \in \{1, 2, ..., N\}. \tag{29}$$

While these expressions may look formidable, the computational requirements for calculating the sensitivities are only twice of those for the single filter which is very cheap compared to solving the FEM problem and the optimization problem.

10.2 Double filtered standard approach

The double filter has been used with the standard approach replacing the single filter. Results for the four excitation frequencies are presented here. The SPS variables and final designs (PSPS variables, projected at $\eta_2 = 0.5$) are shown in Fig. 8i and ii, respectively.

Figure 8i clearly shows that the SPS-variables only change along design feature edges. Hence the problem of unpredictably varying intermediate design variable values has been resolved. Comparing the designs in Fig. 8ii to those in Fig. 3ii it is seen that for $f \in \{69.42\ \text{Hz}, 206.3\ \text{Hz}\}$ both the topology and overall appearance of the designs have changed. These changes may be attributed to the additional restrictions on the optimization imposed by the double filter and the fact that many local minima exist for the model problems.

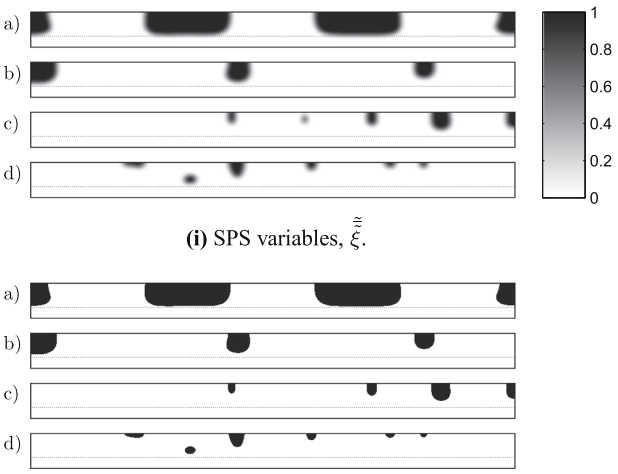

(i) SPS variables, $\tilde{\bar{\xi}}$.

(ii) Final design (PSPS variables projection at $\eta_2 = 0.5$).

Fig. 8 **(i)** SPS and **(ii)** PSPS design variables for the four excitation frequencies, **a)** $f = 34.36$ Hz, **b)** $f = 51.32$ Hz, **c)** $f = 69.42$ Hz, **d)** $f = 206.3$ Hz. The standard approach with the double filter has been used for the optimization

10.2.1 Sensitivity to design variations

Using the double filter it is now meaningful to investigate the sensitivity of the designs towards near-uniform spatial variations by varying the projection level η_2. This has been done for $\eta_2 \in [0.1, 0.9]$ which corresponds to a large near-uniform variation of approximately ± 0.1 meter ($\approx \pm 4$ elements for the chosen discretization) for each design feature. $\langle L_{\hat{p}} \rangle_{\mathbf{\Omega}_{\mathrm{OP}}}(\eta_2)$ (scaled by $\langle L_{\hat{p}} \rangle_{\mathbf{\Omega}_{\mathrm{OP_{ED}}}}$) for each of the four excitation frequencies is shown in Fig. 9i. A dashed line showing $\langle L_{\hat{p}} \rangle_{\mathbf{\Omega}_{\mathrm{OP_{FD}}}}$ (scaled by $\langle L_{\hat{p}} \rangle_{\mathbf{\Omega}_{\mathrm{OP_{ED}}}}$) corresponding to the average sound pressure level in $\mathbf{\Omega}_{\mathrm{OP}}$ when simply filling the entire design domain with material has been included. The interested reader may use the value of $\langle L_{\hat{p}} \rangle_{\mathbf{\Omega}_{\mathrm{OP_{ED}}}}$ from Table 2 to obtain values in db SPL.

By considering $\langle L_{\hat{p}} \rangle_{\mathbf{\Omega}_{\mathrm{OP}}}(\eta_2 = 0.5)$ it can be seen that a significant reduction in SPL is obtained for all excitation frequencies for the nominal designs. A reduction between 40 and 70 percent is observed across the four frequencies. The design for $f = 34.36$ Hz is observed to be highly robust with increases of only a few percent for large variations in projection level. For this low frequency the observed behavior is exactly what is expected since the wavelength is much

[2]The interested reader may find a derivation of the new sensitivities in Appendix.

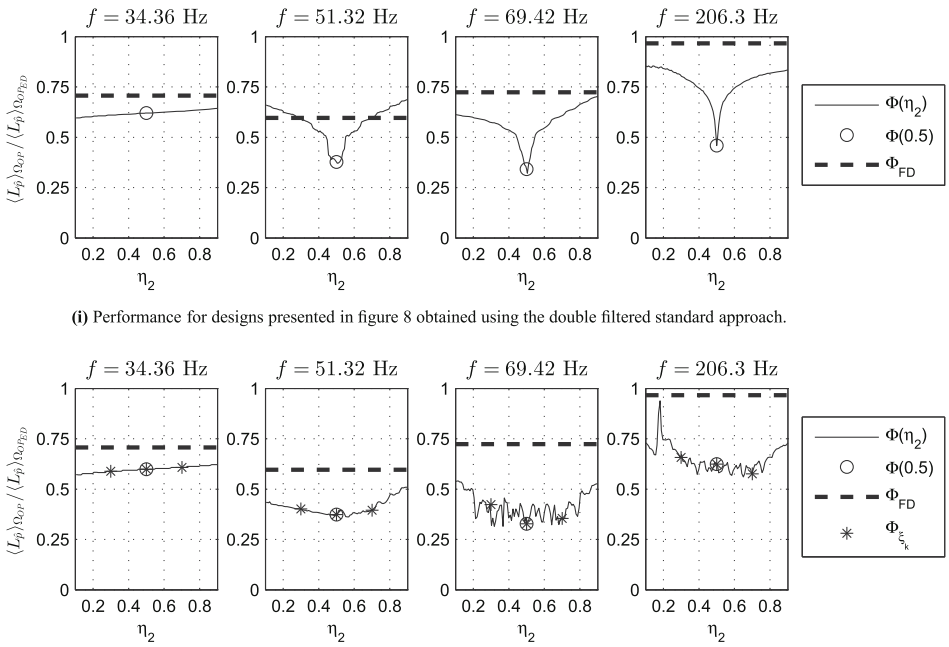

(i) Performance for designs presented in figure 8 obtained using the double filtered standard approach.

(ii) Performance for designs presented in figure 10 obtained using the double filtered robust approach.

Fig. 9 $\langle L_{\hat{p}}\rangle_{\mathbf{\Omega}_{\mathrm{OP}}}/\langle L_{\hat{p}}\rangle_{\mathbf{\Omega}_{\mathrm{OP_{ED}}}}$ as a function of projection level. **(i)** and **(ii)**: $\langle L_{\hat{p}}\rangle_{\mathbf{\Omega}_{\mathrm{OP}}}(\eta_2)/\langle L_{\hat{p}}\rangle_{\mathbf{\Omega}_{\mathrm{OP_{ED}}}}$ is denoted by the thin black line. The performance of the nominal design ($\eta_2 = 0.5$) is denoted by ∘. For comparison, $\langle L_{\hat{p}}\rangle_{\mathbf{\Omega}_{\mathrm{OP_{FD}}}}/\langle L_{\hat{p}}\rangle_{\mathbf{\Omega}_{\mathrm{OP_{ED}}}}$ is denoted by a thick dashed black line. **(ii)**: The realisations of η_2 for which the design has been optimized are denoted with *

longer than the design variations. Thus the variations are not expected to have much influence on the pressure-field. If one considers the three higher frequencies a different picture starts to emerge however. As a first example consider the case of $f = 69.42$ Hz. Here an increase from $\eta = 0.5$ to $\eta = 0.55$ corresponding to a near-uniform decrease in feature size of approximately $V_u \approx -1$ cm causes the relative performance improvement to deteriorate by more than 17 percent. As a second example consider the design optimized for $f = 206.3$ Hz. Here a deterioration of ≈ 24 percent is observed for variations in η_2 of about 0.05. Such large deteriorations in performance under small near-uniform variations are troublesome, especially considering that the scale is relative dB. What is observed from Fig. 8 is that the designs become increasingly sensitive towards small near-uniform geometric variations with increasing frequency. This high sensitivity towards spatial variations creates an interest in investigating a robust design approach.

10.3 Double filtered robust approach

In order to investigate whether it is possible to obtain robust designs for all four excitation frequencies the robust approach with the double filter is used. The resulting SPS- and PSPS-variables for the nominal design are presented in Fig. 10. It is again observed that intermediate values of the SPS-variables are only found along the edges of design features. The design for $f = 34.36$ Hz resembles the one optimized for a single projection level while the three designs for the higher excitation frequencies are very different in both shape and topology. This agrees with the lack of robustness observed in Fig. 9i. Figure 11 shows projections of the SPS-variable at $\eta_2 \in \{0.3, 0.4, 0.6, 0.7\}$. From here it is clearly seen that PSPS-variables now vary in a spatially near-uniform manner with projection level.

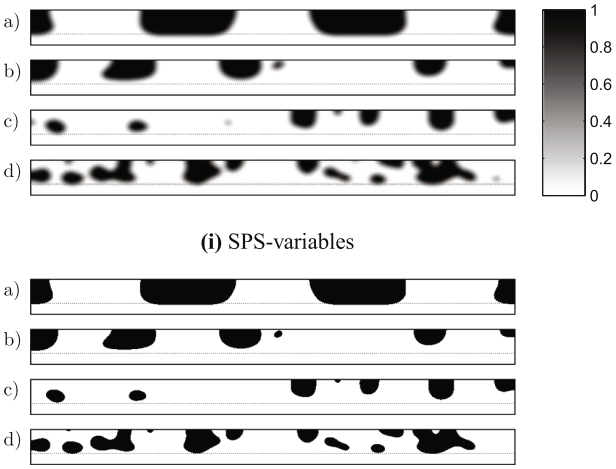

(i) SPS-variables

(ii) Final design (PSPS second projection at $\eta_2 = 0.5$).

Fig. 10 **(i)** SPS and **(ii)** PSPS design variables for the four excitation frequencies, **a)** $f = 34.36$ Hz, **b)** $f = 51.32$ Hz, **c)** $f = 69.42$ Hz, **d)** $f = 206.3$ Hz. The designs has been obtained using the robust approach with the double filter using three realizations for the second projection, $\eta_2 \in \{0.3, 0.5, 0.7\}$

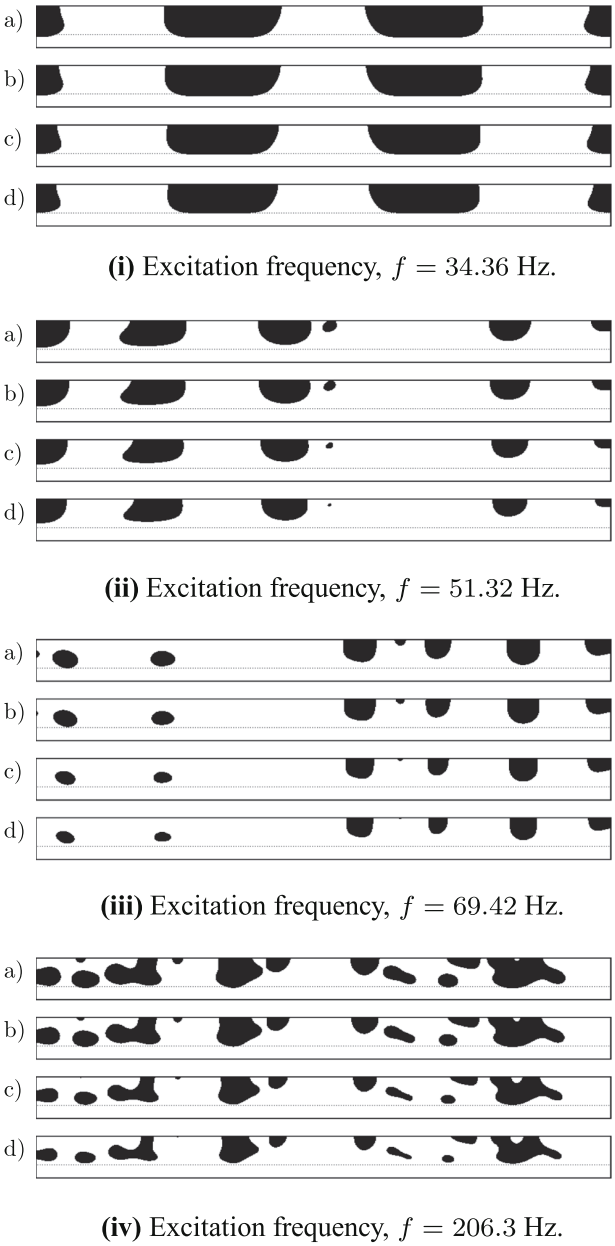

Fig. 11 Projection of SPS design variables at four different η_2-values, **a**) $\eta_2 = 0.3$, **b**) $\eta_2 = 0.4$, **c**) $\eta_2 = 0.6$, **d**) $\eta_2 = 0.7$ for the four designs shown in Fig. 10i

10.3.1 Sensitivity to design variations

Figure 9ii shows the variation in $\langle L_{\hat{p}} \rangle_{\mathbf{\Omega}_{\mathrm{OP}}}(\eta_2)/\langle L_{\hat{p}} \rangle_{\mathbf{\Omega}_{\mathrm{OP_{FD}}}}$ with η_2 for the four designs presented in Fig. 10ii. All the designs are seen to perform robustly for large variations of η_2 when compared to the results seen in Fig. 9i. For the case with $f = 34.36$ Hz almost no change in performance is observed compared to Fig. 9i. For $f = 51.32$ Hz the robustness of the performance is seen to have improved for a large η_2-interval. Here the robust design maintain a performance improvement of 60 percent or more for $\eta_2 \in [0.3, 0.7]$ compared to $\langle L_{\hat{p}} \rangle_{\mathbf{\Omega}_{\mathrm{OP_{FD}}}}$. For $f = 69.42$ Hz oscillations of up to 14 percent in performance improvement are observed. These are large fluctuations, however the performance increase for all $\eta_2 \in [0.22, 0.78]$ is more than 55 percent, which compared to the performance observed in Fig. 9i is a significant improvement in robustness. For $f = 206.3$ Hz oscillations of up to 10 percent are seen for $\eta_2 \in [0.3, 0.7]$ however the performance improvement stays above 33 percent which is good compared to the non-robust case if perturbations of η_2 of 0.05 or more is considered. Another important note is that the performance increase for the robust designs for the three lowest frequencies for all $\eta_2 \in [0.3, 0.7]$ are very close to the level of the nominal design obtained using the standard approach. Thus optimizing the designs for robustness under near-uniform variations does not significantly reduce the obtained performance for the nominal designs.

10.4 The penalization approach

A well known way of restricting the number of ξ-variables taking intermediate values is to penalize the design field explicitly (Bendsøe and Sigmund 2003). The penalization can be done by either adding an artificial penalization term, Φ_p, to the objective or introducing an additional constraint. Here we consider penalizing the filtered design variables, $\tilde{\xi}$, as suggested by Borrvall and Petersson (2001). The penalization term given in (30) is used.

$$\Phi_p(\mathbf{x}) = \alpha_{\Phi_p} \int \tilde{\xi}(\mathbf{x})(1 - \tilde{\xi}(\mathbf{x}))d\mathbf{\Omega}_{\mathrm{d}} \Big/ \int d\mathbf{\Omega}_{\mathrm{d}}, \quad \alpha_{\Phi_p} > 0. \tag{30}$$

The sensitivities of (30) with respect to $\tilde{\xi}$ are trivial to calculate. The value of $\Phi_p(\mathbf{x})$ is zero in areas with $\tilde{\xi} = 0$ or $\tilde{\xi} = 1$ while it assumes its maximum value for $\tilde{\xi} = \frac{1}{2}$. For sufficiently high values of α_{Φ_p} the approach forces the smoothed design variables towards 0/1 which will ensure narrow ranges of intermediate values for the smoothed design variables. This leads to near-uniform variations in the design along the edges of design features when the projection level is varied. While this attribute is appealing one significant problem exists: The choice of α_{Φ_p}. If α_{Φ_p} is chosen too large the penalization term will dominate the optimization which will result in poorly performing designs. If α_{Φ_p} is chosen too small, however, the penalization will not be effective and therefore the listed benefits are lost.

Designs obtained using the robust formulation where the penalization term has been added to the objective using $\alpha_{\Phi_p} = 6 \cdot 10^{-2}$ are presented here. This choice of α_{Φ_p}

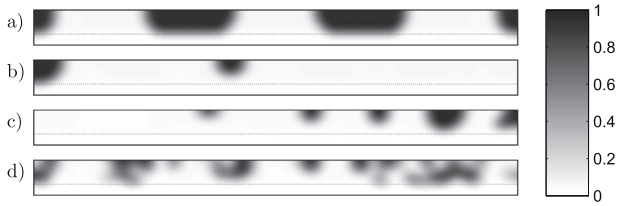

(i) Smoothed design variables

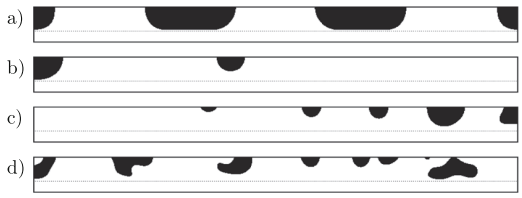

(ii) Projected final design at $\eta = 0.5$.

Fig. 12 **(i)** Smoothed and **(ii)** projected design variables for the four excitation frequencies, **a)** $f = 34.36$ Hz, **b)** $f = 51.32$ Hz, **c)** $f = 69.42$ Hz, **d)** $f = 206.3$ Hz, obtained with the robust approach with three realizations and the penalisation term added to Φ using $\alpha_{\Phi_p} = 6 \cdot 10^{-2}$

illustrates both good and bad performance of the approach distributed over the four excitation frequencies. A filter range of $R = 20$ has been used. The resulting designs are presented in Fig. 12.

From the figure it is seen that at the three lower excitation frequencies near 0/1 $\tilde{\xi}$ variables with smoothed edges along design features are obtained. Meanwhile for $f = 206.3$ Hz this property is seen to have disappeared. Figure 13 shows the design obtained for $f = 206.3$ Hz projected at the four different η-values. The design is seen to change topology and vary non-uniformly. Hence the design has not been optimized for near-uniform spatial variations as intended due to a too weak penalization. Another worrying result is the design obtained for the excitation frequency $f = 51.32$ Hz. Here the choice of $\alpha_{\Phi_p} = 6 \cdot 10^{-2}$ turns out to be too restrictive causing the optimization algorithm to get stuck in a local minimum with a poor performance. The performance obtained with this design is $\langle L_{\hat{p}} \rangle_{\Omega_{\mathrm{OP}}} \approx 56$ dB for the nominal design which is more than 19 dB worse than the performance of the design obtained using the double filter approach, as may be deduced from Fig. 9ii combined with $\langle L_{\hat{p}} \rangle_{\Omega_{\mathrm{OP_{ED}}}}$ from Table 2.

These examples illustrate the main problem with the penalization approach. That is, the correct choice of α_{Φ_p} depends on the parameters of the problem in a non-obvious way which makes experimentation necessary for each excitation frequency. On the other hand the examples also illustrate that if α_{Φ_p} is chosen correctly the approach may work well. For the excitation frequencies studied here results similar to those obtained using the double filter approach are obtained if α_{Φ_p} is chosen correctly.

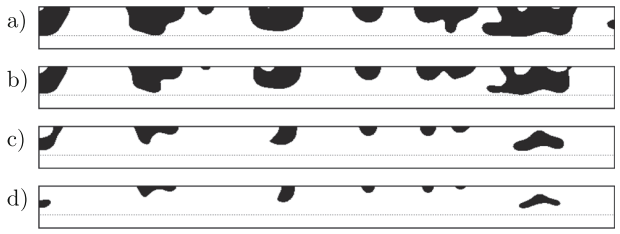

Fig. 13 Smoothed design variables presented in Fig. 12i for the frequency, $f = 206.3$ Hz projected at, **a)** $\eta = 0.3$, **b)** $\eta = 0.4$, **c)** $\eta = 0.6$, **d)** $\eta = 0.7$

11 Non-uniform design variations

We have demonstrated that using the robust approach with the double filter it is possible to create designs which are highly robust towards near-uniform geometric variations. In real applications however, during the production, installation and use of a given design it is more likely that small non-uniform errors are introduced. An interesting question now becomes whether small non-uniform variations (NUVs) cause significant deteriorations in performance for designs optimized for near-uniform variations. A natural extension of this question is to investigate whether it is possible to create designs that are more robust towards NUVs. In this section we demonstrate that by using the robust approach with the double filter it is possible to consider non-uniform variations in the optimization. We present results showing that the performance of designs optimized for near-uniform variations may deteriorate significantly under small NUVs. Then we show that it is possible to obtain designs that maintain a more robust performance under both non-uniform and near-uniform variations by including samples of the NUVs in the optimization process.

When taking NUVs into account during the optimization process a high number of realizations is needed in order to assure that the space of possible perturbations is covered. In this case the computational resources required for the standard FEM approach become a limiting factor. Therefore a hybrid finite element and wave based method (FE-WBM) was implemented, in order to reduce the cost of modeling the non-design domain, and used to obtain the results presented in the following. The wave based method was proposed by Desmet (1998) and the hybrid FE-WBM by Hal et al. (2003). The hybrid FE-WBM has just recently been applied to topology optimization by Goo et al. (2014). The strength of the hybrid method is that it is possible to significantly reduce the number of degrees of freedom used in the parts of the simulation domain where the model parameters are homogeneous.

The hybrid method is applied by discretizing the non-design domain $\Omega_{\text{WBM}} = \Omega \backslash \Omega_{\text{d}}$ using a set of wave basis functions which are themselves solutions to the Helmholtz equation. This reduces the number of degrees of freedom needed in Ω_{WBM} significantly. The design domain Ω_{d} is still discretized exactly as described in Section 5. Finally the two domains are coupled by introducing a set of coupling degrees of freedom along the interface between the Ω_{WBM} and Ω_{d}. Since Ω_{d} is discretized as described in Section 5 the parametrization of $\xi(\mathbf{x})$, the formulation of the optimization problem, the application of the smoothing and projection operators and the interpretation of the design domain does not change in any way.

By applying the hybrid method to the present problem where the ratio of the full model domain to the design domain is approximately $\Omega_{\text{d}} \approx 0.1\Omega$ the computational time was reduced by approximately a factor of ten. We emphasize that other than a reduction in computational time the application of the hybrid FE-WBM method does not change the optimization problem in any way and as such all results may be replicated using pure FEM if sufficient computational resources are available. The reported performance of all the designs obtained using the hybrid method was acquired using a pure FEM discretization.

A slightly different model problem, illustrated in Fig. 14, was considered in the following. Here the vibrational source was moved to one of the outer domain boundaries and was imposed using (3) keeping $U = 0.01$, hence modeling a vibrating piston set in the wall. The movement of the source was done solely due to implementation choices made for the WBM-FEM hybrid method which required placing the source on the domain boundary.

It is possible to model NUVs in many ways. One way is to consider random non-uniform variations as was done for structural and heat conduction problems by Schevenels et al. (2011) and Lazarov et al. (2012). In the present case we consider only one type of non-random variation. Namely sinusoidal variations in one spatial direction and no variation in the other. This is only a small subset of all possible NUVs but it works for illustrating the desired points. The NUVs are included in the optimization process by introducing a variable projection field, $\eta(\mathbf{x})$, (Schevenels et al. 2011). This field replaces the constant projection level η, leading to varying projection levels across the domain. When using the double filter approach it is η_2 which is replaced with the varying projection field. The NUVs in the projection level have been modeled as,

$$\eta_2(\mathbf{x}) = \eta_{\min} + (\eta_{\max} - \eta_{\min}) \cdot \mathrm{P}(A \cdot \cos(Bx + C)). \quad (31)$$

Here P is the normal cumulative distribution function with unit standard deviation and unit mean. $\eta_{\max} \in]\eta_{\min}, 1]$ and $\eta_{\min} \in [0, \eta_{\max}[$ are the maximum and minimum projection values, respectively. B and C were allowed to vary while A was kept fixed. Samples of the projection field for different B and C are shown in Fig. 15.

For the results presented here the following values have been used for the non-uniformly varying projection field: $A = 6$, $B \in \{2, 4, 8\}$, $C \in [0, 2\pi]$, $\eta_{\min} = 0.4$ and $\eta_{\max} = 0.6$. The optimizations were initialized with the material fraction $\xi_{\text{ini}} = 0.5 \; \forall \, \mathbf{x} \in \Omega_{\text{d}}$ and a filter radius of $R = 16$ was used.

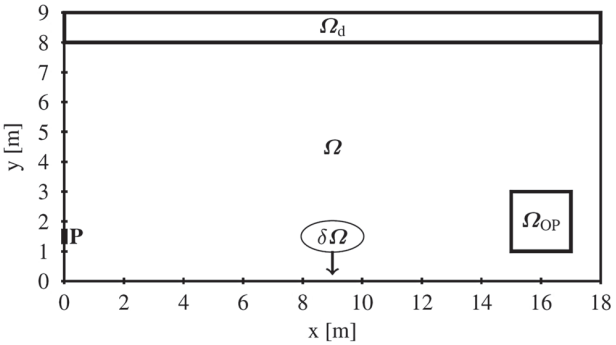

Fig. 14 Illustration of the modified model problem domain. $\Omega_{\text{OP}} \in [15.5, 16.5] \times [1.5, 2.5]$ is the optimization domain, $\Omega_{\text{d}} \in [0, 18] \times [8, 9]$ is the design domain and $\mathbf{P} \in 0 \times [1.3, 1.7]$ denotes the region where an acoustic excitation is imposed

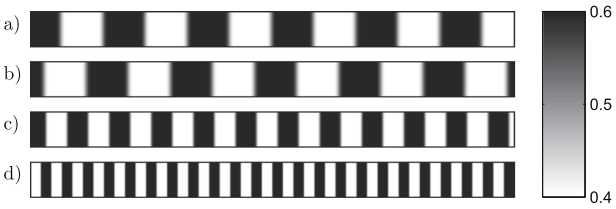

Fig. 15 Samples of the non-uniformly varying projection field for **a)** $B = 2, C = \frac{4}{5}\pi$, **b)** $B = 2, C = \frac{6}{5}\pi$, **c)** $B = 4, C = \frac{6}{5}\pi$, **d)** $B = 8, C = \frac{8}{5}\pi$

11.1 Imposing NUV on robust designs

In the following the two excitation frequencies, $f \in \{69.42, 206.3\}$ Hz are considered. Optimized designs were created using the robust approach with the double filter and three realizations of the second projection at $\eta_2 \in \{0.3, 0.5, 0.7\}$. The designs are presented in Fig. 16.

Fig. 16 Nominal designs optimized using uniform variations for the excitations frequencies **a)** $f = 69.42$ Hz, and **b)** $f = 206.3$ Hz

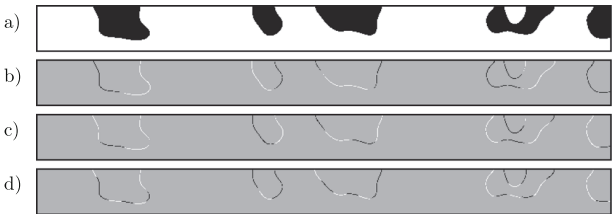

Fig. 17 Non-uniform variations in the design optimized for $f = 69.42$ Hz. **a)** Design. **b)-d)** Difference between the nominal design and the non-uniformly perturbed designs. White shows removed material and black shows added material

The designs were subjected to small non-uniform variations given by (31). Figure 17 shows representative examples of the non-uniform changes in the design optimized for $f = 69.42$ Hz when the variations are imposed. In the sub figures **b)-d)** the white areas denote removed material while the black areas denote added material.

It is seen that the non-uniform variations are small (2.5 cm - 5 cm in terms of the model dimensions). Nevertheless a significant reduction in performance is observed. Figure 18 shows $\langle L_{\hat{p}} \rangle_{\Omega_{\mathrm{OP}}}(\eta_2)/\langle L_{\hat{p}} \rangle_{\Omega_{\mathrm{OP_{ED}}}}$ for varying projection level, $\eta \in [0.3, 0.7]$ overlaid with a graph of $\langle L_{\hat{p}} \rangle_{\Omega_{\mathrm{OP}}}(\eta_{2,k}(\mathbf{x}))/\langle L_{\hat{p}} \rangle_{\Omega_{\mathrm{OP_{ED}}}}$ for 80 different realizations of the non-uniform variations with $A = 6$, $B \in \{2, 4, 8, 16\}$ and C uniformly distributed at 20 points in $[0, 2\pi[$.

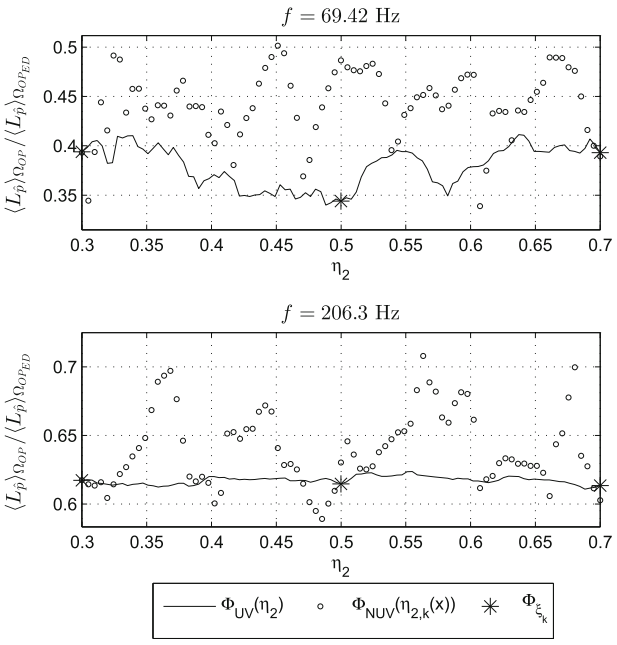

Fig. 18 $\langle L_{\hat{p}} \rangle_{\Omega_{\mathrm{OP}}}/\langle L_{\hat{p}} \rangle_{\Omega_{\mathrm{OP_{ED}}}}$ for designs in Fig. 16 exposed to near-uniform, $\Phi_{\mathrm{UV}}(\eta_2)$, and non-uniform, $\Phi_{\mathrm{NUV}}(\eta_{2,k}(\mathbf{x}))$, spatial variations. The performance at the three realization for which the designs were optimized, Φ_{ξ_k}, are marked

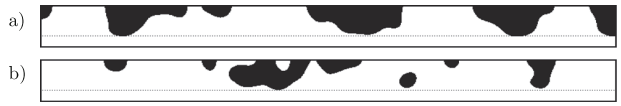

Fig. 19 Nominal designs optimized using non-uniform variations for **a)** $f = 69.42$ Hz, and **b)** $f = 206.3$ Hz

Figure 18 clearly shows the lack of robustness of the designs towards non-uniform variations. The observed performance deteriorations are less significant than what was seen by comparing designs optimized using the robust approach and using the standard approach under near-uniform variations, however they are clearly still significant. Compared to the nominal designs ($\eta_2 = 0.5$) a deterioration of up to 15 % is seen for the design optimized at $f = 69.42$ Hz and up to 9 % for the design optimized at $f = 206.3$ Hz. Considering comparable near-uniform variations ($\eta_2 \in [0.4, 0.6]$) we only observe deteriorations of 5 % and 1 % respectively.

11.2 Optimizing for NUV

In order to reduce the observed deterioration in performance under non-uniform variations a new optimization was performed using the robust approach with the double filter. Here non-uniform variations were included in the realizations. A total of 18 realizations were used. Three used the constant projection levels $\eta_2 \in \{0.3, 0.5, 0.7\}$. The remaining fifteen realizations used the variable projection level

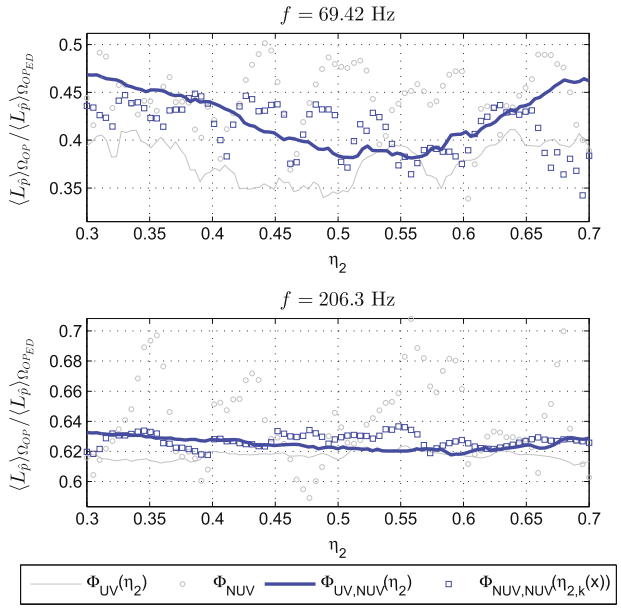

Fig. 20 $\langle L_{\hat{p}} \rangle_{\Omega_{\mathrm{OP}}}/\langle L_{\hat{p}} \rangle_{\Omega_{\mathrm{OP_{ED}}}}$ for the designs in Fig. 19 exposed to near-uniform, $\Phi_{\mathrm{UV,NUV}}(\eta_2)$, and non-uniform, $\Phi_{\mathrm{NUV,NUV}}(\eta_{2,k}(x))$, variations. For easy comparison the data from Fig. 18 is plotted in light gray

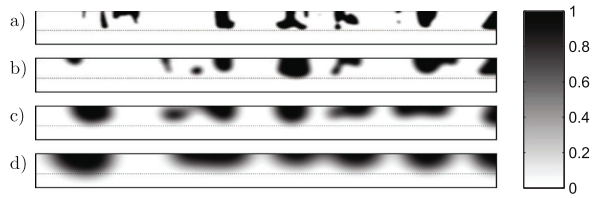

(i) Final SPS-variables for four different filter radii .

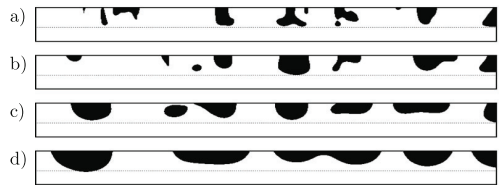

(ii) Final SPSP-variables for four different filter radii projected at $\eta_2 = 0.5$.

Fig. 21 **(i)** SPS and **(ii)** PSPS design variables obtained using the robust approach with different filter radii and six realizations of the uniform projection level at $\eta_{2,k} \in \{0.3, 0.38, 0.46, 0.54, 0.62, 0.7\}$ for the excitation frequency $f = 69.42$ Hz, discretized using $(n_x, n_y) = (720, 360)$ finite elements. SPS-variables **(i)**. **a**) $R_1 = 10$ **(i)**. **b**) $R_1 = 20$ **(i)**. **c**) $R_1 = 40$ **(i)**. **d**) $R_1 = 60$. **(ii)** PSPS-variables projected at $\eta_2 = 0.5$ for designs in **(i)**

given by (31) with all combinations of $B \in \{2, 4, 8\}$ and $C \in \left\{\frac{2}{5}\pi, \frac{4}{5}\pi, \frac{6}{5}\pi, \frac{8}{5}\pi, 2\pi\right\}$. Figure 19 show the designs resulting from the optimizations.

The performance of the designs under both near-uniform and non-uniform variations have been investigated in the same manner as in the previous section. The results are presented in Fig. 20.

From Fig. 20 it is immediately observed that the designs optimized for the non-uniform variations are more robust under non-uniform variations than the designs only optimized for uniform variations. Considering first the design for $f = 69.42$ Hz. Here the ratio of $\langle L_{\hat{p}}\rangle_{\mathbf{\Omega}_{\mathrm{OP}}}/\langle L_{\hat{p}}\rangle_{\mathbf{\Omega}_{\mathrm{OP_{ED}}}}$ for all variations in η_2 within $[0.4, 0.6]$ is now under 45 % compared to the earlier design's 50 %. Thus an improvement in worst case performance of 5 %. The trade off is a decrease in performance of the nominal design by approximately 4 % compared to the earlier design. Consider now the design optimized for $f = 206.3$ Hz. This design is seen to perform highly robustly under both near-uniform and non-uniform variations with a maximum of 2 % variation in performance. The deterioration in performance of the nominal design compared to the earlier design is only 1 % while the worst case performance is now below 64 % compared to the earlier 71 %. Hence a 7 % better worst case performance.

A thorough study of the performance of the designs in Fig. 19 with more than 2500 realizations for uniformly distributed value of $B \in [2, .., 16]$ and $C \in [0, 2\pi]$ was performed to assure the correctness of the conclusions drawn above. This test did not reveal any results that contradict our conclusions for the presented cases.

12 Varying the filter radius

This section investigates the behavior of the double filter approach for varying filter radius. We consider the model problem in Fig. 14 and take the excitation frequency to be, $f = 69.42$ Hz. We optimize using the doubly filtered robust approach for four different filter radii $R_1 \in \{10, 20, 40, 60\}$ elements, $R_2 = \frac{1}{2}R_1$ and near-uniform variations. We use six realizations for the projection level, $\eta_{2,k} \in \{0.3, 0.38, 0.46, 0.54, 0.62, 0.7\}$. The remaining parameters are set at the values given in Table 1. The reason for using six realizations for $\eta_{2,k}$ instead of three as in the earlier cases is that it we found that for $R_1 \in \{40, 60\}$ three realization for the second projection level are not enough to obtain a high performance across all values of $\eta_2 \in [0.3, 0.7]$. This finding is sensible since increasing R_1 while keeping the variation in η_2 fixed leads to an increased spatial variation in the design. Figure 21 presents

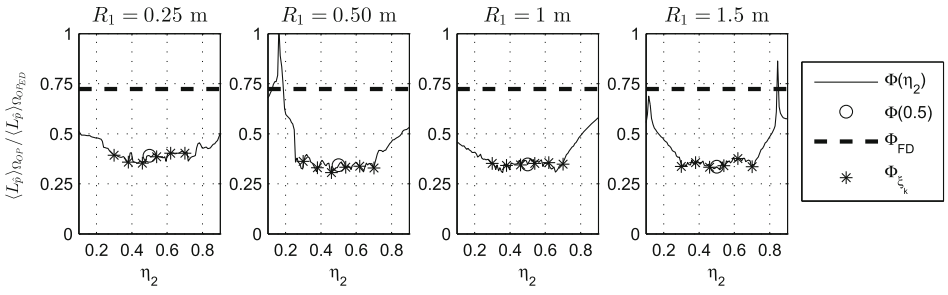

Fig. 22 $\langle L_{\hat{p}}\rangle_{\mathbf{\Omega}_{\mathrm{OP}}}/\langle L_{\hat{p}}\rangle_{\mathbf{\Omega}_{\mathrm{OP_{ED}}}}$ as a function of projection level for designs presented in Fig. 21, obtained using the double filtered robust approach, under uniform erosion/dilation. $\langle L_{\hat{p}}\rangle_{\mathbf{\Omega}_{\mathrm{OP}}}(\eta_2)/\langle L_{\hat{p}}\rangle_{\mathbf{\Omega}_{\mathrm{OP_{ED}}}}$ is denoted by the thin black line. The performance of the nominal design ($\eta_2 = 0.5$) is denoted by ∘. For comparison, $\langle L_{\hat{p}}\rangle_{\mathbf{\Omega}_{\mathrm{OP_{FD}}}}/\langle L_{\hat{p}}\rangle_{\mathbf{\Omega}_{\mathrm{OP_{ED}}}}$ is denoted by a thick dashed black line. The realizations of η_2 for which the design has been optimized are denoted with *

the final SPS- and SPSP-variables for the four different cases.

It is seen that the double filter performs as expected for all filter radii, in the sense that it produces SPS-variables which consists of areas of material ($\bar{\bar{\tilde{\xi}}}(\mathbf{x}) = 1$) with smoothed edges. Figure 22 shows the performance of each of the four designs under near-uniform erosion/dilation performed by varying η_2 in the interval [0.1, 0.9].

It is observed that the performance is similar in terms of the reduction in dB SPL for all four cases inside the interval of optimization.

13 Conclusions

We considered the minimization of sound pressure in part of a 2D domain for an acoustic cavity problem by placing material in another part of the domain using topology optimization. We showed that the direct application of a standard technique for robust topology optimization encounters a problem of uncontrollable intermediate design variables making it unusable. A novel double filter was introduced and it was shown to alleviate the problem thus allowing for the application of the robust optimization approach. It was demonstrated that small near-uniform geometric variations can cause significant deteriorations in the performance of designs optimized using the standard approach. Applying the robust approach with the double filter and optimizing for near-uniform geometric variations was shown to create highly robust designs under large near-uniform variations for all investigated frequencies. It was then demonstrated that imposing small non-uniform variations on designs optimized for near-uniform variations could lead to smaller but still significant deteriorations in performance. Finally it was shown to be possible to obtain designs which performed robustly under both near-uniform and selected non-uniform geometric variations by taking both types of variations into account during the optimization process. The proposed double filter approach is useful for highly shape sensitive optimization problems as demonstrated here. For less sensitive problems standard single filter approaches may be sufficient. When solving the acoustic cavity problem considered in this paper for a wider frequency band instead of for a single frequency (or narrow frequency band) the extreme sensitivity disappears and the problem may be solved using the single filter approach, see Appendix.

Acknowledgments This work was financially supported by Villum Fonden through the research project *Topology Optimization - the Next Generation* NextTop.

Appendix

Derivation of sensitivities for the double filter

The sensitivities, $\frac{\mathrm{d}\Phi}{\mathrm{d}\xi_i}$, for the double filter may be derived as follows:

1. Apply the chain rule for calculating the sensitivities.

$$\frac{\mathrm{d}\Phi}{\mathrm{d}\xi_i} = \sum_{j,k,l,h} \frac{\partial\tilde{\xi}_l}{\partial\xi_i} \frac{\partial\bar{\bar{\xi}}_h}{\partial\tilde{\xi}_l} \frac{\partial\bar{\bar{\bar{\xi}}}_k}{\partial\bar{\bar{\xi}}_h} \frac{\partial\bar{\bar{\bar{\xi}}}_j}{\partial\bar{\bar{\bar{\xi}}}_k} \frac{\mathrm{d}\Phi}{\mathrm{d}\bar{\bar{\bar{\xi}}}_j}. \tag{32}$$

2. Eliminate two sums using the fact that $\frac{\partial\bar{\bar{\xi}}_h}{\partial\tilde{\xi}_l} = 0 \,\forall\, l \neq h$ and that $\frac{\partial\bar{\bar{\bar{\xi}}}_j}{\partial\bar{\bar{\bar{\xi}}}_k} = 0 \,\forall\, k \neq j$ due to the locality of (23).

$$\frac{\mathrm{d}\Phi}{\mathrm{d}\xi_i} = \sum_j \sum_h \frac{\partial\tilde{\xi}_h}{\partial\xi_i} \frac{\partial\bar{\bar{\xi}}_h}{\partial\tilde{\xi}_h} \frac{\partial\bar{\bar{\bar{\xi}}}_j}{\partial\bar{\bar{\xi}}_h} \frac{\partial\bar{\bar{\bar{\xi}}}_j}{\partial\bar{\bar{\bar{\xi}}}_j} \frac{\mathrm{d}\Phi}{\mathrm{d}\bar{\bar{\bar{\xi}}}_j} \quad i \in \{1, 2, ..., N\}. \tag{33}$$

3. Utilize that $\tilde{\xi}_h$ only depends on the design variables ξ_i within the density filter radius reducing the sum over h significantly. The same argument applied to $\bar{\bar{\bar{\xi}}}_j$ and $\bar{\bar{\xi}}_h$ reduces the sum over j. The set of indices for the dependent variables are denoted, $\mathcal{B}_{e,i}$ and $\mathcal{B}_{e,h}$ respectively. The sensitivities now take the form,

$$\frac{\mathrm{d}\Phi}{\mathrm{d}\xi_i} = \sum_{j\in\mathcal{B}_{e,h}} \sum_{h\in\mathcal{B}_{e,i}} \frac{\partial\tilde{\xi}_h}{\partial\xi_i} \frac{\partial\bar{\bar{\xi}}_h}{\partial\tilde{\xi}_h} \frac{\partial\bar{\bar{\bar{\xi}}}_j}{\partial\bar{\bar{\xi}}_h} \frac{\partial\bar{\bar{\bar{\xi}}}_j}{\partial\bar{\bar{\bar{\xi}}}_j} \frac{\mathrm{d}\Phi}{\mathrm{d}\bar{\bar{\bar{\xi}}}_j}. \tag{34}$$

4. Rewriting the expression gives,

$$\frac{\mathrm{d}\Phi}{\mathrm{d}\xi_i} = \sum_{h\in\mathcal{B}_{e,i}} \frac{\partial\tilde{\xi}_h}{\partial\xi_i} \frac{\partial\bar{\bar{\xi}}_h}{\partial\tilde{\xi}_h} \left[\sum_{j\in\mathcal{B}_{e,h}} \frac{\partial\bar{\bar{\bar{\xi}}}_j}{\partial\bar{\bar{\xi}}_h} \frac{\partial\bar{\bar{\bar{\xi}}}_j}{\partial\bar{\bar{\bar{\xi}}}_j} \frac{\mathrm{d}\Phi}{\mathrm{d}\bar{\bar{\bar{\xi}}}_j} \right]. \tag{35}$$

5. For a given h the expression in the bracket in (35) only depends on j. Thus we may define,

$$\Delta\Phi_h = \sum_{j\in\mathcal{B}_{e,h}} \frac{\partial\bar{\bar{\bar{\xi}}}_j}{\partial\bar{\bar{\xi}}_h} \frac{\partial\bar{\bar{\bar{\xi}}}_j}{\partial\bar{\bar{\bar{\xi}}}_j} \frac{\mathrm{d}\Phi}{\mathrm{d}\bar{\bar{\bar{\xi}}}_j}, \quad h \in \{1, 2, ..., N\}. \tag{36}$$

This illustrates that the application of the double filter simply corresponds to applying the single filter twice.

□

Application of robust approach for frequency bands

Single frequency problems have been the focus of the paper due to the high sensitivity in the performance of the

optimized designs under geometric variations. In this section we provide an example showing the method applied for a band of frequencies as well. As will be demonstrated, this problem is far less sensitive towards geometric variations in the design. A requirement for considering optimization for a band of frequencies for the cavity problem is that a small amount of damping is added to the model problem to avoid problems caused by resonances in the frequency band of interest. The need for damping has nothing to do with the double filter or the robust approach and must be added regardless of the optimization strategy. Mass proportional damping is introduced by adding the term "$\alpha_{\text{damp}}\,\mathrm{i}\,\hat{\omega}\hat{p}$" to (7) where $\alpha_{\text{damp}} = 0.01$ is the damping factor.

In the following we consider the model problem presented in Fig. 14 and seek to minimize the mean of the average sound pressure in $\mathbf{\Omega}_{\text{OP}}$ over a 1/3 octave frequency band, $f_{\text{b}} \approx [61.85, 77.92]$ Hz, centered at, $f_{\text{c}} = 62.5$ Hz. The objective function may thus be stated as,

$$\Phi(\xi) = \frac{1}{N_i}\sum_{i=1}^{N_i}\frac{1}{A_{\text{OP}}}\int |\hat{p}(\tilde{\tilde{\xi}}, f_i)|^2 d\mathbf{\Omega}_{\text{OP}}, \tag{37}$$

where f_i are the frequencies optimized for and N_i is the number of frequencies. An optimization is performed using the standard approach with the double filter and the second projection at $\eta_2 = 0.5$. For comparison an optimization is performed using the robust approach with double filtering and five realizations of the second projection level, $\eta_2 \in \{0.3, 0.4, 0.5, 0.6, 0.7\}$. For both cases we use $N_i = 20$ and consider equidistant frequencies in f_{b} including both endpoints. For the PDE problem we use a pure FEM discretization with $\mathcal{N}_x = 216$, $\mathcal{N}_y = 108$ elements. A filter range of $R_1 = 5$ elements is used. Figure 23 shows the resulting SPS and SPSP variables for the two optimizations.

(i) Final SPS-variables for designs optimized for a frequency band.

(ii) Final SPSP-variables for designs optimized for a frequency band.

Fig. 23 **(i)** SPS and **(ii)** PSPS design variables obtained using the **a)** standard and **b)** robust approach for the 1/3 octave frequency band optimization

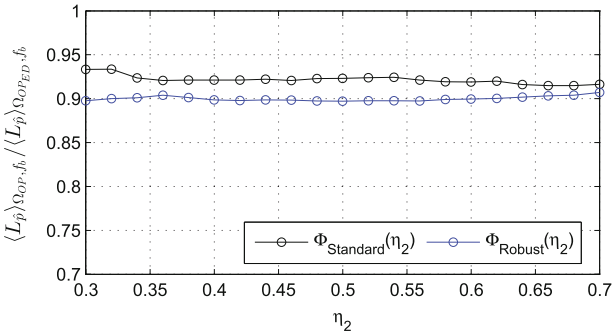

Fig. 24 $\langle L_{\hat{p}}\rangle_{\mathbf{\Omega}_{\text{OP}},f_{\text{b}}}/\langle L_{\hat{p}}\rangle_{\mathbf{\Omega}_{\text{OP}_{\mathbf{ED}}},f_{\text{b}}}$ for the designs in Fig. 23 under near-uniform variations imposed by varying η_2. The performance of the designs is seen to be almost constant under the prescribed uniform variations

Figure 24 shows the mean of the average sound pressure level in $\mathbf{\Omega}_{\text{OP}}$ over the 1/3 octave frequency band, $\langle L_{\hat{p}}\rangle_{\mathbf{\Omega}_{\text{OP}},f_{\text{b}}}$, scaled by the same quantity in $\mathbf{\Omega}_{\text{OP}}$ for the empty cavity, $\langle L_{\hat{p}}\rangle_{\mathbf{\Omega}_{\text{OP}_{\mathbf{ED}}},f_{\text{b}}} \approx 89.79$ dB, as a function of projection level η_2, for both the standard and the robust approach. The mean over the frequency is calculated using 100 equidistant frequencies in f_{b}. This variation in projection level corresponds to a near-uniform erosion/dilation of 1 element or approximately 8 cm in the design. The presented results have been evaluated with the same amount of damping as the one used in the optimization.

From the figure it is clearly observed that both the standard and robust approach produce results which do not show any significant sensitivity towards uniform erosion or dilation of the design. It is noted that the robust approach produces a design with better performance. This is likely due to the additional restrictions on the optimization when using the robust approach which eliminates the local minimum trapping the optimization performed with the standard approach.

An investigation of the sensitivity of the performance under non-uniform geometric variations for the design optimized using the standard approach is also performed. Here it is shown that, just as for the uniform geometric perturbations, the sensitivity drops significantly when considering a band of frequencies compared to a single frequency. Twenty five non-uniform geometric variations are applied as described in Section 11 using $A = 6$, $B \in \{2, 3.5, 5, 6.5, 8\}$, $C \in 2\pi \cdot \{1, 2, 3, 4, 5\}$, $\eta_{\min} = 0.3$, $\eta_{\max} = 0.7$. Figure 25i show the sensitivity of the performance under the twenty five non-uniform geometric variations for the average response over f_b while Fig. 25ii show the performance sensitivity under the same twenty five non-uniform geometric variations for the single frequency $f_s = 70.15$ Hz.

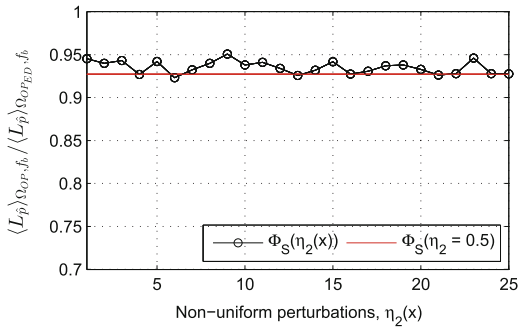

(i) $\langle L_{\hat{p}} \rangle \boldsymbol{\Omega}_{\mathrm{OP},f_b} / \langle L_{\hat{p}} \rangle \boldsymbol{\Omega}_{\mathrm{OP}_{\mathbf{ED}},f_b}$ for 1/3 octave frequency band, f_b.

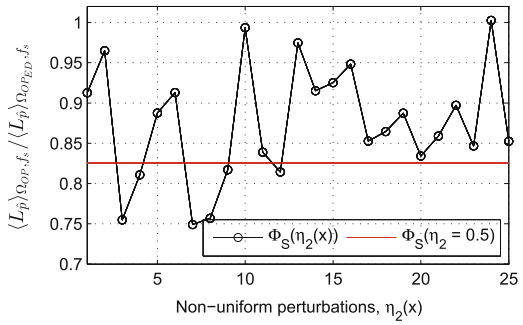

(ii) $\langle L_{\hat{p}} \rangle \boldsymbol{\Omega}_{\mathrm{OP},f_s} / \langle L_{\hat{p}} \rangle \boldsymbol{\Omega}_{\mathrm{OP}_{\mathbf{ED}},f_s}$ for single frequency, $f_s = 70.15$ Hz

Fig. 25 Scaled performance for the design in Fig. 23. **a**) under non-uniform variations imposed through $\eta_2(x)$. The performance of the design is seen to be less sensitive for a frequency band **(i)** then for a single frequency **(ii)**. The red line marks the performance of the nominal design while the black line with circles mark the performance for the perturbed design

From the figure it is clearly seen that the average response over f_b is far less sensitive to geometric perturbations than when only considering f_s.

References

Bendsøe MP, Sigmund O (2003) Topology optimization - theory, methods and application. Springer

Borrvall T, Petersson J (2001) Topology optimization using regularized intermediate density control. Computer methods in applied mechanical and engineering 190:4911–4928

Bourdin B (2001) Filters in topology optimization. Int J Numer Methods Eng 50:2143–2158

Bruns TE, Tortorelli DA (2001) Topology optimization of nonlinear elastic structures and compliant mechanisms. Computational Methods for Applied Mechanical Engineering 190:3443–3459

Clausen A, Aage N, Sigmund O (2015) Topology optimization of coated structures and material interface problems. Computational Methods for Applied Mechanical Engineering 290:524–541

Desmet W (1998) A wave based prediction technique for coupled vibro-acoustic analysis. PhD thesis, Katholieke Universitet Leuven

Dühring MB, Jensen JS, Sigmund O (2008) Acoustic design by topology optimization. J Sound Vib 317:557–575

Du J, Olhoff N (2007) Minimization of sound radiation from vibrating bi-material structures using topology optimization. Structural and Multidiciplinary Optimization 33:305–321

Elesin Y, Lazarov B, Jensen J, Sigmund O (2012) Design of robust and efficient photonic switches using topology optimization. Photonics and Nanostructures Fundamentals and Applications 10:153–165

Goo S, Kook J, Koo K, Hyun J, Wang S (2014) Acoustic topology optimization for interior acoustic problem using the hybrid finite element - wave based method. In: The Eighth China-Japan-Korea Joint Symposium on Optimization of Structural and Mechanical Systems

Guest JK, Prévost JH, Belytschko T (2004) Achieving minimum length scale in topology optimization using nodal design variables and projection functions. Int J Numer Methods Eng 61:238–254

Hal BV, Desmet W, Pluymers B, Sas P, Vandepitte D (2003) A coupled finite element - wave based approach for the steady-state dynamics analysis of acoustic systems. J Comput Acoust:285–303

Jacobsen F, Juhl PM (2013) Fundamentals of General Linear Acoustics. Wiley

Kook J, Koo K, Hyun J, Jensen JS, Wang S (2012) Acoustical topologi optimization for zwicker's loudness model - application to noise barriers. Computational Methods for Applied Mechanical Engineering 237:130–151

Lazarov BS, Schevenels M, Sigmund O (2012) Topology optimization considering material and geometric uncertainties using stochastic collocation methods. Structural Multidiciplinary Optimization 46:597–612

Lee JW, Kim YY (2009) Ridig body modeling issue in acoustic topology optimization. Computational Methods for Applied Mechanical Engineering 198:1017–1030

Lyon RH, DeJONG RG (1998) Statistical Energy Analysis. RH Lyon Corp

Schevenels M, Lazarov B, Sigmund O (2011) Robust topology optimization accounting for spatially varying manufacturing errors. Computational Methods for Applied Mechanical Engineering 200:3613–3627

Sigmund O (2009) Manufacturing tolerant topology optimization. Acta Mech Sinica 25:227–239

Svanberg K (1987) The method of moving asymptotes - a new method for structural optimization. Int J Numer Methods Eng 24:359–373

Wadbro E (2014) Analysis and design of acoustic transition sections for impedance matching and mode conversion. Structural and Multidiciplinary Optimization 50:395–408

Wadbro E, Berggren M (2006) Topology optimization of an acoustic horn. Computational Methods for Applied Mechanical Engineering 196:420–436

Wang F, Jensen JS, Sigmund O (2011a) Robust topology optimization of photonic crystal waveguides with tailored dispersion properties. Opt Soc Am 28:387–397

Wang F, Lazarov BS, Sigmund O (2011b) On projection methods, convergence and robust formulations in topology optimization. Structural Multidiciplinary Optimization 43:767–784

Xu S, Cai Y, Cheng G (2010) Volume preserving nonlinear density filter based on heaviside projections. Structural and Multidiciplinary Optimization 41:495–505

Yoon GH, Jensen JS, Sigmund O (2007) Topology optimization of acoustic-structure interaction problems using a mixed finite element formulation. Int J Numer Methods Eng 70:1049–1075

Publication [P3]

Experimental validation of a topology optimized acoustic cavity

Experimental validation of a topology optimized acoustic cavity

Rasmus E. Christiansen[a] and Ole Sigmund
Section for Solid Mechanics, Department of Mechanical Engineering, Technical University of Denmark (DTU), Building 404, Nils Koppels Allé, DK-2800 Kongens Lyngby, Denmark

Efren Fernandez-Grande
Acoustic Technology, Department of Electrical Engineering, Technical University of Denmark (DTU), Building 352, Oersteds Plads, DK-2800 Kongens Lyngby, Denmark

(Received 7 July 2015; revised 29 October 2015; accepted 5 November 2015; published online 8 December 2015)

This paper presents the experimental validation of an acoustic cavity designed using topology optimization with the goal of minimizing the sound pressure locally for monochromatic excitation. The presented results show good agreement between simulations and measurements. The effect of damping, errors in the production of the cavity, and variations in operating frequency is discussed and the importance of taking these factors into account in the modeling process is highlighted.
 [http://dx.doi.org/10.1121/1.4936905]

[FCS] Pages: 3470–3474

I. INTRODUCTION

Topology optimization,[1] is a method for creating designs optimized for specific objective functions without enforcing *a priori* restrictions on the design's topology. The method has been used in structural mechanics for more than two decades and has also been successfully applied to other areas of engineering such as fluid mechanics,[2] optics,[3] and acoustics.[4–7] Christiansen *et al.*[8] and Dühring *et al.*[9] have treated the application of topology optimization to the problem of minimizing the sound pressure locally in an acoustic cavity for monochromatic and polychromatic excitation. Despite the interest in applying topology optimization to problems in acoustics, to our knowledge only little work has been reported on the important step of experimentally validating optimized designs for acoustic problems, see, e.g., the work by Akl *et al.*[10] and Lee.[11] In this work we report on the experimental validation of a topology optimized design for an acoustic cavity. This problem was previously addressed by Christiansen *et al.*[8] using numerical simulations where the design was optimized to be robust toward small geometric variations that might occur during production or installation. The optimization objective is to provide a localized substantial reduction in pressure in a part of the cavity. Although the considered problem is of a rather academic nature, it is expected that the results regarding experimental validation, calibration of damping properties between experiments and numerical model as well as the study of robustness with respect to manufacturing uncertainties will be important for various real life acoustic design problems within internal automotive noise reduction, hearing aids, and other interior acoustic devices. The modeling approach, optimization problem, and experimental procedure are outlined, followed by numerical and experimental results.

II. THE MODEL PROBLEM

We consider the domain $\mathbf{\Omega} \subset \mathbb{R}^2$ shown in Fig. 1. The boundary of $\mathbf{\Omega}$, denoted $\delta\mathbf{\Omega}$, is assumed to be perfectly rigid (fully reflecting) except for the section $\delta\mathbf{\Omega_P}$ where a vibrational boundary condition is imposed, modeling a piston vibrating at a single frequency. We seek to minimize the average pressure magnitude, in $\mathbf{\Omega}_{\mathrm{OP}}$ by introducing solid material in $\mathbf{\Omega}_{\mathrm{d}}$. The experimental measurements of the sound pressure, p, were performed in $\mathbf{\Omega}_{\mathrm{M}}$.

The acoustic field is modeled using the Helmholtz equation along with the appropriate boundary conditions,

$$\begin{aligned} &\nabla \cdot (\rho(\mathbf{x})^{-1} \nabla p(\mathbf{x})) + \omega^2 \kappa(\mathbf{x})^{-1} p(\mathbf{x}) = 0, \quad \mathbf{x} \in \mathbf{\Omega}, \\ &\mathbf{n} \cdot (\rho(\mathbf{x})^{-1} \nabla p(\mathbf{x})) = \begin{cases} 0, & \forall \mathbf{x} \in \delta\mathbf{\Omega} \\ -\mathrm{i}\omega U, & \forall \mathbf{x} \in \delta\mathbf{\Omega_P}, \end{cases} \end{aligned} \tag{1}$$

where $\mathbf{x}$ denotes the spatial dependence, i is the imaginary unit, p is the sound pressure, $\omega = 2\pi f$ is the angular frequency, f is the frequency, and U is the vibrational velocity of the acoustic source, i.e., the particle velocity at $\delta\mathbf{\Omega_P}$. $\rho(\mathbf{x})$

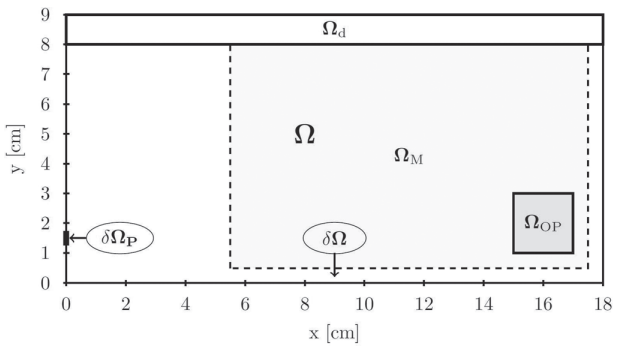

FIG. 1. Model problem diagram. All measures are given in centimeters. Domain: $\mathbf{\Omega} = [0, 18] \times [0, 9]$. Target sub-domain: $\mathbf{\Omega}_{\mathrm{OP}} = [15, 17] \times [1, 3]$. Design sub-domain: $\mathbf{\Omega}_{\mathrm{d}} = [0, 18] \times [8, 9]$. Experimental measurement sub-domain: $\mathbf{\Omega}_{\mathrm{M}} = [5.5, 17.5] \times [0.5, 7.5]$. Reflecting boundary: $\delta\mathbf{\Omega}$. Excitation boundary: $\delta\mathbf{\Omega_P} = 0 \times [1.3, 1.7]$.

[a]Electronic mail: raelch@mek.dtu.dk

and $\kappa(\mathbf{x})$ are the density and bulk modulus, respectively, which both depend on the material at point $\mathbf{x}$. The two materials considered are solid and air. The contrast in material parameters between solid and air is chosen such that no transverse waves of significant amplitude are excited in solid regions and consequently these waves are excluded from the model. Boundaries of solid regions thereby act nearly identically to perfectly reflecting boundaries. The values used for the density and bulk modulus of the air are $\rho = 1.205\,\mathrm{kg/m^3}$ and $\kappa = 1.42 \times 10^5\,\mathrm{Pa}$. This choice corresponds to 0% humidity, a temperature of 20 °C and a background pressure of 1 atm. The excitation frequency $f = 6.942\,\mathrm{kHz}$, corresponding to a natural frequency for the empty cavity, is considered. The vibrational velocity $U = 0.01\,\mathrm{m/s}$ for the acoustic input is used.

The application of a continuous optimization approach is facilitated by introducing the auxiliary density field, $\xi(\mathbf{x}) \in [0,1]\,\forall\,\mathbf{x} \in \boldsymbol{\Omega}_\mathrm{d}, \xi(\mathbf{x}) = 0\,\forall\,\mathbf{x} \in \boldsymbol{\Omega}\backslash\boldsymbol{\Omega}_\mathrm{d}$, to interpolate between the inverse material parameters for solid and air as $\rho(\xi)^{-1} = \rho_\mathrm{air}^{-1} + \xi(\rho_\mathrm{solid}^{-1} - \rho_\mathrm{air}^{-1})$ and $\kappa(\xi)^{-1} = \kappa_\mathrm{air}^{-1} + \xi(\kappa_\mathrm{solid}^{-1} - \kappa_\mathrm{air}^{-1})$. This material interpolation is chosen based on the work by Dühring *et al.*[9] It is the natural interpolation since the inverse material parameters appear directly in the Helmholtz equation. The minimization of the average pressure level in $\boldsymbol{\Omega}_\mathrm{OP}$ may be stated as the continuous optimization problem,

$$\begin{aligned} &\min_{\xi}.\ \Phi(\xi) = \frac{1}{\int d\boldsymbol{\Omega}_\mathrm{OP}} \int |p(\mathbf{x},\xi)|^2 d\boldsymbol{\Omega}_\mathrm{OP}, \\ &\text{s.t. } 0 \le \xi(\mathbf{x}) \le 1 \quad \forall\,\mathbf{x} \in \boldsymbol{\Omega}_\mathrm{d}, \end{aligned} \tag{2}$$

where $p(\mathbf{x},\xi)$ is obtained by solving Eq. (1) for a given realization of ξ. We used topology optimization in conjunction with adjoint sensitivity analysis and the gradient based optimization method, *The Method of Moving Asymptotes*,[12] to solve Eq. (2). For the optimization procedure we consider a modified version of Eq. (2) using filtering, including smoothing and projection with a continuation scheme on the projection strength. This approach results in near-perfect solid/void designs as a direct result of the optimization, thus limiting the need for post processing. In addition, the design has been optimized for both uniform and non-uniform perturbations of the geometry to assure high performance if any errors are introduced in the geometry during production, installation, or use. The stopping criteria used for in optimization process is $|\Phi_n - \max_{j\in n-10,\ldots,n-1}(\Phi_j)| < 0.01\Phi_n$, where Φ_n is the objective value at the nth iteration. The interested reader is referred to Christiansen *et al.*[8] for further details on the modeling and optimization process. To obtain the final design used as a blueprint for production a threshold at $\xi(\mathbf{x}) = 0.5$ is applied to the optimized design. For the design treated in the following below 0.2% of the optimized density distribution was composed of values different from either fully solid or fully air.

III. NUMERICAL RESULTS

The final design obtained from the optimization process, along with contours indicating the bounds of the uniform and non-uniform geometric perturbations for which the design was optimized, are shown in Fig. 2.

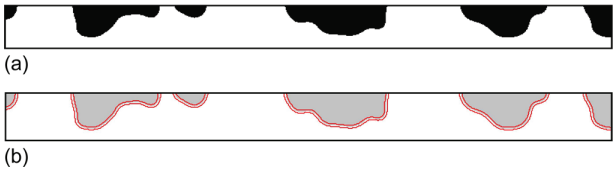

FIG. 2. (Color online) Design optimized for local pressure minimization in $\boldsymbol{\Omega}_\mathrm{OP}$ at $f = 6.942\,\mathrm{kHz}$ (corresponding to $\boldsymbol{\Omega}_\mathrm{d}$ in the acoustic cavity shown in Fig. 1). (a) Final design, black is solid and white is air. (b) Bounds on geometric perturbations considered in the optimization process. The final design is shown in gray and the bounds on the geometric perturbations considered in the optimization are outlined.

Figure 3(a) shows a plot of the simulated pressure field, reported in dB sound pressure level (SPL) ref 20 μPa, for the model problem given in Fig. 1 with the design presented in Fig. 2 introduced in $\boldsymbol{\Omega}_\mathrm{d}$. The pressure is seen to be significantly lowered in $\boldsymbol{\Omega}_\mathrm{OP}$ compared to the rest of $\boldsymbol{\Omega}$. Figure 3(b) shows the simulated pressure in the empty cavity. The average sound pressure in $\boldsymbol{\Omega}_\mathrm{OP}$ in the empty cavity is $\langle L\rangle_{\boldsymbol{\Omega}_\mathrm{OP,no\ design}} = 125$ dB, while this average is reduced to $\langle L\rangle_{\boldsymbol{\Omega}_\mathrm{OP,design}} = 44.9$ dB, when the design is introduced in $\boldsymbol{\Omega}_\mathrm{d}$.

An extruded three-dimensional (3D) model of the cavity containing the optimized design is created using COMSOL version 4.3b. The extrusion distance is chosen to be 0.6 cm which is large enough for experimental practicalities while remaining much smaller than the wavelength of the monochromatic excitation to assure that the pressure field remains two-dimensional (2D) inside the cavity (the cutoff frequency in the extruded dimension is around 30 kHz. Below the cutoff frequency the sound field in the cavity remains 2D). A full elasto-acoustic multi-physics model is applied to confirm the pressure field in the extruded cavity. The model accounts for acoustic waves in air regions and transverse elastic waves in solid regions. The material parameters of the solid are set to $\rho = 9.54 \times 10^2\,\mathrm{kg/m^3}$ and $\kappa = 1.9\,\mathrm{GPa}$, respectively, corresponding to measured values for the acrylonitrile butadiene styrene (ABS) plastic used for the fabrication. The investigation confirms that no transverse waves of significant amplitude are excited in the solid regions and that the pressure field remains 2D inside the cavity.

IV. EXPERIMENTAL RESULTS

A solid open faced version of the extruded design and cavity, shown in Fig. 4, is produced in ABS plastic using 3D-printing. The open faced cavity is produced in two parts to allow for testing multiple designs with ease. The top part contains the design while the bottom part consists of the remaining part of the cavity. The bottom part has a circular hole of 4 mm diameter on the side corresponding to the section $\delta\boldsymbol{\Omega}_\mathbf{P}$ shown in Fig. 1. The dimensions of the printed design are given in Table I.

The experimental setup, see Fig. 5, consists of the 3D-printed open face cavity placed face down on a 1 cm thick PVC plate with a 1/8 in. B&K microphone (Brüel & Kjær, Nærum, Denmark) flush mounted in its center. The cavity is movable, making it possible to scan the sound field inside it.

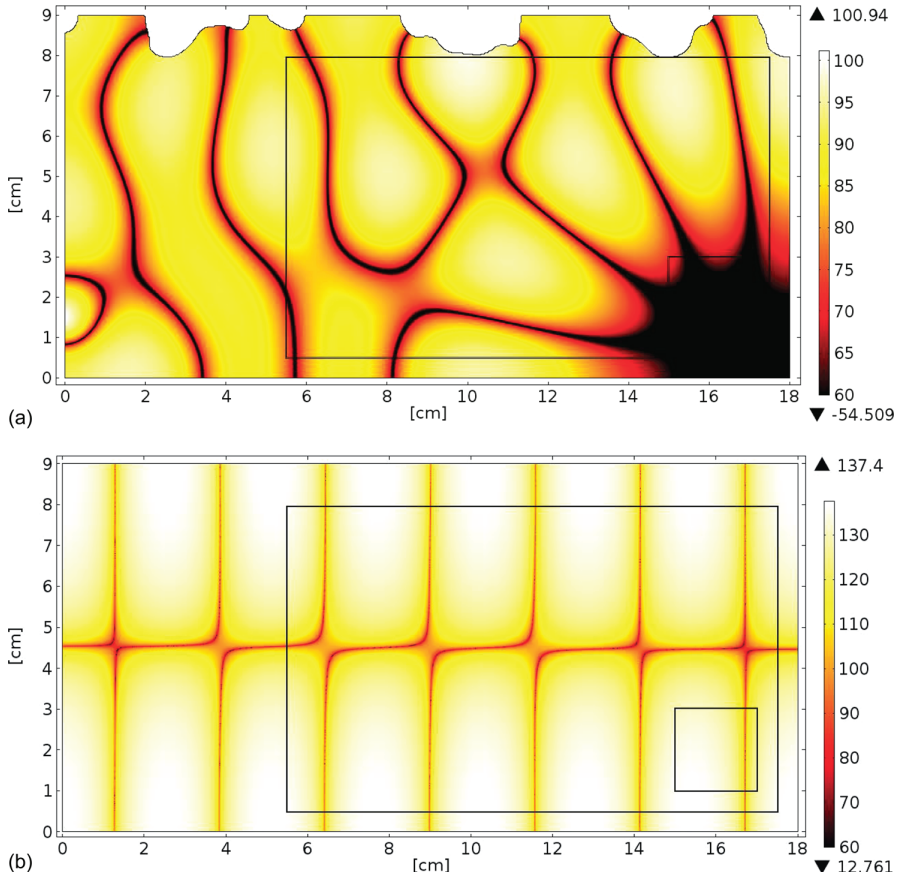

FIG. 3. (Color online) Simulated pressure [dB SPL ref 20 μPa] in the cavity at $f = 6.942$ kHz. $\mathbf{\Omega}_{\mathrm{M}}$ and $\mathbf{\Omega}_{\mathrm{OP}}$ are outlined using thin black lines. (a) Optimized design introduced. (b) Empty cavity. Note the difference in the maximal dB value between (a) and (b).

The source consists of a 3 in. loudspeaker (Tymphany, Sausalito, CA) connected to a waveguide that radiates into the cavity through the hole at $\delta\mathbf{\Omega}_{\mathbf{P}}$. The temperature and humidity are measured and the excitation frequency adjusted to account for perturbations of ρ and κ, compared to the values used in the simulation. This adjustment results in a frequency of, $f_{\mathrm{adj}} = 7.011$ kHz (monochromatic excitation). The microphone is connected to a B&K pulse analyzer. The pressure field is measured in a regular grid, in $\mathbf{\Omega}_{\mathrm{M}}$, with the inter-spacing between each measurement point being 5 mm in both spatial directions. The positioning of the scanning system is adjusted manually to within 0.5 mm accuracy for each measurement. The measurements are performed with a spectral resolution of 1 Hz centered at f_{adj}. The background noise level in the cavity was measured at 55 dB SPL providing a lower limit on the measurements and a way of estimating the signal-to-noise ratio.

FIG. 4. (Color online) Extruded 3D-printed design and cavity.

Figure 6(a) presents a contour plot of the measured sound pressure field in $\mathbf{\Omega}_{\mathrm{M}}$. For comparison Fig. 6(b) shows a contour plot of the simulated pressure field in $\mathbf{\Omega}_{\mathrm{M}}$, smoothed using a constant filter, with a radius of 1/16 in. ($\approx$0.159 cm), to mimic the resolution of the microphone, sampled at the positions where the experimental measurements were performed. The result presented in Fig. 6(b) is obtained from a simulation where the modeling domain dimensions are chosen to be identical to those of the 3D-printed open faced cavity to a precision of 0.02 cm (corresponding to the accuracy of the 3D-printer used for production). This change in the numerical model results in changes in the simulated pressure field compared to Fig. 3(a) mainly observable in low pressure regions. By comparing the measured result with the simulated result a good qualitative agreement is found. The position of the nodal lines and pressure maxima agree with only some discrepancy

TABLE I. Cavity and PVC plate data. The inner dimensions of the cavity without the design are reported to within 0.02 cm accuracy.

Component	(x,y,z)
Cavity (top), [cm]	$18.00 \times 2.00 \times 0.60$
Cavity (bottom), [cm]	$18.02 \times 7.00 \times 0.60$
Wall thickness [cm]	$1.2 \times 1.2 \times 1.0$
PVC plate [cm]	$40.0 \times 20.0 \times 1.0$

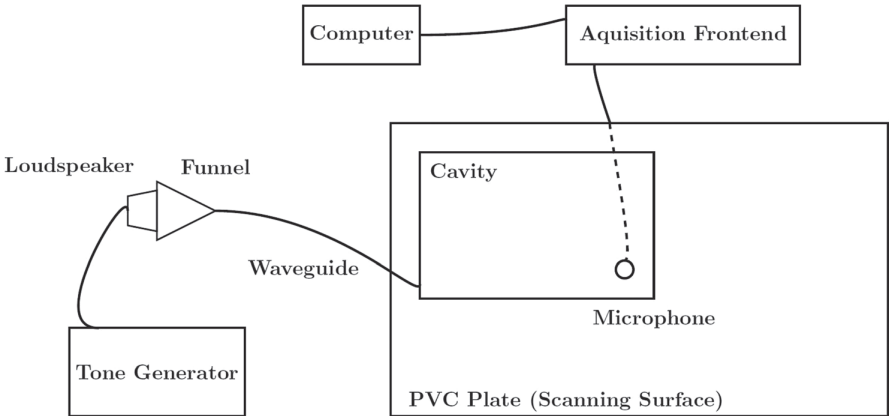

FIG. 5. Schematics illustrating the experimental setup. The cavity and PVC plate can slide relative to each other to scan the microphone across the cavity.

in the lower left and right corners of $\mathbf{\Omega}_{\mathrm{M}}$. A difference in the pressure magnitude close to nodal lines is observed. This difference can be explained partly by the background noise in the measurements, both due to transducer noise, and due to background noise in the measurements caused by sound being transmitted through the walls of the acoustic cavity. Also, close to the nodal lines, the sound field changes rapidly. Hence small positioning errors of the microphone result in significant deviations in the measured pressure. Finally the finite size of the microphone results in a spatial averaging, particularly notable around the nodal lines. As mentioned above, near $\mathbf{\Omega}_{\mathrm{OP}}$ and in the lower left corner of $\mathbf{\Omega}_{\mathrm{M}}$, there are noticeable discrepancies in the pressure field, with the measurement result showing a higher sound pressure. A reasonable explanation for the difference between the measured and simulated pressure field is the existence of damping in the physical cavity which was neglected in the simulation and optimization. In short, damping inside the rigid cavity occurs mostly because the process tends to be isothermal close to rigid walls, rather than adiabatic as is assumed in the derivation of the Helmholtz equation. In addition there are also viscous losses in the system. A description of damping for room acoustics may be found in Chapter 8 of the book by Jacobsen and Juhl.[13] To test this theory mass proportional damping is introduced in the computer model by adding the term $i\eta\omega p(\mathbf{x})$, to Eq. (1) where η is a freely chosen parameter. A parameter study for η is performed to find the amount of damping which provides the smallest discrepancies between the measurements and the simulation in $\mathbf{\Omega}_{\mathrm{M}}$. From this study $\eta = 0.02$ is obtained. Figure 6(c) shows a simulation result obtained using the mass proportional damping with $\eta = 0.02$. In this simulation the vibrational velocity is increased to $U = 0.013\,\mathrm{m/s}$ to account for the overall decrease in the sound pressure caused by the damping. Comparing the pressure field in Fig. 6(c) to the pressure fields in Figs. 6(a) and 6(b), a better overall agreement between simulation and measurement is found when damping is included. It is seen that the discrepancies between simulation and measurement in the area around $\mathbf{\Omega}_{\mathrm{OP}}$ and in the bottom left part of $\mathbf{\Omega}_{\mathrm{M}}$ have decreased significantly. In addition, a better agreement for the pressure along the nodal lines has been obtained. At the same time no significant deterioration in the agreement of the two results elsewhere in $\mathbf{\Omega}_{\mathrm{M}}$ is observed. This finding supports that the inclusion of mass proportional damping results in more realistic modeling for the investigated case of an extruded 2D cavity.

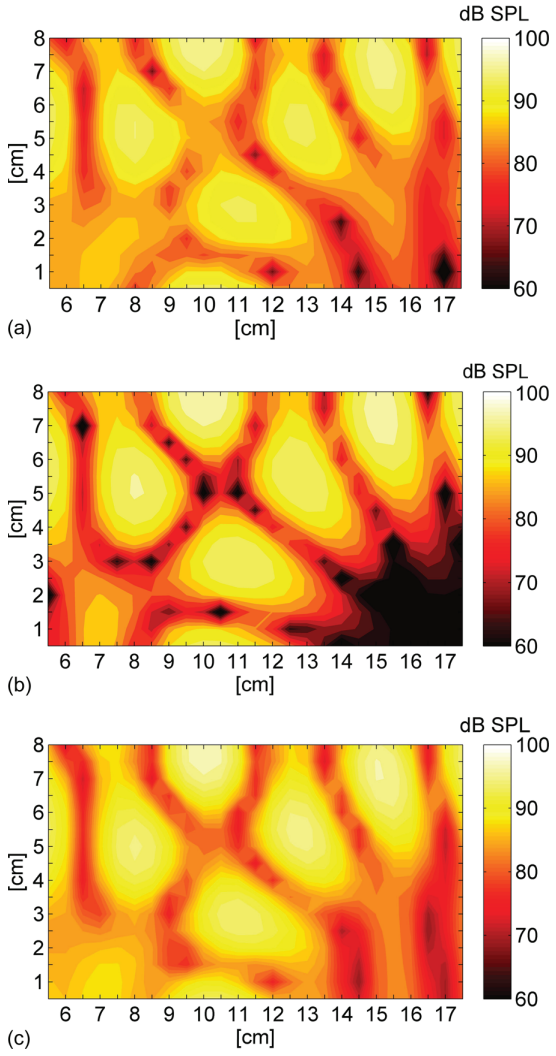

FIG. 6. (Color online) Contour plot of sound pressure field in $\mathbf{\Omega}_{\mathrm{M}}$. (a) Experimentally measured field for the 3D-printed acoustic cavity. (b) Simulated field. (c) Simulated field with mass proportional damping. (b) and (c) The field is smoothed with a constant filter with 1/16 in. (≈0.159 cm) radius, sampled at the measurement positions.

In addition to the possible effect of damping, the discrepancy between the undamped simulation result and the

measurements may be caused by the following. The model problem is sensitive to geometric perturbations of the cavity elsewhere than in $\mathbf{\Omega}_\mathrm{d}$, as seen from the difference in $\langle L\rangle_{\mathbf{\Omega}_{\mathrm{OP,sim}}}$ between the result presented in Fig. 6(b) and the result presented in Fig. 3(a). The problem is also sensitive toward the source position and the operating frequency. The sensitivity toward the operating frequency was observed from measurements performed without the adjustment of the operating frequency from $f = 6.942\,\mathrm{kHz}$ to $f_\mathrm{adj} = 7.011\,\mathrm{kHz}$ where the performance of the design decreased in terms of the value of $\langle L\rangle_{\mathbf{\Omega}_{\mathrm{OP,sim}}}$ (not shown). This sensitivity is due to the main effect responsible for producing a localized low sound pressure being the alignment of nodal lines in $\mathbf{\Omega}_\mathrm{OP}$. Such an alignment is highly sensitive to small changes in geometry, frequency, and source position.

The average sound pressure in Ω_OP for the experimental measurement is $\langle L\rangle_{\mathbf{\Omega}_{\mathrm{OP,mea}}} \approx 78.6$ dB. From the simulation result reported in Fig. 6(b), $\{L\}_{\mathbf{\Omega}_{\mathrm{OP,sim}}} = 59.1$ dB, is obtained, while for the simulation including the damping it is $\langle L\rangle_{\mathbf{\Omega}_{\mathrm{OP,sim,damp}}} \approx 78.1$ dB. The difference between $\langle L\rangle_{\mathbf{\Omega}_{\mathrm{OP,sim}}}$ and $\langle L\rangle_{\mathbf{\Omega}_{\mathrm{OP,mea}}}$ is approximately 19.5 dB whereas this difference between $\langle L\rangle_{\mathbf{\Omega}_{\mathrm{OP,sim,damp}}}$ and $\langle L\rangle_{\mathbf{\Omega}_{\mathrm{OP,mea}}}$ is 0.5 dB. In spite of the difference between $\langle L\rangle_{\mathbf{\Omega}_{\mathrm{OP,sim}}}$ and $\langle L\rangle_{\mathbf{\Omega}_{\mathrm{OP,mea}}}$, the experimentally verified reduction in sound pressure in $\mathbf{\Omega}_\mathrm{OP}$ is still significant compared to the sound pressure elsewhere in the cavity and to the sound pressure in the empty cavity, see Fig. 3(b).

As general lessons to be learned with regards to using topology optimization for acoustic design problems we list the following. To minimize the discrepancy between the predicted and experimental performance of the design it is suggested to take manufacturing uncertainties and uncertainties in other model parameters into account in the modeling process. For example, accounting for small changes in the operating frequency which may be caused by changes in humidity and/or temperature. It is also suggested to include an amount of damping in the model corresponding to experimental findings. Using these suggestions may allow the final design to maintain the predicted performance under a range of varying real world operating conditions. The focus of the present study was on experimentally validating a design, created using topology optimization, optimized to perform well under a range of geometric perturbations, under monochromatic excitation. It is straight forward to extend the topology optimization method applied in this paper to wider frequency bands. As the frequency band is widened the sensitivity of the average response in $\mathbf{\Omega}_\mathrm{OP}$ to geometric variations and the possible reduction in sound pressure are both expected to be reduced, cf. Ref. 8.

V. CONCLUSION

An approach for experimentally measuring the pressure field in a 2D acoustic cavity was presented. An optimized design created using topology optimization was tested and good agreement between the simulated and the measured pressure field was shown. The presented results illustrate the usefulness of the approach as a tool for designing acoustic cavities for local pressure minimization. A description of the steps needed to assure that the physical design functions as predicted by the pure acoustic model was outlined. It was furthermore shown that adding mass proportional damping to the mathematical model improves the agreement between simulation and measurement, suggesting the inclusion of damping in the design process will result in a better agreement between predicted and measured results. Finally it was highlighted that the inclusion of manufacturing uncertainties and operating conditions in the design process is important to minimize the discrepancies between the mathematical model and the final physical design when considering sensitive problems.

ACKNOWLEDGMENTS

The 3D-printing laboratory FabLab at the Technical University of Denmark produced the optimized design and acoustic cavity. Assistant Engineer Jørgen Rasmussen at the Department of Electrical Engineering at the Technical University of Denmark helped with preparing the experiment. Niklas Flink Hansen and Peter Toftemann performed the measurements of the material parameters for the ABS plastic used in the 3D-printing process. The work was financially supported by Villum Fonden through the research project *Topology Optimization - the Next Generation* (*NextOpt*).

[1]M. P. Bendsøe and O. Sigmund, *Topology Optimization*, 2nd ed. (Springer-Verlag, Berlin Heidelberg, 2003), 370 pp.
[2]T. Borrvall and J. Petersson, "Topology optimization of fluid in stokes flow," Int. J. Numer. Methods Fluids **41**, 77–107 (2003).
[3]J. S. Jensen and O. Sigmund, "Topology optimization for nano-photonics," Laser Photonics Rev. **5**, 308–321 (2011).
[4]J. Kook, K. Koo, J. Hyun, J. S. Jensen, and S. Wang, "Acoustical topology optimization for Zwicker's loudness model—Application to noise barriers," Comput. Methods Appl. Mech. Eng. **237**, 130–151 (2012).
[5]J. W. Lee and Y. Y. Kim, "Rigid body modeling issue in acoustic topology optimization," Comput. Methods Appl. Mech. Eng. **198**, 1017–1030 (2009).
[6]E. Wadbro, "Analysis and design of acoustic transition sections for impedance matching and mode conversion," Struct. Multidiscipl. Optimization **50**, 395–408 (2014).
[7]E. Wadbro and M. Berggren, "Topology optimization of an acoustic horn," Comput. Methods Appl. Mech. Eng. **196**, 420–436 (2006).
[8]R. E. Christiansen, B. S. Lazarov, J. S. Jensen, and O. Sigmund, "Creating geometrically robust designs for highly sensitive problems using topology optimization—acoustic cavity design," Struct. Multidiscipl. Optimization **52**, 737–754 (2015).
[9]M. B. Dühring, J. S. Jensen, and O. Sigmund, "Acoustic design by topology optimization," J. Sound Vib. **317**, 557–575 (2008).
[10]W. Akl, A. El-Sabbagh, K. Al-Mitani, and A. Baz, "Topology optimization of a plate coupled with acoustic cavity," Int. J. Solids Struct. **46**, 2060–2074 (2009).
[11]J. W. Lee, "Optimal topology of reactive muffler achieving target transmission loss values: Design and experiment," Appl. Acoust. **88**, 104–113 (2015).
[12]K. Svanberg, "The method of moving asymptotes—a new method for structural optimization," Int. J. Numer. Methods Eng. **24**, 359–373 (1987).
[13]F. Jacobsen and P. M. Juhl, *Fundamentals of General Linear Acoustics* (John Wiley & Sons, Ltd., Chichester, UK, 2013), pp. 127–157.

Publication [P4]

Designing meta material slabs exhibiting negative refraction using topology optimization

Struct Multidisc Optim (2016) 54:469–482
DOI 10.1007/s00158-016-1411-8

RESEARCH PAPER

Designing meta material slabs exhibiting negative refraction using topology optimization

Rasmus E. Christiansen[1] · **Ole Sigmund**[1]

Received: 20 August 2015 / Revised: 16 December 2015 / Accepted: 27 January 2016 / Published online: 18 March 2016

Abstract This paper proposes a topology optimization based approach for designing meta materials exhibiting a desired negative refraction with high transmission at a given angle of incidence and frequency. The approach considers a finite slab of meta material consisting of axis-symmetric designable unit cells subjected to an exterior field. The unit cell is designed to achieve the desired properties based on tailoring the response of the meta material slab under the exterior field. The approach is directly applicable to physical problems modeled by the Helmholtz equation, such as acoustic, elastic and electromagnetic wave problems. Acoustic meta materials with unit cell size on the order of half the wave length are considered as examples. Optimized designs are presented and their performance under varying frequency and angle of incidence is investigated.

Keywords Topology optimization · Negative refraction · Wave propagation · Meta materials · Acoustics · Electromagnetics · Elastics

1 Introduction

In this paper the negative refraction of waves at a material interface is understood from Snell's law and the refractive index, n, is defined accordingly. This is not identical to the definition $n = c/c_p$, where c is the wave speed in vacuum and c_p is the wave phase velocity in the material.

Materials exhibiting negative refraction of acoustic, elastic or electromagnetic waves have been of great interest over the last decades, see e.g. Krowne and Zhang (2007) and Craster and Guenneau (2013) for an introduction to and overview of the topic. The work by Pendry (2000) discussing the application of materials exhibiting negative refraction in designing a perfect optical lens was instrumental in sparking the interest in negative refraction. Another reason for the interest is that a material exhibiting this behavior may simultaneously have negative material parameters, as first discussed theoretically for the electromagnetic case by Veselago (1968). Having access to materials exhibiting negative refraction and to materials with negative material parameters, and even better being able to fine-tune the behavior of such materials, opens up a range of new possibilities in science and engineering by offering a new way of manipulating fields. The most studied example being improvements in focusing and lensing, see e.g. Mills et al. (2003), Xu et al. (2013), and Zhang et al. (2009).

Materials exhibiting negative refraction and/or having negative material parameters are not readily available in nature however. Therefore so called meta materials (MMs) consisting of an array of unit cells with the desired properties must be created artificially through careful design. A vast amount of research has gone into understanding and designing MMs with negative material parameters and MMs exhibiting negative refraction, see e.g. Zhang and Liu (2004), Zhang et al. (2005), and Philippe et al. (2015) for examples for acoustic, electromagnetic and elastic waves respectively.

✉ Rasmus E. Christiansen
raelch@mek.dtu.dk

[1] Department of Mechanical Engineering, Solid Mechanics, Technical University of Denmark, Nils Koppels Allé, B. 404, DK-2800 Lyngby, Denmark

In most previous work the design of the MMs has relied on a range of simplifying assumptions for the model problem used to model the physics under consideration, such as: Homogenization techniques where effective parameters for the MM can be extracted from a given unit cell design, which are only strictly valid when the unit cell size is much smaller than the wave length; Considering a single unit cell with the assumptions of an infinitely periodic MM hereby neglecting any edge effects at interfaces; Considering band diagrams and identifying a (k, ω)-range with negative slope under the assumption that only a single mode is excited inside the MM, hereby disregarding more complex wave interactions inside the MM.

In this work a novel approach to the problem of designing meta material slabs exhibiting negative refraction is suggested. The approach is based on applying topology optimization, Bendsøe and Sigmund (2003), to determine the material distribution inside the unit cells of the MM in order to achieve the desired property. Whereas most other publications on the topic have assumed either infinite periodicity or have based their meta material design on the evaluation of transmission studies through just one layer of unit cells, we here base our designs on finite slabs with arbitrary numbers of layers and model the full wave field impinging on the slab. In this way both edge effects of the slab as well as the complete field inside the MM are automatically accounted for in the design process. When applied successfully, the proposed approach allows for the design of MM slabs exhibiting a desired negative refraction to within a $\approx$ 10 % − 20 % margin of error with a transmittance through the full slab of more than 95 % for a given incoming angle and frequency. Previous work applying topology optimization as a tool for designing MMs exhibiting effective negative parameters include, Diaz and Sigmund (2009), Zhou et al. (2010), and Lu et al. (2013). Other interesting recent applications of topology optimization for designing MMs with exotic behavior include the work by Park et al. (2015) on self collimating phononic crystals and the work by Andkjær and Sigmund (2013) on designing cloaks for acoustics and electromagnetics.

Although this paper presents examples for two dimensional acoustics the approach has also successfully been tested for designing MMs exhibiting negative refraction for both TE and TM polarized electromagnetic waves and shear waves in solids, in two dimensions. During the testing it was found that problems with high contrast in material parameters, such as the acoustic case treated here, are the most challenging to treat. Except for computational limitations, the method is not restricted to two dimensions.

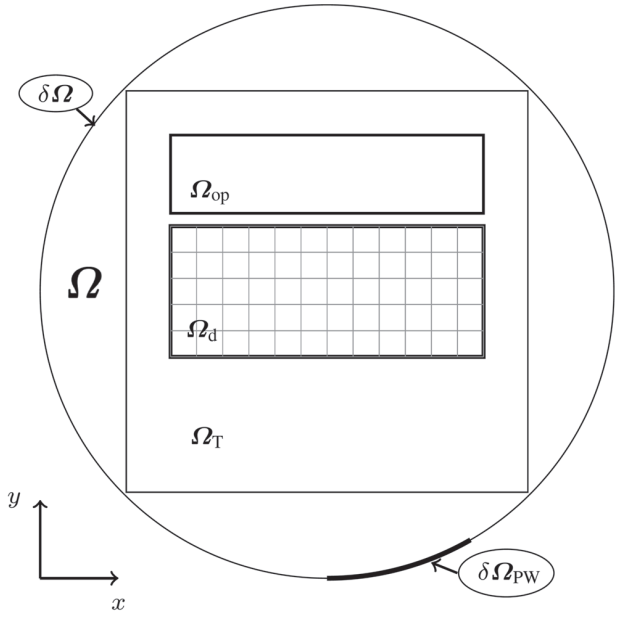

Fig. 1 Model problem sketch. $\boldsymbol{\Omega}$: Truncated Domain. $\boldsymbol{\Omega}_{\text{op}}$: Optimization domain. $\boldsymbol{\Omega}_{\text{d}}$: Design domain. $\delta\boldsymbol{\Omega}$: Truncated Domain boundary. $\delta\boldsymbol{\Omega}_{\text{PW}}$: Excitation boundary

2 The model problem

Consider an exterior wave problem governed by the Helmholtz equation (1), defined on the domain, $\boldsymbol{\Omega} \subset \mathbb{R}^2$, illustrated in Fig. 1.

$\boldsymbol{\Omega}$ is truncated by the curve $\delta\boldsymbol{\Omega}$, along which a far field matching condition is imposed to fulfill the Sommerfeld radiation condition (2) corresponding to perfectly absorbing boundary conditions. A boundary condition (3) is imposed along a section of $\delta\boldsymbol{\Omega}$, denoted $\delta\boldsymbol{\Omega}_{\text{PW}}$ in order to excite a localized plane wave entering and traveling through $\boldsymbol{\Omega}$. For use in the optimization problem two subdomains, $\boldsymbol{\Omega}_{\text{d}}$ and $\boldsymbol{\Omega}_{\text{OP}}$ are defined. $\boldsymbol{\Omega}_{\text{d}}$ denotes the design domain and is where the designable MM slab consisting of an array of axis symmetric unit cells is placed. $\boldsymbol{\Omega}_{\text{OP}}$ denotes the optimization domain and is where the objective function for the optimization problem is defined. $\boldsymbol{\Omega}_{\text{T}}$ denotes the truncated modeling domain used when displaying the solution field and design. The model problem can be written as

$$\nabla \cdot \left(\frac{1}{\alpha(\mathbf{x})} \nabla \psi(\mathbf{x}) \right) + \omega^2 \frac{1}{\gamma(\mathbf{x})} \psi(\mathbf{x}) = 0, \quad \mathbf{x} \in \boldsymbol{\Omega}, \tag{1}$$

$$\lim_{|\mathbf{r}| \to \infty} \sqrt{|\mathbf{r}|} \cdot \left(\frac{\partial \psi(\mathbf{r})}{\partial |\mathbf{r}|} + \mathrm{i}\omega \cdot \sqrt{\frac{\alpha}{\gamma}} \psi(\mathbf{r}) \right) = 0, \quad \mathbf{x} \in \delta\boldsymbol{\Omega}, \tag{2}$$

$$\mathbf{n} \cdot \left(\frac{1}{\alpha(\mathbf{x})} \nabla \psi \right) = a_n, \ \mathbf{x} \in \delta\boldsymbol{\Omega}_{\text{PW}}. \tag{3}$$

In (1)-(3) $\mathbf{x}$ and $\mathbf{r}$ denote the spatial dependence in Cartesian and polar coordinates respectively, i is the imaginary

unit, ψ is the field of interest, $\omega = 2\pi f$ is the angular frequency with f being the frequency. $\alpha(\mathbf{x})$ and $\gamma(\mathbf{x})$ are material parameters and depend on the material at the point $\mathbf{x}$. Finally a_n is calculated by prescribing a known ψ on $\delta\boldsymbol{\Omega}_{\text{PW}}$ using the following expression describing a Gaussian shaped plane wave

$$\psi_{\text{GPW}} = \mathrm{e}^{-\left(\frac{(\mathbf{x}-\mathbf{x}_w)\cdot\hat{\mathbf{d}}}{\delta_x}\right)^2} \mathrm{e}^{-\mathrm{i}\hat{\omega}(\mathbf{x}\cdot\mathbf{d})}, \tag{4}$$

$$\mathbf{d} = \begin{pmatrix} \cos(\pi/2+\theta) \\ \sin(\pi/2+\theta) \end{pmatrix}, \quad \mathbf{x}_w = \begin{pmatrix} x_w \\ y_w \end{pmatrix}. \tag{5}$$

Here δ_x controls the width of the Gaussian envelope, $\mathbf{d}$ controls the propagation direction of the wave, $\hat{\mathbf{d}}$ denotes the transpose direction vector, finally $\mathbf{x}_w$ controls the position of the center of the wave. Henceforth the spatial dependence of quantities is suppressed for brevity, except when needed. See Fig. 2 for a simplified sketch of the solution of (1)-(3) superimposed on $\boldsymbol{\Omega}$ in light gray, given the imposition of (4) on $\delta\boldsymbol{\Omega}_{\text{PW}}$ with an empty $\boldsymbol{\Omega}_{\text{d}}$. Note that $\theta = \theta_1$ is measured positively as illustrated in Fig. 2.

For the examples treated in this paper the model problem is non-dimensionalized and rescaled as

$$\hat{\alpha} = \begin{cases} 1 & \text{void} \\ \frac{\alpha_{\text{solid}}}{\alpha_{\text{void}}} & \text{solid} \end{cases}, \quad \hat{\gamma} = \begin{cases} 1 & \text{void} \\ \frac{\gamma_{\text{solid}}}{\gamma_{\text{void}}} & \text{solid} \end{cases}, \quad \hat{\omega} = \frac{\omega}{c}. \tag{6}$$

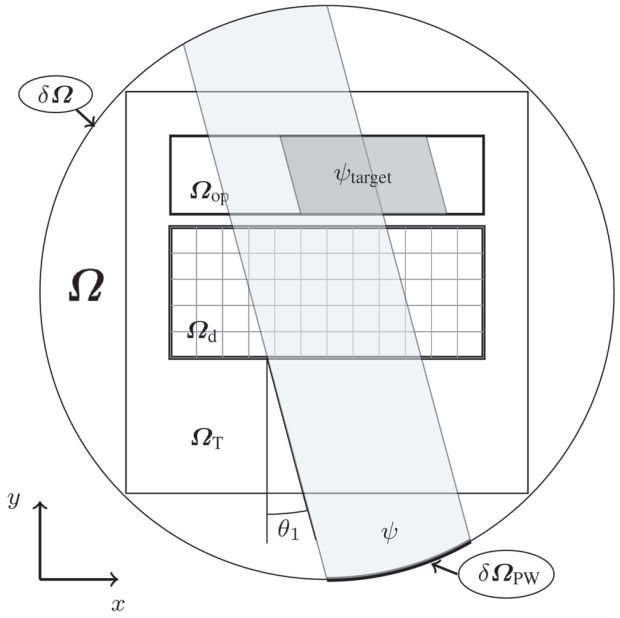

Fig. 2 ψ: Enveloped plane wave (Solution to (1)-(3)) and ψ_{target}: Target wave, overlaid on modeling domain. $\boldsymbol{\Omega}$: Truncated Domain. $\boldsymbol{\Omega}_{\text{op}}$: Optimization domain. $\boldsymbol{\Omega}_{\text{d}}$: Design domain. $\delta\boldsymbol{\Omega}$: Truncated Domain boundary. $\delta\boldsymbol{\Omega}_{\text{PW}}$: Excitation boundary

Here $c \equiv 1$ is a normalized and non-dimensional wave speed. For the acoustic problem treated in the paper, ψ is the sound pressure while $\alpha = \rho$ and $\gamma = \kappa$ are the density and the bulk modulus, respectively. Each position in space may either consist of a solid perfectly reflecting material or void (air). For the elastic case, ψ is the displacement field while α and γ relate to the density and shear modulus. For the transverse electromagnetic cases ψ is either the electric or magnetic field while α and γ relate to the electric permeability and permittivity.

2.1 Discretization

For the simulation results presented in this work the model problem is discretized using a hybrid wave based method and a finite element method (hybrid WBM-FEM method), developed for acoustic problems modeled using the Helmholtz equation in 2D and 3D, Desmet (1998) and Pluymers (2006). The method has previously been applied for topology optimization by Goo et al. (2014) and Christiansen et al. (2015b). The design domain, $\boldsymbol{\Omega}_{\text{d}}$, is discretized using $\mathcal{N}_e$ bi-linear finite elements and the rest of the domain, $\boldsymbol{\Omega}\backslash\boldsymbol{\Omega}_{\text{d}}$ is discretized using the wave based method. The two disjoint subdomains are coupled using an indirect impedance coupling described in chapter 7 of Pluymers (2006). The far field boundary condition is implemented using the method proposed in chapter 6 of Pluymers (2006). Although the hybrid WBM-FEM method is more complex to implement than a pure FEM method and has certain restrictions, it has the strength that very few degrees of freedom are needed in the WBM part of the domain. This significantly reduces the size of the linear system to be solved to obtain ψ hereby saving significant computational resources.

3 The optimization problem

The proposed approach applies topology optimization as the tool for designing the meta material slabs and consists of formulating and solving a constrained optimization problem. The objective of the problem is to minimize the amplitude difference between a target enveloped plane wave, ψ_{target} (illustrated in Fig. 2 using dark gray), and ψ, the solution of (1)-(3) over $\boldsymbol{\Omega}_{\text{OP}}$. This difference is minimized by introducing a periodic array of axis-symmetric identical unit cells in $\boldsymbol{\Omega}_{\text{d}}$ (the MM slab). The chosen ψ_{target} takes the form given in (4) with identical direction, $\mathbf{d}$, and width, $\delta_{x_{\text{target}}}$, as the wave generated by the imposed boundary condition on $\delta\boldsymbol{\Omega}_{\text{PW}}$. The position of the center of ψ_{target}, $\mathbf{x}_{w_{\text{target}}}$, is chosen based on the desired refractive index, n for a given θ_1 using (22) in Section 4.

The objective function, Φ, to be minimized, is formulated based on the standard deviation, $\mathbf{STD}(x)$, between $|\psi|^2$ and $|\psi_{\text{target}}|^2$ and is defined on $\boldsymbol{\Omega}_{\text{OP}}$ as

$$\Phi = c_s \cdot \underset{\boldsymbol{\Omega}_{\text{OP}}}{\mathbf{STD}}\left(|\psi|^2 - |\psi_{\text{target}}|^2\right), \tag{7}$$

$$\underset{\boldsymbol{\Omega}_{\text{OP}}}{\mathbf{STD}}(x) = c_s \cdot \frac{\int \left(x - \frac{\int x \, d\boldsymbol{\Omega}_{\text{OP}}}{\int d\boldsymbol{\Omega}_{\text{OP}}}\right)^2 d\boldsymbol{\Omega}_{\text{OP}}}{\int d\boldsymbol{\Omega}_{\text{OP}}}, \tag{8}$$

where c_s is a scaling parameter used to adjust the magnitude of Φ to improve the performance of the optimization algorithm. If Φ reaches a very low value it is beneficial to modify it by applying the natural logarithm to further improve the performance of the optimization algorithm.

The discrete optimization problem of minimizing Φ by placing solid material in $\boldsymbol{\Omega}_{\text{d}}$ is replaced by a continuous optimization problem through the introduction of an auxiliary design field, $\xi(\mathbf{x}) \in [0, 1] \; \forall \; \mathbf{x} \in \boldsymbol{\Omega}_{\text{d}}, \xi(\mathbf{x}) = 0 \; \forall \; \mathbf{x} \in \boldsymbol{\Omega} \backslash \boldsymbol{\Omega}_{\text{d}}$. This field is used to interpolate between the inverse material parameters for solid and void as, $\hat{\alpha}(\xi)^{-1} = \alpha_{\text{void}}^{-1} + \xi\left(\alpha_{\text{solid}}^{-1} - \alpha_{\text{void}}^{-1}\right)$ and $\hat{\gamma}(\xi)^{-1} = \gamma_{\text{void}}^{-1} + \xi\left(\gamma_{\text{solid}}^{-1} - \gamma_{\text{void}}^{-1}\right)$, which allows for a continuous transition between solid and void at a given position in space. This material interpolation agrees with the choice by Dühring et al. (2008) and is natural for the acoustic case since the inverse material parameters appear directly in the Helmholtz equation (1). The design field, ξ, is discretized into a piecewise constant field leading to a finite number of design variables (one per finite element used to discretize $\boldsymbol{\Omega}_{\text{OP}}, \mathcal{N}_e$), i.e.

$$\xi = \sum_{i \in \mathcal{N}_e} \xi_i, \quad \xi_i = \begin{cases} [0, 1] & \text{in the } i\text{'th finite element} \\ 0 & \text{elsewhere} \end{cases} \tag{9}$$

the design field of one unit cell is mapped to all the other unit cells. A volume constraint (11) is imposed on the amount of material that may be used in the design and the continuous optimization problem is stated as a min/max problem (10) allowing for optimizing for multiple frequencies and multiple angles of incidence simultaneously.

$$\min_{\xi} \max_{\theta_1, f} \left(\Phi(\psi(\mathbf{x}, \xi, \theta_1, f), \psi_{\text{target}}(\mathbf{x}, \theta_1, f)) \right), \tag{10}$$

$$\text{s.t.} \; \frac{1}{A_{\boldsymbol{\Omega}_{\text{d}}}} \int \xi \; \text{d}\boldsymbol{\Omega}_{\text{d}} \leq V, \quad V \in]0, 1], \; A_{\boldsymbol{\Omega}_{\text{d}}} = \int \text{d}\boldsymbol{\Omega}_{\text{d}} \tag{11}$$

Here $\psi(\mathbf{x}, \xi, \theta_1, f)$ is obtained by solving (1)-(3) for a given realization of ξ, θ_1 and f while $\psi_{\text{target}}(\mathbf{x}, \theta_1, f)$ is calculated using (4)-(5).

The optimization problem (10)-(11) is recast to the standard bound-formulation presented in (2.3) in Svanberg (2002) and solved accordingly using *The Globally Convergent Method of Moving Asymptotes* (GCMMA) (Svanberg 1987; 2002), by selecting the appropriate constants in the call to GCMMA. A maximum of 3 inner iterations per outer iteration and move limits on ξ_i of 0.05 for each outer iteration are used. The gradient information, $\frac{\text{d}\Phi}{\text{d}\xi_i}$, needed in the optimization, (12)-(13), is obtained by calculating the sensitivites of Φ towards changes in ξ using discrete adjoint sensitivity analysis, see (Dühring et al. 2008) and references therein,

$$\frac{\text{d}\Phi}{\text{d}\xi_i} = \frac{\partial \Phi}{\partial \xi_i} + \Re\left(\boldsymbol{\lambda}^{\text{T}} \frac{\partial \mathbf{S}}{\partial \xi_i} \boldsymbol{\psi}\right), \quad \mathbf{S}^T \boldsymbol{\lambda} = -\left(\frac{\boldsymbol{\delta \Phi}}{\boldsymbol{\delta \psi}}\right)^{\text{T}}. \tag{12}$$

The j'th component of $\left(\frac{\boldsymbol{\delta \Phi}}{\boldsymbol{\delta \psi}}\right)^{\text{T}}$ is given as

$$\left(\frac{\boldsymbol{\delta \Phi}}{\boldsymbol{\delta \psi}}\right)_j = \left(\frac{\partial \Phi}{\partial \psi_{R_j}} - \text{i}\frac{\partial \Phi}{\partial \psi_{I_j}}\right) = 4 \cdot c_s \cdot \frac{1}{\int d\boldsymbol{\Omega}_{\text{OP}}} \cdot \tag{13}$$

$$\int \left((|\psi|^2 - |\psi_{\text{target}}|^2) - \frac{\int (|\psi|^2 - |\psi_{\text{target}}|^2) d\boldsymbol{\Omega}_{\text{OP}}}{\int d\boldsymbol{\Omega}_{\text{OP}}} \right) \cdot$$

$$\left(\phi_j \overline{\psi} - \frac{\int (\phi_i \overline{\psi}) d\boldsymbol{\Omega}_{\text{OP}}}{\int d\boldsymbol{\Omega}_{\text{OP}}} \right) d\boldsymbol{\Omega}_{\text{OP}}.$$

In (12)-(13) $\mathbf{S}$ is the discretized system matrix for (1)-(3), $\boldsymbol{\psi}$ is the solution vector for the discrete problem $\mathbf{S}\boldsymbol{\psi} = \mathbf{f}$ and $\mathbf{f}$ is introduced by the boundary conditions (2)-(3) as well as the coupling between the FEM and WBM subdomains. ϕ_j is the j'th basis function used to represent the solution, $\psi = \sum_j \psi_j \phi_j$, with $\psi_j = \psi_{R_j} + \text{j}\psi_{I_i}$. Finally $\bar{\cdot}$ denotes the complex conjugate.

To assure that the final design is physically admissible, i.e. consisting purely of solid and void regions, a projection operator along with a smoothing filter is applied to the design field, Guest et al. (2004), Xu et al. (2010), and Wang et al. (2011). The projection operator is given as

$$\hat{\tilde{\xi}}(\tilde{\xi}) = \frac{\tanh(\beta\eta) + \tanh(\beta(\tilde{\xi} - \eta))}{\tanh(\beta\eta) + \tanh(\beta(1 - \eta))}. \tag{14}$$

where η is the projection level and β is the projection strength. A continuation scheme for β is applied, where $\beta = 1$ is used initially and β is doubled every 25 iterations or whenever the objective value changes less than 10^{-3} of the previous objective value for 5 consecutive iterations. The smoothing filter is given as

$$\tilde{\xi}(\mathbf{x}_i) = \frac{\int_{\boldsymbol{\Omega}_{\text{d}}} w(\mathbf{x}_i - \mathbf{x}_j) \xi(\mathbf{x}_j) \text{d}\mathbf{x}_j}{\int_{\boldsymbol{\Omega}_{\text{d}}} w(\mathbf{x}_i - \mathbf{x}_j) \text{d}\mathbf{x}_j}, \tag{15}$$

$$w(\mathbf{x}) = \begin{cases} R - |\mathbf{x}| & \forall \; |\mathbf{x}| \leq R \wedge \mathbf{x} \in \boldsymbol{\Omega}_{\text{d}} \\ 0 & \text{otherwise} \end{cases}, \tag{16}$$

where R is the filter radius.

The application of the smoothing and projection on ξ means that instead of interpolating the material parameters, α^{-1} and γ^{-1} using ξ, the smoothed and projected field $\hat{\tilde{\xi}}$ is used.

The application of the smoothing filter and projection operator requires a modification of the sensitivities given as

$$\frac{\mathrm{d}\Phi}{\mathrm{d}\xi_i} = \sum_{h\in\mathcal{B}_{e,i}} \frac{\partial\tilde{\xi}_h}{\partial\xi_i}\frac{\partial\hat{\tilde{\xi}}_h}{\partial\tilde{\xi}_h}\frac{\mathrm{d}\Phi}{\mathrm{d}\hat{\tilde{\xi}}_h}, \tag{17}$$

$$\frac{\partial\tilde{\xi}_h}{\partial\xi_i} = \frac{w(\mathbf{x}_h-\mathbf{x}_i)A_i}{\sum_{j\in\mathcal{B}_{e,h}} w(\mathbf{x}_h-\mathbf{x}_j)A_j}, \tag{18}$$

$$\frac{\partial\hat{\tilde{\xi}}_h}{\partial\tilde{\xi}_h} = \frac{\beta\,\mathrm{sech}^2(\beta(\tilde{\xi}_h-\eta))}{\tanh(\beta\eta)+\tanh(\beta(1-\eta))}. \tag{19}$$

Here $\mathcal{B}_{e,i}$ denotes the indices of the design variables, ξ_e, which are within the filter radius of design variable ξ_i, $\mathbf{x}_{(\cdot)}$ denotes the coordinate of the center of element $(\cdot)$ and $A_{(\cdot)}$ is the area of the $(\cdot)$'th finite element.

The final stopping criterion used in the optimization procedure is given as

$$\beta > 1000 \wedge |\Phi_{n+1}-\Phi_n| < 10^{-3}\cdot\Phi_n, \tag{20}$$

where Φ_n is the objective value at the n'th iteration.

4 The "refractive index" and the evaluation of ψ_{target}

Snell's law, (21), relates the refractive index, n, of a material placed in vacuum to the incident angle, θ_1, and the refracted angle, θ_2, of a plane wave impinging on the material as

$$n = \frac{\sin(\theta_1)}{\sin(\theta_2)} \Leftrightarrow \theta_2 = \arcsin\left(\frac{\sin(\theta_1)}{n}\right). \tag{21}$$

Figure 3 provides an illustration of the negative refraction of a beam, from a slab of material (located in $\boldsymbol{\Omega}_\mathrm{d}$). The beam enters the domain, $\boldsymbol{\Omega}_\mathrm{T}$, at the lower edge centered at $\langle x_0, y_0\rangle$. It is refracted with full transmission at the lower interface of the material slab, continues through the slab and is again refracted with full transmission at the top interface. By convention θ_1 is measured positivity and θ_2 is measured negatively as shown in Fig. 3.

By using (21) and the sketch in Fig. 3 it is straight forward to derive an expression for the x-coordinate, x_3, of the center of the beam exiting the MM, based on the following parameters $\{x_0, y_0, y_1, y_2, y_3, \theta_1, \theta_2\}$. I.e the position of the center of the incoming beam $\langle x_0, y_0\rangle$, the position of the interfaces of the material slab, y_1, y_2, the angle of incidence, θ_1, the angle of refraction, θ_2, and the y-coordinate of the center of the target wave, y_3.

$$\begin{aligned} x_3 = x_0 &+ \tan(\theta_1)\,(y_3-y_2+y_1-y_0) \\ &+ \tan(\theta_2)\,(y_2-y_1)\,. \end{aligned} \tag{22}$$

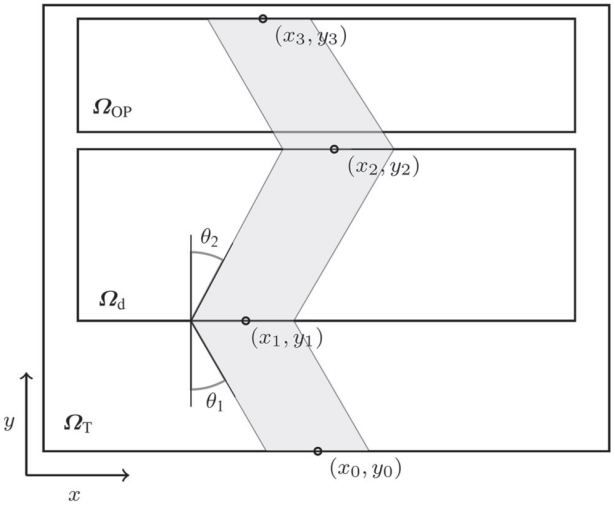

Fig. 3 Sketch of negative refraction of a beam entering the domain centered at $\langle x_0, y_0\rangle$, including quantities needed to calculate the placement of the center of ψ_{target}, $\langle x_3, y_3\rangle$, in order to obtain a desired n for a given θ_1

The procedure for evaluating the target wave, ψ_{target}, needed for the optimization problem (10)-(11) for a desired n at a given θ_1 and f may now be described as follows.

1. Select the target n, θ_1 and f.
2. Calculate the refracted angle θ_2 using (21).
3. Select the dimensions and position of $\boldsymbol{\Omega}_\mathrm{T}$, $\boldsymbol{\Omega}_{\mathrm{OP}}$, $\boldsymbol{\Omega}_\mathrm{d}$ (this provides $\{y_0, y_1, y_2, y_3\}$).
4. Select the position of the center of the enveloped plane wave ψ generated at $\delta\boldsymbol{\Omega}_{\mathrm{PW}}$: $\mathbf{x}_{w_{\mathrm{PW}}} = \langle x_0, y_0\rangle$.
5. Calculate the x-coordinate of the position of ψ_{target}, x_3, using (22).
6. Select the width of ψ_{target}: $\delta_{x_{\text{target}}} = \delta_{x_{\mathrm{PW}}}$.
7. Evaluate ψ_{target} using (4)-(5).

Note that the definition of n from Snell's law is not guaranteed to coincide with the definition of the refractive index given as $n = \frac{c}{c_p}$, where c is the wave speed in vacuum and c_p is the phase velocity of the wave in the medium through which it propagates. That is, it is possible to observe negative refraction of the wave without the resulting field inside the slab having a negative phase velocity.

5 Transmittance of sound power

A strength of the proposed objective function is the high level of transmission obtained for the designed meta material slabs. The measure of the transmission through the full MM slab used in the following sections is the transmittance, T. T is obtained by integrating the incoming and

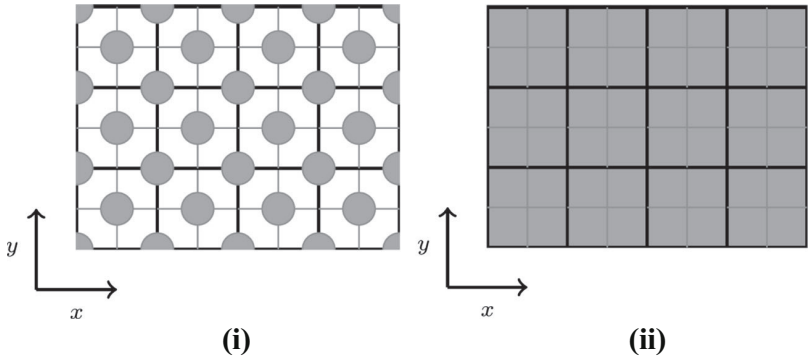

Fig. 4 Sketch of a **(i)** Restricted and **(ii)** Free periodic design domain consisting of 4 × 3 doubly axis symmetric unit cells

transmitted field at the second interface of a slab of MM using the following expression:

$$T = \frac{\int_{\delta_{\boldsymbol{\Omega}_d}} \psi_{\mathrm{S}}(x, y_2)\overline{\psi_{\mathrm{S}}(x, y_2)}\mathrm{d}x}{\int_{\delta_{\boldsymbol{\Omega}_d}} \psi_{\mathrm{E}}(x, y_2)\overline{\psi_{\mathrm{E}}(x, y_2)}\mathrm{d}x}. \tag{23}$$

Here y_2 denotes the y-coordinate of the second interface of the slab, see Fig. 3, $\delta_{\boldsymbol{\Omega}_d}$ denotes the x-coordinate interval along the second interface of the slab of MM. $\psi_{\mathrm{S}}(y, x)$ denotes the field in the modeling domain containing the MM slab, and $\psi_{\mathrm{E}}(x, y)$ denotes the incident wave in the domain without the slab.

6 Important observations

It is stressed that not all initial configurations lead to final designs with a low objective value, i.e. a MM slab with high T and near the target n_{target}. Tuning the unit cell dimensions relative to the target frequency is necessary to obtain highly performing results. This tuning was performed by numerical experimentation. For the examples considered in the following, a wave length on the order of two times the unit cell size was found to be a good choice. Also, starting the optimization process with a small spatial overlap between ψ and ψ_{target} was found to be important for the optimization to converge to well-performing final designs. Requiring this overlap sets bounds on the values of θ_1 and n for which it is possible to start the optimization. These bounds may be calculated from the width of the Gaussian envelope and the thickness of the MM slab used in the optimization using simply trigonometry. By applying a continuation approach where θ_1 and/or n is increased during the optimization it is possible to extend their values beyond those bounds.

It has been found that dividing the optimization process in to two phases, where a restriction is imposed on the design domain in the first phase (Fig. 4i), while the second phase is unrestricted (Fig. 4ii), yields a significant improvement in the convergence of the method to highly performing designs. The restriction used in the numerical examples presented in Section 7 consists of restricting the designable part of $\boldsymbol{\Omega}_{\mathrm{d}}$ to an FCC crystal-like grid. The radius of the inclusions in the FCC grid relative to the unit cell size is denoted r_{FCC}. During the first phase all ξ_i outside the designable part are fixed at $\xi_i = 0$, while in the second phase all ξ_i are allowed to change. Figure 4 illustrates the designable part of $\boldsymbol{\Omega}_{\mathrm{d}}$, highlighted in gray, in the two phases using a sample 4 × 3 unit cell slab.

For all examples presented in the paper $r_{\text{FCC}} = 0.25$ is used and the duration of the two phases is linked to the β-continuation scheme. Phase one is executed for $\beta \leq 4$ and phase two is executed for $\beta > 4$.

By tuning the unit cell size and using the two phase approach the proposed method has been found to converge to MMs with low objective value, i.e. $T > 0.95$ and n within ≈ 10 % of n_{target} when evaluated at the target θ_1 and n, for all tested values of $n \in [-4, -0.5]$ and $\theta_1 \in [2.5^{\mathrm{o}}, 15^{\mathrm{o}}]$[1]. Designing MMs for values of n and/or θ_1 outside the range stated above may be done by applying a continuation approach for θ_1 and the position of ψ_{target}, $\mathbf{x}_{w_{\text{target}}}$. In the continuation scheme θ_1 and/or n are changed gradually from an initial value to the final desired value during the optimization. Applying the continuation approach with four changes of θ_1 and/or n during the initial part of the optimization with 20 iteration between each change, it has been found possible to design MMs with $T > 0.85$ and within ≈ 25 % of the desired n for $n \in [-4, -0.35]$ for $\theta_1 = 10^{\mathrm{o}}$ and for $\theta_1 \in [2.5^{\mathrm{o}}, 30^{\mathrm{o}}]$ for $n = -1$. The reason for the upper limits on θ_1 and n when using the continuation scheme is that the width of the slab becomes a limiting factor (a wider slab is more expensive from a computational perspective). The authors find it reasonable to expect that

[1] Note that the proposed formulation does not allow $\theta_1 = 0^{\mathrm{o}}$ due to the formulation relying on (21).

MMs may be designed for larger θ_1 and/or n closer to zero if the width of the slab is increased.

7 Numerical results

Numerical results demonstrating the proposed method are presented. The material parameters for the solid and void regions are chosen to be those of aluminum; $\rho_{\text{solid}} = 2630.0\ \text{kg m}^{-3}$, $\kappa_{\text{solid}} = 6.87 \cdot 10^{10}\ \text{N m}^{-2}$ and air; $\rho_{\text{air}} = 1.204\ \text{kg m}^{-3}$, $\kappa_{\text{air}} = 141.921 \cdot 10^{3}\ \text{N m}^{-2}$, respectively. This provides a high contrast between solid and void resulting in near perfect reflection of the acoustic waves from solid regions, corresponding to a zero Neumann boundary condition along solid/void interfaces. The high impedance mismatch between the air and solid ensures that no significant excitation of elastic waves occurs in the solid material. Thus in the present case, where aluminum and air are considered, the elastic-acoustic interactions may be ignored, as is the standard procedure when performing topology optimization of high contrast acoustic problems (Dühring et al. 2008). The authors have investigated and validated this assumption both numerically and experimentally in previous work, concerning a topology optimized acoustic cavity (Christiansen et al. 2015a).

The parameter values used in the numerical examples are given in Table 1. The designable MM slab consists of 22×6 unit cells. Each unit cell is discretized into 80×80 finite elements, with each element containing a single design variable, yielding a total of 844800 finite elements in $\boldsymbol{\Omega}_{\text{d}}$ and 3600 design variables. If the full domain $\boldsymbol{\Omega}$ is discretized using a FEM method $\approx 3 \cdot 10^6$ finite elements are needed yielding $\approx 3 \cdot 10^6$ degrees of freedom. Using the Hybrid WBM-FEM method the total number of degrees of freedom is reduced to $\approx 0.88 \cdot 10^6$, at the expense of a small fraction of the system matrix being dense. The software used to solve the problem is written in MATLAB. When executing the code on a single 2.40 GHz Intel Core i7-3630 QM processor for the chosen parameters optimizing for one θ_1 and one f a design iteration uses 100-300 seconds (depending on the number of inner iterations in GCMMA). A total of 200-250 design iterations are used for the investigated cases.

For all examples an enveloped plane wave with the non-dimensionalized wavelength, $\lambda = \frac{1}{3}$, is excited at $\delta\boldsymbol{\Omega}_{\text{PW}}$. The unit cell size is $(a_x, a_y) = \left(\frac{1}{6}, \frac{1}{6}\right)$ in non-dimensional units; hence there are 2 unit cells per free space wavelength of the pressure field. The performance of the designed MMs in terms of n and T is in all cases investigated by considering a slab consisting of 22×12 unit cells, i.e. a slab of twice the depth of the slab used in the optimization procedure. The increased depth is used to highlight that the optimized design works as a bulk material and not only for the thickness of the slab used in the optimization. That is, the performance of the designed MM slabs consisting of the optimized unit cell designs show little dependence on slab thickness.

Table 1 $x_{[\cdot]} \times y_{[\cdot]}$: Non-dimensional domain sizes. $\mathcal{N}_{\text{e,x}} \times \mathcal{N}_{\text{e,y}}$: Number of finite elements per unit cell. $\mathcal{N}_{\text{uc,x}} \times \mathcal{N}_{\text{uc,y}}$: Number of unit cells in the material slab. $\mathbf{x}_{w\text{PW}}$: Center of incoming wave. $\delta_{\text{x,PW}}$: Width of Gaussian envelope on incoming wave. $\delta_{\text{x,target}}$: Width of Gaussian envelope on target wave. $\delta\boldsymbol{\Omega}_{[\cdot]}$: Domain boundary. R: Filter radius. η: Projection level. V: Volume constraint. c_s: Objective function scaling

Parameter	Value
$x_{\boldsymbol{\Omega}_{\text{T}}} \times y_{\boldsymbol{\Omega}_{\text{T}}}$	$[-26/12, 26/12] \times [-18/12, 18/12]$
$x_{\boldsymbol{\Omega}_{\text{op}}} \times y_{\boldsymbol{\Omega}_{\text{op}}}$	$[-26/12, 26/12] \times [8/12, 18/12]$
$x_{\boldsymbol{\Omega}_{\text{d}}} \times y_{\boldsymbol{\Omega}_{\text{d}}}$	$[-22/12, 22/12] \times [-6/12, 6/12]$
$\mathcal{N}_{\text{e,x}} \times \mathcal{N}_{\text{e,y}}$	80×80
$\mathcal{N}_{\text{uc,x}} \times \mathcal{N}_{\text{uc,y}}$	22×6
$\mathbf{x}_{w\text{PW}}$	$\langle 0.0, -26/12 \rangle$
$\delta_{\text{x,PW}} = \delta_{\text{x,target}}$	0.7
$\delta\boldsymbol{\Omega}$	$\delta\boldsymbol{\Omega}_{\text{T}}$
$\delta\boldsymbol{\Omega}_{\text{PW}}$	$[-26/12, 26/12] \times -18/12$
R	$\frac{1}{240}$
η	0.5
V	0.25
c_s	10^3

7.1 Single angle of incidence, $n_{\text{target}} = -1$

As a first demonstration of the proposed method, we consider designing a MM for the target negative refractive index, $n_{\text{target}} = -1$, at the incident angle, $\theta_1 = 10^{\text{o}}$ and the non-dimensional frequency $f = 3$.

Figure 5i shows the initial guess for a unit cell in the design domain, where the gray area corresponds to $\xi = 0.25$ and the white area to $\xi = 0$. Figure 5ii shows a unit cell in

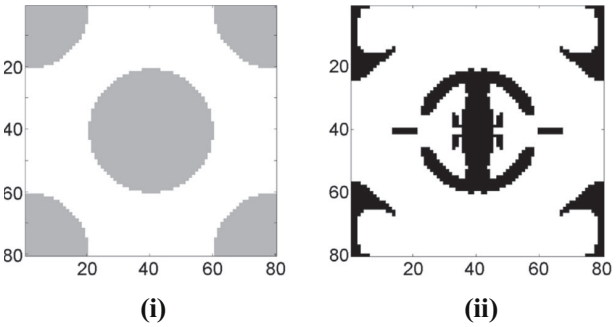

Fig. 5 **(i)** Initial guess for a unit cell in the restricted design. **(ii)** Unit cell in the final design for the example in Section 7.1

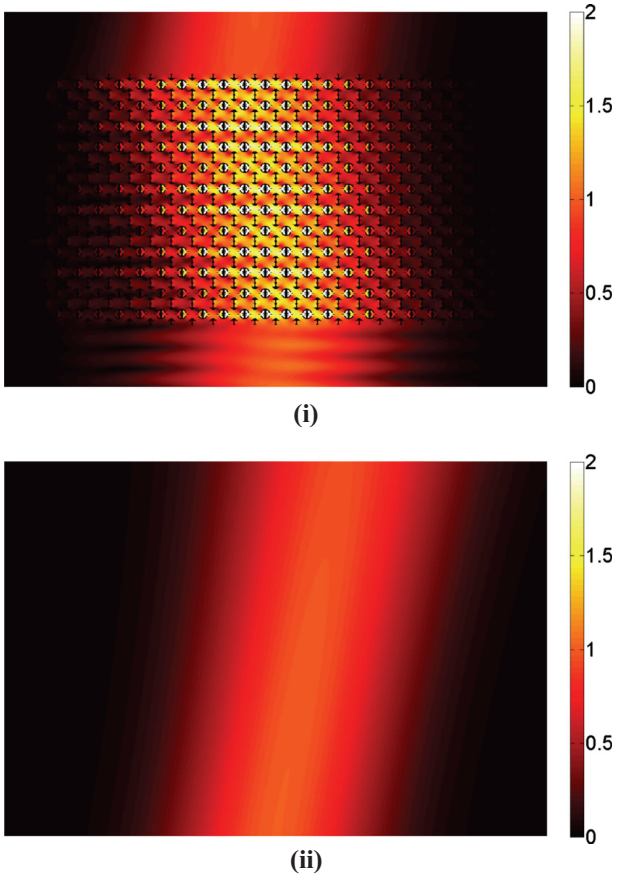

Fig. 6 (color online) Amplitude of the solution to the model problem (1)-(3), $|\psi|$, in $\boldsymbol{\Omega}_{\mathrm{T}}$ for an incident angle $\theta_1 = 10^{\mathrm{o}}$ **(i)** containing a MM slab of 22×12 unit cells consisting of the optimized design in Fig. 5ii. **(ii)** In an empty $\boldsymbol{\Omega}_{\mathrm{T}}$

the final design where black is material ($\hat{\tilde{\xi}} = 1$) and white is void ($\hat{\tilde{\xi}} = 0$).

Figure 6 shows the amplitude of the pressure field, $|\psi|$, in $\boldsymbol{\Omega}_{\mathrm{T}}$ for an incident enveloped plane wave at $\theta_1 = 10^{\mathrm{o}}$, Fig. 6i with and Fig. 6ii without the MM slab placed in the center of the modeling domain.

The refractive index of the MM slab is estimated by applying the following procedure. The field inside the MM, ψ, is fitted to a perfect Gaussian envelope, ψ_{PGE}:

$$\psi_{\mathrm{PGE}} = A_{\mathrm{PGE}} \mathrm{e}^{-\left(\frac{(\mathbf{x}-\mathbf{x}_w)\cdot\hat{\mathbf{d}}}{\delta_x}\right)^2} \tag{24}$$

$$= A_{\mathrm{PGE}} \mathrm{e}^{-\left(\frac{-(x-x_w)\sin(\pi/2+\theta_{2,\mathrm{fit}})+(y-y_w)\cos(\pi/2+\theta_{2,\mathrm{fit}})}{\delta_x}\right)^2}, \tag{25}$$

whose width δ_x, amplitude A_{PGE}, position $\mathbf{x}_w$, and angle for the direction of propagation $\theta_{2,\mathrm{fit}}$ are free parameters. The fit is made using a nonlinear least-squares curve fitting tool which solves the minimization problem;

$$\min_{\delta_x, A_{\mathrm{PGE}}, \mathbf{x}_w, \theta_{2,\mathrm{fit}}} \|\psi - \psi_{\mathrm{PGE}}\|_2^2$$

over the meta material slab. The angle of refraction of the incoming enveloped plane wave, $\theta_2 \approx \theta_{2,\mathrm{fit}}$, is obtained from the fit.

The angle $\theta_{2,\mathrm{fit}}$ obtained from the fit along with the angle θ_1 of the incoming wave is used to estimate n using (21). It is noted that $\theta_{2,\mathrm{fit}}$ in some cases were found to be sensitive to the initial guess of the fitting parameters in the fit with a maximal variation of $\Delta\theta_2 = 0.5^{\mathrm{o}}$. Hence a bound on $\theta_2 \approx \theta_{2,\mathrm{fit}}$ is $\theta_{2,\mathrm{bound}} \in [\theta_{2,\mathrm{fit}} - \Delta\theta_2, \theta_{2,\mathrm{fit}} + \Delta\theta_2]$. The uncertainty in θ_2 propagates to uncertainty in the refractive index. Therefore bounds on n have been calculated, providing an estimate of a minimum value, $n_{\min} = \frac{\sin(\theta_1)}{\sin(\theta_{2,\mathrm{fit}}+\Delta\theta_2)}$ and maximum value $n_{\max} = \frac{\sin(\theta_1)}{\sin(\theta_{2,\mathrm{fit}}-\Delta\theta_2)}$ for n for a given θ_1. These bounds are included in all reported values of n.

Using this procedure for the present case one obtains $n \approx -1.06 \pm 0.05$ and $T \approx 0.98$ for the bulk MM at the prescribed frequency $f = 3$ and angle of incidence $\theta_1 = 10^{\mathrm{o}}$. Hence the designed acoustic MM is exhibiting the desired negative refraction to within ≈ 10 % and with high transmission at the prescribed angle of incidence.

7.1.1 Angular and frequency dependence

An investigation of the angular and frequency dependence of T and n are presented in Fig. 7i and ii respectively.

Figure 7i shows $T(\theta_1)$ for five equidistant frequencies in the interval, $f \in [2.7, 3.3]$. Here it is seen that T remains above 0.95 for the frequencies $f \in [2.7, 3.0]$ for $\theta_1 \in [2.5^{\mathrm{o}}, 15^{\mathrm{o}}]$ after which it drops off for all frequencies. For the two higher frequencies the transmission quickly drops off. This is in part due to some of the energy being reflected from the interfaces of the MM and in part due to n going towards zero, i.e. a large value of $|\theta_2|$ which results in part of the energy being refracted towards the left side of the MM slab.

Consider now the refractive index shown in Fig. 7ii for $f \in \{2.85, 3.00, 3.15, 3.30\}$. Here it is seen that n is sensitive towards both angular changes and frequency changes, however it remains negative across all investigated frequencies and angles. n for $f = 2.75$ is $-475 < n < -17 \; \forall \, \theta_1$ meaning that the refracted angle, θ_2 is in the interval $0.0^{\mathrm{o}} \leq \theta_2 \leq 0.5^{\mathrm{o}}$. Hence for this frequency the refracted field is transmitted through the slab almost without any transverse change in position.

Figure 8 illustrates the variation in the field across a range of incoming angles, $\theta_1 \in [2.5^{\mathrm{o}}, 15^{\mathrm{o}}]$ for $f = 3.0$.

7.1.2 The field inside the MM

By looking at the temporal and spatial variations of the pressure field inside the MM it is observed that the field pattern is non-trivial. I.e. the field inside the MM slab cannot be described exactly by a simple plane wave traveling through

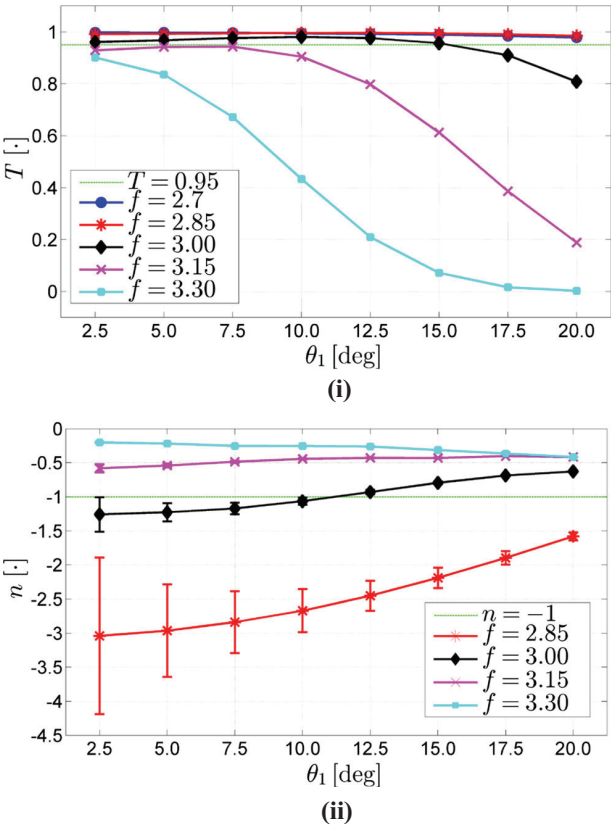

Fig. 7 (color online) **(i)** Transmittance and **(ii)** refractive index, including error bars denoting the uncertainty in n stemming from the uncertainty in $\theta_{2,\text{fit}}$, for MM slab consisting of 22×12 unit cells containing the optimized design shown in Fig. 5ii as a function of incident angle, θ_1, for different frequencies

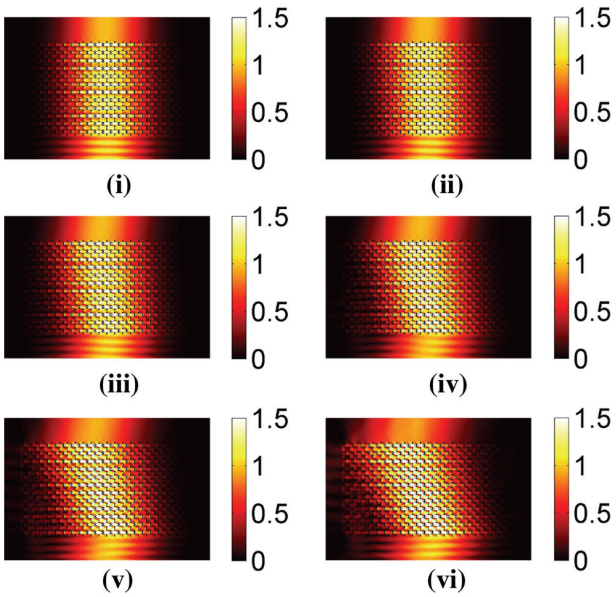

Fig. 8 (color online) Amplitude of the solution to the model problem (1)-(3), $|\psi|$, in $\boldsymbol{\Omega}_\text{T}$ containing a MM slab of 22×12 unit cells consisting of the optimized design in Fig. 5ii for six different incident angles θ_1 at the target frequency $f = 3.0$. **(i)** $\theta_1 = 2.5^\text{o}$ **(ii)** $\theta_1 = 5.0^\text{o}$ **(iii)** $\theta_1 = 7.5^\text{o}$ **(iv)** $\theta_1 = 10.0^\text{o}$ **(v)** $\theta_1 = 12.5^\text{o}$ **(vi)** $\theta_1 = 15.0^\text{o}$

the slab. As an example of investigating the field inside the MM slab, consider a plane wave with $f = 3$ impinging on the meta material slab at a right angle ($\theta_1 = 0$). For this investigation infinite periodicity in the x-direction is assumed. By performing a Fourier transform, $F(\psi, k)$, of the field inside the MM, utilizing the periodicity to only consider a 1×12 column of unit cells, and recording the magnitude $|F|^2$ for wave vectors, $\mathbf{k} = \langle k_x, k_y \rangle$, with zero x-component, one obtains the spectrum shown in Fig. 9. From here it is seen that four modes are excited inside the MM. A dominant mode centered at the positive wave number $\text{sgn}(k_y) \cdot |k_p| \approx 3.9 \cdot 2\pi$ along with a number of side lobes as well as three modes being approximately an order of magnitude smaller with negative wave numbers centered at, $\text{sgn}(k_y) \cdot |k_{n_1}| \approx -2 \cdot 2\pi$, $\text{sgn}(k_y) \cdot |k_{n_2}| \approx -3.9 \cdot 2\pi$, $\text{sgn}(k_y) \cdot |k_{n_3}| \approx -8.1 \cdot 2\pi$, respectively. This example indicates that the designed MM slab exhibits negative refraction through an interaction of excited waves having both positive and negative phase velocity, $c_p = \frac{\omega}{k}$. The finding that several modes contribute to the field inside the MM agrees with the findings in Mortensen et al. (2010), where an optical material is considered.

7.2 Multiple incoming angles, $n_\text{target} = -1$

The first example illustrated that the proposed method can be used to design MMs exhibiting a given negative n for a single incoming angle and frequency with good accuracy and high T. Furthermore, it was seen that the refractive index remains negative across a wide range of

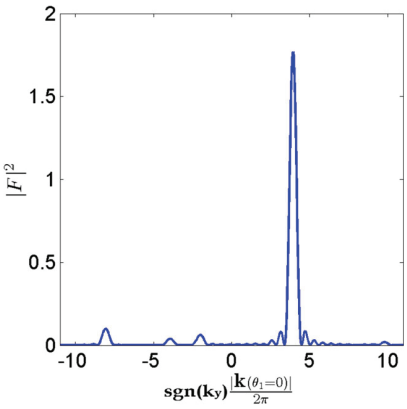

Fig. 9 (color online) Squared magnitude of the Fourier transform of the field inside the MM slab across 1×12 unit cells for an incident plane wave, ψ, at $\theta_1 = 0°$ and $f = 3$ for the design shown in Fig. 5ii, for a k-vector with zero x-component

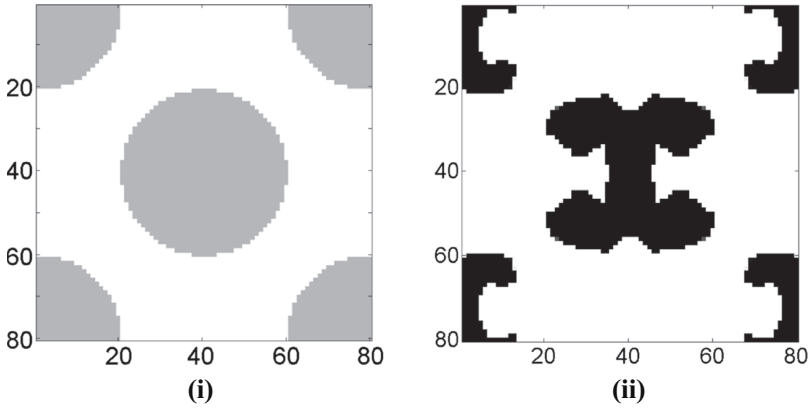

Fig. 10 **(i)** Initial guess for a unit cell in the restricted design. **(ii)** Unit cell in the final design for the example in Section 7.2. *Black* is solid, *white* is void and *gray* is an intermediate between solid and void

incoming angles and a frequency band of 20 %. However, both the refractive index and transmittance exhibit a strong dependence on both θ_1 and f. This example illustrates that the variation with θ_1 may be reduced and the overall performance increased by optimizing the MM across a range of incoming angles. The same parameters as the first example are used in the optimization problem, except that three incident angles are considered simultaneously, $\theta_1 \in \{5^o, 10^o, 15^o\}$. Figure 10ii shows the unit cell for the final design.

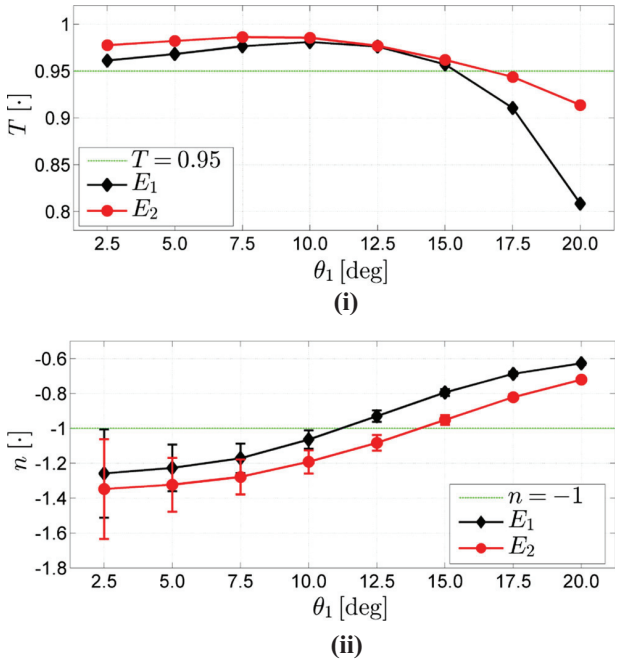

Fig. 11 (color online) Comparison of **(i)** Transmittance and **(ii)** refractive index, including error bars denoting the uncertainty in n stemming from the uncertainty in $\theta_{2,\text{fit}}$, for MM slab consisting of 22 × 12 unit cells seen in Fig. 5ii (E_1) and a MM slab of 22 × 12 unit cells seen in Fig. 10ii (E_2). The frequency used for the calculations is the target frequency for the optimization $f = 3$

Figure 11i and ii show a comparison of T and n, respectively, for the MM seen in Fig. 5ii, denoted E_1, and the MM seen in Fig. 10ii, denoted E_2, evaluated at the target frequency $f = 3.0$.

From Fig. 11i it is observed that the transmission has improved for all investigated angles such that $T(\theta_1) > 0.96 \; \forall \; \theta_1 \in [2.5, 15]$ and from Fig. 11ii it is seen that the variation in n has decreased slightly across $\theta_1 \in [5, 15]$. An increase in transmittance of $\approx .005$ is seen even for the angle $\theta_1 = 10^o$ for which E_1 was optimized. The explanation for this unexpected increase is the decrease in n compared to the target value. I.e. in terms of the objective function value for $(f, \theta_1) = (3, 10^o)$, E_1 still outperforms E_2; $\Phi_{E_1}(f = 3, \theta_1 = 10) \approx 0.17$ and $\Phi_{E_2}(f = 3, \theta_1 = 10) \approx 1.7$.

7.2.1 Uniform spatial variations

The ultimate goal of designing MM slabs exhibiting negative refraction is using the resulting designs in real world applications. Hence the optimized designs have to be manufactured and regardless of the chosen method, production errors may occur. It is therefore valuable to know how production errors affect the designs performance. Common manufacturing errors in micro-nano-processing are over- and under-etching or over- and under exposure which can be observed as near uniform erosion or dilation of manufactured devices (Zhou et al. 2016; Jansen et al. 2013). Hence, this section presents an investigation of how uniform dilation/erosion of the optimized design considered in Section 7.2, optimized for multiple incoming angles, affects its transmittance and index of refraction. The dilation/erosion of the design is performed by adding/removing a single element of material to/from the edge of each feature, corresponding to 1/80 or 1.25 % of unit cell size. The unit cells for the dilated, $E_{2,Dilate}$, and eroded, $E_{2,Erode}$, design are presented in Fig. 12 along with illustrations of the changes from the optimized unit cell seen in Fig. 10ii. For

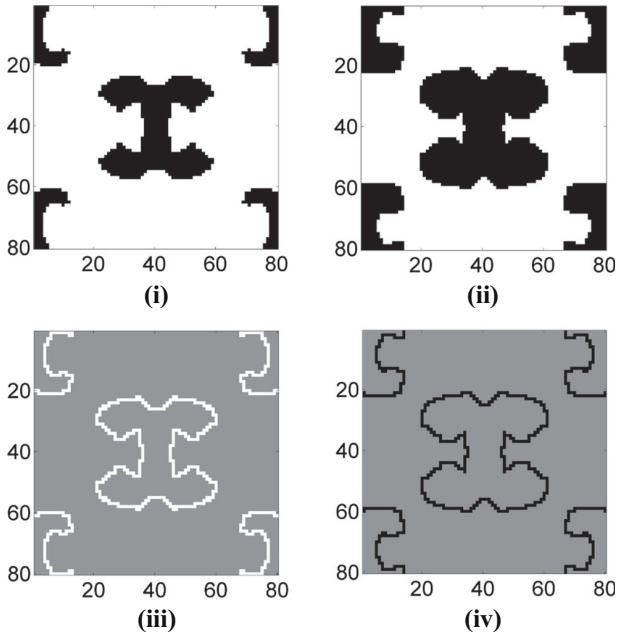

Fig. 12 **(i)** Eroded, $E_{2,Erode}$, and **(ii)** Dilated, $E_{2,Dilate}$, unit cell for the optimized design, E_2, presented in Fig. 10ii. Here black denotes material and white denotes void. **(iii)** and **(iv)** show the difference between the optimized design and the eroded and dilated designs respectively. Here gray denotes unchanged areas of the unit cell while white denotes removed material and black denotes added material

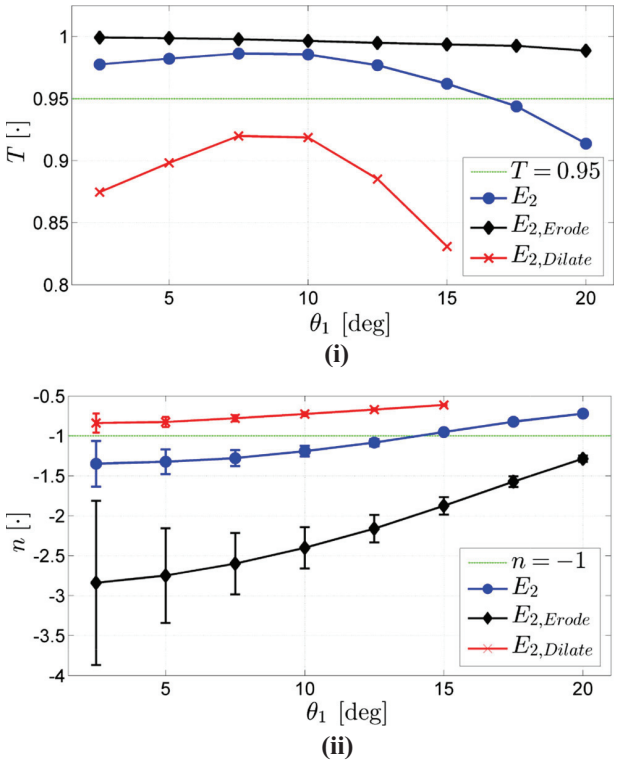

Fig. 14 (color online) **(i)** Transmittance and **(ii)** refractive index, including error bars denoting the uncertainty in n stemming from the uncertainty in $\theta_{2,\text{fit}}$, as a function of θ_1 for a MM slab consisting of 22×12 unit cells of the optimized E_2, eroded $E_{2,Erode}$ and dilated $E_{2,Dilate}$ designs presented in Figs. 10ii, 12i and ii respectively

the eroded design the narrow features along the top and bottom edges of the unit cell disappear completely, while for the dilated design all features remain intact.

Figure 13 shows the amplitude of the pressure field $|\psi|$ in Ω_T for an enveloped plane wave incident at $\theta_1 = 10^o$ for the eroded, optimized and dilated design. Changes in both n and T introduced by the erosion/dilation can be observed.

An investigation of $n(\theta_1)$ and $T(\theta_1)$, $\theta_1 \in [0^o, 20^o]$, for E_2, $E_{2,Erode}$ and $E_{2,Dilate}$ is presented in Fig. 14. Both $n(\theta_1)$ and $T(\theta_1)$ are affected by the dilation/erosion, which is not unexpected as the design was not optimized for spatial robustness. Although the performance of the MM slab deteriorates in both cases the index of refraction remains negative for all θ_1 and $T > 0.8$ for $\theta_1 < 15^o$. Considering $E_{2,Erode}$, T is observed to increase for all θ_1, whereas n deteriorates compared to E_2 and the optimization target $n_{\text{target}} = -1$. For $E_{2,Dilate}$ the transmittance decreases and the index of refraction increases, i.e. θ_2 increases for all θ_1. It is interesting to note that the erosion and the dilation have opposite effects on T and n, with T increasing and n decreasing for the erosion and vise versa for the dilation.

7.3 Frequency band, $n_{\text{target}} = -1$

The example in Section 7.2 demonstrated that it is possible to increase the transmission and reduce the variation in n across an interval of incoming angles by accounting for multiple angles in the design process. The next example

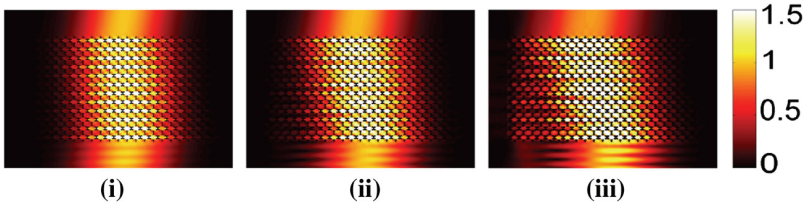

Fig. 13 (color online) Amplitude of the solution to the model problem (1)-(3), $|\psi|$, with $\theta_1 = 10^o$, in Ω_T containing a MM slab of 20×12 unit cells consisting of the **(i)** eroded, **(ii)** optimized and **(iii)** dilated design presented in Figs. 10ii, 12i and ii, respectively

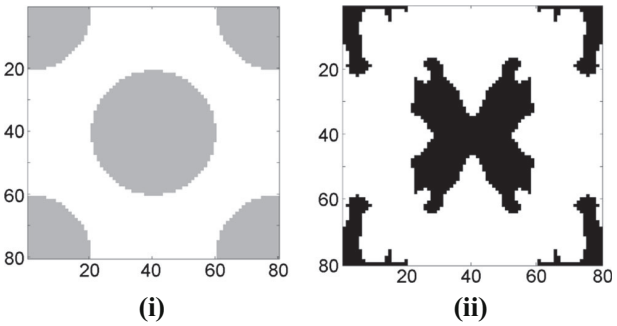

Fig. 15 **(i)** Initial guess for a unit cell in the restricted design. **(ii)** Unit cell in the final design for the example in Section 7.3. Black is solid, white is void and gray is an intermediate between solid and void

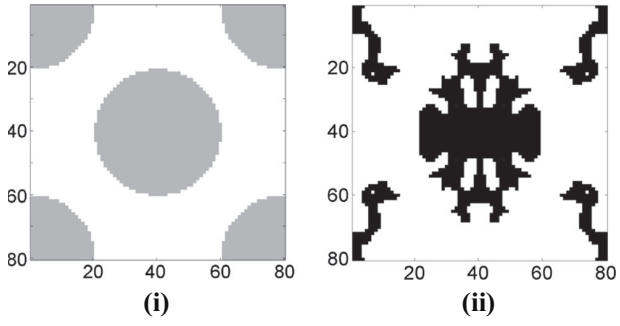

Fig. 17 **(i)** Initial guess for a unit cell in the restricted design. **(ii)** Unit cell in the final design for the example in Section 7.4. *Black* is solid, *white* is void and *gray* is an intermediate between solid and void

investigates if it is possible to obtain similar results across a frequency band as well. Consider the same parameters used in the first example except that the design is optimized for three wave lengths simultaneously. The non-dimensional wavelengths are $\lambda_i \in \{10/27, 10/30, 10/33\}$ corresponding to $f \in \{2.85, 3, 3.15\}$ i.e. a 10 % frequency band centered at $f_c = 3$. The resulting unit cell design is shown in Fig. 15ii.

Figure 16 shows a comparison of T and n between the MM shown in Fig. 5ii optimized for a single frequency, denoted E_1, and the MM shown in Fig. 15ii optimized for the three frequencies $f \in [2.85, 3.00, 3.15]$, denoted E_3, both at the incoming angle $\theta_1 = 10^o$.

Considering the transmittance in Fig. 16 it is seen that it oscillates for both E_1 and E_3. For E_3 the oscillations have peaks at the three frequencies for which the MM slab was designed (as is to be expected). Calculating the average transmittance from Fig. 16i across the frequency interval

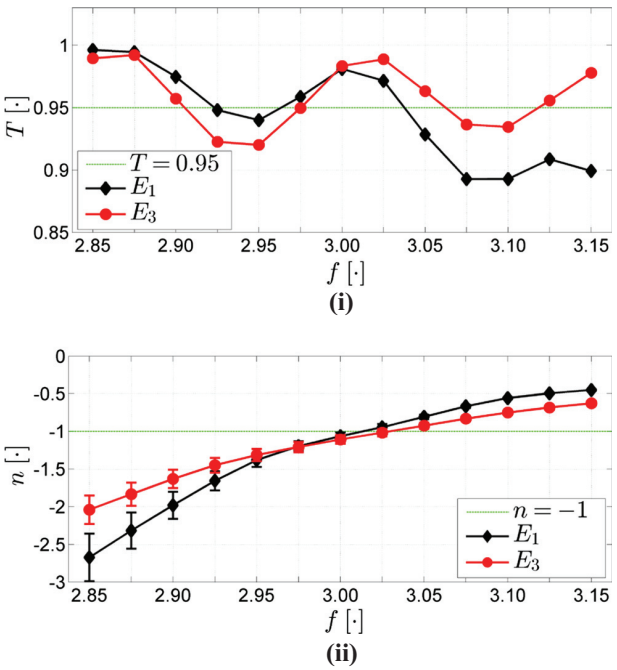

Fig. 16 (color online) Comparison of **(i)** Transmittance and **(ii)** refractive index, including error bars denoting the uncertainty in n stemming from the uncertainty in $\theta_{2,\text{fit}}$, for MM slab consisting of 22 × 12 unit cells seen in Fig. 5ii (E_1) and a MM slab of 22 × 12 unit cells seen in Fig. 15ii (E_2) as a function of frequency, f, for the incident angle $\theta_1 = 10^o$

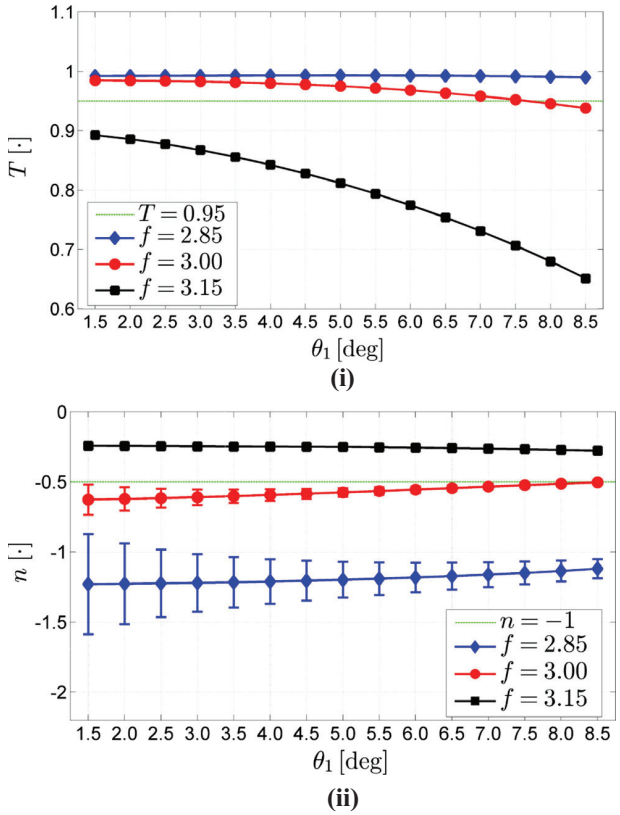

Fig. 18 (color online) **(i)** Transmittance and **(ii)** refractive index, including error bars denoting the uncertainty in n stemming from the uncertainty in $\theta_{2,\text{fit}}$, for MM slab consisting of 22 × 12 unit cells containing the optimized design shown in Fig. 17ii as a function of incident angle, θ_1, for different frequencies

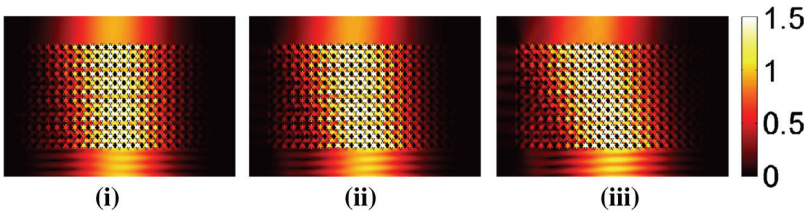

Fig. 19 (color online) Amplitude of the solution, $|\psi|$, to the model problem (1)-(3), in $\boldsymbol{\Omega}_{\mathrm{T}}$ containing a MM slab of 22×12 unit cells consisting of the optimized design in Fig. 17ii for three different incident angles θ_1 at the target frequency $f = 3.0$. **(i)** $\theta_1 = 2.5^{\mathrm{o}}$ **(ii)** $\theta_1 = 5.0^{\mathrm{o}}$ **(iii)** $\theta_1 = 7.5^{\mathrm{o}}$

$f \in [2.85, 3.15]$ one gets $\langle T_{E_3} \rangle \approx 0.960$ and $\langle T_{E_1} \rangle \approx 0.945$ for the frequency band and single frequency optimization respectively. An improvement of ≈ 0.015. If one considers the worst case transmittance it has seen to improve from $\min(T_{E_1}) \approx 0.893$ to $\min(T_{E_3}) \approx 0.920$. Regarding the refractive index Fig. 16ii shows a reduction in the variation of n with frequency as well as an overall improvement in accuracy compared to the target $n_{\mathrm{target}} = -1$. Although the accuracy at $f = 3.0$ has decreased by ≈ 4 %, it has increased in the rest of the interval. At $f = 3.15$ the increase is ≈ 40 % while at $f = 2.85$ the increase is between 6 % and 38 % when the uncertainty in n, caused by the uncertainty in $\theta_{2,\mathrm{fit}}$, is taken into account.

7.4 Multiple incoming angles, $n_{\mathrm{target}} = -0.5$

The final example shows the design for an MM optimized for $n_{\mathrm{target}} = -0.5$ and the angular range, $\theta_1 \in [2.5^{\mathrm{o}}, 7.5^{\mathrm{o}}]$. Three target angles $\theta_1 \in \{2.5^{\mathrm{o}}, 5.0^{\mathrm{o}}, 7.5^{\mathrm{o}}\}$ are used in the optimization. All other parameters are the same as those used in the first example. The resulting design is presented in Fig. 17ii. The dependence of T and n on incoming angle and frequency is illustrated in Fig. 18. An illustration of the field in and around the MM slab as a function of θ_1 is presented in Fig. 19. By comparing the field in Figs. 8 and 19 the change in n for the two MM slabs is observed.

Figure 18i shows $T(\theta_1)$ for three equidistant frequencies in the interval, $f \in [2.85, 3.15]$. T remains above 0.95 for the frequencies $f \in [2.85, 3.0]$ for $\theta_1 \in [1.5^{\mathrm{o}}, 7.5^{\mathrm{o}}]$. For $f = 3.15$ the transmission quickly drops off. As for the first examples this is in part due to some of the energy being reflected from the interfaces of the MM and in part due to $n_{f=3.15} \approx -0.25$ which results in $|\theta_2|$ growing quickly, in turn resulting in part of the energy being refracted towards the left side of the MM slab. Considering the refractive index shown in Fig. 18ii for $f \in \{2.85, 3.00, 3.15\}$, it is seen that n varies with both f and θ_1 while remaining negative across all investigated values. The variations in n are larger with f than with θ_1. Compared to the first example the variations in both f and θ_1 are slightly smaller across the investigated range of θ_1.

8 Conclusions

A topology optimization based approach for designing meta material slabs exhibiting a prescribed negative refraction under illumination of a plane wave at a specified angle of incidence and target frequency has been proposed. Examples for varying refractive index, angle of incidence and frequency demonstrated the method. An MM slab exhibiting the targeted negative refraction to within ≈ 10 % error with high transmittance, $T \approx 0.98$ for the targeted angle of incidence and frequency was presented. It was shown to be possible to increase the transmittance and reduce the variation in n with incoming angle by taking multiple angles into account in the design process. It was also shown to be possible to improve the transmittance and reduce the variation of n across a band of frequencies by optimizing for multiple frequencies simultaneously. The influence of uniform spatial variations of a design optimized for $\theta_1 \in \{-5^{\mathrm{o}}, -10^{\mathrm{o}}, -15^{\mathrm{o}}\}$ was investigated. While the variations were found to have an impact on the designs performance it was also found that the index of refraction remained negative and the transmittance above ≈ 0.8 for $\theta_1 \in [-15^{\mathrm{o}}, 15^{\mathrm{o}}]$ for both the eroded and dilated versions of the design.

The presented approach has the clear benefit that no assumptions that reduce the physical model are imposed, such as applying homogenization, assuming infinite periodicity of the MM, assuming a given boundary condition at the MM interface or considering only the dominant mode inside the MM. On the contrary, the method inherently accounts for edge effects and the more advanced behavior of the field inside the MM. Thus it is expected that any manufactured MMs, designed using the presented approach, should directly function as predicted by the simulation results.

Although the paper treats the acoustic case, the method is directly applicable to both electromagnetic and elastic wave problems by adjusting the relevant material parameters, α and γ, the wave speed, c, and the spatial dimensions. As the contrast in material parameters can be orders of magnitude smaller for both electromagnetic and elastic shear waves, it is the authors' experience that the optimization problem is less challenging in those cases.

Acknowledgments The work was financially supported by Villum Fonden through the research project *Topology Optimization - the Next Generation (NextOpt)*.

References

Andkjær J, Sigmund O (2013) Topology optimized cloak for airborn sound. J Vib Acoust 135:041,011–1–041,001–5

Bendsøe MP, Sigmund O (2003) Topology optimization. Springer

Christiansen RE, Fernandez-Grande E, Sigmund O (2015a) Experimental validation of topology optimized acoustic cavity. J Acoust Soc Am 138(6):3470–3474. doi:10.1121/1.4936905

Christiansen RE, Lazarov BS, Jensen JS, Sigmund O (2015b) Creating geometrically robust designs for highly sensitive problems using topology optimization - acoustic cavity design. Structural and Multidiciplinary Optimization 52:737–754. doi:10.1007/s00,158–015–1265–5

Craster RV, Guenneau S (2013) Acoustic metamaterials - negative refraction, Imaging, Lensing and Cloaking. Springer Science+Business Media Dordrecht

Desmet W (1998) A wave based prediction technique for coupled vibro-acoustic analysis. PhD thesis, Katholieke Universiteit Leuven

Dühring MB, Jensen JS, Sigmund O (2008) Acoustic design by topology optimization. J Sound Vib 317:557–575

Diaz AR, Sigmund O (2009) A toplogy optimization method for design of negative permeability metamaterials. Structural and Multidiciplinary Optimization 41:163–177

Goo S, Kook J, Koo K, Hyun J, Wang S (2014) Acoustic topology optimization for interior acoustic problem using the hybrid finite element - wave based method. In: The Eighth China-Japan-Korea Joint Symposium on Optimization of Structural and Mechanical Systems

Guest JK, JH Prévost, Belytschko T (2004) Achieving minimum length scale in topology optimization using nodal design variables and projection functions. Int J Numer Methods Eng 61:238–254

Jansen M, Lazarov B, Schevenels M, Sigmund O (2013) On the similarities between micro/nano lithography and topology optimization projection methods. Struct Multidiscip Optim 48:717–730

Krowne CM, Zhang Y (2007) Physics of Negative Refraction and Negative Index Material - Optical and Electronic Aspects and Diversified Approaches. Springer, Berlin Heidelberg

Lu L, Yamamoto T, Otomori M, Yamada T, Kazuhiro NS (2013) Topology optimization of an acoustic metamaterial with negative bulk modulus using local resonance. Finite Elem Anal Des 72:1–12

Mills EM, Banks ML, Sprague JE, Finkel T (2003) Imaging by flat lens using negative refraction. Nature 426:404

Mortensen NA, Yan M, Sigmund O, Breinbjerg O (2010) On the unambiguous determination of effeffect optical properties of periodic metamaterials: a one-dimensional case study. Journal of the European Optical Society 5

Park JH, Ma PS, Kim YY (2015) Design of phononic crystals for self-colimation of elastic waves using topology optimization method. Structural and Multidiciplinary Optimization 51:1199–1209

Pendry JB (2000) Negative refraction makes a perfect lens. Phys Rev Lett 85:3966–3969

Philippe FD, Murray TW, Prada C (2015) Focusing on plates: controlling guided waves using negative refraction. Scientific Report 5:11,112–1–11,112–4

Pluymers B (2006) Wave based modelling methods for steady-state vibro-acoustics. PhD thesis, Katholieke Universiteit Leuven

Svanberg K (1987) The method of moving asymptotes - a new method for structural optimization. Int J Numer Methods Eng 24:359–373

Svanberg K (2002) A class of globally convergent optimization methods based on conservative convex seperable approximations. SIAM Journal of Optimization 12:555–573

Veselago VG (1968) The electrodynamics of substances with negative values of ϵ and μ. Soviet Physics Uspekhi 10:509–514

Wang F, Lazarov BS, Sigmund O (2011) On projection methods, convergence and robust formulations in topology optimization. Structural Multidiciplinary Optimization 43:767–784

Xu S, Cai Y, Cheng G (2010) Volume preserving nonlinear density filter based on heaviside projections. Structural and Multidiciplinary Optimization 41:495–505

Xu T, Agrawal A, Abashin M, Chau KJ, Lezec HJ (2013) All-angle negative refraction and active flat lensing of ultraviolet light. Nature 497:470–474

Zhang S, Fan W, Panoiu NC, Malloy KJ, Osgood RM, Brueck SRJ (2005) Experimental demonstration of near-infrared negative-index metamaterials. Phys Rev Lett 95:137,404–1–137,404–4

Zhang S, Yin L, Fang N (2009) Focusing ultrasound with an acoustic metamaterial network. Phys Rev Lett 102:194,301–1–194,301–4

Zhang X, Liu Z (2004) Negative refraction of acoustic waves in two-dimensionl phononic crystals. Appl Phys Lett 85:341–343

Zhou M, Lazarov b, Sigmund O (2016) Topology optimization for optical microlithography with partially coherent illumination. Submitted

Zhou S, Li W, Sun G, Li Q (2010) A level-set procedure for the design of electromagnetic metamaterials. Optical Express 18

Publication [P5]

Experimental Validation of Systematically Designed Acoustic Hyperbolic Meta Material Slab Exhibiting Negative Refraction

Experimental validation of systematically designed acoustic hyperbolic meta material slab exhibiting negative refraction

Rasmus E. Christiansen[a)] and Ole Sigmund
Department of Mechanical Engineering, Solid Mechanics, Technical University of Denmark, Nils Koppels Allé, B. 404, DK-2800 Lyngby, Denmark

(Received 19 May 2016; accepted 27 August 2016; published online 8 September 2016)

This Letter reports on the experimental validation of a two-dimensional acoustic hyperbolic metamaterial slab optimized to exhibit negative refractive behavior. The slab was designed using a topology optimization based systematic design method allowing for tailoring the refractive behavior. The experimental results confirm the predicted refractive capability as well as the predicted transmission at an interface. The study simultaneously provides an estimate of the attenuation inside the slab stemming from the boundary layer effects—insight which can be utilized in the further design of the metamaterial slabs. The capability of tailoring the refractive behavior opens possibilities for different applications. For instance, a slab exhibiting zero refraction across a wide angular range is capable of funneling acoustic energy through it, while a material exhibiting the negative refractive behavior across a wide angular range provides lensing and collimating capabilities. *Published by AIP Publishing.*
[http://dx.doi.org/10.1063/1.4962441]

This Letter presents the experimental validation of an acoustic hyperbolic metamaterial (AHMM) slab obtained using a systematic design method proposed recently in Ref. 1. The negative refraction exhibited by the slab stems from a hyperbolic band effect in the second acoustic band. Negative refraction is demonstrated in a 10% frequency band for a localized acoustic wave, incident on the AHMM slab across the angular interval, $\theta_1 \in [0°, 25°]$. Predicted high energy transmittance through the material-air interface is experimentally verified at normal incidence. The index of refraction, n, is defined according to Snell's law.

All known naturally occurring materials have positive n. Over the last two decades, significant effort, initiated by Pendry[2] and the earlier work by Veselago,[3] has been devoted to designing metamaterials (MMs) exhibiting exotic refractive behavior, e.g., $n \leq 0$, across several areas of physics. This includes electromagnetics, solid mechanics, and acoustics, see e.g., Refs. 4–6.

Having access to MMs with exotic material parameters opens a range of engineering possibilities. These range from exotic applications, like cloaking or beating the diffraction limit,[7] to the more "mundane" such as creating energy focusing and funneling devices[8] or flat lenses.[9] AHMMs like the one investigated in this Letter may find use in medical ultrasound, spatial filtering, or subwavelength imaging.

A recent paper[10] investigated quasi-two-dimensional acoustic MMs simultaneously exhibiting the effective negative mass density and bulk modulus. Promising theoretical results were presented, whereas experiments showed strong attenuation in the frequency region of doubly negative material parameters, severely limiting the practical usability of the exotic material property. While attenuation is observed for the AHMM slab considered in this Letter, it is smaller and the refractive behavior is clearly demonstrated.

Another recent Letter on the topic of AHMMs exhibiting negative refraction is Ref. 8. Here, a 3D AHMM slab, exhibiting $n \leq 0$, was investigated numerically and experimentally. Frequency dependent negative refraction was demonstrated over a ≈5% frequency band for waves at high angle of incidence, $\theta_1 \geq 25°$, and close to no refraction for $\theta_1 < 25°$. Where the AHMM considered in Ref. 8 only exhibits negative refraction for high values of θ_1, the AHMM slab considered in this Letter is specifically tailored to exhibit negative refraction from $\theta_1 = 0°$.

The systematic design method suggested in Ref. 1 considers a finite arrangement of identical unit cells inserted in a homogeneous acoustic medium, thereby inherently accounting for the coupling between the slab and the external field. Thus, the method simultaneously optimizes the slabs towards exhibiting the desired refractive behavior and a high energy transmission. This is in contrast to much earlier work on designing MMs with exotic material parameters which is based on a single periodic unit cell, not taking the finite size of the physical system into account, hereby neglecting the coupling into and out of the MM.

In short, the method considers a 2D exterior acoustic problem, modeled using the Helmholtz equation in a finite domain $\boldsymbol{\Omega}$, see Fig. 1(a), with a far field matching condition imposed along $\delta\boldsymbol{\Omega}$. The slab consists of an array of identical axisymmetric unit cells in $\boldsymbol{\Omega}_{\mathrm{d}}$. A localized near-plane wave, ψ, impinging on the slab at a prescribed angle of incidence, θ_1, and frequency, f, is introduced using a Neumann boundary condition at $\delta\boldsymbol{\Omega}_{\mathrm{PW}}$. The design problem is formulated as a partial differential equation (PDE)-constrained minimization problem with the objective function being the standard deviation between $|\psi|$ and the absolute value of a prescribed wave $|\psi_{\mathrm{target}}|$ over the sub-domain $\boldsymbol{\Omega}_{\mathrm{op}}$. The position of ψ_{target} selects the desired refraction angle at the slab interface, θ_{ref}, and by extension the index of refraction, $n_{\mathrm{target}}(\theta_1, f)$. The discrete material distribution problem is replaced by a continuous problem and is solved using density based topology optimization.[11]

[a)]Author to whom correspondence should be addressed. Electronic mail: raelch@mek.dtu.dk

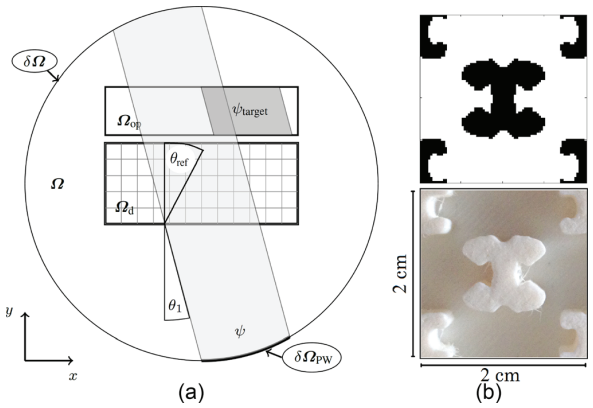

FIG. 1. (a) Sketch of model problem used in the systematic design method. Reproduced with permission from Christiansen and Sigmund, Struct. Multidiscip. Optim. **54**, 469–482 (2016). Copyright 2016 Springer Verlag. (b) [Top] Designed unit cell, Reproduced with permission from Christiansen and Sigmund, Struct. Multidicip. Optim. **54**, 469–482 (2016). Copyright 2016 Springer Verlag. [Bottom] 3D-printed unit cell.

The AHMM slab studied in this Letter consists of 20×9 unit cells of size $2\,\text{cm} \times 2\,\text{cm}$. The unit cell, originally presented in Ref. 1, is shown in the top image of Fig. 1(b). The slab was produced in ABS plastic [Stratasys ABS-P430] with measured values of density $\rho = 9.54 \times 10^2\,\text{kg/m}^3$ and bulk modulus $\kappa = 1.9\,\text{GPa}$, using 3D-printing (with an accuracy of 0.2 mm) as two blocks of 10×9 unit cells consisting of a $20\,\text{cm} \times 20\,\text{cm}$ baseplate of 1 cm thickness with the slab printed on top to a height of 0.6 cm. A 3D-printed unit cell is shown in the bottom image of Fig. 1(b). A result of the design and manufacturing process is that the unit cells along the edge of the MM slab have a slightly altered geometry, effectively removing the thin horizontal features at the top/bottom in the top image of Fig. 1(b).

The experimental setup, building on the approach in Ref. 12, is shown in Fig. 2(a). A $110\,\text{cm} \times 110\,\text{cm}$, 1 cm thick Polyvinyl chloride (PVC) plate served as a baseplate, [D]. A circular hole of radius 25 cm was cut in its center. A 1 cm thick freely rotatable PVC disk of (near) identical radius (0.5 mm accuracy) was placed into the hole. A rectangular hole of $40\,\text{cm} \times 20\,\text{cm}$ was cut in the disk and the AHMM slab inserted, [A]. A rectangular hole of $19\,\text{cm} \times 2\,\text{cm}$ was cut in the baseplate used to mount a line-array of 8 mini-loudspeakers, [B]. Wooden strips of 0.6 cm height were fixed along the baseplate edges. 13 cm wide blocks of open cell absorbing foam made from melamine resin [Basotec from BASF] of 0.6 cm height, [F], were attached along the strips. 6.5 cm deep, 1.5 cm wide wedges were cut into the blocks at a 2 cm interval for increased attenuation. A freely movable solid $150\,\text{cm} \times 150\,\text{cm}$, 1 cm thick transparent acrylic plate, [E], was placed on top of the wooden strips, forming a closed cavity. The cavity height assures an essentially two dimensional pressure field for $f < f_{\text{cut}} \approx 28.5\,\text{kHz}$. An 1/8'th in. microphone (Brüel and Kjær, Nærum Denmark) was flush mounted in the acrylic plate, [C]. The microphone was attached to a computer through a NEXUS pre-amplifier and a PULSE analyzer (Brüel and Kjær, Nærum Denmark). The loudspeakers were connected to a tone generator [Type 1049 (Brüel and Kjær, Nærum Denmark)] through a RME sound card [Hammerfall DSP Multiface II]. The output of each loudspeaker, $\psi_i, i \in \{1, 2, .., 8\}$, was calibrated to a level of (75 ± 0.1) dB SPL ref 20 μPa measured in the empty cavity at 7 cm distance. The output was then modulated from left to right as: $\psi_i = \psi_i + \Delta\psi_i, \Delta\psi_i \in \{-13.5, -7.0, -2.0, 0.0, 0.0, -2.0, -7.0, -13.5\}$ dB SPL ref 20 μPa. In this configuration, the loudspeakers emit a localized approximate plane wave front perpendicular to the array. Fig. 2(b) shows an aerial view of the setup, including markings of different measurement areas for later reference.

The angle of incidence, θ_1, of the pressure wave onto the slab was adjusted by rotating the disk (with uncertainty in θ_1 of $\leq \pm 0.25^\circ$). The pressure field was recorded by translating the acrylic plate, hereby scanning the flush mounted microphone across the cavity. An average of 20 measurements was used for each position (with uncertainty in position $\leq \pm 1\,\text{mm}$). The setup allows for measuring the field inside the slab, by aligning the microphone with void regions in the slab.

First, the pressure field for $\theta_1 = 14^\circ$ and $f = 8575\,\text{Hz}$ is considered. Outside the slab, the pressure was measured in a Cartesian grid with 1 cm spacing for $x \in [-20\,\text{cm}, 22\,\text{cm}]$ and $y \in [-20\,\text{cm}, 20\,\text{cm}]$. Inside the slab, it was measured in a staggered grid with two grid points per unit cell. A contour plot of the measured field is shown in Fig. 3(a). The black

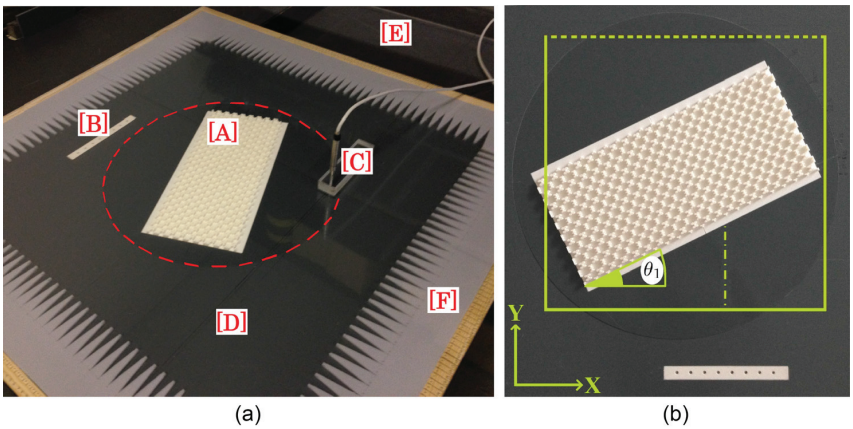

FIG. 2. (a) Experimental setup. [A]: AHMM slab, [B]: mini-loudspakers array, [C]: Flush mounted microphone, [D]: PVC baseplate, [E] Acrylic top plate, [F] Absorbing foam. The dashed red line indicates the rotatable disk. (b) Aerial view of experimental setup. The square outlines the measurement area for the data in Fig. 3(a). The data in Figs. 4(a)–4(c) and 5(c) were obtained along the horizontal dashed line and the dashed-dotted vertical line, respectively.

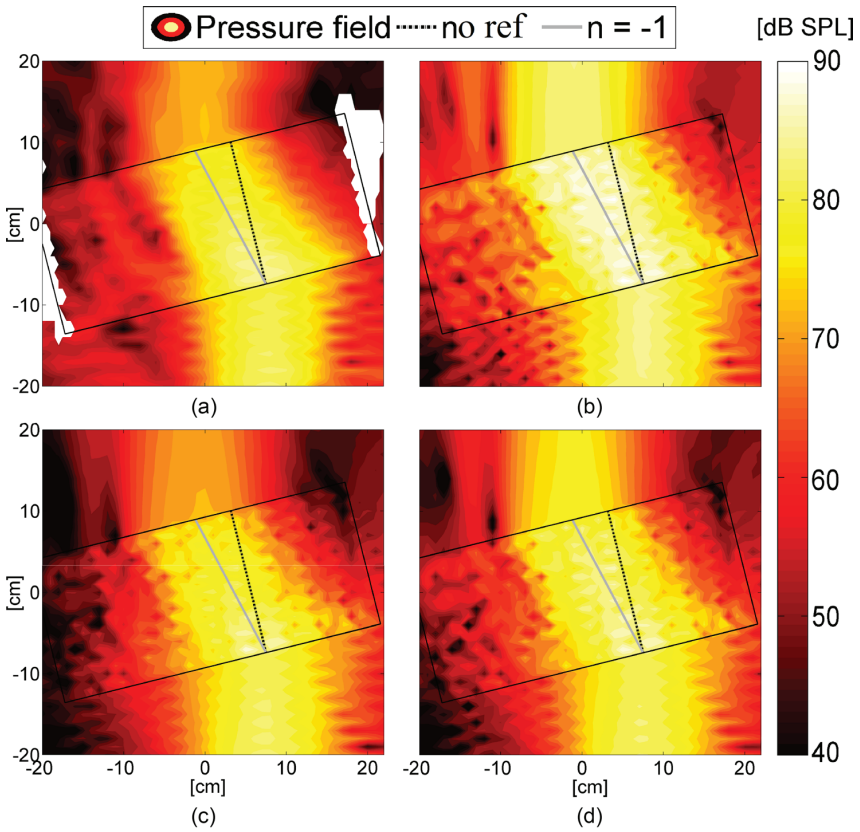

FIG. 3. Pressure field (dB SPL ref 20 μPa) in the area outlined by the square in Fig. 2(b), with $\theta_1 = 14°$ and $f = 8575$ Hz. (a) Measured field. (b) Simulated field (no attenuation). (c) Simulated field (attenuation in cavity and slab). (d) Simulated field (attenuation in cavity). Black square: Position of the slab. The black and gray lines indicate the direction of no refraction and the direction with $n = -1$, respectively.

square shows the position of the slab. The black dashed line denotes the direction with no refraction and the gray line denotes the direction of $n = -1$. White regions correspond to missing data. A simulation was performed in COMSOL 5.2 using a 2D setup mimicking the experimental setup. A line-array of eight point-like sources (modulated as in the experimental setup) was used to generate the pressure. Absorbing material was introduced along the domain edges. An acoustic model was used in the cavity and the Johnson-Champoux-Allard poroacoustic model was used in the absorbing material with the material parameters for the melamine foam sample number 33 in Ref. 13. A contour plot of the simulated pressure field, sampled similarly to the measurements, is presented in Fig. 3(b). A good agreement is observed between the two plots, the greatest discrepancy being the attenuation observed in the measured field. Another small discrepancy is a slight shift in position of the pressure field behind the slab. The physical reasons for the attenuation are discussed below. To estimate the magnitude of the attenuation, a reference measurement of the pressure field inside the empty cavity was performed and a value of 0.4 dB per wavelength identified. The result of a simulation including this estimated attenuation is presented in Fig. 3(d). This result shows an improved agreement with the measured result. An estimate of the attenuation in the slab was made by fitting simulated data to the measured field in Fig. 3(a) in the area $x \in [-20\,\text{cm}, 22\,\text{cm}]$, $y \in [12\,\text{cm}, 20\,\text{cm}]$. Additional attenuation of $\approx$0.56 dB per free field wavelength was identified inside the slab. The result of a simulation using the estimated attenuation inside the slab is presented in Fig. 3(c). The agreement between the field in Figs. 3(a) and 3(c) is now remarkable in terms of the pressure level and distribution.

The experimentally observed attenuation inside the chamber and slab can be explained by viscous and thermal boundary effects at surfaces. Based on a model for a circular duct with a diameter of 6 mm an attenuation of $\approx$0.32 dB per wavelength is calculated (see Chap. 7.7.1 of Ref. 14). This is close to the experimentally estimated 0.4 dB per wavelength in the cavity. Considering that the unit cell making up the slab contains narrow passages ($\approx$3 mm wide), increasing the influence of the boundary effects provides an explanation of the additional attenuation observed inside the slab.

Next, the field transmitted through the slab is considered, to investigate its refractive properties as a function of f and θ_1. Measurements were performed along the line $x \in [-20\,\text{cm}, 20\,\text{cm}]$ at a regular spacing of 1 cm at $y = 20$ cm (the dashed line in Fig. 2(b)). The frequencies $f \in \{8150\,\text{Hz}, 8575\,\text{Hz}, 9000\,\text{Hz}\}$ and the angular interval $\theta_1 \in [0°, 25°]$ were considered. Fig. 4 shows contour plots of the pressure as a function of horizontal position and θ_1. The black and gray lines correspond to no refraction and $n = -1$, respectively. The red line, with asterisks marking the measured angles, corresponds to the center of a Gaussian envelope fitted to the pressure data at each θ_1-value used to provide a consistent estimate of the refractive index. The first row of Fig. 4 presents measured data while the second row presents simulated data obtained using the COMSOL 5.2 model without attenuation. Negative refraction is seen for

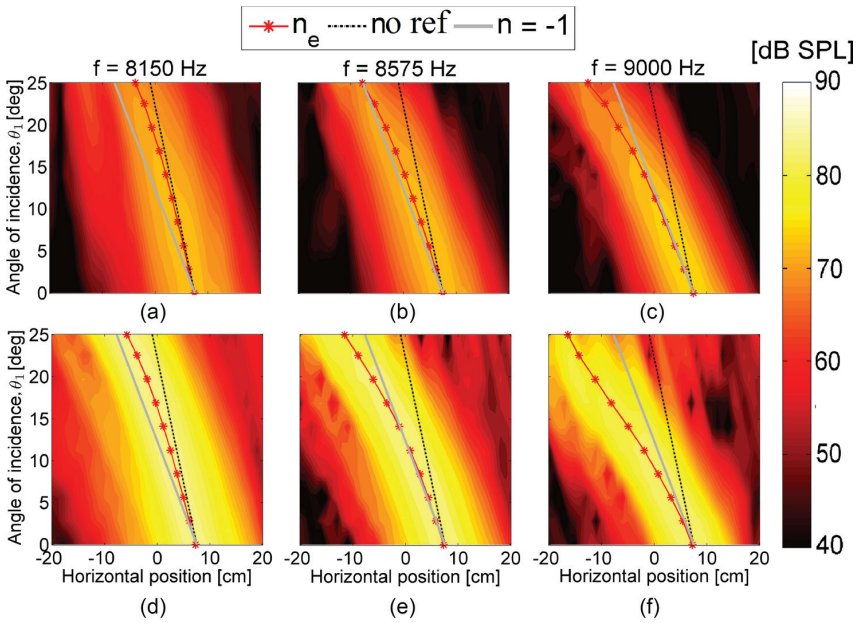

FIG. 4. Pressure field (dB SPL ref 20 μPa) along the horizontal dashed line in Fig. 2(b) as a function of θ_1. Black line: direction of no refraction. Gray line: direction with $n=-1$. Red line with asterisks: The position of the center of a Gaussian envelope fitted to the pressure data. (a)–(c) Measured pressure. (d)–(f) Simulated pressure (no attenuation).

all f and θ_1 in both the simulated and experimental data. While the pressure field is clearly transmitted through the slab across the full angular interval the field strength is seen to drop at high values of θ_1. In addition to the experimental and simulation results, Equal Frequency Surface (EFS) analysis is used to estimate $\theta_{\text{ref}}(f,\theta_1)$ as illustrated on Fig. 5(b). Fig. 5(a) shows the angle of refraction, θ_{ref} (see Fig. 1(a)), at the air to slab interface, calculated from the red line in Fig. 4, as a function of θ_1 for the six cases in Fig. 4 along with the three EFS calculations. Simulated data are plotted with unmarked solid curves, measured data with dashed curves and circles denoting the measured angles and the EFS result with solid curves and crosses. In all cases, the AHMM slab is observed to exhibit negative refraction across the full angular interval. A consistent increase in θ_{ref} is observed from the simulated to the measured data for all f. It is believed that the shift in θ_{ref} can be explained by a combination of the following effects. First, the effect of going from the 2D numerical model to the quasi 2D experimental setup. Second, a shift in the speed of sound, c, caused by differences in operating conditions, e.g., temperature, between the experimental and numerical setups. Third, the aforementioned boundary effects can cause a shift of the phase speed, c_p, inside the cavity, compared to the free field speed of sound c (see an analysis for a circular duct in Chapter 7.7 of Ref. 14). The EFS results agree qualitatively with the simulation results, but predict a higher value for θ_{ref} at high values of θ_1 for $f \in \{8575\,\text{Hz}, 9000\,\text{Hz}\}$. The small discrepancies are attributed to differences between the finite slab and the infinite EFS case.

Finally, the acoustic energy transmission at the air to slab interface at normal incidence is considered. The pressure field at $f=8575$ Hz and $\theta_1 = 0°$ was measured for $y \in [-22\,\text{cm}, -10\,\text{cm}]$, $x = 7.5$ cm (along the dashed–dotted line in Fig. 2(b)) at a 0.5 cm regular spacing. The measured field is shown in Fig. 5(c) (red line with asterisks). Two other graphs obtained from simulation data are included. These are: the pressure obtained from the COMSOL 5.2 model without attenuation (blue line) and with attenuation in the cavity and slab (magenta line). The magnitude of the reflection

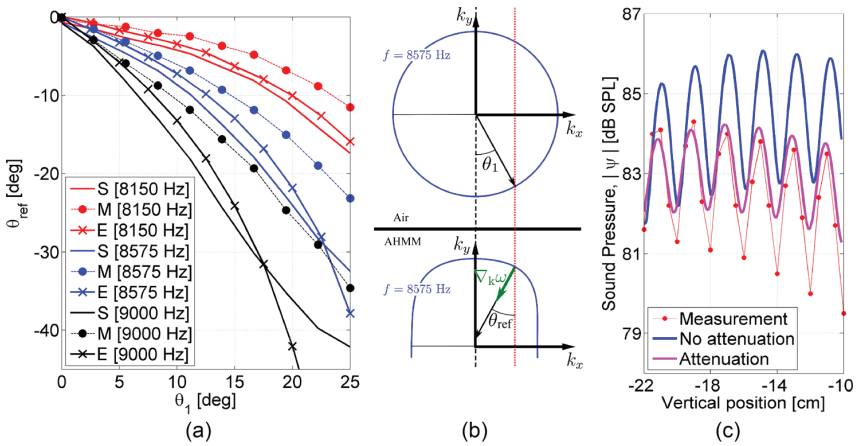

FIG. 5. (a) θ_{ref}, as a function of θ_1. Unmarked full curves correspond to the simulated data in the bottom row of Fig. 4. Dashed curves with circles correspond to the measured data in the top row of Fig. 4. Full curves with crosses correspond to the EFS analysis. (b) Illustration of EFS analysis for determining $\theta_{\text{ref}}(f,\theta_1)$ at air to AHMM interface. (c) Pressure along the vertical dashed dotted line in Fig. 2(b) at $\theta_1 = 0°$ and $f=8575$ Hz.

TABLE I. Reflectance, $|R|^2$, and transmittance, τ, for the air to AHMM interface, obtained from the data in Fig. 5(c).

Name	Reflectance: $\lvert R\rvert^2$	Transmittance: τ
Measurement	≈0.027	≈0.973
No attenuation	≈0.035	≈0.965
Attenuation	≈0.014	≈0.986

factor, $|R|$, at a material interface at normal incidence, may be calculated from the interference pattern in the reflected field using the peak ratio $s = \min|\psi|/\max|\psi|$, as $|R| = (1-s)/(1+s)$. $|R|$ is used to determine the transmittance, τ, through the interface as $\tau = 1 - |R|^2$, see Chapter 3.1 of Ref. 14.

$|R|^2$ and τ for the slab at $f = 8575$ Hz and $\theta_1 = 0°$ are estimated using the mean value (in Pascal) of $\max|\psi|$ and $\min|\psi|$ obtained from the six maxima and five intermediate minima for the data series in Fig. 5(c) (see Table I).

Agreement in τ, to within few percent, is observed when comparing simulation with measurement. The measured value of τ is smaller than the value which can be calculated from the data in Ref. 1 for the idealized model problem for which the AHMM was designed ($\tau_{\text{ideal}} \approx 0.985$). The deviation may be explained by limitations in the experimental setup. First, eight point-like sources do not perfectly model a plane wave front, leading to interference in the pressure field. Second, the slab was designed using a different number of layers, and a change in slab thickness can be expected to introduce Fabry Pérot like variations in the transmittance.

In summary, an AHMM slab obtained using the systematic design method proposed in Ref. 1 was investigated experimentally. When accounting for attenuation, a remarkable agreement was observed between simulated and measured data. Even without attenuation, good qualitatively agreement was shown, both with respect to the refractive behavior of the slab and the interface transmission, validated at normal incidence. The presence of thermal and viscous boundary layers at the cavity and slab surfaces is believed to be responsible for the observed attenuation. Negative refraction was demonstrated across a full 10% frequency band for $\theta_1 \in [0°, 25°]$. The experimentally observed refractive index was consistently shifted compared to the simulated results, a phenomenon also observed for the AHMM considered in Ref. 8.

Assistant Engineers Jørgen Rasmussen and Tom Arent Petersen at the Department of Electrical Engineering at the Technical University of Denmark assisted in preparing the experiments. The workshop at the Department of Mechanical Engineering at the Technical University of Denmark aided in the processing of components for the experimental setup. The 3D-printing laboratory FabLab at the Tecnical University of Denmark produced the test specimen. The work was financially supported by Villum Fonden through the research project *Topology Optimization—the Next Generation (NextTop)*.

[1]R. E. Christiansen and O. Sigmund, Struct. Multidiscip. Optim. **54**, 469–482 (2016).
[2]J. B. Pendry, Phys. Rev. Lett. **85**, 3966 (2000).
[3]V. G. Veselago, Sov. Phys. Usp. **10**, 509 (1968).
[4]X. Zhang and Z. Liu, Appl. Phys. Lett. **85**, 341 (2004).
[5]S. Zhang, W. Fan, N. C. Panoiu, K. J. Malloy, R. M. Osgood, and S. R. J. Brueck, Phys. Rev. Lett. **95**, 137404 (2005).
[6]F. D. Philippe, T. W. Murray, and C. Prada, Sci. Rep. **5**, 11112 (2015).
[7]R. V. Craster and S. Guenneau, in *Acoustic Metamaterials-Negative Refraction, Imaging, Lensing and Cloaking*, edited by R. Hull, C. Jagadish, J. R. M. Osgood, J. Parisi, and Z. M. Wang (Springer Science+Business Media, Dordrecht, 2013).
[8]V. M. Garciá-Chocano, J. Christensen, and J. Sánchez-Dehesa, Phys. Rev. Lett. **112**, 144301 (2014).
[9]P. V. Parimi, W. T. Lu, P. Vodo, and S. Sridhar, Nature **426**, 404 (2003).
[10]R. Graciá-Salgado, V. M. Garciá-Chocano, D. Torrent, and J. Sánchez-Dehesa, Phys. Rev. B **88**, 224305 (2013).
[11]M. P. Bendsøe and O. Sigmund, *Topology Optimization* (Springer, 2003).
[12]R. E. Christiansen, E. Fernandez-Grande, and O. Sigmund, J. Acoust. Soc. Am. **138**(6), 3470 (2015).
[13]N. Kino and T. Ueno, Appl. Acoust. **69**, 325 (2008).
[14]F. Jacobsen and P. M. Juhl, *Fundamentals of General Linear Acoustics* (Wiley, 2013).

Publication [P6]

Designing Directional Acoustic Devices Using Topology Optimization - from method to experimental validation

Design of directional acoustic devices using Topology Optimization – from method to experimental validation

Rasmus E. Christiansen[a)]
Section for Solid Mechanics, Department of Mechanical Engineering, Technical University of Denmark (DTU), Building 404, Nils Koppels Allé, DK-2800 Kongens Lyngby, Denmark

Efren Fernandez-Grande[b)]
Acoustic Technology, Department of Electrical Engineering, Technical University of Denmark (DTU), Building 352, Oersteds Plads, DK-2800 Kongens Lyngby, Denmark

(Dated: May 26, 2016)

The paper presents a topology optimization based method for designing acoustic focusing devices, capable of tailoring the sound emission pattern of one or several sources. The method is demonstrated numerically considering devices optimized for directional sound emission in two dimensions and is experimentally validated using three dimensional prints of the optimized designs. The emitted fields exhibit a level difference of at least 15 dB on axis relative to the off-axis directions, and over frequency bands of approximately an octave. It is demonstrated to be possible to design focusing devices of dimensions comparable to the acoustic wavelength, a frequency range which is typically problematic, as well as devices operating at higher frequencies. The classical parabolic reflector is used as a benchmark. The devices designed using the proposed method are shown to outperform the latter in terms of directivity and maximum side-lobe level over nearly an octave band. Performance robustness towards uniform spatial production errors in the designed devices is assured by including perturbations of the geometry in the design formulation.

PACS numbers: 43.20.-f
Keywords: Topology Optimization; Acoustic focusing; Directional acoustic radiation; Experimental validation

I. INTRODUCTION

The paper proposes a method for designing directional sound emission devices based on the gradient based optimization technique of topology optimization.[2] Examples of optimized devices are provided along with the experimental validation of several devices. The agreement between the predicted performance and the experimental measurements underline the effectiveness of the model and method.

In acoustics it is often of interest to generate directionally focused sound fields, i.e. sound fields where the waves are emitted in a specific direction, and the acoustic energy is spatially confined. The problem is of fundamental interest for sound field reproduction purposes,[6,7,28] acoustic measurements,[20] long range emission,[15,30] noise control and others,[22]. However acoustic perturbations will in the general case not result in a directional and spatially confined sound field. The problem is thus of relevance both for sound emission problems, and the reciprocal problem of acoustic reception/sensing,[1] mostly concerned with enhancing the directional sensitivity of a measurement system.

The most common and perhaps most intuitive focusing device is the parabolic reflector,[10,19,30] which is based on basic geometrical considerations that are valid when assuming ray propagation. Nonetheless, these considerations do not contemplate the actual wave behavior of sound waves observed at low frequencies, and fail to account for fundamental phenomena such as scattering and diffraction. As a result, these devices are effective at high frequencies and perform quite well in a wide frequency sense, but their effective directionality is compromised, particularly at low frequencies. A fundamentally different alternative is the use of active systems, where the phase reproduction via an array of loudspeakers can be used to achieve the wanted directivity. This requires the introduction of additional sources, which can give rise to unwanted artifacts due to constructive interference between the sources.[17]

Extensive work, which served as inspiration for the present work, has treated the shape and/or topology optimization of an acoustic horn, for improved transmission among other goals.[3,29] Other work[11] treating the application of topology optimization to the problem of local pressure reduction also served as a basis for this work. Other works of interest concerning the application of topology optimization to problems in acoustics, focused on limiting sound emission include, Du and Olhoff[12], Kook et al[18].

The proposed method allows for designing focusing devices that use multiple sources, in order to maximize the total power output of the device, without relying on ac-

[a)]Electronic address: raelch@mek.dtu.dk
[b)]Electronic address: efg@elektro.dtu.dk

tive cancellation of the emitted fields, but rather on the focusing of the total energy emitted. The devices are designed using density based topology optimization, assuming free-field propagation (in 2D) governed by the Helmholtz equation with suitable boundary conditions. The design problem is formulated as a minimization problem. The objective function being the difference, in a suitable measure, between the pressure field emitted by on or more acoustic sources and a prescribed target pressure field. A continuous design field, used to control the material distribution, is introduced and the objective function minimized over the design field. The design field is subjected to a double filtering and projection strategy,[9]. This is done, in part to decrease the sensitivity of the device towards uniform geometric perturbations, which might be encountered in production, and in part as the method result in designs consisting nearly purely of solid and air as the direct output from the design process. Hereby limiting the need for post processing. The use of the continuous design field allows for the application of the mathematical programming based optimization algorithm GCMMA,[25] to solve the minimization problem.

Although the present work only considers a 2D problem the proposed design formulation can be extended to cylindrically symmetric problems by considering the appropriate PDE,[27] as well as full 3D problems, however with a significant increase in the computational efforts in solving the PDE-problem.

II. THE DESIGN PROCEDURE

The goal of the design procedure is to create devices capable of shaping the pressure field emitted by a number of point-like sources inside the device to approximate a specified target pressure field. The examples presented in the paper address the design of devices emitting locally plane wavefronts in the near field, resulting in directional far field emission. However the proposed method can be used to design devices which generate other specific pressure fields as well.

A. The Model Problem

An exterior acoustic model problem is used as the basis for the design problem. It is defined on the domain, $\mathbf{\Omega} \subset \mathbb{R}^2$, sketched in Fig. 1. $\mathbf{\Omega}$ is truncated by the curve $\delta\mathbf{\Omega}$, along which a far field matching condition is imposed to fulfill the Sommerfeld radiation condition. Two sub-domains are defined on $\mathbf{\Omega}$. These are the design domain, $\mathbf{\Omega}_\mathrm{d}$: the sub-domain containing the directional sound emission device under design and the target domain, $\mathbf{\Omega}_\mathrm{op}$: the sub-domain on which the objective function to be minimized is defined. Finally a collection of $i \in \mathbb{N}$ point-like sources, denoted δP_i, are distributed in $\mathbf{\Omega}_\mathrm{d}$ and modeled using a Neumann

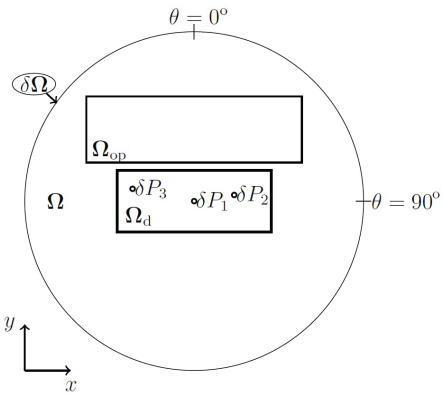

FIG. 1: Model problem sketch. $\mathbf{\Omega}$: Truncated Domain. $\delta\mathbf{\Omega}$: Truncation boundary. $\mathbf{\Omega}_\mathrm{op}$: Optimization domain. $\mathbf{\Omega}_\mathrm{d}$: Design domain. $\delta\mathbf{P}_i$: Point-like sources. $\theta = 0^\mathrm{o}$ and $\theta = 90^\mathrm{o}$: Denote the angular convention.

boundary condition allowing for an arbitrary shape and size of the sources if desired. The system is modeled using the Helmholtz equation and boundary conditions,

$$\nabla \cdot (\rho(\mathbf{x})^{-1}\nabla p(\mathbf{x})) + \omega^2\kappa(\mathbf{x})^{-1}p(\mathbf{x}) = 0, \quad \mathbf{x} \in \mathbf{\Omega}, \tag{1}$$

$$\lim_{|\mathbf{r}|\to\infty} \sqrt{|\mathbf{r}|} \cdot \left(\frac{\partial p(\mathbf{r})}{\partial |\mathbf{r}|} - \mathrm{i}\sqrt{\frac{\rho}{\kappa}}\omega p(\mathbf{r}) \right) = 0, \quad \mathbf{x} \in \delta\mathbf{\Omega} \tag{2}$$

$$\mathbf{n} \cdot \nabla p = -\mathrm{i}\rho\omega U, \quad \mathbf{x} \in \delta P. \tag{3}$$

Here $\mathbf{x}$ and $\mathbf{r}$ denote the spatial dependence in Cartesian and Polar coordinates respectively and $\mathbf{n}$ denotes the normal vector. i is the imaginary unit, p denotes the pressure field, $\omega = 2\pi f$ is the angular frequency and f is the frequency. U is the vibrational velocity of the source. $\rho(\mathbf{x})$ and $\kappa(\mathbf{x})$ are the density and bulk modulus respectively, taking values of either solid material or fluid medium (air). The introduction of a solid material in $\mathbf{\Omega}_\mathrm{d}$ would in the general case require a modification of the model problem to account for waves exited in the solid. However, in the present case, the choice of materials result in an impedance difference of more than three orders of magnitude between solid and air regions. Hence any waves excited in the solid will not perturb the pressure field in the air significantly and vise versa. This assertion has been validated using a full elasto-acoustic model in COMSOL Multiphysics 5.2a and through the experiments presented in the paper, see also Christiansen et al [8].

B. The Design Problem

The design problem is formulated as a PDE-constrained optimization problem, for which the following objective function to be minimized is defined,

$$\Phi = c_s \int \left(|p|^2 - |p_{\text{target}}|^2\right)^2 \mathrm{d}\boldsymbol{\Omega}_{\text{op}} \geq 0. \tag{4}$$

Here p_{target} describes the desired pattern of the sound pressure field emitted by the device and c_s is a scaling parameter chosen to improve the convergence of the design process. $\Phi = 0$ corresponds to a perfect match in pressure level between p and p_{target} everywhere in $\boldsymbol{\Omega}_{\text{op}}$.

For all cases treated in this paper the target field, p_{target}, is chosen to be a localized plane wave, p_{EPW}, truncated by a Gaussian envelope, originating in and traveling away from $\boldsymbol{\Omega}_{\text{d}}$. For this choice of p_{target}, minimizing Φ in (4), may be thought of as maximizing the energy in the main lobe in front of the device while minimizing side lobe levels.

$$p_{\text{EPW}} = A\mathrm{e}^{-\left(\frac{(\mathbf{x}-\mathbf{x}_w)\cdot\hat{\mathbf{d}}}{\delta_w}\right)^2} \mathrm{e}^{-\mathrm{i}\omega(\mathbf{x}\cdot\mathbf{d})} \mathrm{H}((\mathbf{x}-\mathbf{x}_w)\cdot\mathbf{d}), \tag{5}$$

$$\mathbf{d} = \begin{pmatrix} \cos(\theta+\pi/2) \\ -\sin(\theta+\pi/2) \end{pmatrix}, \quad \mathbf{x}_w = \begin{pmatrix} x_w \\ y_w \end{pmatrix}. \tag{6}$$

Here A is the wave amplitude, $\mathbf{d}$ controls the propagation direction, $\hat{\mathbf{d}}$ denotes the transpose of $\mathbf{d}$, $\mathbf{x}_w$ is the position of the center of the wave, δ_w controls the width of the envelope and $\mathrm{H}(\cdot)$ denotes the Heaviside projection function. Note the untraditional angular convention illustrated in Fig. 1.

The amplitude of p_{EPW} is selected by equating the power contained in p_{EPW} to the power emitted from all sources placed in $\boldsymbol{\Omega}_{\text{d}}$, denoted $\mathrm{P_s}$, and solving for A. The sound power emitted from a collection of time harmonic acoustic sources is calculated as,[16]

$$\mathrm{P_s} = \int_S \mathbf{n}\cdot\mathbf{I}\ \mathrm{dS} = \int_S \mathbf{n}\cdot\left(\frac{1}{2}\Re(p\ \mathbf{u}^*)\right)\mathrm{dS}, \tag{7}$$

where S denotes the surface, $\mathbf{n}$ is the surface normal, $\mathbf{I}$ is the time averaged sound intensity, p is the pressure, $\mathbf{u}$ is the particle velocity, $\Re$ denote the real part and $(\cdot)^*$ denotes the complex conjugate.

The objective function, Φ, is minimized by introducing an optimized design in $\boldsymbol{\Omega}_{\text{d}}$ consisting of a distribution of solid material placed in an air background. The distribution of the solid material is controlled by an auxiliary field $\xi(\mathbf{x})$ used to interpolate the material parameters, ρ and κ between solid and air as,

$$\rho^{-1} = \rho_{\text{air}}^{-1} + \xi(\rho_{\text{solid}}^{-1} - \rho_{\text{air}}^{-1})\ , \tag{8}$$

$$\kappa^{-1} = \kappa_{\text{air}}^{-1} + \xi(\kappa_{\text{solid}}^{-1} - \kappa_{\text{air}}^{-1}). \tag{9}$$

A detailed description of the optimization problem solved to minimize (4), the discretization of the design field, ξ, into a piecewise constant field of a finite number of design variables and the techniques used to regularize the design field, minimize the need for post processing and assure geometric robustness towards prescribed variations in the design is provided in appendix A.

C. The Design Domain

The design domain $\boldsymbol{\Omega}_{\text{d}}$, is further divided into three subdomains denoted; the designable $\boldsymbol{\Omega}_{\text{d,d}}$, the empty $\boldsymbol{\Omega}_{\text{d,e}}$, and the filled $\boldsymbol{\Omega}_{\text{d,f}}$, sub-domain. $\boldsymbol{\Omega}_{\text{d,d}}$ is the freely designable part of $\boldsymbol{\Omega}_{\text{d}}$, where material can be introduced and removed during the design procedure. $\boldsymbol{\Omega}_{\text{d,e}}$ and $\boldsymbol{\Omega}_{\text{d,f}}$ are fixed to be empty of and filled with solid material, respectively. In the numerical examples presented in the following, two configurations for $\boldsymbol{\Omega}_{\text{d}}$ are considered. These are illustrated in Fig. 2a and Fig. 2b respectively. Here, $\boldsymbol{\Omega}_{\text{d,d}}$ is colored light gray while $\boldsymbol{\Omega}_{\text{d,f}}$ is marked using dark gray and $\boldsymbol{\Omega}_{\text{d,e}}$ is colored white. The first configuration seen in Fig. 2a, henceforth denoted C_1, consists of a fixed sub-domain with one edge shaped as a parabolic reflector with the acoustic source placed in its focal point and a fixed shielding in front of the point source. The boundary of the reflector is defined by e_1 through e_4 in (10),

$$\mathrm{e}_1 : y = \frac{0.8}{\mathrm{w}}x^2 - 0.25\mathrm{w}, \quad \mathrm{e}_2 : y = -0.25\mathrm{w}, \tag{10}$$
$$\mathrm{e}_3 : x = -0.5\mathrm{w}, \quad \mathrm{e}_4 : x = 0.5\mathrm{w}.$$

The second configuration seen in Fig. 2b and denoted C_2, consists of the fixed sub-domain along three of the four edges of $\boldsymbol{\Omega}_{\text{d}}$ to help guide the sound and three point like sources distributed inside $\boldsymbol{\Omega}_{\text{d}}$. For both configurations the origin is taken to be the center of $\boldsymbol{\Omega}_{\text{d}}$.

Through experimentation it was found that restricting $\boldsymbol{\Omega}_{\text{d,d}}$ in front of the acoustic source(s) to a equiangular triangular grid, with grid size d_{G} and circular inclusions of radius r_{G}, as illustrated by the light gray circles in Fig. 2, improved the reliability of the design procedure. The restriction makes it impossible for a large region of intermediate material/air to form in front of the source during the design process, which at a the later stages of the design process risks turning into a block of solid material, as the projection strength in the continuation approach increases, effectively blocking the pressure field emitted from the device. (See section A.2 regarding the continuation approach). For both cases a circular region of radius r_P around each acoustic source is fixed as air, i.e. belonging to $\boldsymbol{\Omega}_{\text{d,e}}$. A number of additional parameters are used to define the different regions of $\boldsymbol{\Omega}_{\text{d}}$ as seen from Fig. 2.

III. IMPLEMENTATION AND PARAMETER CHOICES

An implementation of the design procedure was written using MATLAB R2013a. A hybrid wave based and finite element method (hybrid WBM-FEM),[14,21] was used to discretize the model equations. $\boldsymbol{\Omega}_{\text{d}}$ was discretized with the FEM using first order bi-linear finite elements. $\boldsymbol{\Omega}\backslash\boldsymbol{\Omega}_{\text{d}}$ was discretized using the WBM. An impedance coupling was used to connect the FEM and WBM domains, described in

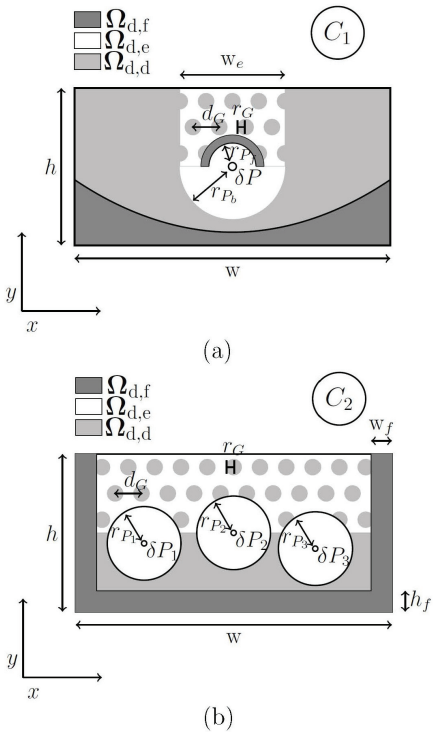

FIG. 2: Configurations of the design sub-domain, $\mathbf{\Omega}_{\mathrm{d}}$. Filled sub-domain: $\mathbf{\Omega}_{\mathrm{d,f}}$. Empty sub-domain: $\mathbf{\Omega}_{\mathrm{d,e}}$. Designable sub-domain: $\mathbf{\Omega}_{\mathrm{d,d}}$. Domain width: w. Domain height: h. (a) Single source configuration, denoted C_1, with fixed parabolic reflector and shielding plate. (b) Three source configuration, denoted C_2, with fixed box along three of four edges.

TABLE I: Parameters used in the design problems.

Domain: (Fig. 1)	
Simulation domain, $\mathbf{\Omega}$:	$[-1.25, 1.25]\mathrm{w} \times [-1.25, 1.25]\mathrm{w}$.
Design domain, $\mathbf{\Omega}_{\mathrm{d}}$:	$[-0.5, 0.5]\mathrm{w} \times [-0.25, 0.25]\mathrm{w}$.
Optimization domain, $\mathbf{\Omega}_{\mathrm{op}}$:	$\mathbf{\Omega} \backslash \mathbf{\Omega}_{\mathrm{d}}$.
Design: (Fig. 2)	
Design width and height:	$\mathrm{w} = 0.1$ m, $h = 0.5\mathrm{w} = 0.05$ m.
Triangular grid restriction:	$r_G = 0.01\mathrm{w}$, $d_G = 0.05\mathrm{w}$.
Case $\mathbf{C}_1$: (Fig. 2a)	
	$\delta P = \langle 0, 0.0625\mathrm{w} \rangle$.
	$r_{P_f} = 0.05\mathrm{w}$, $r_{P_b} = 0.1\mathrm{w}$.
	$\mathrm{w}_e = 2r_P = 0.1\mathrm{w}$.
Initial field value in $\mathbf{\Omega}_{\mathrm{d,d}}$:	$\xi_{\mathrm{ini}}(\mathbf{x}) = 0.2, \mathbf{x} \in \mathbf{\Omega}_{\mathrm{d,d}}$.
Case $\mathbf{C}_2$: (Fig. 2b)	
	$\delta P_1 = \langle -0.3125\mathrm{w}, -0.0875\mathrm{w} \rangle$
	$\delta P_2 = \langle 0, 0 \rangle$
	$\delta P_3 = \langle 0.1875\mathrm{w}, -0.05\mathrm{w} \rangle$.
	$r_{P_i} = 0.1\mathrm{w}, i \in \{1, 2, 3\}$.
	$\mathrm{w}_f = \mathrm{h}_f = 0.03\mathrm{w}$.
Initial field value in $\mathbf{\Omega}_{\mathrm{d,d}}$:	$\xi_{\mathrm{ini}}(\mathbf{x}) = 0.0, \mathbf{x} \in \mathbf{\Omega}_{\mathrm{d,d}}$.
Target field: (Eqn. (5))	
Envelope width:	$\delta_{\mathrm{w}} = 0.6\mathrm{w}$.
Wave center position:	$\mathbf{x}_{\mathrm{w}} = \langle 0, 0 \rangle$.
Propagation direction:	$\mathbf{d} = \langle 0, 1 \rangle$.
Optimization: (App. A)	
Projection strength: (A7)	$\beta_{\mathrm{ini}} = 2$.
Projection levels: (A7)	$\eta_1 = 0.5, \eta_2 \in \{0.3, 0.7\}$.
Filter radius: (A5)	$R_1 = 0.02\mathrm{w}$.
Volume constraint: (A2)	$V = 0.25$.
Discretization:	300 finite elements per w.
Material parameters:	
Density, [kg/m^3]: (8)	$(\rho_{\mathrm{solid}}, \rho_{\mathrm{air}}) = (2643, 1.204)$.
Bulk modulus, [N/m^2]: (9)	$(\kappa_{\mathrm{solid}}, \kappa_{\mathrm{air}}) = (142 \cdot 10^3, 687 \cdot 10^8)$.

chapter 7 of Pluymers[21]. The Sommerfeld radiation condition was implemented using the proposal in chapter 6 of Pluymers[21]. COMSOL Multiphysics 5.2a was used to validate the hybrid WBM-FEM solver. All numerical performance results presented in the following, was obtained using an acoustic model in COMSOL Multiphysics 5.2a on thresholded versions of the optimized devices.

The devices considered in the following have been designed using the parameter values provided in table I. A total of $300 \times 150 = 45000$ quadrilateral first order finite elements are used to discretize $\mathbf{\Omega}_{\mathrm{d}}$, matching the resolution of the 3D-printer used to produce the devices used in the experimental validation.

IV. EXPERIMENTAL SETUP

No design or design methodology can be fully trusted before it has been experimentally validated. With this in mind a two-dimensional anechoic chamber is built in order to provide a two-dimensional free-field space in which to test the designs. A schematic of the experimental setup is provided in Fig. 3a and a picture of the setup in Fig. 3b including a test specimen and the flush mounted microphone. The dimensions of the chamber and specifications regarding the components as well as relevant material parameters may be found in table II in appendix B. The chamber is constructed using a PVC plate as a bottom-plate, with wooden strips at its edges, and an acrylic plate as a top-plate, resting on the wooden strips. Open cell absorbing foam strips of 0.13 m width, made from melamine resin [Basotec from BASF, Germany], with 6.5 cm deep wedges cut into them, are placed along the wooden strips. The limited height of the chamber ensures that only a two dimensional sound field can propagate in the chamber below the cutoff frequency, $f_{\mathrm{cutoff}} \approx 28.5$ kHz (assuming a speed of sound of $c_{\mathrm{sound}} = 343\frac{\mathrm{m}}{\mathrm{s}}$). The source used is a 6 inch loudspeaker connected to a funnel and a wave guide which is connected to a hole in the specimen under test, effectively acting as an approximate point source. A circular hole is drilled in the center of the top-plate allow-

ing for the flush mounting of an 1/8'th inch microphone (Brüel and Kjær (Naerum, Denmark)). The microphone is connected to the data acquisition system, a NEXUS pre-amplifier and a PULSE analyzer manufactured by Brüel and Kjær (Naerum, Denmark), and a computer for data acquisition. The measurements are performed as follows. A test specimen is placed in the chamber and the wave guide attached appropriately. The source is driven with pseudorandom noise bandlimited to 6.4 kHz, using 1 Hz spectral resolution and 20 averages. The flush mounted microphone is then scanned manually along the measurement points: a half circle of radius $r_c = 0.22\ \text{m} \pm 10^{-3}\ \text{m}$, centered at the hole in the test specimen. The angular resolution of the scanning is 2.5° from $\theta = 0°$ to $\theta = 180°$. A grid is marked on the chamber for precision of the positioning system. The uncertainty in the microphone placement is estimated to ≈ 1 mm in both spatial directions.

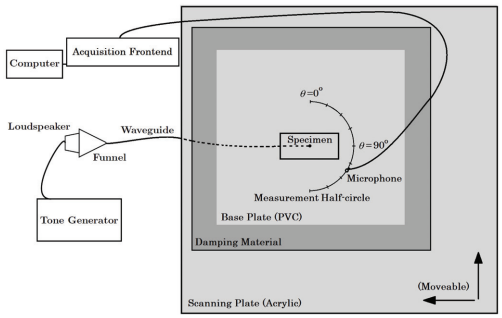

(a)

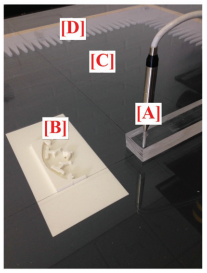

(b)

FIG. 3: (color online) (a) Schematic of the experimental setup including the chosen angular convention ($\theta = 0°$ in front of the test specimen). (b) Picture of the anechoic chamber, [A] the microphone, [B] a test specimen, [C] the PVC base plate under the acrylic scanning plate and [D] the absorbing foam and wooden strips.

A reference measurement on a test specimen without a design (i.e. a point source in the empty chamber) is performed for calibration purposes and to investigate the field in the cavity. For frequencies, $f > 4,8$ kHz ($\frac{\text{w}}{\lambda} \gtrsim 1.4$) a maximal variation in the pressure of 2 dB SPL as a function of angle ($\theta \in [0°, 180°]$) is observed. For 3.4 kHz $< f <$ 4.8 kHz a maximal variation in pressure of 3 dB SPL is observed and for $f <$ 3.4 kHz a maximal variation of 6 dB SPL is observed. The background noise in the chamber is measured at $\theta = 0°$ across the full frequency spectrum considered. Based on the measurement a lower limit on all subsequent measurements is defined to be 3 dB SPL above the background. All measured data points below this limit are removed, and for the visualization of the results replaced with dark gray (see e.g. Fig. 8k).

V. RESULTS

Two measures are used to evaluate the devices. The first is the far field sound pressure as a function of angle, θ, relative to the far field sound pressure at $\theta = 0$,

$$P_m(\theta, f) = 20 \log_{10} \left(\frac{|p_{\text{far}}(\theta, f)|}{|p_{\text{far}}(\theta = 0°, f)|} \right). \qquad (11)$$

The far field pressure, $p_{\text{far}}(\theta, f)$, is approximated using the Kirchoff-Helmholtz integral equation, see e.g. Appendix A.2 of Bai et al[1]. The second measure is the far field sound pressure on axis ($\theta = 0°$) relative to the far field of a monopole radiating identical power into free space,

$$\Delta L_{\text{dB}}(f) = 20 \log_{10} \left(\frac{|p_{\text{far}}(\theta = 0°, f)|}{|p_{\text{monopole,far}}(f)|} \right). \qquad (12)$$

A. Reference - The Parabolic Reflector

The parabolic reflector is a well known and frequently used design for directional emission/reception in both acoustics and electromagnetics. Assuming ray based propagation for the sound field and using geometric arguments it is easy to show that the parabola is an optimal solution for converting the field impinging on it from a point source placed at its focal point to a localized near-plane wave, as illustrated in Fig. 4a. However, the fact that the ray-based model is only strictly valid for $f \to \infty$ and disregard fundamental wave propagation phenomena, opens a potential for design improvement. Another obvious limitation of the reflector is that it is ill-suited if several sources are considered.

A parabolic reflector of width w, described by the equations in (10), with a shielding in front of the source identical to the one for C_1 in section II.C, is considered as a reference, R_p. Figure 4b shows the design field for R_p with a source at its focal point ($\delta P = \langle 0, 0.0625w \rangle$), illustrated by a red circle. Figure 4c shows the calculation of $P_m(\theta, f)$ for the parabolic reflector, R_p. It is observed that for $\frac{\text{w}}{\lambda} < 1.5$ the directivity of R_p is poor and that for $1.1 < \frac{\text{w}}{\lambda} < 1.5$

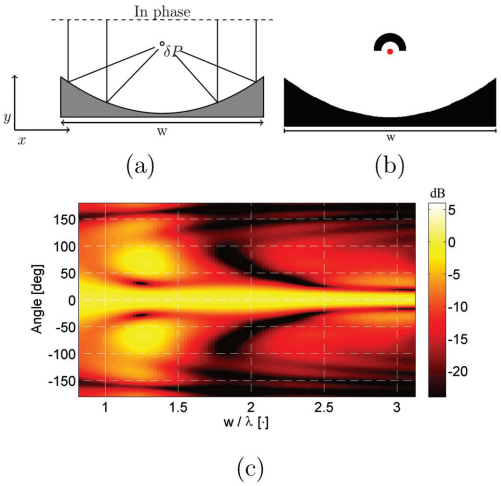

FIG. 4: (color online) (a) Ray-based model for pressure field emitted by point source placed in front of a parabolic reflector. (b) Design field for reference parabolic reflector R_P. (c) Performance measure $P_m(\theta, f)$ for R_p measured in dB. The first axis indicate the parabola width w, relative to the wavelength in air, λ.

the side lobes and main lobe are seen to have equal value of P_m.

B. A Low Frequency Device

As a first example of applying the proposed method, consider the problem of designing a device, with a width approximately equal to the wavelength in the frequency range where the device is designed to operate. This design problem is denoted D_1. The central frequency of operation, f_{c,D_1}, is chosen to correspond to the wavelength $\lambda_1 \approx 0.89$w, and a $\Delta f_{D_1} = 50\%$ frequency band centered at f_{c,D_1} is considered. The design process is executed using $i = 9$ equidistant frequency values in $f \in [f_{c,D_1} - 0.5\Delta f_{D_1}, f_{c,D_1} + 0.5\Delta f_{D_1}]$ and $j = 2$ projection levels, $\eta_2 \in \{0.3, 0.7\}$.

Figure 5 shows a convergence plot for the design process for D_1, using a total of 333 design iterations. It presents $\Phi_{i,j}$ as a function of design iteration number for all, $i \cdot j = 18$ realizations. The maximum value of Φ across the 18 realizations for each design iteration is marked with a black square. It is observed that the active objective function value, $\max_{i,j}(\Phi)$, changes several times during the optimization. The iteration numbers at which the β-value for the projection scheme increased are indicated in the figure using gray vertical lines. Jumps in the objective value are observed at semi-regular intervals. The jumps coincide with increases in the β-value for the projection operation in all but one case. These jumps are to be expected since increasing the β-value, i.e. steeper projection, causes an abrupt change in the design which in turn affects the objective value.

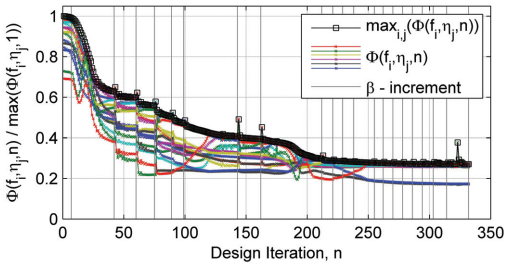

FIG. 5: (color online) (Crosses) Normalized objection function value as a function of design iteration, n, for the $i \cdot j = 18$ realizations. (Black squares) $\max_{i,j}(\Phi)$ at each iteration. (Gray vertical lines) β-increments.

1. Design

The final design field, $\hat{\hat{\xi}}(\eta_j), j \in \{1, 2\}$, for the two projection levels used in the optimization, are presented in gray scale in Figs. 6a and 6b respectively. Black indicates solid material and white indicates air and a red circle is included to illustrate the position of the point-like source. As is the point of applying the robust approach small variations are observed around each design feature for the designs in Figs. 6a and 6b, showing that the design has indeed been optimized to function under a small uniform geometric variation. The output of the design procedure is seen to consist almost exclusively of solid and air regions. A post processing step is performed on the design in Fig. 6b, where the smallest features removed as seen in in Fig. 6c. The effect of the feature removal on the sound field was found to have negligible impact on the designs performance, while in turn improving producibility.

2. Numerical Performance

Figures 7a and 7b show the performance measure $P_m(\theta, f \sim \frac{w}{\lambda})$ (11), for the post processed design in Fig. 6c for the design problem, D_1, and for the reference parabolic reflector, R_p, respectively. The frequency interval for which D_1 was optimized is marked by white vertical lines and a green bar in both figures. From Fig. 7a it is seen that in the frequency interval for which D_1 was optimized, the main lobe (centered at $\theta = 0^o$) contains most of the emitted sound. In fact the pressure in the main lobe is more

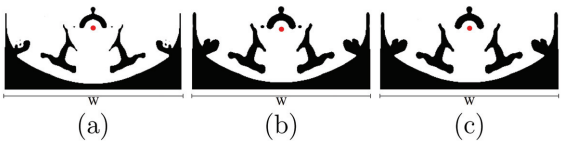

(a) (b) (c)

FIG. 6: (color online) Design field, $\tilde{\tilde{\tilde{\xi}}}$. (a) Design field projected at $\eta_2 = 0.7$. (b) Design field projected at $\eta_2 = 0.3$. (c) Post processed design field projected at $\eta_2 = 0.3$ using Heaviside projection. Black corresponds to solid material and white corresponds to air.

than 15dB higher than in the rest of the angular interval. In contrast when considering the result for the reference reflector in Fig. 7b it is seen that the pressure in the main lobe is similar to the pressure in the side lobe (centered at $\theta \approx 75^{\circ}$), and that the reflector generally emits a higher sound pressure in all directions outside of the main lobe ($|\theta| > 35^{\circ}$). Hence across the interval of optimization the optimized design clearly outperforms the reflector in terms of directivity.

The increase in ΔL_{dB}, (12), is shown in Fig. 7c for D_1 (blue circles) and R_p (black squares). The optimization interval is highlighted using vertical lines. It is seen that the optimized design, D_1 emits a higher sound pressure than the reference, R_p, across the full optimization interval. The increase in sound pressure ranges from 5 dB to 10 dB. In addition the variations in the pressure level are smaller. Variations of $\approx$ 3 dB, are observed for D_1 compared to ≈ 6 dB for R_p.

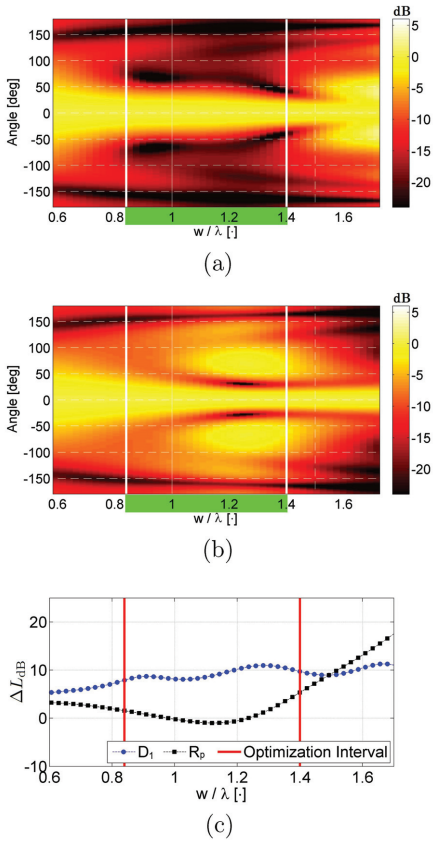

FIG. 7: (color online) (a)-(b) Performance measure, $P_m(\theta, f)$, for (a) the optimized design, D_1, (b) the reference reflector, R_p. The vertical white lines and green bars denotes the boundaries of the frequency interval considered in the design problem D_1. (c) ΔL_{dB} for (blue circles) D_1 and (black squares) R_p. Vertical red lines denotes the boundaries of the frequency interval considered in the design problem D_1.

C. Considering Higher Frequencies

Two additional design problems, denoted D_2 and D_3, are considered to demonstrate the effectiveness of the proposed method over a wider frequency range. The central frequencies for D_2 and D_3 are denoted f_{c,D_2} and f_{c,D_3}, and correspond to the wavelengths, $\lambda_2 \approx 0.54$w and $\lambda_3 \approx 0.38$w respectively. Frequency bands of $\Delta f_{D_2} = 50\%$ and $\Delta f_{D_3} = 30\%$ centered at f_{c,D_2} and f_{c,D_3} are considered. Like for D_1, the design processes are executed using $i = 9$ equidistant frequency values and $j = 2$ projection levels.

1. Designs

Post processed versions of the design fields for the devices obtained for the design problems D_1, D_2 and D_3 are presented in Figs. 8a-8c. Test specimens used in the experimental investigation of the devices, were manufactured in ABS plastic using 3D-printing, based on extruded versions of the post processed design fields. Images of the 3D-printed specimens are provided in Figs. 8d-8f. The specimens consist of a base plate with the extruded device on top. The base plate has the dimensions of the hole in the PVC base plate in the experimental chamber, see Fig. 3b, while the extruded device is printed with an precision of 0.2 mm (the resolution of the 3D-printer).

2. Numerical Performance

The directivity measure, P_m, for the three devices obtained for the design problems D_1, D_2 and D_3 is presented in Figs. 8g-8i. Vertical white lines and green bars are used to indicate the frequency interval across which the devices

are designed to operate. For all three cases it is seen that, in these frequency intervals, the main lobe contains most of the emitted energy. Comparing across the three cases it is seen that both the fraction of the energy in the main lobe and the directivity increase from design D_1 to design D_2 and again from design D_2 to design D_3. All three devices outperform the reference parabolic reflector with respect to directivity as seen by comparing with Fig. 4c. The performance increase is most evident for design D_1 and design D_3 since the reflector already performs well in the frequency interval where design D_2 is optimized to operate. An important and obvious observation is that the directivity for all three devices deteriorate significantly outside the frequency range where they are optimized to operate, limiting the devices to be used inside the considered frequency ranges.

Figures 8m-8o present ΔL_{dB} for the designs D_1-D_3. The frequency intervals for which the devices are designed to operate are highlighted using vertical lines. Considering these intervals, it is seen that ΔL_{dB} varies less for the three designs than it does for the reference, R_p. Furthermore it is seen that ΔL_{dB} increases with frequency, in agreement with the increasing directivity observed in Figs. 8g-8i. Outside the frequency intervals, where the devices were designed to operate, ΔL_{dB} is seen to decrease and/or vary rapidly for all three designs.

VI. EXPERIMENTAL VALIDATION

The magnitude of the pressure field was measured experimentally, across $f \sim \frac{\mathrm{w}}{\lambda} \in [0.8, 3.15]$ and $\theta \in [0^{\mathrm{o}}, 180^{\mathrm{o}}]$, for each of the three test specimens in Figs. 8d-8f, using the procedure described in section IV. The results of the measurements are reported in Figs. 8j-8l using the measure P_m from (11), with the far field pressure, $|p_{\mathrm{far}}|$, replaced by the measured pressure, $|p_{\mathrm{meas}}|$.

Consider first the experimental results on their own. Oscillations in the measured pressure, as a function of both θ and $\frac{\mathrm{w}}{\lambda}$, are clearly observed for $\frac{\mathrm{w}}{\lambda} < 1.4$ and are observed to decrease with increasing frequency. This observation is in agreement with the findings from the reference measurement discussed in IV. That is, the damping material along the edges of the chamber is observed to have poorer absorption characteristics in the lower frequency range. It is further observed that in regions with low values of P_m, the limit of 3 dB above background noise is reached for all three designs.

A remarkable agreement is found when comparing simulations and experiments. Consider here the measured data in Figs. 8j-8l and the numerical data in Figs. 8g-8i. Note that the range of the data is identical, i.e. going from -24 dB to 6 dB. The major features and variations observed in the numerical data are also found in the experimental data. I.e. Agreement is found in the magnitude and width of the main lobe, as well as in the distribution of low and high values of P_m in the parameter domain, for all three designs. The largest deviations are found for $\frac{\mathrm{w}}{\lambda} < 1.4$ and are, as mentioned in the previous paragraph, believed to stem from the poor absorption characteristics of the damping material in the lower frequency range. I.e. the disagreement stems from experimental errors due to reflections from the boundaries.

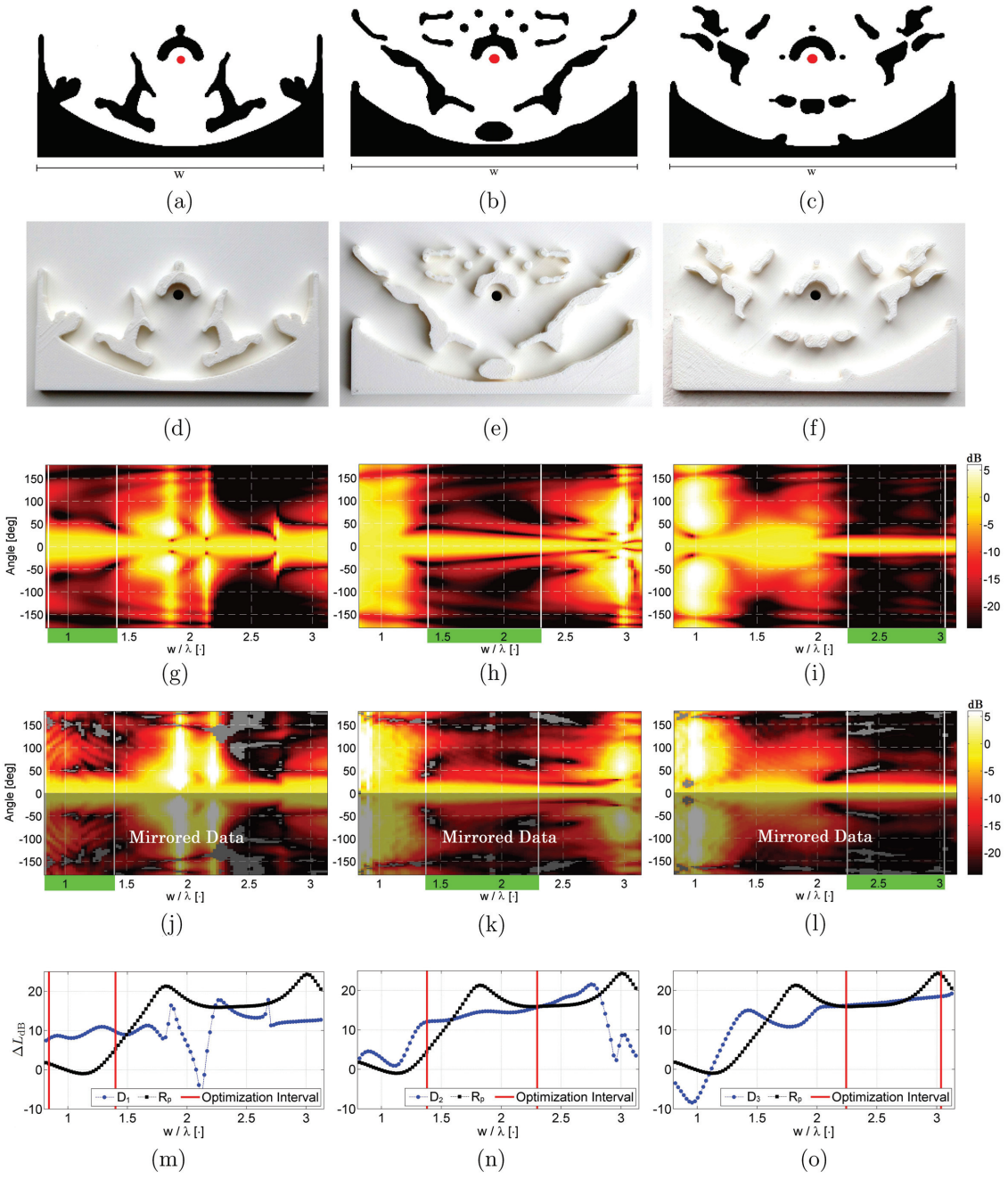

FIG. 8: (color online) (a)-(c) Post processed design field for D_i, (a) $i = 1$, (b) $i = 2$, (c) $i = 3$. (d)-(f) 3D-printed test specimen for D_i, (d) $i = 1$, (e) $i = 2$, (f) $i = 3$. (g)-(i) $P_m(\theta, f)$ calculated for the post processed design field for D_i, (g) $i = 1$, (h) $i = 2$, (i) $i = 3$. (j)-(l) Experimentally measured pressure at $r \approx 0.22$m, scaled by the on axis measured pressure ($\theta = 0$), for the test specimens for D_i, (j) $i = 1$, (k) $i = 2$, (l) $i = 3$. For (g)-(l) white lines and green bars illustrate the boundaries of the frequency bands considered in the design problems. (m)-(o) ΔL_{dB} calculated for R_p (black squares) and the post processed design field for D_i, (m) $i = 1$, (n) $i = 2$, (o) $i = 3$ (blue circles). Vertical red lines illustrate the boundaries of the frequency bands considered in the design problems.

A. Multiple Source Device

As a final example of the generality of the proposed method, consider the problem of designing a device for directional sound emission which contain three point-like sources placed asymmetrically inside $\mathbf{\Omega}_\mathrm{d}$ as sketched in Fig. 2b. This design problem is denoted D_4. The central frequency for D_4, denoted f_{c,D_4}, corresponds to the wavelength $\lambda_4 \approx 0.625$w. A frequency band $\Delta f_{D_4} = 40\%$ centered around f_{c,D_4} is considered. The design process is executed using $i = 9$ equidistant frequency values and $j = 2$ projection levels.

The post processed design for D_4 is presented in Fig. 9a with black being solid material and white being air. As for the illustrations of the design fields for the devices D_1-D_3 red circles are used to denote the position of the sources.

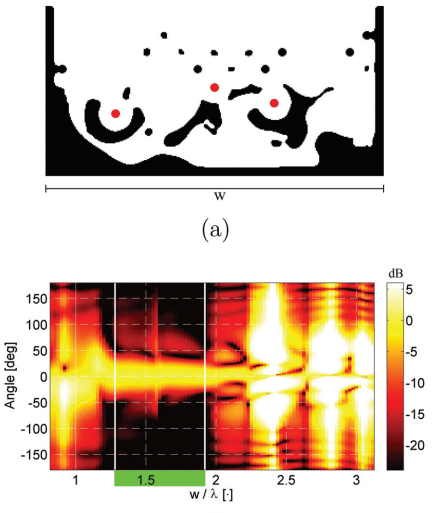

FIG. 9: (color online) (a) Post processed design field for the device obtained in the design problem D_4 including red circles denoting the position of the point like sources. (b) $P_m(\theta, f)$ for the device obtained in the design problem D_4, including vertical white lines and a green ar to illustrate the boundaries of the frequency interval considered in the design problem.

Figure 9b shows P_m, obtained numerically for D_4 in the intervals $\theta \in [-180^\mathrm{o}, 180^\mathrm{o}]$ and $\frac{w}{\lambda} \in [0.8, 3.15]$. The asymmetry of the problem is clearly observed in the figure. The interval for which D_4 is optimized is marked by white vertical lines and a green bar. In this frequency interval, the main lobe is seen to contain most of the emitted energy. A sudden increase in P_m is observed at $\frac{\mathrm{w}}{\lambda} \approx 1.6$. This value corresponds to a frequency not considered in the optimization, suggesting that including more frequency values in the optimization would remove the jump. Just as for the designs obtained for D_1-D_3 it is observed that in several regions outside the interval for which D_4 was optimized to function its performance drops below that of the reference reflector, R_p.

VII. CONCLUSIONS

In summary, the paper has presented a topology optimization based design method for creating acoustic focusing devices exhibiting high directivity and power output. The method is demonstrated in 2D using the parabolic reflector design as a reference. It is shown that the method is capable of designing devices functioning across broad frequency bands, at wavelengths comparable to the device dimensions, a frequency range which is typically problematic. An experimental approach and setup for validating the optimized devices is presented. Three designed devices were 3D-printed and their performance investigated using the experimental setup. The measured and numerical data show remarkable agreement, supporting the "real world" applicability of the method (barring implementing 2D circular symmetrical or 3D version of the code). While the majority of the examples focused on the parabolic like reflector, the method is not restricted to this case. This was demonstrated by considering an alternate configuration with three point sources scattered asymmetrically inside the design domain. Other configurations and more complex near fields may be considered with the method by simple modifications of the target field and/or design domain.

As a final remark it is noted that relatively small changes in the choice of model parameters have been found to result in large changes in the geometry of devices obtained using the proposed method. In all cases the changes in device geometry have been found to have limited effects on the performance of the device however and are thus not deemed problematic. The reason behind the observed sensitivity towards parameter choices is believed to be the nature of the design problem, having a vast design space, coupled with the nature of the acoustic problem. The finding is in agreement with the conclusion reached in Wadbro and Berggren [29] regarding the underdeterminedness of a problem with similar characteristics considered there. A number of comments and guidelines intended to help in using the proposed method are included in Appendix C.

Acknowledgments

Assistant Engineer Jørgen Rasmussen at the Department of Electrical Engineering at the Technical University of Denmark helped to a large degree in preparing the experimental setup. The workshop at the Department of Mechanical Engineering at the Technical University of Denmark aided in the processing of select components for the

experimental setup. The 3D-printing laboratory FabLab at the Tecnical University of Denmark produced the test specimens with Technician Jannick Schultz at the Department of Mechanical Engineering at the Technical University of Denmark in charge of the printing. The work was financially supported by Villum Fonden through the research project *Topology Optimization - the Next Generation*.

APPENDIX A: DESIGN PROCEDURE DETAILS

1. Design Problem

The design problem is formulated as a min/max problem, where maximum value of $\Phi(p(f_i,\eta_{2,j}))$, see (4), for $i \in \{1,2,...,\mathcal{N}_f\}$ frequencies and $j \in \{1,2,...,\mathcal{N}_{\eta_2}\}$ projection levels, is minimized over $\xi(\mathbf{x})$. That is, over the distribution of solid material in $\mathbf{\Omega}_{\mathrm{d,d}}$. Two constraints are considered. The first is that p must be a solution to the model equations, (1)-(3). The second is a volume constraint, imposed on the double filtered field, see (A2).

$$\min_{\xi} \max_{f_i,\eta_{2,j}} \left(\Phi(p(\mathbf{x},\hat{\tilde{\xi}}(\eta_{2,j}),f_i),p_{\mathrm{target}}(\mathbf{x},f_i)) \right), \quad \text{(A1)}$$

$$\text{s.t. } \frac{1}{\int \mathrm{d}\mathbf{\Omega}_{\mathrm{d}}} \int \max_{\eta_{2,j}}(\hat{\tilde{\xi}}(\eta_{2,j}))\ \mathrm{d}\mathbf{\Omega}_{\mathrm{d}} \leq V, \quad V \in]0,1]. \quad \text{(A2)}$$

The min/max problem, (A1)-(A2) is recast to the bound formulation proposed in Svanberg [25] and solved using *The Globally Convergent Method of Moving Asymptotes* (GCMMA),[24,25] with a maximum of 3 inner iterations per design iteration.

The following stopping criterion is used for the design procedure,

$$\beta_1 > 80 \wedge \max_{m\in 1,2,...,5} \frac{|\Phi_n - \Phi_{n-m}|}{|\Phi_n|} < 10^{-2}, \quad \text{(A3)}$$

where Φ_n is the objective value at the n'th iteration. To improve the convergence of the design procedure the problem is non-dimensionalized and the following rescaling and normalization is applied for α, κ and ω,

$$(\hat{\rho},\hat{\kappa}) = \begin{cases} (1,1) & \text{for air} \\ \left(\frac{\rho_{\mathrm{solid}}}{\rho_{\mathrm{air}}}, \frac{\kappa_{\mathrm{solid}}}{\kappa \mathrm{air}}\right) & \text{for solid} \end{cases}, \quad \hat{\omega} = \frac{\omega}{c}. \quad \text{(A4)}$$

2. The Design Field

During the design process, the design itself is modeled as a distribution of solid material in an air background within $\mathbf{\Omega}_{\mathrm{d}}$. The auxiliary design field, ξ, controls the distribution by interpolating the inverse material parameters, ρ^{-1} and κ^{-1} between solid material ($\xi = 1$) and air ($\xi = 0$). The introduction of ξ allows for a mix of solid material and air to exist at each point in space during the intermediate stages of the design process. This mix is gradually removed by applying a projection scheme with a continuation approach on the projection strength as part of the design process,[13,32]. The bounds on ξ are defined as: $\xi(\mathbf{x}) \in [0,1]\ \forall\ \mathbf{x} \in \mathbf{\Omega}_{\mathrm{d,d}},\ \xi(\mathbf{x}) = 0\ \forall\ \mathbf{x} \in \mathbf{\Omega}\backslash(\mathbf{\Omega}_{\mathrm{d}}\backslash\mathbf{\Omega}_{\mathrm{d,e}}),\ \xi(\mathbf{x}) = 1\ \forall\ \mathbf{x} \in \mathbf{\Omega}_{\mathrm{d,f}}$.

The proposed design method allows for designing devices which perform robustly under geometric perturbations, like what might occur during production, installation or use. For the presented examples only near-uniform geometric perturbations are included,[31] where the size of all features in the design device is varied in a near-identical manner. However non-uniform spatial perturbations of the designs can also be considered,[23]. The robustness is assured by using a double filtering technique,[9] consists of applying a smoothing operator,[4,5],

$$\tilde{\xi}(\mathbf{x}_i) = \frac{\int_{\mathbf{\Omega}_{\mathrm{d}}} w(\mathbf{x}_i - \mathbf{x}_j)\xi(\mathbf{x}_j)\mathrm{d}\mathbf{x}_j}{\int_{\mathbf{\Omega}_{\mathrm{d}}} w(\mathbf{x}_i - \mathbf{x}_j)\mathrm{d}\mathbf{x}_j}, \quad \text{(A5)}$$

$$w(\mathbf{x}) = \begin{cases} R - |\mathbf{x}| & \forall\ |\mathbf{x}| \leq R \wedge \mathbf{x} \in \mathbf{\Omega}_{\mathrm{d}} \\ 0 & \text{otherwise} \end{cases}, \quad \text{(A6)}$$

where R is a filter radius, followed by a projection operator,[31],

$$\hat{\xi}(\xi) = \frac{\tanh(\beta\eta) + \tanh(\beta(\xi - \eta))}{\tanh(\beta\eta) + \tanh(\beta(1 - \eta))}, \quad \text{(A7)}$$

where η is the projection level and β is the projection strength, to ξ twice.

The double filter requires two filter radii, $R_1 = 2R_2$ as well as two projection strengths $\beta_1 = 2\beta_2$ and two projection levels η_1, η_2. A continuation scheme on the projection strength is applied on β_1 with $\beta_1 = \beta_{\mathrm{ini}}$ as the initial value and this value is then increased by a factor of 1.2 every 50 design iterations or when the objective function value changes by less than one percent over 5 consecutive iterations. This procedure is continued until $\beta_1 \geq 80$ is reached. At this value for β_1 the distribution of solid material and air resulting from the design process is close to being discrete throughout $\mathbf{\Omega}_{\mathrm{d}}$, limiting the need for a post processing step. The application of the double filter on ξ means that the interpolation of ρ^{-1} and κ^{-1} in (A8) is performed using the doubly filtered field as,

$$\rho^{-1} = \rho_{\mathrm{air}}^{-1} + \hat{\tilde{\xi}}(\rho_{\mathrm{solid}}^{-1} - \rho_{\mathrm{air}}^{-1}), \quad \text{(A8)}$$

$$\kappa^{-1} = \kappa_{\mathrm{air}}^{-1} + \hat{\tilde{\xi}}(\kappa_{\mathrm{solid}}^{-1} - \kappa_{\mathrm{air}}^{-1}). \quad \text{(A9)}$$

For the software implementation, the doubly filtered auxiliary field is discretized into a piecewise constant field consisting of $\mathcal{N}_{\mathrm{e}}$ discrete design variables coinciding with the

finite element discretization of $\mathbf{\Omega}_\mathrm{d}$. The sensitivities of the objective function with respect to the design variables, $\frac{\mathrm{d}\Phi}{\mathrm{d}\xi_j}, j \in \{1, 2, ..., \mathcal{N}_\mathrm{e}\}$, needed for solving the optimization problem using GCMMA, are calculated using adjoint sensitivity analysis,[26].

APPENDIX B: EXPERIMENTAL SETUP DATA

See table II.

TABLE II: Dimensions of components used in the experimental setup along with material types and parameter values. An upper bound on the uncertainty is included where deemed relevant.

Component:	**width × breadth × height**
Chamber:	
Chamber, [m]	$0.785 \times 0.785 \times 0.006 \pm 5 \cdot 10^{-4}$,
PVC (base) plate [m]	$1.1 \times 1.1 \times 0.01$
Acrylic (top) plate [m]	$1.5 \times 1.5 \times 0.01$
Wooden strips [m]	$1.1 \times 0.026 \times 0.006 \pm 5 \cdot 10^{-4}$
Absorbing foam strips [m]	$1.05 \times 0.130 \times 0.006 \pm 5 \cdot 10^{-4}$
Test specimen:	
Base [m]	$(0.2 \times 0.1 \times 0.01) \pm 2 \cdot 10^{-4}$
Device [m]	$(0.1 \times 0.05 \times 0.006) \pm 2 \cdot 10^{-4}$
Material:	**value or type**
Absorbing foam:	Basotec from BASF
PVC Plate:	Trovidur EC
Acrylic Plate:	Plexiglas XT
ABS plastic:	
- Density, ρ [kg/m^3]	954
- Bulk Modulus, κ [GPa]	1.9

APPENDIX C: COMMENTS AND GUIDELINES

During the development and testing of the proposed method it was found that special care should be exercised regarding the points listed below.

1. The energy contained in p_target must be equal to the energy emitted by the sources to obtain a high transmission of energy from the device. E.g. if more energy is emitted from the sources than are present in p_target it is impossible to achieve full transmission of the energy from the sources into p_target.

2. Select a correct scaling of optimization parameters. Tuning may be needed to assure smooth convergence for the problem.

3. The frequency bandwidth for which the device should operate and the size of the geometric perturbations are important to the convergence behavior of the design procedure, as well as for the performance of the final designs. E.g. if an overly wide frequency band is considered the resulting design may perform poorly and/or the optimization algorithm may have problems converging.

[1] M. Bai, J. Ih, J. *Benesty Acoustic Array Systems: Theory, Implementation, and Application.* (John Wiley & Sons Singapore Pte. Ltd. 2013) pp. 1-510.

[2] M. Bendsøe, Sigmund O, *Topology Optimization.* (Springer-Verlag Berlin Heidelberg, 2nd edition, 2003), pp 1-370.

[3] E. Bängtsson, D. Noreland, M. Berggren, *Shape optimization of an acoustic horn.* Computational Methods in Applied Mechanical Engineering **192**, 1533–1571 (2003).

[4] B. Bourdin, *Filters in topology optimization.* International Journal for Numerical Methods in Engineering **50**, 2143–2158 (2001).

[5] T. Bruns, D. Tortorelli Topology, *optimization of non-linear elastic structures and compliant mechanisms.* Computational Methods for Applied Mechanical Engineering **190**, 3443–3459 (2001).

[6] J. Chang, F. Jacobsen, *Sound field control with a circular double-layer array of loudspeakers.* Journal of the Acoustical Society of America **131**(6), 4518–4525 (2012).

[7] J. Chang, F. Jacobsen, *Experimental validation of sound field control with a circular double-layer array of loudspeakers.* Journal of the Acoustical Society of America **133**(4), 2046–2054 (2013).

[8] R. Christiansen, E. Fernandez-Grande, Sigmund O, *Experimental validation of topology optimized acoustic cavity.* Journal of the Acoustical Society of America **138**(6), 3470–3474 (2015).

[9] R. Christiansen, B. Lazarov, J. Jensen, O. Sigmund, *Creating geometrically robust designs for highly sensitive problems using topology optimization - acoustic cavity design.* Structural and Multidiciplinary Optimization **52**, 737–754 (2015).

[10] M. Clark, *An acoustic lens as a directional microphone.* Journal of the Acoustical Society of America **25**, 1152–1153 (1953).

[11] M. Dühring, J. Jensen, O. Sigmund, *Acoustic design by topology optimization.* Journal of Sound and Vibration **317**, 557–575 (2008).

[12] J. Du, N. Olhoff, *Minimization of sound radiation from vibrating bi-material structures using topology optimization.* Structural and Multidiciplinary Optimization **33**, 305–321 (2007).

[13] J. Guest, J. Prévost, T. Belytschko, *Achieving minimum length scale in topology optimization using nodal design variables and projection functions.* International Journal for Numerical Methods in Engineering **61**, 238–254 (2004).

[14] B. Hal, W. Desmet, B. Pluymers, P. Sas, D. Vandepitte, *A coupled finite element - wave based approach for the steady-state dynamics analysis of acoustic systems.* Journal of Computational Acoustics **11**, 285–303 (2003).

[15] T. Hueter, *Twenty years in underwater acoustics: generation and reception.* Journal of the Acoustical Society of America **51**(3), 1025–1040 (1972).

[16] F. Jacobsen, P. Juhl, *Fundamentals of General Linear Acoustics.* (John Wiley and Sons, Inc. Boschstrasse 12, D-69469 Weinheim Germany, 2013), Chap. 6.

[17] F. Jacobsen, P. Juhl, *Fundamentals of General Linear Acous-*

tics. (John Wiley and Sons, Inc. Boschstrasse 12, D-69469 Weinheim Germany, 2013), Chap. 9.
[18] J. Kook, K. Koo, J. Hyun, J. Jensen, S. Wang, *Acoustical topology optimization for zwicker's loudness model - application to noise barriers.* Computational Methods for Applied Mechanical Engineering **237**, 130–151 (2012).
[19] R. Little, *acoustic properties of parabolic reflectors.* Journal of the Acoustical Society of America **40**, 919–920 (1966).
[20] M. McKemie, C. McKinney, *An experimental investigation of the parabolic reflector as a nearfield calibration device for underwater sound transducers.* Journal of the Acoustical Society of America **67**, 523–529 (1980).
[21] B. Pluymers, *Wave based modelling methods for steady-state vibro-acoustics.* (PhD thesis, Katholieke Universiteit Leuven - Oude Markt 13 - bus 5005, 3000 Leuven, Belgium, 2006), Chapter 6 and Chapter 7, pp 1-342.
[22] R. van der Rots, A. Berkhoff, *Directional loudspeaker arrays for acoustic warning systems with minimised noise pollution.* Applied Acoustics **89**, 345–354 (2015).
[23] M. Schevenels, B. Lazarov, O. Sigmund, *Robust topology optimization accounting for spatially varying manufacturing errors.* Computational Methods for Applied Mechanical Engineering **200**, 3613–3627 (2011).
[24] K. Svanberg, *The method of moving asymptotes - a new method for structural optimization.* International Journal for Numerical Methods in Engineering **24**, 359–373 (1987).
[25] K. Svanberg, *A class of globally convergent optimization methods based on conservative convex seperable approximations.* SIAM Journal of Optimization **12**, 555–573 (2002).
[26] D. Tortorelli, P. Michaleris, *Design sensitivity analysis: Overview and review.* Inverse Problems in Engineering **1**, 71–103 (1994).
[27] R. Udawalpola, M. Berggren, *Optimization of an acoustic horn with respect to efficiency and directivity.* International Journal for Numerical Methods in Engineering **73**, 1571–1606 (2007).
[28] M. Ureda, *Analysis of loudspeaker line arrays.* Journal of the Audio Engineering Society **52**(5), 467–495 (2004).
[29] E. Wadbro, M. Berggren, *Topology optimization of an acoustic horn.* Computational Methods for Applied Mechanical Engineering **196**, 420–436 (2006).
[30] S. Wahlström, *The parabolic reflector as an acacoustic amplifier.* Journal of the Audio Engineering Society **33**(6), 418–429 (1985).
[31] F. Wang, B. Lazarov, O. Sigmund, *On projection methods, convergence and robust formulations in topology optimization.* Structural Multidiciplinary Optimization **43**, 767–784 (2011).
[32] S. Xu, Y. Cai, G. Cheng, *Volume preserving nonlinear density filter based on heaviside projections.* Structural Multidiciplinary Optimization **41**, 495–505 (2010).

DTU Mechanical Engineering
Section of Solid Mechanics
Technical University of Denmark

Nils Koppels Allé, Bld. 404
DK-2800 Kgs. Lyngby
Denmark
Phone (+45) 4525 4250
Fax (+45) 4593 1475
www.mek.dtu.dk
ISBN: 978-87-7475-460-2

DCAMM
Danish Center for Applied Mathematics and Mechanics

Nils Koppels Allé, Bld. 404
DK-2800 Kgs. Lyngby
Denmark
Phone (+45) 4525 4250
Fax (+45) 4593 1475
www.dcamm.dk
ISSN: 0903-1685